Surface Formation Routes of Interstellar Molecules
A Laboratory Study

Surface Formation Routes of Interstellar Molecules - A Laboratory Study
Sergio Ioppolo
Thesis Universiteit Leiden - Illustrated - With summary in Dutch - With references
ISBN/EAN 978-90-9025854-6
Printed by Ipskamp Drukkers
Cover by Petra Vacková - pet.vackova@gmail.com

Surface Formation Routes of Interstellar Molecules
A Laboratory Study

PROEFSCHRIFT

ter verkrijging van
de graad van Doctor aan de Universiteit Leiden,
op gezag van de Rector Magnificus prof.mr. P.F. van der Heijden,
volgens besluit van het College voor Promoties
te verdedigen op donderdag 9 december 2010
klokke 15.00 uur

door

Sergio Ioppolo
geboren te Catania, Italië
in 1980

Promotiecommissie

Promotores:	Prof. dr. H. V. J. Linnartz	
	Prof. dr. E. F. van Dishoeck	
Co-promotor:	Dr. H. M. Cuppen	
Overige Leden:	Prof. dr. K. Kuijken	
	Prof. dr. A. G. G. M. Tielens	
	Prof. dr. E. Herbst	Ohio State University
	Dr. W. Brown	University College London
	Dr. M. E. Palumbo	Catania University

Contents

CHAPTER 1

Introduction

1.1 The interstellar medium

Our Galaxy is largely empty. By terrestrial standards the space between the stars can be considered as a near-perfect vacuum: the average particle density in the solar neighborhood is roughly a factor of 10^{19} less than in the terrestrial atmosphere at sea level. However, the highly diluted material present between the stars, the so-called InterStellar Medium (ISM), plays a central role in the chemical evolution of the Galaxy. The ISM is the repository of ashes from previous generations of stars and it is itself the birthplace of new stars and planetary systems. The interstellar matter consists of about 99% gas and 1% (sub)micron size silicate and carbonaceous dust grains by mass. The interstellar gas is composed of roughly 89% hydrogen, 9% helium and 2% heavier elements. The gas in the ISM is found in a variety of phases: coronal gas, ionized gas, neutral atomic gas and molecular gas (Tielens 2005). The physical properties of these phases are summarized in Table 1.1. Hot ionized gas is observed in X-ray emission and as UV absorption lines of highly ionized atoms (*e.g.*, C IV, N V, O VI). It is present in the coronal gas of stars and composes the Hot Ionized Medium (HIM), a hot and tenuous phase of the ISM. The gas in these regions is heated and ionized through shocks driven by stellar winds from early type stars and by supernova explosions. Diffuse ionized gas is observed mainly through emission in the Hα recombination line and resides in both a diffuse component, the so-called Warm Ionized Medium (WIM), as well as in the classical H II regions surrounding hot O and B stars. Neutral atomic gas is traced though the 21 cm line of atomic hydrogen, and is found in the Warm Neutral Medium (WNM) and Cold Neutral Medium (CNM). Molecular gas represents the densest component of the ISM. Although H_2 is the dominant molecular species in space followed by CO (H_2/CO = 10^4 – 10^5), it cannot be routinely detected in cold gas by infrared telescopes because of the lack of dipole allowed transitions. Therefore, molecular gas is commonly traced through the CO rotational transitions, such as $J = 1-0$ at 2.6 mm. Molecular gas is localized in discrete Giant Molecular Clouds (GMC), which tend to be irregularly shaped with a density distribution far from homogeneous. Molecular clouds contain embedded cores in which new stars form.

Table 1.1 Main characteristics of interstellar medium components: coronal gas and hot ionized medium (HIM), H II regions, warm ionized medium (WIM), warm neutral medium (WNM), cold neutral medium (CNM), and molecular clouds. The values in this Table are taken from Tielens (2005) and Visser (2009).

Component	Fractional Volume (%)	Scale Height (pc)	Temperature (K)	Density (cm^{-3})	State of hydrogen
Coronal gas					
HIM	30–70	1000–3000	10^6 – 10^7	10^{-4} – 10^{-2}	ionized
WIM	20–50	1000	8000	0.2–0.5	ionized
H II regions	<1	70	8000	10^2 – 10^4	ionized
WNM	10–20	300–400	6000–10000	0.2–0.5	neutral atomic
CNM	1–5	100–300	50–100	20–50	neutral atomic
Molecular clouds	<1	70	10–50	10^2 – 10^6	molecular

1.2 The cycle of matter

The evolution of gas and dust in the ISM from stellar birth to death can be described as a cyclic event as shown in Fig. 1.1. The complete cycle takes some 2×10^9 years. In the first step, stellar winds and/or explosions enrich the diffuse interstellar medium in dust and gas. Carbonaceous dust grains are ejected by carbon-rich stars (C/O>1) at high densities and temperatures, and silicates originate from oxygen-rich star ejecta. Observations combined with models showed that $\lesssim$10% of the interstellar dust mass has a "stardust" origin (*i.e.*, formation in the atmospheres of evolved stars), and that interstellar grains are mostly formed in the ISM by some chemical mechanism which is not yet characterized (Draine 2009, and references therein). The interstellar grains pass through the various aforementioned phases of the interstellar medium several times on a typical scale of $\sim3\times10^7$ years, before they take part in the formation of a new star. In the intercloud phase, grains can coagulate leading to an increase in their size, while strong shocks destroy dust and change its size distribution. Supernova shocks can also trigger the collapse of diffuse clouds into dense clouds. In the denser phase, atomic gas is converted into simple molecules, like CO, through gas-phase reactions, while H-rich species such as H_2O, NH_3, and CH_4 are formed on the grains through surface reactions, resulting in a polar ice mantle. For densities higher than 10^5 cm^{-3} most of the gas-phase molecules, mainly CO, freeze-out onto the dust grains on timescales shorter than the lifetime of a core. The resulting apolar ice, which is typically a few tens of monolayers (ML) thick, is further involved in chemical reactions. The composition and evolution of interstellar ices are described in more detail in § 1.3.1.

Molecular clouds are stable over timescales of $\sim3\times10^7$ years because of a balance of turbulent and magnetic pressure and gravity. Physically this is expressed by the virial theorem, which states that, to maintain equilibrium, the gravitational potential energy must equal twice the internal thermal energy. The gravitational collapse of the core is initiated by the loss of turbulent or magnetic support. As it collapses, a molecular cloud can fragment into smaller pieces. Each of the cold cores collapses in an isothermal manner since the gas (atoms and molecules) releases energy in the form of radiation (Bergin & Tafalla 2007). While the density increases (10^5–10^7 cm^{-3}), the fragments become optically opaque and are thus less efficient at releasing their energy through radiation. During the collapse the central cores (*i.e.*, the protostars) gradually warm up and emit a continuum of infrared radiation. The warm-up of cloud cores ($20\ \mathrm{K} < T < 100\ \mathrm{K}$) induces the desorption of volatile species, like CO, O_2 and N_2, from dust grains and the segregation of less volatile ones, like CO_2. At such temperatures H atoms are no longer residing onto the grains, and therefore hydrogenation reactions are no longer a dominant process. Moreover, the increase in temperature facilitates a higher mobility of the solid species still frozen on the grains and, therefore, drives a rich grain-surface chemistry.

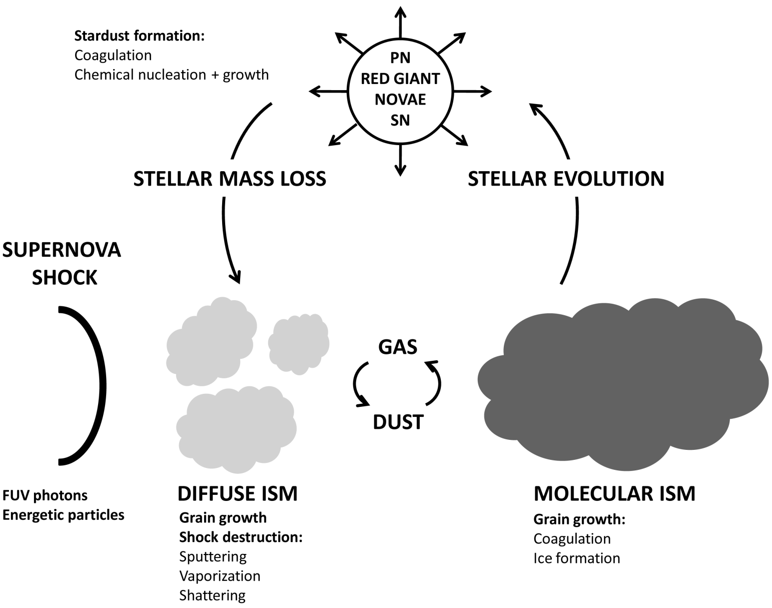

Figure 1.1 Schematic representation of the lifecycle of cosmic dust. Dust is formed in stellar ejecta (planetary nebulae, red giants, novae and supernovae) and mainly in the interstellar medium itself, where it cycles rapidly between the different phases. In the intercloud phase, strong shocks destroy dust and change its size distribution. In the denser phase, the accretion of gas-phase species onto grains forms an ice mantle, which is exposed to atoms and processed by FUV photons and energetic particles. Coagulation leads to an increase in the grain size. Ultimately, dust particles are involved in the star and planet formation process. Figure adapted from Tielens & Allamandola (1987b) and Tielens (2005).

The objects resulting from the cloud collapse are called Young Stellar Objects (YSOs). At this stage, YSOs are rotating spheres of gas with a central protostar. Stars of different masses are thought to form by slightly different mechanisms. The process of single low- and intermediate-mass star formation ($M_\star < 8\ M_\odot$), schematically displayed in Fig. 1.2, is well understood (*e.g.*, Evans 1999, van Dishoeck 2004, and references therein). Because of the conservation of angular momentum the collapse of a rotating sphere of gas and dust (Fig. 1.2b) leads to the formation of an accretion disk through which matter is guided onto the central protostar (Fig. 1.2c). The temperature in the midplane of the disk drops to 10 K and the density increases to $\sim 10^{12}$ cm^{-3}. Therefore, gas-phase species will accrete onto the grains again. Also grains will coagulate, forming most likely larger and larger boulders, and eventually planets, even though this process is not completely understood yet. The surface of the disk is affected by a strong UV field from the protostar, the gas temperature often exceeds 100 K in the outer disk (>1000 K in the inner disk) and the density is $\sim 10^6$ cm^{-3}.

Under such harsh conditions, ices cannot survive and, therefore, only gas-phase species will participate in the chemistry of the warm inner envelope, known as hot core (Herbst & van Dishoeck 2009). Hot cores are characterized by a density of 10^7–10^8 cm^{-3}, a temperature of $\sim$100 K and size of $\sim$100 AU. Some excess angular momentum is also dissipated through large bipolar outflows, launched along the core's rotation axis near the protostar (Shu et al. 1991, Bally 2007). The gas present in the circumstellar disk will eventually fall onto the star, planets and small bodies present in the disk, or will be cleared by irradiation and winds from the star in a timescale of $\sim 10^6$ years (Fig. 1.2d-e). For low-mass stars, the disk will slowly evolve into a planetary system such as our Solar system (Fig. 1.2f). When the temperature of the protostar is sufficiently high to initiate nuclear burning of hydrogen into helium, a new star is born.

The formation process of high-mass stars ($M_\star > 8\ M_\odot$) is not yet fully understood because of observational problems: they are embedded objects that evolve rapidly to the main sequence. However, except for the most massive ones, massive stars most likely form by a mechanism similar to that observed for low-mass stars. It is likely that the initial phase involves the collapse of infrared dark clouds within giant clouds. High-mass young stellar objects are associated with ultra- or hypercompact H II regions, masers, outflows, and/or warm ambient gas at average temperatures of 300 K, known as hot cores (Herbst & van Dishoeck 2009). The hot cores usually have a size of 10^4 AU and often are associated with a rich organic chemistry. It is not yet clear whether disks are formed in high-mass star regions. If newly formed luminous O and B stars are in the proximity of cool interstellar matter, their UV radiation heats the neighboring gas and photodissociates molecules, producing heterogeneous Photon-Dominated Regions (PDRs) (van Dishoeck 2004).

Ongoing and future key new instrumentation, such as the *Herschel Space Observatory* and ALMA, will unravel the chemistry and dynamics of star and planet formation with more detail than possible so far. This will allow us to resolve the physical processes taking place during the collapse of molecular clouds, to image the structure of protostars and of protoplanetary disks, and to determine the chemical composition of the material from which future solar systems are made (van Dishoeck & Jørgensen 2008).

The final stages of the star evolution are well understood. Protostars with masses less than roughly 0.08 $M_\odot$ never reach temperatures high enough for nuclear fusion of hydrogen to begin. These are known as brown dwarfs. For $0.08 < M_\star < 8\ M_\odot$, the star will spend a long time on the main-sequence phase (10^7-10^{10} yr) and nuclear fusion will form elements up to C, O and N. After leaving this phase, stars below $0.23\ M_\odot$ become white dwarfs, while more massive stars will move into the Red Giant and Asymptotic Giant Branch (RGB and AGB) phases and eventually evolve into a planetary nebula with a white dwarf core. Red giant winds and planetary nebulae are important sources of gas and dust enrichment in the ISM. In this way the matter cycle of low-mass stars is complete.

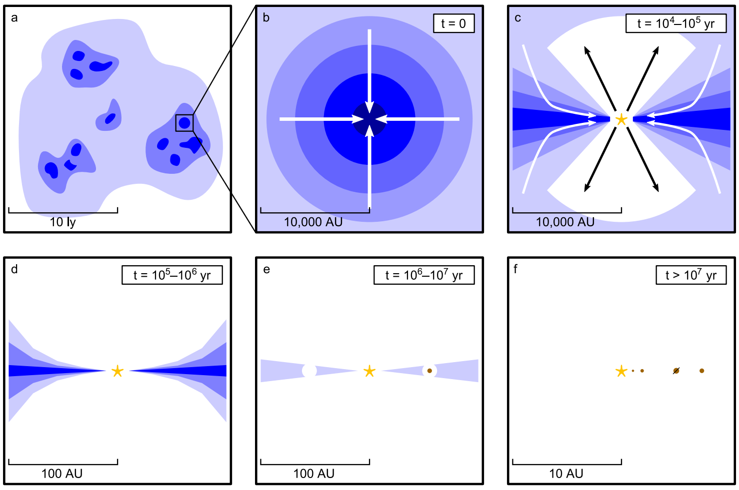

Figure 1.2 Schematic illustration of the different stages of low-mass star formation. Dense clouds can form when the diffuse medium is compressed by a shock event such as a supernova explosion (a). Once the density in the core of dense clouds gets high enough and support is lost, the core starts to collapse (b). Conservation of angular momentum results in the formation of a circumstellar disk and bipolar outflows (c). The disk will eventually evolve into a planetary system (d-f). Figure taken from Visser (2009), based on Hogerheijde (1998).

High-mass stars spend a shorter time along the evolutionary phases, burning elements up to Fe. Since no further energetically favorable nuclear reactions can occur, the core will collapse. Depending on the initial mass, the core can become a neutron star, a pulsar or a black hole. The outer shells of the star will explode in a violent event, a so-called supernova explosion, which can trigger the nucleosynthesis of elements heavier than Fe. These shocks can perturb the surrounding ISM and therefore trigger star formation closing the cycle of matter.

1.3 Interstellar ices

1.3.1 Interstellar ice composition

Rotational, vibrational, and electronic spectroscopy has established the presence of a large variety of polyatomic molecules, ions and radicals in space, both in the gas phase and in the solid state. In fact, over 150 different molecular species (excluding isotopomers) have been detected in the inter- and circumstellar medium. These species include a variety of inorganic compounds (*e.g.*, H_2O, CO, CO_2, NH_3, SO and SO_2), organics (*e.g.*, CH_4, H_2CO, CH_3OH, HCOOH, and CH_3CH_2OH), ions (*e.g.*, C_6H^-) and species identified only in the ice like OCN^- and NH_4^+), and unsaturated hydrocarbon chains (*e.g.*, HCN, HC_3N). Recently, large carbonaceous species like the fullerenes C_{60} and C_{70} have been unambiguously detected (Cami et al. 2010, Sellgren et al. 2010). However, aromatic species such as polycyclic aromatic hydrocarbons (PAHs) are not included in the count, since they are not uniquely identified. PAHs are detected only as a class through their infrared features. The spectra of molecular species are probes of the physical conditions and chemical history of the regions in space where they reside. Hence, high-resolution rotational and vibrational spectra improve our knowledge about the density and temperature of the gas as well as collapse of interstellar clouds, whereas vibrational spectra of solid phase molecules give information on the nature of the ice mantles covering dust grains.

The presence of ice in the interstellar medium was already proposed by Eddington (1937) before its spectral detection, which came almost four decades later: H_2O ice was detected at 3 μm by Gillett & Forrest (1973). Most ices can be detected in absorption in the mid-IR of an embedded object or along the line of sight of a background star. However, ground based observations in the mid-IR spectral window are limited because of telluric absorption. Airborne and space observatories have therefore been used to identify solid phase species in space in the last decades. In the 1990's the launch of the *Infrared Space Observatory* (ISO) revolutionized our understanding of interstellar ices. Because of its limited sensitivity, ISO observed mostly bright sources, such as high-mass YSOs and quiescent dense clouds toward luminous background stars (Gibb et al. 2000b, 2004). Observations show that H_2O, CO, CO_2, and, in some cases, CH_3OH represent the bulk of solid-state species in dense molecular clouds and star-forming regions. Minor ice components, such as CH_4, NH_3, H_2CO, HCOOH, SO_2, OCS, OCN^-, NH_4^+, and $HCOO^-$, are also observed, although their identification is sometimes controversial. Completely isolated single bands from species such as solid CH_4 at 7.67 μm and OCS at 4.92 μm are confidently assigned (see Table 1.2). However, the identification of other species like H_2CO, HCOOH and NH_3 is more problematic because all their strong vibrational modes overlap with features of other species (Table 1.2; van Dishoeck 2004, and references therein).

More recently, the *Spitzer Space Telescope* characterized the molecular content of icy grain mantles in the 5−35 μm wavelength range towards more than 40 low-mass protostars within the c2d (cores to disks) program (Boogert et al. 2008, Pontoppidan et al. 2008, Öberg et al. 2008, Bottinelli et al. 2010) and dozens more within other programs

Table 1.2 Interstellar ice inventory with respect to H_2O ice towards dark clouds, low- and high-mass YSOs. Selected solid state infrared transitions are also listed.

Species	Mode	λ (μm)	Dark cloud (Elias 16)	Low-mass YSO (HH 46)	High-mass YSO (W33A)
H_2O	O-H stretch	3.05	100	100	100
	H-O-H bend	6.0			
	libration	12			
CO	C=O stretch	4.67	26[a]	20[b]	8.1[c]
CO_2	C=O stretch	4.27	24[d]	21.6[e]	14.1[e]
	O=C=O bend	15.3			
HCOOH	C=O stretch	5.85	≤1.4[f]	2.7[f]	5.2[f]
	CH deformation	7.25			
	C-O stretch	8.1			
H_2CO	C-H (asym., sym.)	3.47, 3.54	...	6.0[f]	3.1[c]
	C=O stretch	5.81			
	CH_2 scissor	6.69			
CH_3OH	O-H stretch	3.08	<2.3[f]	6.1[g]	14.7[f]
	C-H stretch	3.53			
	CH_3 deformation	6.85			
	CH_3 rock	8.85			
	C-O stretch	9.75			
NH_3	N-H stretch	2.96	≤8[d]	6.1[g]	15[c]
	deformation	6.16			
	umbrella	9.0			
NH_4^+	deformation	6.85	5.2[f,i]	6.3[f,i]	8.1[f,i]
CH_4	C-H stretch	3.32	<3[d]	5.0[h]	1.5[c]
	deformation	7.67			
OCN^-	C≡N stretch	4.62	<2.3[d]	≤0.6[j]	1.9[j]
OCS	O=C=S stretch	4.92	<0.27[c]	<0.04[k]	0.2[c]

[a] Chiar et al. (1995); [b] Boogert et al. (2004); [c] Gibb et al. (2004); [d] Knez et al. (2005); [e] Pontoppidan et al. (2008); [f] Boogert et al. (2008); [g] Bottinelli et al. (2010); [h] Öberg et al. (2008); [i] The entire band is assumed to be due to NH_4^+; [j] van Broekhuizen et al. (2005); [k] This value is taken from another low-mass YSO, Elias 29 (Gibb et al. 2004).

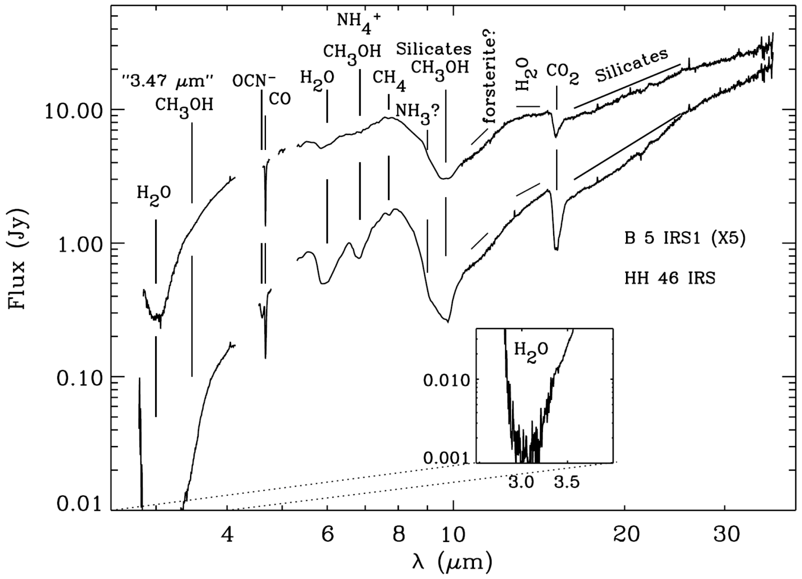

Figure 1.3 *Spitzer* infrared absorption spectrum combined with L and M band ground-based observations of two low-mass embedded stars: B5 IRS1 (*top, multiplied by a factor of 5 for clarification*) and HH46 IRS (*bottom*). Spectra taken from Boogert et al. (2004).

(*e.g.*, Zasowski et al. 2009). These data have been complemented with spectra at 2–4 μm obtained with ground-based facilities. These surveys provide the opportunity to unambiguously identify solid H_2O, CO_2, CH_4, CH_3OH, and NH_3. Figure 1.3 shows the *Spitzer* infrared absorption spectrum combined with L and M band observations of two low-mass embedded stars. In addition, *Spitzer* detected ices towards field stars behind quiescent dark clouds (*e.g.*, Bergin et al. 2005, Knez et al. 2005). Table 1.2 lists ice abundances with respect to H_2O ice towards high and low-mass protostars and quiescent dark clouds.

The general formation scenario can be summarized in four steps, as shown in Fig. 1.4.

1. In quiescent dark clouds, H_2O-rich ice is formed via surface reactions with a large amount of CO_2, and traces of CH_4 and NH_3 ice. Some CH_3OH is also associated with the H_2O-rich ice (Fig. 1.4a).

2. In the prestellar core, when densities are as high as 10^5 cm^{-3} and temperatures amount to ~10 K, CO and probably N_2 and O_2 molecules freeze-out on top of the H_2O-rich mantle, forming an apolar (water poor) ice layer. Before the turning-on of the protostar, a second CO_2 formation phase takes place resulting in a CO dominated CO:CO_2 ice mixture. During this phase, also CH_3OH ice is formed (Fig. 1.4b). Energetic processing, such as UV photolysis and cosmic rays irradiation, contributes to the production of new molecular species.

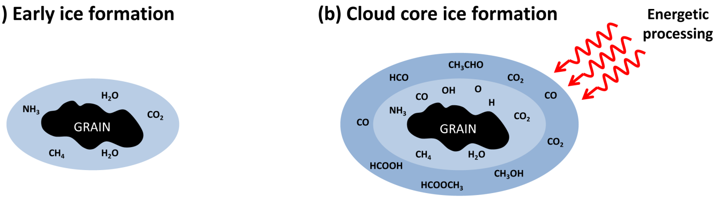
(a) Early ice formation

(b) Cloud core ice formation

(c) Lukewarm protostellar envelope >20 K

(d) Protostellar hot core >100 K

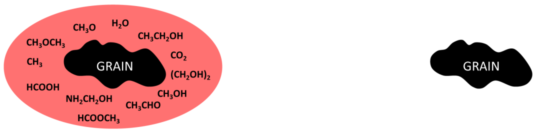

Figure 1.4 Suggested evolution of ices during star formation. Light-blue indicates a H_2O-dominated ice and dark-blue a CO-dominated ice. At each cold stage a small amount of the ice is released non-thermally. Early during cloud formation (a) a H_2O-rich ice forms. Once a critical density and temperature is reached CO freezes-out catastrophically (b), providing reactants for the formation of species like CH_3OH. Energetic processing (UV photolysis and cosmic rays irradiation) of the CO-rich ice results in the production of complex species. Closer to the protostar (c), following sublimation of CO, other complex molecules become abundant. Finally, all ice close to the protostar >100 K desorbs thermally (d). Figure adapted from Öberg et al. (2010a).

3. When the luminosity of the forming star increases, the more volatile species in the ice desorb, H_2O and CO_2 segregate, and more complex solid state chemistry is driven by the strong UV field coming from the young star (Fig. 1.4c).
4. When the temperature exceeds 90 K, the ice mantles evaporate completely and complex gas-phase chemistry can proceed in the hot cores (Fig. 1.4d).

The next section discusses the origin of the observed interstellar ices.

1.3.2 Interstellar ice chemistry

In quiescent dark clouds, grains provide a surface on which species can accrete, meet and react and to which they can donate excess energy. Grain surface chemistry is governed by the accretion rate of the gas phase species onto the grains, the surface migration rate, which sets the reaction network, and the desorption rate. The timescale at which gas phase species deplete-out onto grains is $\sim 10^5$ years in dense cores. This time is shorter than the lifetime of dense cores, which is between 10^5 and 10^6 years. Hence, in dense regions, during the first stage of star formation virtually all species (except H_2) are frozen-out onto interstellar grains.

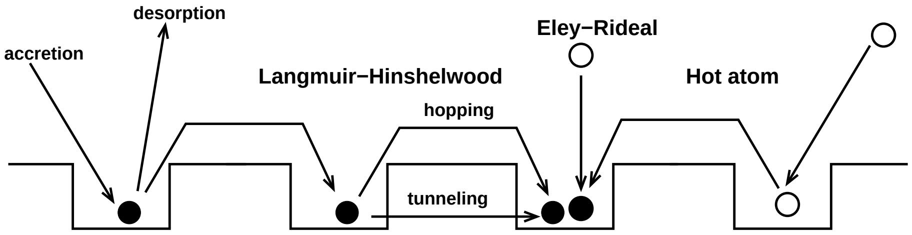

Figure 1.5 Three mechanisms for surface reactions on a regular grain surface: Langmuir-Hinshelwood (diffusive), Eley-Rideal, and hot atom mechanism. Closed circles are thermalized species and open circles non-thermalized. Reaction can occur when two species are in the same well. Figure provided by H. M. Cuppen.

As adsorbates accrete onto a cold surface, a complex chemistry occurs, leading to the production of new molecules in the ices through surface reactions (Herbst & van Dishoeck 2009, and references therein). There are three major mechanisms for surface reactions: Langmuir-Hinshelwood (diffusive), Eley-Rideal, and hot atom mechanism (see Fig. 1.5). In a Langmuir-Hinshelwood (LH) reaction the reactants are initially adsorbed onto the surface and in thermal equilibrium with the solid. Diffusion of one or more of the reactants on the surface leads to the formation of new products. In an Eley-Rideal (ER) reaction a particle coming from the gas phase reacts more or less directly with a surface-adsorbed species. In the hot atom mechanism, a gas-phase species lands on the surface and moves considerably before thermalization. In this way it is able to collide and react with an adsorbate.

In dense clouds, the flux of incoming species on a specific grain is typically very low ($\sim$1 per day). In contrast, on the grain surface, the abundant accreting atoms, H, C, N, and O, are relatively mobile and they can move around the grain on timescales less than the timescale for another gas phase species to accrete on the same grain. Moreover, the residence time of a species on a grain depends on its binding energy and grain temperature. As a result, for a 10 K grain with a site coverage of $\sim 10^6$ sites, an accreted H atom is expected to visit all sites on the surface many times before it desorbs. If co-reactants are present, H atoms can react before the next radical lands (Tielens & Charnley 1997, Tielens 2005). In considering possible co-reactants for atomic H, one has to distinguish between radicals and non-radicals. The former generally react with zero activation barriers; *i.e.*, upon collision on the grain surface. The latter may possess appreciable activation barriers, but, in each collision, there is a small probability that H will tunnel through the activation barrier and react. The reaction could also proceed thermally, depending on the residence time of both species (Herbst & van Dishoeck 2009).

Grain surface chemistry dates back to Allen & Robinson (1977), although the first realistic gas-grain model was proposed by Tielens & Hagen (1982) in 1982. Their astrochemical model includes a complex grain surface reaction network to explain molecule formation in quiescent dark clouds. According to this model in a first phase, H_2O ice (the dominant solid phase species) can be produced by the sequential hydrogenation of

O atoms landing on the grain (a process first proposed by van de Hulst; for a review see van de Hulst 1996). Atomic oxygen can also react with other O atoms to form O_2 and O_3. Reaction of O_3 with H reforms O_2 and OH. O_2 can be hydrogenated to form H_2O, while the OH radical can react with H or H_2 to form again H_2O, or it can form CO_2 and H_2 with the CO accreted on the surface. Under these conditions, also other H-rich species such as CH_4 and NH_3 can be formed. This first phase of grain-surface chemistry results in the formation of a polar ice mantle (water-rich) onto the dust grains. During the second phase, when the density increases in the molecular cloud, CO freezes-out onto the grains (its accretion rate is higher than that of H) forming an apolar ice layer (water-poor) on top of the polar one. Under these conditions, the hydrogenation of CO ice can lead to the formation of H_2CO and CH_3OH (Tielens & Hagen 1982, Charnley et al. 1997). CO_2 can be formed through the reaction CO + OH (Goumans et al. 2008). As suggested by Charnley et al. (2001), the reaction between CO and heavier elements than H may lead to the formation of more complex molecules such as CH_3COH and C_2H_5OH.

All these astrochemical reaction networks were based on chemical intuition and analogues from gas phase routes. It took several decades before experimental techniques allowed laboratory astrochemists to put all these reactions to the test. This is now done by several groups across the world and is the main topic of this thesis (Chapters 2-8). In this experimental process, several of these reactions were proven to be efficient, whereas others were not. Also several new reaction routes were revealed. Thus, laboratory work combined with theoretical models plays an essential role in disentangling the astrochemistry of the ISM.

The mathematical treatment of grain-surface reactions is not straightforward because of the heterogeneity and small size of the grains (Herbst & van Dishoeck 2009). Rate equations[1] are better used to reproduce the diffusive chemistry on homogeneous larger grains, on which at least several reactive adsorbate species exist on average (Green et al. 2001, Tielens & Hagen 1982). So-called macroscopic stochastic methods such as the master equation approach[2] and the Monte Carlo method [3] eliminate the problem caused by the small numbers of adsorbates, which is significant on smaller grains, but do not solve the problem of inhomogeneity (Barzel & Biham 2007, Charnley 2001, Green et al. 2001, Stantcheva et al. 2002). A special Monte Carlo method known as the "continuous-time, random-walk" approach handles this latter problem (Chang et al. 2007). This Monte Carlo method follows the species on the surface of the grain; explicitly takes into account processes, such as accretion, hopping, reaction, and desorption; takes into account the layering, investigating the penetration of species into the ice; and is a stochastic approach.

Several of these mathematical methods are implemented in Chapters 2 and 3. In Chapter 2, for instance, a Monte Carlo approach is used to simulate CO hydrogenation under laboratory conditions. Cuppen et al. (2009) extended this model using the continuous-

---

[1] Rate equations are differential equations which link the reaction rate for a chemical reaction with concentrations of reactants and constant parameters (like rate coefficients and partial reaction orders).

[2] The master equation is a set of first-order differential equations describing the time evolution of the probability of a system to occupy each one of a discrete set of states.

[3] The Monte Carlo method is based on a class of computational algorithms that rely on repeated random sampling to compute their results.

time, random-walk Monte Carlo method in order to simulate microscopic grain-surface chemistry over the long timescales in interstellar space, including the layering of ices during CO freeze-out. In Chapter 3, reaction rates are obtained by fitting a set of differential equations to the time evolution experimental curves of newly formed H_2O (D_2O) and H_2O_2 (D_2O_2) through O_2 hydrogenation (deuteration).

Surface reactions between thermalized reactants are not the only mechanism leading to the formation of new molecular species in the solid phase. Interstellar ices undergo energetic processing due to cosmic ions and UV photons, which may induce non-thermal desorption of surface molecules as well as the production of complex species. Fast ions passing through molecular solids release their energy into the target material. As a consequence, many molecular bonds are broken along the ion-track and, in a short time (less than one picosec), the molecular fragments recombine to produce a rearrangement of the chemical structure that leads to the formation of new molecular species. In the case of UV photolysis, the energy is released into the target material by a single photodissociation or photoexcitation event. In this particular case, new molecular species are also formed. Energetic processing, thus, offers a complementary pathway to atomic addition reactions towards chemical complexity in space (*e.g.*, Hagen et al. 1979, Gerakines et al. 1995, Hudson & Moore 2000, Palumbo et al. 2008, Chapter 9). This thesis shows that, for instance, the total observed abundance of molecules like CO_2 can be formed in the solid phase through surface reactions without energetic input (Chapter 7) as well as through energetic processing of C- and O- bearing molecules that induces surface chemistry (Chapter 9). Recent models supported by laboratory studies show that UV photolysis and ion irradiation of simple ices, such as CH_3OH, NH_3, and CH_4, trigger a complex surface chemistry. The desorption of these products in the warm inner regions of protostellar envelopes may explain the observed gas-phase abundances of complex organic molecules in such environments (*e.g.*, Garrod et al. 2008, Öberg et al. 2009b, Modica & Palumbo 2010).

1.4 Laboratory ices

Laboratory setups that record vibrational spectra of ices typically consist of a radiation source, a sample chamber, and an instrument for spectra acquisition. These elements are also present in space: the radiation source is a field star or an embedded source, the sample chamber is the interstellar medium, with dust grains as the surface, and the recording instrument is the spectrograph mounted onto the telescope. The interpretation of ice data is achieved by studying interstellar ice analogues in the laboratory spectroscopically and comparing spectra directly to astronomical observations. Spectra acquired in transmission[4] provide information on the ice constituents in space, their corresponding mixing ratios, ice structure and temperature. From such a comparison it was found that dust grains in cold (<100 K) and dense interstellar environments are covered by 50−100 monolayers thick icy mantles, which comprise primarily H_2O, but also other species, like CO, CO_2,

---

[4] The IR light passes through the icy sample, which is deposited onto a cold (10−300 K) infrared transparent window (CsI, Si or KBr) and then detected by an infrared spectrometer.

CH_3OH, HCOOH, NH_3, CH_4, and traces of more complex molecules. These ices are mainly amorphous and have a layered structure consisting of H_2O- and CO-dominated ice mixtures, as discussed in §1.3.1. Spectroscopic ice work is still ongoing, even after more than 30 years of dedicated work. Recent examples comprise work performed in the Sackler Laboratory for Astrophysics in Leiden on the effect of CO_2 and CO on H_2O band profiles and band strengths by Öberg et al. (2007a) and Bouwman et al. (2007), respectively. Figure 1.6 shows infrared spectra in transmittance of the four H_2O band modes, ranging between 4000 cm^{-1} and 500 cm^{-1}, for six different ice compositions: from pure H_2O ice (*bottom panels*) to a H_2O:CO = 1:4 mixture (*top panels*) (Bouwman et al. 2007). For different mixture ratios the shape and peak position of the absorption bands vary. This allows to use the laboratory data to conclude on ice parameters in the ISM.

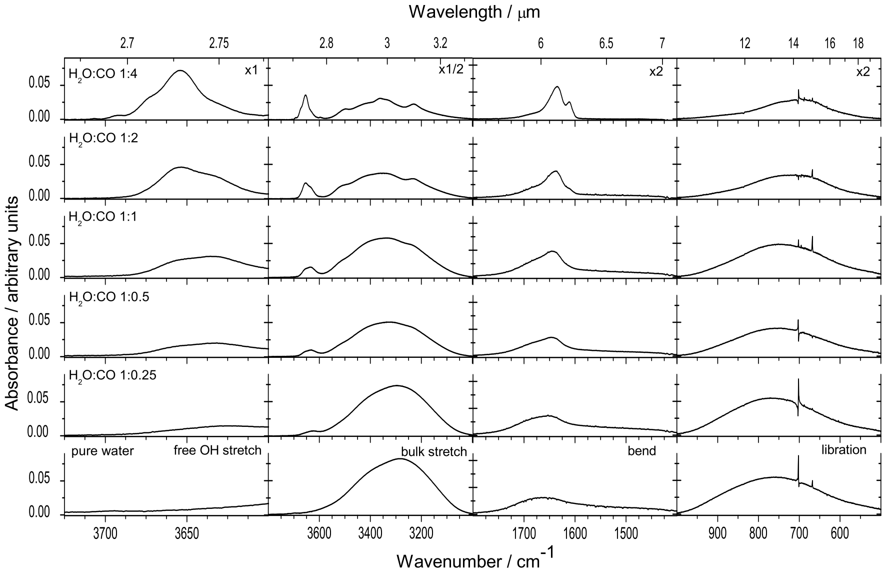

Figure 1.6 The 15 K infrared absorption spectra in transmittance of the four H_2O band modes between 4000 cm^{-1} and 500 cm^{-1} for six different ice compositions, ranging from pure water ice (*bottom panels*) to a H_2O:CO = 1:4 mixture (*top panels*). For different mixture ratios the shape and peak position of the absorption bands vary. Note that the wavelength ranges for separate modes are different. The small structures on the libration mode are experimental artifacts. Spectra are taken from Bouwman et al. (2007).

The experimental setup used for these measurements consists of a High Vacuum (HV) setup in which ices are grown onto a cold infrared-transmitting window (10−300 K). The window is cooled down by a closed-cycle He refrigerator and the sample temperature is controlled by resistive heating. A Fourier transform infrared (FTIR) spectrometer is used to record the ice spectra in transmission between 4000−400 cm^{-1} (2.5−25 μm) with a typical resolution of 1−2 cm^{-1}. This allows a straightforward detection in a single pass experiment. The main weakness of this method is that the base pressure in the main chamber is $1\times10^{-8}-1\times10^{-7}$ mbar, which is orders of magnitude higher than the densest interstellar cloud, and water pollution is not negligible (>100 ML of H_2O deposited per hour on a 10 K substrate), since the vacuum is mainly composed by background H_2O. In order to minimize these effects, experiments are performed in a short timescale (~few hours) and thick layers of ice are usually deposited on the substrate (>0.1 μm).

The formation of complex species through energetic processing (ions and UV photons) of simple ices have been experimentally investigated for decades using HV setups (*e.g.*, Hagen et al. 1979, Allamandola et al. 1988, Gerakines et al. 1995, Hudson & Moore 2000, Strazzulla & Palumbo 2001, Mennella et al. 2004, Mennella et al. 2006, Bennett & Kaiser 2007, Palumbo et al. 2008, Chapter 9). With few exceptions, these experiments are meant to investigate qualitatively and, more recently, quantitatively the effect of energetic processing on the interstellar chemistry, with the intent to mimic ice composition in star forming regions. The work presented in Chapter 9 is performed in a HV system and a quantitative comparison between laboratory and observational infrared spectra is made. In this chapter the interstellar ice analogs are obtained in situ upon ion irradiation of selected ice samples.

Another main objective of laboratory work is the characterization of astrophysically relevant ice processes, such as surface formation, diffusion, segregation, and thermal and non-thermal desorption of molecules. The investigation of these ice processes started only roughly a decade ago with the introduction of a new generation of systems derived from standard surface science techniques, called Ultra High Vacuum (UHV) setups ($1\times10^{-10}-1\times10^{-11}$ mbar). The gas composition in UHV setups reproduces the interstellar environment in the sense that it is mainly composed of H_2 with densities comparable to the disk midplane. The surface temperatures reached in these chambers are as low as <10 K. The water contamination rate on a 10 K substrate is <1 ML per 3 hours. Two UHV surface techniques are used as analytical tools: Reflection-Absorption InfraRed Spectroscopy (RAIRS) to investigate species in the solid phase, and Temperature Programmed Desorption (TPD) using a Quadrupole Mass Spectrometer (QMS) in order to monitor gas-phase species desorbed from the ice.

Although the importance of surface reactions for interstellar chemistry was already realized in the 1940s, the surface formation of complex molecules in interstellar ice analogs has only been investigated recently by atomic addition experiments (*e.g.*, Hiraoka et al. 1998, Watanabe et al. 2006a, Matar et al. 2008, Chapters 2-8). Most of the laboratory work so far focuses on the hydrogenation/deuteration of simple ices such as CO, O_2, and O_3 (*e.g.*, Chapters 2-6 and references therein; see Fig. 1.7). In Chapters 7-8 the hydrogenation of $CO:O_2$ binary mixtures is presented. Chapter 7 focuses on the formation of solid CO_2 through direct dissociation of the HO-CO complex. This chapter investigates at the same time the competition between the different hydrogenation channels (CO + H vs. O_2 + H), while Chapter 8 focuses on the formation of HCOOH ice through the hydrogenation of the HO-CO complex. Neither the surface formation of CO_2 nor that of HCOOH have been observed in hydrogenation experiments of pure CO and O_2 ices. The experiments presented in all these chapters are not designed to simulate a realistic interstellar ice, but to test surface reaction pathways. So far few studies have investigated the hydrogenation of more complex species, such as CO_2, HCOOH, and CH_3CHO containing ices (Bisschop et al. 2007b), or focused on the bombardment of simple ices with heavier species than hydrogen/deuterium atoms, using a single or a double beam line (*e.g.*, Oba et al. 2010, Dulieu et al. 2010).

UHV setups have been recently used to investigate UV induced ice chemistry. Also in this case experimental results are not meant to be directly compared to astronomical observations. Rather a synergic use of RAIRS and TPD is meant to study the physical properties of the ice. Examples are the systematic investigation of photodesorption of simple molecules, such as CO, N_2, H_2O and D_2O, as well as the study of photochemistry in CH_3OH-rich ices and H_2O:CO_2:NH_3:CH_4 mixtures (*e.g.*, Öberg et al. 2007b, 2009d,c,b, 2010b).

1.4.1 RAIR spectroscopy

The main advantage of the RAIRS detection technique is that the reactants and products are monitored in the solid phase at the time and temperature of interest. Figure 1.7 shows the RAIR spectra from a CO hydrogenation experiment, as presented in Chapter 2. The top panel of Fig. 1.7 shows the 15 K CO ice spectrum after deposition, while the bottom panel shows the RAIR difference spectra with respect to the initial deposited ice acquired during H-atom exposure. Quantifying the formed product with the RAIRS technique is relatively simple, provided that the RAIRS is calibrated with an independent method, even though, not all species can be detected in the infrared[5]. The column densities of reactants and products are usually obtained from the integrated intensity of the selected infrared bands, using a modified Lambert-Beer equation (Bennett et al. 2004):

$$N_X = \frac{\int A(\nu)\mathrm{d}\nu}{S_X} \tag{1.1}$$

where $A(\nu)$ is the integrated absorbance and S_X is the corresponding band strength for species X (see Chapter 2 and 4). Since literature values of transmission band strengths cannot be used directly in reflectance measurements, an apparent absorption strength of the various species is obtained from calibration experiments. The determination of this apparent absorption strength is set-up specific. The calibration method (isothermal desorption of a selected ice) is described in detail in Chapters 2 and 4.

The RAIR technique has both advantages and disadvantages over transmission infrared spectroscopy. Since RAIRS is performed in a grazing incidence configuration with respect to the substrate, which is often a copper plate covered by a film of polycrystalline gold[6], the resulting enhancement of the p-polarized electric field at the surface leads to a sensitivity advantage. Furthermore, in the reflection mode a double-pass geometry is used. The incident beam must pass once through the surface layer before hitting the reflecting substrate, and a second time on its way to the detector. The adoption of a grazing

---

[5] Diatomic homonuclear molecules like O_2 and N_2 are infrared in-active, except when embedded in an ice matrix (Ehrenfreund et al. 1992).

[6] The gold substrate is chemically inert, *i.e.*, it does not have a direct effect on the behavior of the ice.

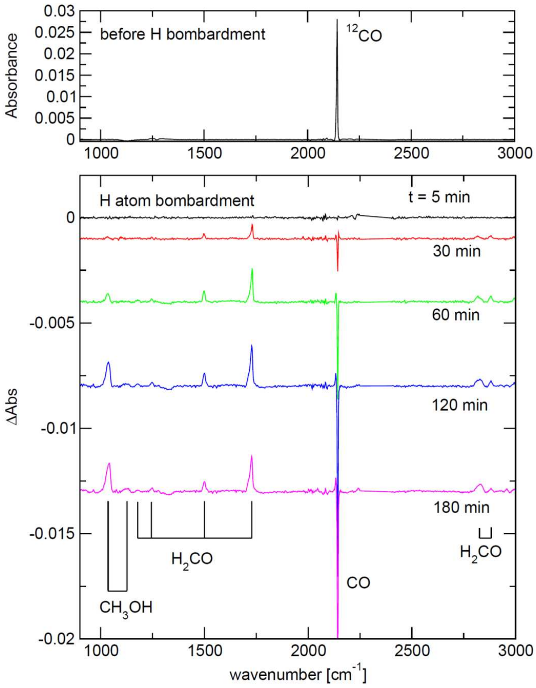

Figure 1.7 The RAIR spectra of a CO hydrogenation experiment taken from Chapter 2. The top-panel shows the CO ice spectrum at T = 15 K. The bottom panel shows the RAIR difference spectra with respect to the initial deposited ice acquired during H-atom exposure.

incidence geometry also leads to a rapid increase in path length, hence increasing the sensitivity for very thin ice layers. Thus, in a surface analysis experiment, RAIRS can probe ice layers down to the monolayer regime and therefore it can be considered a more sensitive technique than transmission infrared spectroscopy. However, the main disadvantage is that RAIR spectra cannot be directly compared to astronomical spectra. Therefore, as previously mentioned, experiments using RAIRS are often not meant to reproduce interstellar ice analogs, but to investigate interstellar relevant solid state processes. Moreover, the RAIRS detection technique is often complimented by the TPD technique for these kind of experiments of which Chapters 2 and 8 are two examples. In the experiments shown in these two chapters, after H-atom addition a TPD experiment is performed and gas-phase molecules are detected by a QMS. The combination of the two techniques led to the unambiguous identification of surface CH_3OH and HCOOH formation at low temperatures, respectively.

1.4.2 Mass spectrometry

As discussed in the first part of this chapter, in the earliest stages of star formation virtually all species (excluding H_2) accrete onto grains in dense cold cores. In the later stages, grains are warmed to temperatures where molecules desorb into the gas phase. Thus, the less volatile species will still reside on the grain surface and participate in reactions in the solid state, until the grain temperature will exceed 90 K, at which the entire interstellar ice mantle is desorbed. This scenario, which takes place at astrophysical timescales of $\sim 10^7$ years, can be experimentally simulated on laboratory timescales of a few hours through a TPD experiment. An ice sample is prepared under UHV conditions with monolayer precision and heated linearly with a selected rate (*e.g.*, Fraser et al. 2001, Collings et al. 2003, 2004, Bisschop et al. 2006, Acharyya et al. 2007). The desorbed species are subsequently recorded as a function of temperature using a QMS, which produces a signal proportional to the number of incoming molecules as a function of their mass to charge ratio (m/z). The incoming molecules first enter the ion source of the QMS, where they are ionized through electron bombardment by electrons released from a hot filament. The resulting ions are then focussed, selected and directed to the detector. Ions are detected by a Faraday detector, which collects the ions directly, allowing the ion current to be monitored. Alternatively, for higher sensitivity, a Channel Electron Multiplier (CEM) can be used. This type of detector is a Secondary Electron Multiplier (SEM) in which a large negative potential (~ - 2000 V) is used to attract the ions into the channel entrance. The channel is coated with a material that readily releases secondary electrons upon ion/electron impact. This produces a cascade of electrons down to the channel which can be detected, either as the electron current, or as a series of pulses.

Whilst the TPD experiment itself is relatively straightforward, the interpretation of the data is often much more challenging. Under conditions where the pumping speed is sufficiently high, the QMS signal for the selected mass is proportional to the rate of desorption of that species, r_d (molecules cm^{-2} s^{-1}). The rate of desorption is given by the Polanyi-Wigner equation:

$$r_\mathrm{d} = \nu_i N_X \exp(-E_\mathrm{d}/RT) \tag{1.2}$$

where ν_i is the pre-exponential factor for the process leading to the desorption, N_X is the surface concentration of adsorbate X, i is the desorption order, E_d is the activation energy for desorption per mole, R is the gas constant and T the temperature. Desorption from multilayers of bulk ice is typically close to zero order ($i = 0$). For perfect zero order desorption, the desorption rate does not depend on the surface concentration. In many cases, desorption of submonolayer coverage results in near first order kinetics ($i = 1$), *i.e.*, indicating that the desorption rate depends linearly on the surface concentration. This two desorption regimes can be experimentally investigated performing an isothermal desorption experiment, as shown in several chapters of this thesis.

The simplest thermal desorption process is the desorption of a pure ice. Desorption of binary or more complex mixtures is less understood. Figure 1.8 shows the TPD curves for CO and CO_2 desorption from pure ice (*solid lines*) and mixed with water (*dotted* *lines*) (Öberg 2009). The desorption energy of the single species depends on the exact ice composition. In addition, the dominant mantle species may prevent other species from desorbing. Molecules can, indeed, get trapped in the matrix and then be released at different temperatures than their thermal desorption temperatures. Laboratory experiments show that ice heating also results in ice segregation of previously mixed ices (*e.g.*, Öberg et al. 2009a, Chapter 9).

Although, TPD is a more sensitive technique than RAIRS, it has however several disadvantages: the surface reaction products, which remain in the solid phase, cannot be probed in situ; additional surface reactions during the TPD (during the linear heating of the ice and before complete desorption of the species) cannot be excluded; quantifying the desorbing species is not straightforward; and some of the interesting species have equal (*i.e.*, undistinguishable) masses or are fractionated in the QMS upon electronic bombardment. A TPD experiment finally destroys the ice.

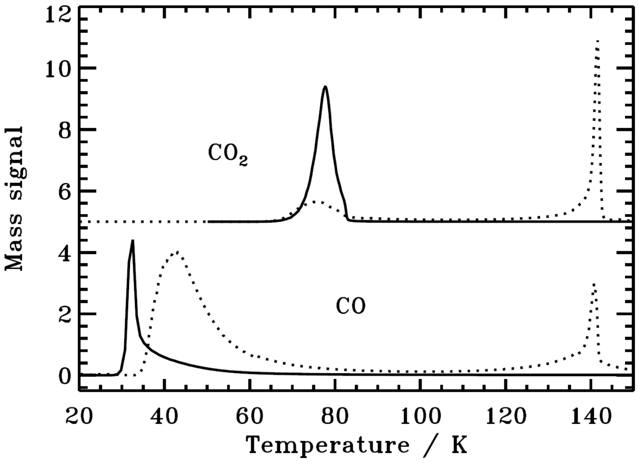

Figure 1.8 TPD curves for CO and CO_2 desorption from pure ice (*solid lines*) and H_2O:CO = 5:1 and H_2O:CO_2 = 4:1 (*dotted lines*) binary mixtures. The TPD spectra are normalized with arbitrary factors for visibility and are taken from Öberg (2009).

1.4.3 Experimental setups used in this thesis

SURFRESIDE

Chapters 2-8 are dedicated to the investigation of surface reactions that can lead to the formation of interstellar relevant molecules. All experiments are performed in the Sackler laboratory for Astrophysics using an UHV setup SURFace REaction SImulation DEvice

(SURFRESIDE), which consists of a stainless steel vacuum main chamber and an atomic line. A schematic view of the experimental apparatus is shown in Fig. 1.9. The gold coated copper substrate temperature is controlled between 12 and 300 K. Deposition of selected gasses proceeds under an angle of 45°, with a controllable flow. Gas phase molecules are monitored during the deposition mass spectrometrically by means of a QMS, which is placed behind the substrate and opposite to the atomic source. A thermal cracking source (Tschersich & von Bonin 1998, Tschersich 2000, Tschersich et al. 2008) is used to hydrogenate the ice sample through heating a capillary pipe, in which H_2 flows, from 300 to 2250 K by a surrounding tungsten filament. A quartz pipe is placed along the path of the dissociated beam to efficiently thermalize all H atoms to room temperature through surface collisions before they reach the ice sample. The Hydrogen Atom Beam Source (HABS) atom fluxes are measured at the substrate position mass spectrometrically, as described in the appendix of Chapter 4.

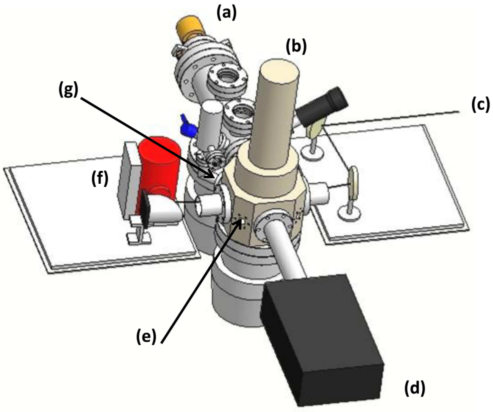

Figure 1.9 Schematic top-view of the solid-state experimental UHV set-up (SURFRESIDE): $^{(a)}$H-atom source; $^{(b)}$cold finger; $^{(c)}$IR beam; $^{(d)}$mass spectrometer; $^{(e)}$main chamber; $^{(f)}$IR detector; $^{(g)}$deposition line.

Ices are monitored by means of RAIRS using a FTIR spectrometer, which covers the range between 4000 and 700 cm^{-1} (2.5−14 μm). A spectral resolution between 1 and 4 cm^{-1} is used and several scans are co-added. In Chapters 2-4 and 6-7, the ice is first deposited and then hydrogenated/deuterated. In this case, RAIR difference spectra with respect to the initial deposited ice are acquired during H/D exposure. In Chapters 5 and 8, molecules are co-deposited with H atoms and RAIR difference spectra with respect to the bare substrate are acquired during co-deposition. In all cases, newly formed solid species are monitored by RAIRS. Spectra are recorded at different stages during an experiment, providing time resolved information about the destruction (*i.e.*, use-up) of the precursor ice (the deposited ice layer) and the formation of new molecules that are identified through their spectral fingerprints. At the end of the atomic addition a TPD can be performed to constrain the experimental results. Surface reactions of simple ices, like CO, O_2, O_3, and

$CO:O_2$ mixtures are investigated during a full range of laboratory conditions including different atomic fluxes, ice temperatures, ice thicknesses, ice structures, and mixture ratios with the intent to unreveal the physics and chemistry of molecule formation more than simulating chemistry in a realistic interstellar ice. However, in Chapter 3 also the astronomical implications of H_2O formation are examined in more detail.

HV setup in LASp

The experiments discussed in Chapter 9 are performed in the Laboratory for Experimental Astrophysics (Laboratorio di Astrofisica Sperimentale - LASp) in Catania (Italy). The experimental setup used to obtain infrared transmission spectra is composed of a stainless steel HV chamber interfaced with a FTIR spectrometer (4400−400 cm^{-1}) comparable to the setup described in § 1.4. Molecules are injected into the chamber through a needle valve and subsequently deposited onto a chosen substrate (Si or KBr) placed in thermal contact with a cold finger (10−300 K). After deposition the samples are bombarded by 200 keV H^+ ions. The ions are obtained from an ion implanter interfaced with the vacuum chamber. The used beam produces current densities in the range from 100 nA cm^{-2} up to a few μA cm^{-2} in order to avoid macroscopic heating of the target. The ion beam and the infrared beam are mutually perpendicular, forming an angle of 45° with the substrate plane. In this way, spectra can be taken at any time of the experiment without tilting the sample. The energy released to the sample by impinging ions (dose) is given in eV/16 u, where u is the unified atomic mass unit defined as 1/12 of the mass of an isolated atom of carbon-12. The polarization of the infrared radiation is selected by rotating a polarizer placed in the infrared beam path before the detector. Therefore, for each single irradiation-step two spectra are acquired in different polarizations: one with the electric vector parallel (P polarized) and one perpendicular (S polarized) to the plane of incidence.

1.5 This thesis

Chapter 2

Chapter 2 focuses on the formation of formaldehyde (H_2CO) and methanol (CH_3OH) by hydrogenation of pure CO ice. Reaction rates are determined from RAIR data for different ice temperatures and ice thicknesses, as well as H-atom fluxes (1×10^{12}–2.5×10^{13} H atoms cm^{-2} s^{-1}). The formation of new molecules in the ice is confirmed by TPD: H_2CO and CH_3OH are also found mass spectrometrically. On the basis of these experiments energy barriers for the H + CO and H + H_2CO reactions are obtained by fitting Monte Carlo simulation results to the experimental data. Using these barriers, the CH_3OH production can be simulated for interstellar conditions (Cuppen et al. 2009) and from this work, surface hydrogenation of CO ice can now be safely used to explain the observed abundance of CH_3OH in the interstellar medium.

Chapters 3-6

Water ice formation through surface reactions is extensively discussed here. In 1982 Tielens & Hagen (1982) proposed that interstellar water forms on grain surfaces through three reaction channels: hydrogenation of atomic oxygen, molecular oxygen and ozone. In Chapter 3, the molecular oxygen channel is investigated for a large range of temperatures. The main and surprising finding is that the initial formation rate of H_2O_2 and H_2O is much less temperature dependent than the analogous reactions for CO hydrogenation. Furthermore, O_2 hydrogenation results in a much larger yield than the few monolayers found for CO hydrogenation. This yield is strongly temperature dependent. In Chapter 4, both effects are shown to be a direct consequence of the competition between the reaction of H atoms with O_2 molecules, which is barrierless and therefore temperature independent, and the H-atom diffusion into the O_2 ice, which is temperature dependent. In Chapter 4, O_2 hydrogenation is investigated extensively from a physical approach, *i.e.*, studying different ice thicknesses, ice temperatures, ice structures and H_2 concentrations in the atomic beam, whereas Chapter 5 focuses more on the reaction scheme with the intent to assess reaction routes and branching ratios. The latter Chapter shows that the initially proposed reaction network of only three channels is too simple and that several of the channels are actually linked through additional reactions.

The hydrogenation of solid O_3 is discussed in Chapter 6. Since this channel is connected to the O_2 channel after the first reaction step, special care is taken in Chapter 6 to deposit a pure O_3 ice (free from O_2 contamination[7]) by keeping the substrate temperature between the O_2 and O_3 desorption temperature during deposition. If such a temperature is also kept during H-atom addition, the O_2 molecules formed upon O_3 hydrogenation will desorb from the surface of the ice. Thus, in this way the reaction of OH to form water by reaction with H or H_2 can be investigated. The hydrogenation of O_3 is found to be more similar to CO hydrogenation in the sense that only the top few monolayers of O_3 are hydrogenated. Moreover, the reaction OH + H_2 could be more efficient than the reaction OH + H: reaction OH + H_2 could proceed through tunneling, while reaction OH + H needs to dissipate 5.3 eV of excess energy with just one final product, which could be difficult. The conclusion that the three channels ($O/O_2/O_3$ + H) are strongly linked, is of importance for astrochemical models focusing on water formation under interstellar conditions.

Chapter 7

Chapter 7 discusses the hydrogenation of $CO{:}O_2$ binary mixtures, which results in the formation of CO_2 through the reaction of OH and CO. Surface CO_2 formation without energetic input is found to be an important formation mechanism, which may explain the formation of CO_2 together with H_2O ice during the dense cold core phase prior to star formation. The competition between CO hydrogenation and O_2 hydrogenation reveals that the penetration depth of H atoms into the ice depends strongly on the ice composition,

---

[7] Some gas phase O_2 can be formed in the deposition line and in the main chamber through O_3 dissociation.

and that the CO and O_2 channels influence each others final product yields. However, the formation rate for all the final products is found to be less sensitive on the mixture composition than the final yield. Therefore, the formation rates found for H_2CO, CH_3OH, H_2O_2 and H_2O in the isolated studies of the CO + H (Chapter 2) and O_2 + H (Chapter 3) channels are valid for use in astrochemical models.

Chapter 8

Chapter 8 deals with the formation of solid formic acid (HCOOH). The aim of Chapter 8 is to give the first experimental evidence for solid HCOOH formation at low temperature through the hydrogenation of the HO-CO complex, stabilized in the ice by intramolecular energy transfer to the surface, as proposed by Goumans et al. (2008). Formation of HCOOH is observed in the infrared after co-deposition of CO:O_2 mixtures and H atoms, increasing the ice temperature below the CO and O_2 desorption temperature (<30 K) and therefore increasing the mobility of the ice components only. At these temperatures H atoms, trapped in the ice matrix or formed through surface reactions, can find and react with the stabilized HO-CO complex. These experiments demonstrate that the reaction HCO + OH is inefficient at low temperatures. In the last part of the chapter, experimental results are placed in an astrophysical context. It is shown that the HO-CO complex channel, which was previously not considered as an important HCOOH formation route, explains the presence of HCOOH in dense cold clouds, at the beginning of the warm-up phase of a protostar.

Chapter 9

Chapter 9 discusses the formation of solid CO_2 through reactions induced by energetic processing of C- and O- bearing molecules. Chemical and structural modifications of the interstellar ice analog samples induced by energetic processing are analyzed using infrared spectroscopy in transmittance. Therefore, a quantitative study is obtained with the intent to compare laboratory results to observations. Experiments show that laboratory spectra are a good spectroscopic analogue of the interstellar features. Even if the comparison between laboratory and observed spectra presented here cannot be considered unique and complete, our results quantitatively show that interstellar solid CO_2 can form after ion irradiation and UV photolysis of icy mantles. The results presented here complement those shown in Chapter 7, where the CO_2 formation without energetic input is investigated. Both mechanisms can, indeed, contribute to the total CO_2 column density observed in quiescent clouds and star forming regions.

CHAPTER 2

Hydrogenation reactions in interstellar CO ice analogues: a combined experimental/theoretical approach[1]

Hydrogenation reactions of CO in inter- and circumstellar ices are regarded as an important starting point in the formation of more complex species. Previous laboratory measurements by two groups of the hydrogenation of CO ices provided controversial results about the formation rate of methanol. Our aim is to resolve this controversy by an independent investigation of the reaction scheme for a range of H-atom fluxes and different ice temperatures and thicknesses. To fully understand the laboratory data, the results are interpreted theoretically by means of continuous-time, random-walk Monte Carlo simulations. Reaction rates are determined by using a state-of-the-art ultra high vacuum experimental setup to bombard an interstellar CO ice analog with H atoms at room temperature. The reaction of CO + H into H_2CO and subsequently CH_3OH is monitored by a Fourier transform infrared spectrometer in a reflection absorption mode. In addition, after each completed measurement, a temperature programmed desorption experiment is performed to identify the produced species according to their mass spectra and to determine their abundance. Different H-atom fluxes, morphologies, and ice thicknesses are tested. The experimental results are interpreted using Monte Carlo simulations. This technique takes into account the layered structure of CO ice. The formation of both formaldehyde and methanol via CO hydrogenation is confirmed at low temperature (T = 12−20 K). We confirm that the discrepancy between the two Japanese studies is caused mainly by a difference in the applied hydrogen atom flux, as proposed by Hidaka and coworkers. The production rate of formaldehyde is found to decrease and the penetration column to increase with temperature. Temperature-dependent reaction barriers and diffusion rates are inferred using a Monte Carlo physical chemical model. The model is extended to interstellar conditions to compare with observational H_2CO/CH_3OH data.

---

[1] Based on: G. W. Fuchs, H. M. Cuppen, S. Ioppolo, C. Romanzin, S. E. Bisschop, S. Andersson, E. F. van Dishoeck, and H. Linnartz, 2009, Astronomy & Astrophysics, volume 505, pages 629-639

2.1 Introduction

An increasing number of experimental and theoretical studies have focused on the characterization of solid state astrochemical processes. These studies were triggered by the recognition that many simple and more complex molecules in the interstellar medium are most likely to have formed on the surfaces of dust grains. Astronomical observations, detailed laboratory studies, and progress in UHV surface techniques allow experimental verification of the initial surface reaction schemes, as introduced by Tielens, Hagen, and Charnley (Tielens & Hagen 1982, Tielens & Charnley 1997). Recently the formation of water was demonstrated in hydrogenation schemes starting from solid molecular oxygen (Miyauchi et al. 2008, Ioppolo et al. 2008) and the formation of ethanol from acetaldehyde (Bisschop et al. 2007b). The first solid-state astrochemical laboratory studies focused on the formation of formaldehyde and methanol by H-atom bombardment of CO ice. Methanol is observed abundantly in interstellar ices and is considered to be a resource for the formation of more complex molecules through surface reactions and after evaporation in the gas phase (Charnley et al. 1992). The hydrogenation scheme for the solid state formation of methanol was proposed to be

$$\mathrm{CO} + \mathrm{H} \rightarrow \mathrm{HCO} \overset{\mathrm{H}}{\rightarrow} \mathrm{H_2CO} \overset{\mathrm{H}}{\rightarrow} \mathrm{H_3CO} \overset{\mathrm{H}}{\rightarrow} \mathrm{CH_3OH}. \tag{2.1}$$

Laboratory studies of H-atom bombardment of CO ice were performed independently by two groups (Hiraoka et al. 2002, Watanabe & Kouchi 2002). Hiraoka et al. (2002) observed only formaldehyde formation, whereas Watanabe & Kouchi (2002) also found efficient methanol production. In a series of papers, these conflicting results were discussed (Hiraoka et al. 2002, Watanabe et al. 2003, 2004) and the prevailing discrepancy between results was proposed to be a consequence of different experimental conditions, most noticeable the adopted H-atom flux (Hidaka et al. 2004). Understanding the solid-state formation route to methanol became even more important following an experimental finding that the gas-phase formation route via ion-neutral reactions is less efficient than previously estimated and cannot explain the observed interstellar abundances (Geppert et al. 2005, Garrod et al. 2006).

Deuteration experiments were also performed on CO ice, which confirmed the formation of both fully deuterated formaldehyde and methanol, but with substantially lower reaction rates (Nagaoka et al. 2005, Watanabe et al. 2006a). In the presence of both hydrogen and deuterium it was suggested that first normal methanol forms and is then gradually converted in the deuterated species by exchange reactions.

The present chapter strongly supports the flux argument given by Hidaka et al. (2004). Furthermore, in § 2.3 a systematic study of the physical dependencies involved in the CO-ice hydrogenation is presented to place previous work in a context that allows an extension of solid state astrochemical processes to more complex species. Special emphasis is placed on the flux and temperature dependence of the formation rate. An analysis of the spectral changes of CO ice during hydrogenation is included to provide insight into the structure of the reactive layer. Furthermore, in § 2.4 Monte Carlo simulations are presented that allow us to interpret the experimental results in greater detail and to vary parameters that are difficult to study independently by experiment. We conclude with a simulation of H_2CO/CH_3OH formation under interstellar conditions, in particular for low H-atom fluxes (§ 2.5). The outcome is compared with astronomical observations (§ 2.6).

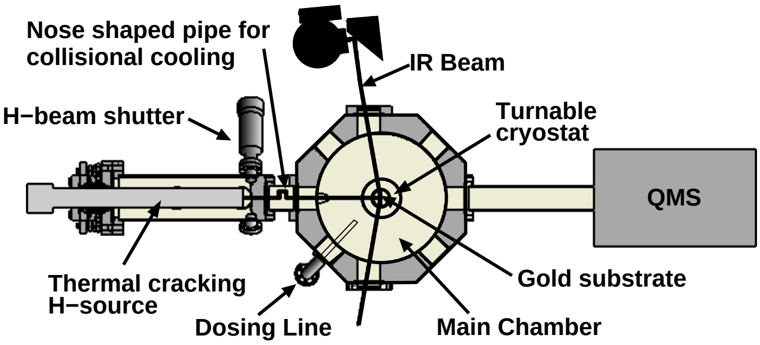

Figure 2.1 Schematic representation of the experimental setup. CO ice is deposited through the dosing line and the products are monitored by means of infrared spectroscopy and quadrupole mass spectroscopy (QMS).

2.2 Experimental procedure

The experiments are performed under UHV conditions. The room temperature base pressure of the vacuum system is better than 3×10^{-10} mbar. Figure 2.1 shows a schematic representation of the setup (see Chapter 4 for additional information). Amorphous CO ices ranging from a few to several monolayers (ML) are grown on a gold coated copper substrate that is located at the center of the main vacuum chamber and mounted on the tip of a cold finger of a 10 K He-cryostat. The temperature of the ice can be controlled between 12 and 300 K with 0.5 K relative precision between experiments. The absolute accuracy is better than 2 K. During deposition, the layer thickness is monitored by simultaneous recording of reflection absorption infrared (RAIR) spectra. To exclude the effects of potential pollution, ices are grown using CO, ^{13}CO, or $C^{18}O$ isotopologues.

During the experiment the ice layers are exposed to a hydrogen atom beam. The atoms are produced by a well-characterized commercial thermal-cracking source (Tschersich & von Bonin 1998, Tschersich 2000) that provides H-atom fluxes on the sample surface of between 10^{12} and 10^{14} atoms cm^{-2} s^{-1}. By comparison, the Hiraoka group used fluxes below 10^{13} atoms cm^{-2} s^{-1} and the Watanabe group worked in the 10^{14}–10^{15} atoms cm^{-2} s^{-1} regime. The hot (~2000 K) hydrogen atoms are cooled to room temperature by surface collisions in a nose-like shaped quartz pipe between the atomic source and the ice sample. In this way, hot hydrogen atoms cannot affect the ice directly. H-atom recombination in this connecting pipe results in a lower final flux. Details about the flux determination are given in Appendix A. The absolute fluxes are estimated to be within a factor of two and the relative fluxes to within 50%.

The relatively high temperature of the incident atoms of 300 K does not affect the process; previous experiments with colder H atoms did not show any substantial temperature dependence because the atoms are immediately thermalized on the surface (Watanabe & Kouchi 2002). It is argued that the surface is covered with a thin layer of hydrogen molecules under these conditions. These molecules are either formed on the surface or originate from the partially dissociated beam. Since the incoming atoms have to penetrate this cold H_2 layer, they are thermally adjusted to the surface temperature once they come in contact with the CO molecules.

Information about the reaction products is obtained using two complementary techniques. During the H-atom bombardment, reactants and products are monitored by recording RAIR spectra. The RAIR spectra are recorded using a Fourier transform infrared spectrometer with 1 and 4 cm^{-1} resolution and covering the spectral region in which CO (2143 (s) cm^{-1}), formaldehyde (1732 (s), 1479, and 2812 (m), and 1246, 1175, 2991, 2880, and 2812 (mw) cm^{-1}) and methanol (1035 (s) and 1125 (w) cm^{-1}) exhibit strong (s), medium (m), or weak (w) absorption bands. The intensity of spectral features is directly related to the density in the ice. The products are monitored by mass spectrometry using temperature programmed desorption (TPD) once a hydrogenation experiment is completed.

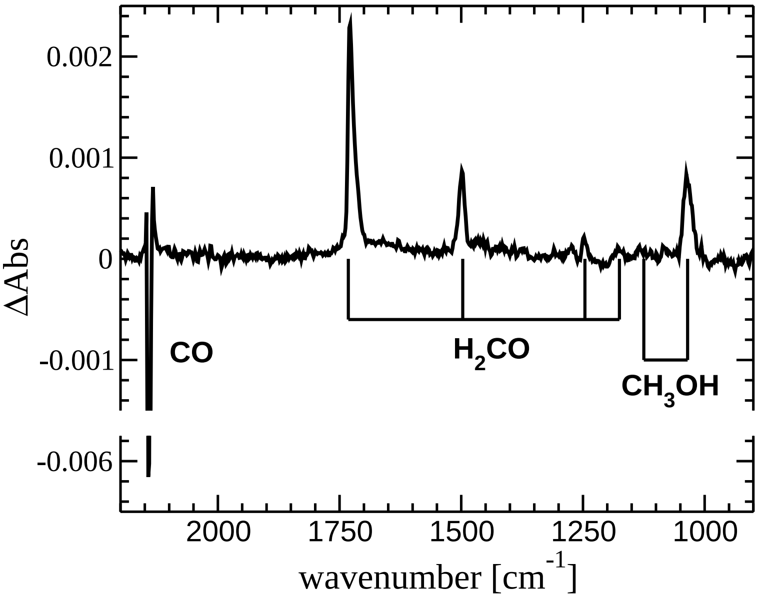

Figure 2.2 RAIR difference spectrum of a CO ice at 12.0 K exposed to 5.4 × 10^{17} cm^{-2} H atoms at a flux of 5 × 10^{13} cm^{-2} s^{-1}. The spectrum after CO deposition is used as the reference spectrum. Note that the CO peak reaches an absorbance difference of -0.006.

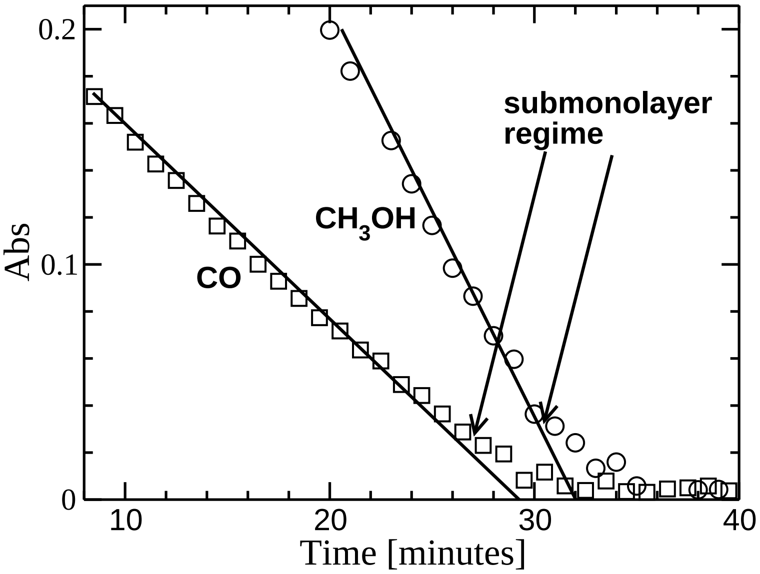

Figure 2.3 The decrease in integrated absorbance of CO and CH_3OH (1035 cm^{-1}) following desorption at a constant temperature of 29 and 135 K, respectively. The arrows indicate the transition points from the multi- to sub-monolayer regime.

2.3 Experimental results

2.3.1 A sample experiment

To illustrate the experimental method, we start by discussing a sample experiment in which a CO ice of 8×10^{15} molecules cm^{-2} is bombarded with H atoms with a flux of 5×10^{13} atoms cm^{-2} s^{-1} for three hours at a surface temperature of 12.0 K. This corresponds to a fluence of 5.4×10^{17} atoms cm^{-2}. Figure 2.2 shows the RAIR difference spectrum (ΔAbs) after these three hours of exposure (after - before). The CO, the H_2CO and the CH_3OH spectral signatures are indicated with respect to the spectrum recorded before the H-atom bombardment started. The CO appears as a negative band, indicating its use-up, and the other bands are positive, indicating the formation of H_2CO and CH_3OH. Neither the intermediate species, HCO and H_3CO, nor more complex species are observed.

The column density N_X (molecules cm^{-2}) of species X in the ice is calculated using

$$N_X = \frac{\int A(\nu)\mathrm{d}\nu}{S_X}, \tag{2.2}$$

where $A(\nu)$ is the wavelength dependent absorbance. Since literature values of transmission band strengths cannot be used in reflection measurements, an apparent absorption band strength, S_X of species X is calculated from a calibration experiment in which an ice layer of species X desorbs at constant temperature until the sub-monolayer regime. This is illustrated in Fig. 2.3, which shows the decrease in integrated absorbance of CO and CH_3OH during such an experiment. The arrows in the graph indicate the deviation onset from constant desorption, which marks the transition point from the multi- to sub-monolayer regime. The apparent absorption band strengths of CO and CH_3OH (1035 cm^{-1}) thus obtained are setup specific. The corresponding uncertainty in the band strengths remains within 50%. The ratio of S_{CO} to S_{CH_3OH} in our reflection experiment is similar to the transmittance ratio, 0.85. The value for S_{H_2CO} is obtained by assuming mass balance

$$N_{CO}(t) + N_{CH_3OH}(t) = -\frac{\int A(\nu)d\nu}{S_{H_2CO}} \tag{2.3}$$

for a set of different experiments. In addition, the results discussed in the present chapter are all in a regime where the proportionality relation (Teolis et al. 2007) still holds ($<3 \times 10^{16}$ molecules cm^{-2}).

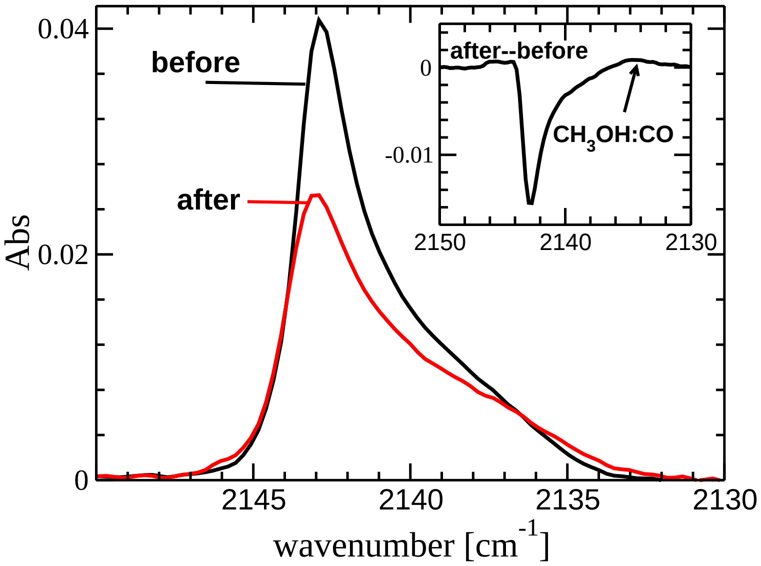

Figure 2.4 Spectral change of the CO 2143 cm^{-1} RAIR band before and after H-atom bombardment. The inset shows the corresponding difference spectrum.

The CO band shape can change when molecules other than CO are formed. Figure 2.4 shows the 2143 cm^{-1} IR peak before and after the H-atom exposure. A clear decrease in the peak height can be observed caused by the use-up of CO during the experiment, as expected. However, an additional peak appears at 2135 cm^{-1} (see inset Fig. 2.5), which is due to a CH_3OH–CO ice interaction. Transmission IR spectra of a CH_3OH:CO mixture show a band at 2136 cm^{-1} (Bisschop 2007, Palumbo & Strazzulla 1993). When the methanol bands grow, the band at 2135 cm^{-1} also increases. Figure 2.5 shows how the peak position of CO shifts with the methanol content in the reflection spectra. The RAIR spectra on which this graph is based, are taken for ice layers that are formed by co-deposition of CO and CH_3OH of known ratio. The CO stretching mode in H_2O:CO and NH_3:CO mixtures shows a similar behavior (Sandford et al. 1988, Bouwman et al. 2007). As for both H_2O and NH_3, CH_3OH is able to form hydrogen bonds and these hydrogen bonds most likely cause the redshift of the CO band. By comparing the position of the peak in Fig. 2.4 at 2135 cm^{-1} to the data in Fig. 2.5, we can constrain the methanol fraction in the top layers, assuming that the formed CH_3OH:CO mixture has the same spectral behavior as the deposited mixtures. The observed data after three hours correspond to a CH_3OH:CO mixture of at least 90%. This means that the top layer of the ice is completely converted into H_2CO and CH_3OH and that no or very little additional mixing with CO occurs. For the H_2CO and CH_3OH band, no spectral changes are observed during the experiments.

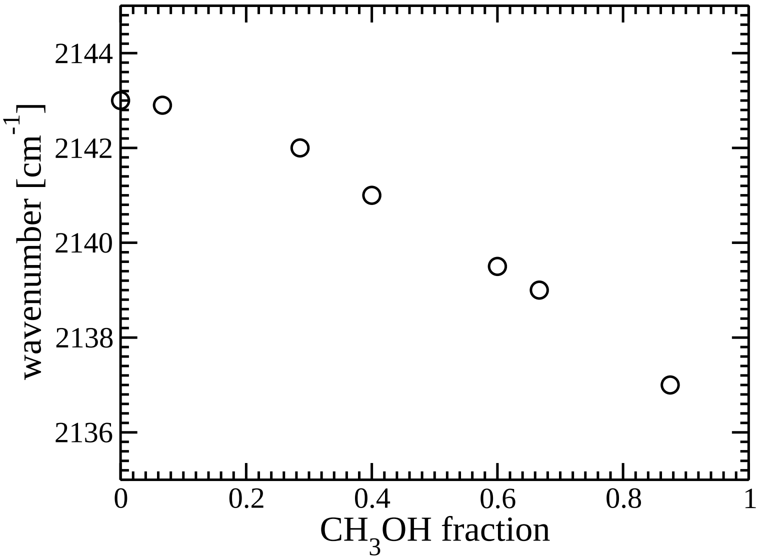

Figure 2.5 CO RAIR band position as a function of CH_3OH content in a CO:CH_3OH mixed ice obtained by co-deposition experiments.

To quantify the use-up of CO and the formation of new products, we have to assume that the apparent absorption band strength is constant during an experiment, *i.e.*, independent of the ice composition. Bouwman et al. (2007) found that the band strength of the 2143 cm^{-1} CO feature is indeed unaffected within the experimental error by the water content in H_2O:CO-ice mixtures up to 4:1. The band strength is expected to behave similarly for a CO:CH_3OH-mixture. Furthermore, if the band strength is strongly affected by the ice composition, the total ice thickness determined using a constant band strength should vary in time, whereas the real thickness is constant. Since this does not occur, we estimate that the change in band strength caused by the change in ice composition is negligible and well within our margins of error.

Figure 2.6 (a) shows the time evolution of the integrated CO, H_2CO, and CH_3OH signals in symbols. It shows how the amount of CO decreases as the abundance of H_2CO increases for four different temperatures. After bombardment with 1×10^{17} H atoms cm^{-2}, the formation of methanol kicks off at the expense of the growth of the H_2CO abundance. Similar trends of abundance evolution as a function of fluence are reported by Watanabe et al. (2006a). This indicates that the fluence is determined with relatively high accuracy since in both experiments different atomic sources (Tschersich vs. microwave induced plasma) and different calibration methods are used.

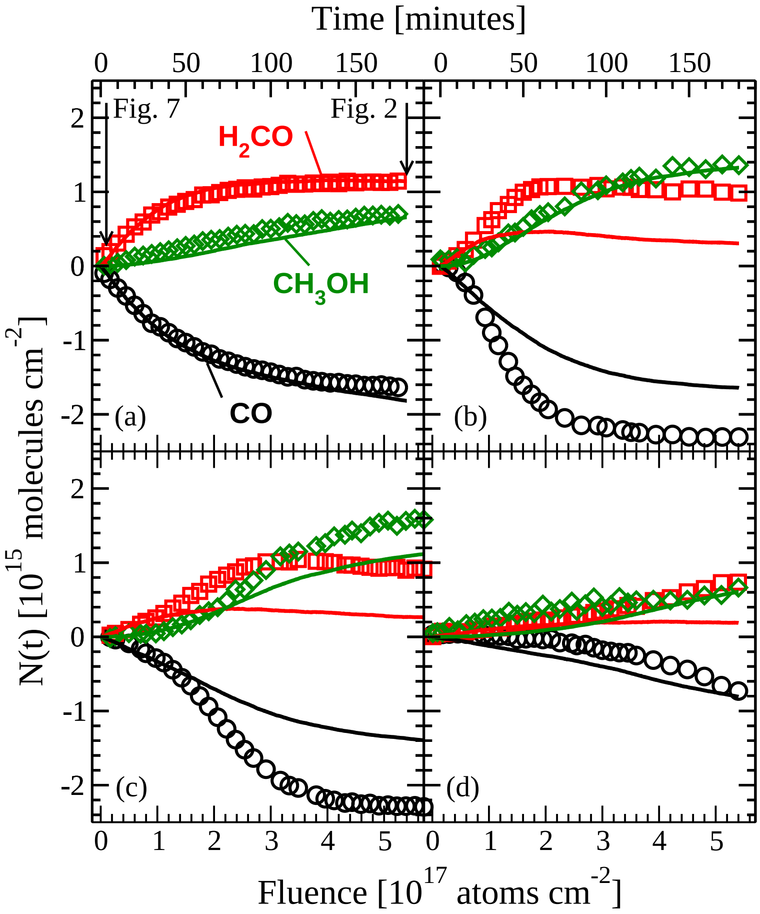

Figure 2.6 Time evolution of the surface abundance (molecules cm^{-2}) of CO, H_2CO and CH_3OH during H-atom bombardment of CO ice with a H-atom flux of 5×10^{13} cm^{-2} s^{-1} at surface temperatures of 12.0 K (a), 13.5 K (b), 15.0 K (c), and 16.5 K (d). Experimental data (*symbols*) and Monte Carlo simulation results (*solid lines*) are shown as well.

2.3.2 Flux dependence

As mentioned in § 2.1, the apparent discrepancy between the results by Hiraoka et al. (2002) and Watanabe & Kouchi (2002) has been attributed to a difference in the H-atom flux used in the respective experiments. The setup in our laboratory is able to cover the entire flux range from 10^{12} to 10^{14} cm^{-2} s^{-1}. For high flux, both formaldehyde and methanol are formed as can be seen in Figs. 2.2 and 2.6 and in the corresponding work of Watanabe & Kouchi (2002).

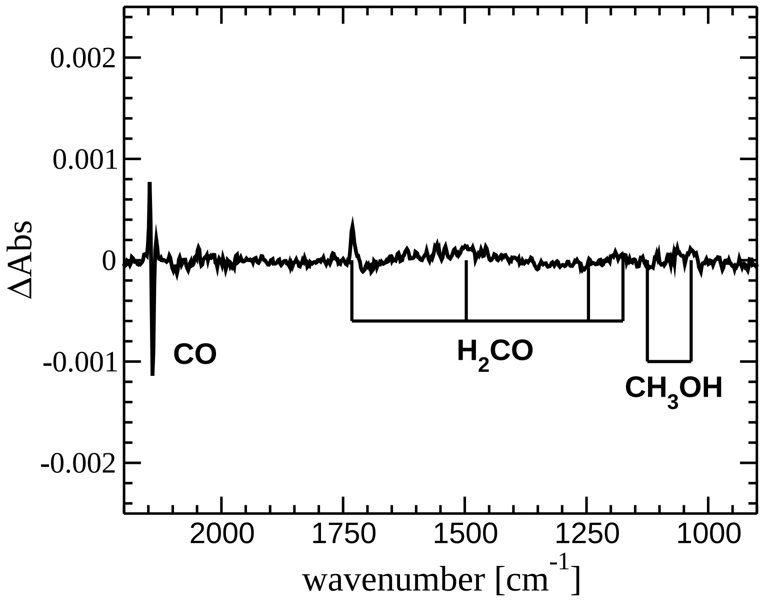

Figure 2.7 RAIR spectrum of a solid CO ice at 12.0 K exposed to a H-atom fluence of 1×10^{16} H atoms cm^{-2}.

A difference spectrum of a similar experiment but with a lower flux of 10^{12} cm^{-2} s^{-1} is plotted in Fig. 2.7. The exposure time here is four hours to reach a higher total fluence of 1×10^{16} cm^{-2}, which is still significantly less than the sample experiment shown in Fig. 2.2. Note that the vertical scales in Figs. 2.2 and 2.7 cover the same range. For longer exposures, surface contamination would become a problem, but methanol features would eventually become detectable. As Fig. 2.7 clearly shows, a smaller fraction of CO is transformed into H_2CO and the sensitivity of the RAIR spectrometer is not sufficiently high to confirm the formation of CH_3OH in these circumstances. TPD, however, is more sensitive as a diagnostic tool, although harder to use for a quantitative or time resolved analysis. Figure 2.8 plots several TPD spectra. It shows a small methanol desorption peak around 150 K. We checked experimentally that the carrier of this peak is indeed formed in the ice during the hydrogen exposure and that the observed CH_3OH is not a contaminant in the UHV chamber. This is a strong indication that the formation mechanism of formaldehyde and methanol does not fundamentally change with varying flux. The H_2O desorption at 20−30 K originates in frozen background water on the surrounding parts of the cryohead.

The arrows in Fig. 2.6 (a) indicate the corresponding fluences for the low and high flux experiments shown in Figs. 2.7 and 2.2, respectively. From this, it is immediately apparent that only a limited amount of methanol can be formed under low flux circumstances. Note that Hiraoka et al. (2002) probably used an even lower fluence since their exposure time was four times shorter than in our experiment. In addition, they used a slightly lower temperature of 10 K.

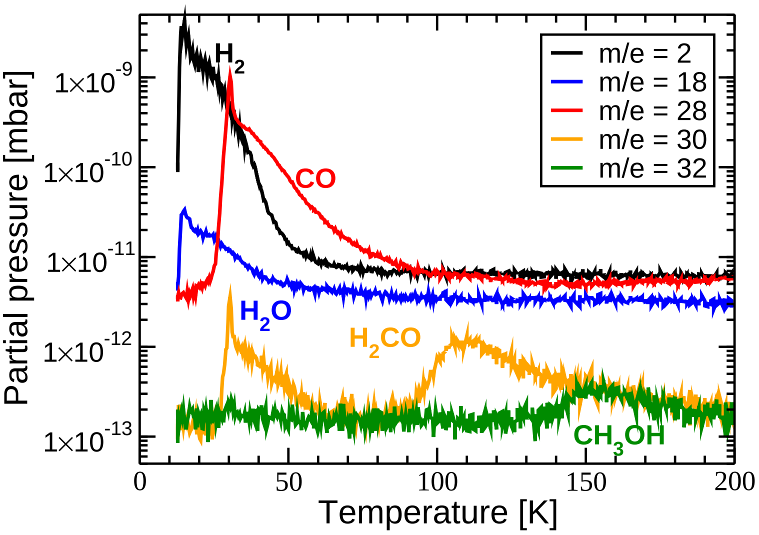

Figure 2.8 The TPD spectra corresponding to Fig. 2.7.

2.3.3 Thickness dependence

The effect of the initial layer thickness on the formation yield of H_2CO and CH_3OH is investigated by repeating the sample experiment for different CO layer thicknesses. Figure 2.9 shows the absolute reaction yield after a fluence of 5.4×10^{17} H atoms cm^{-2} as a function of the layer thickness. In all cases, a steady state value for H_2CO is reached for this fluence. The figure clearly shows that for CO ice layers thicker than 4×10^{15} molecules cm^{-2}, the absolute yield is layer thickness independent and the results are reproducible within the measurement error. The combined H_2CO and CH_3OH yield of 2×10^{15} molecules cm^{-2} is lower than the 4×10^{15} molecules cm^{-2} penetration column. From these experiments, we conclude that the penetration column of the H atoms into the CO ice is at most 4×10^{15} molecules cm^{-2} at 12.0 K. This corresponds to 4 monolayers of solid (bulk) CO molecules. At least half of the CO molecules in the active layer is converted into H_2CO and CH_3OH. The determination of the penetration column by this experiment is only an upper limit because of the low thickness resolution in Fig. 2.9. It however agrees with the previous estimate of nearly 100% conversion.

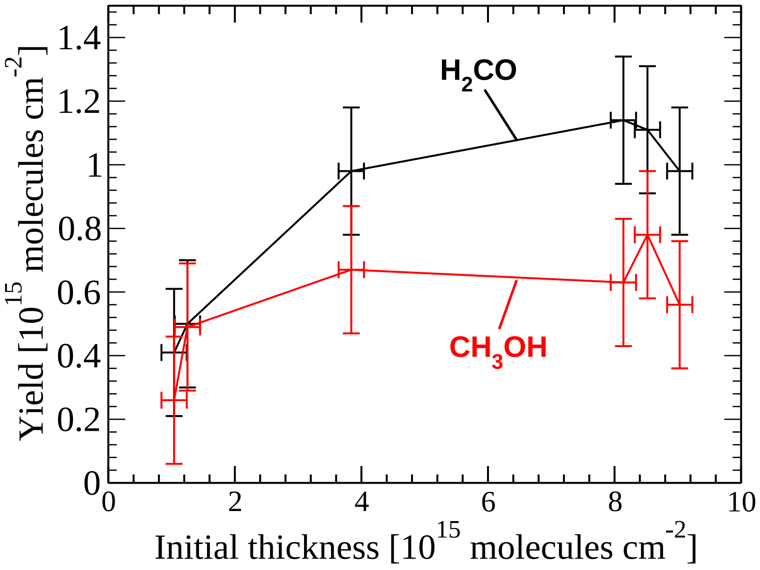

Figure 2.9 The absolute reaction yield of H_2CO and CH_3OH after a fluence of 5.4×10^{17} H atoms cm^{-2} as a function of the layer thickness for experiments at 12.0 K.

2.3.4 Temperature dependence

Several experiments for different surface temperatures have been performed. The initial layer thickness and flux values are comparable to the values used in the sample experiment. Figures 2.6 (b)-(d) show the results for hydrogenation experiments at 13.5, 15.0, and 16.5 K, respectively. These clearly indicate the very different evolution of CO, H_2CO, and CH_3OH abundance with temperature. Table 2.1 gives the initial formation rate of formaldehyde (slope at $t = 0$) and the final H_2CO and CH_3OH yields, and also indicates whether or not a steady state is reached. The table shows that at early times, the formation rate of H_2CO is much lower for higher temperatures than for 12.0 K. We will return to this point later. The final yield of CH_3OH is however larger at 13.5 and 15.0 K. For $T > 15$ K, the production rate of H_2CO is simply so low that a steady state is not reached. Minimal amounts of formed methanol were also detected in experiments at 18.0 and 20.0 K, but since some CO desorption and redeposition occurs at these temperatures, they are not presented here for a quantitative discussion.

The appearance of the extra CO band at 2135 cm^{-1} indicates that for temperatures between 12.0 and 15.0 K a nearly pure methanol layer is formed. We expect a similar behavior for formaldehyde. This means that the active CO layer involved in the reactions can be determined directly from the steady state yield of H_2CO and CH_3OH. This active layer increases with temperature indicating that the penetration column of H atoms into CO ice increases with temperature as one would expect. The CO molecules in the ice are more mobile at higher temperatures making it easier for H atoms to penetrate the CO ice, since the ice becomes less rigid. Note that the absolute temperature calibration in the set-up of Watanabe and ours appears to differ by 1−2 K (comparing Fig. 3 in Watanabe et al. (2006a) and Fig. 2.6 here), but the observed trends are identical.

Table 2.1 The production rate and yield of H_2CO and the yield of CH_3OH.

T (K)	Rate$(H_2CO)_{t=0}$[a] (10^{-3} molec./H atom)	Yield (H_2CO)[b] (10^{15} molec. cm^{-2})	Yield (CH_3OH)[b] (10^{15} molec. cm^{-2})	Steady state	Calc. pen. column[c] (10^{15} molec. cm^{-2})
12.0	9.0	1.2	0.8	yes	2.0
13.5	7.3	1.0	1.4	yes	2.4
15.0	3.2	0.9	1.6	yes	2.5
16.5	1.1	0.8	0.6	no	
18.0	1.0	0.5	0.2	no	
20.0	0.9	0.4	0.1	no	

---

[a] Rate at $t = 0$ determined from slope.

[b] Yield after three hours of H-atom exposure which corresponds to a fluence of 5.4×10^{17} H atoms cm^{-2}. The steady state yield is not reached for all temperatures (fifth column).

[c] Penetration column obtained from columns 3, 4, and 6.

2.4 Monte Carlo simulations

2.4.1 The method

To infer the underlying mechanisms leading to the formation of methanol, a detailed physical-chemical model is required. The present section discusses an approach based on the continuous time, random-walk Monte Carlo simulation technique. This method differs from previous studies based on rate equations and enables the study of surface processes to be performed in more detail. In addition, it provides a clearer understanding about what occurs physically on the surface. In contrast to an analysis using rate laws, the Monte Carlo method determines the H surface abundance by taking into account the layered structure of the ice, the H-atom flux, diffusion, reaction and desorption. This allows an extension of the results to conditions with much lower fluxes such as in the interstellar medium (ISM). For a detailed description of the method and program, we refer to Cuppen & Herbst (2007).

During a simulation, a sequence of processes - hopping, desorption, deposition, and reaction - is performed, where this sequence is chosen by means of a random number generator in combination with the rates for the different processes. First, an initial ice layer is created by deposition of CO on a surface. The resulting surface roughness of this layer depends on temperature and flux. For the experimental conditions simulated here, the CO ice is compact with a maximum height difference across the surface of only 2−3 monolayers. Hydrogen atoms and hydrogen molecules are subsequently deposited, following their relative abundance in the H-atom flux, at an angle perpendicular to the surface to mimic the experimental conditions. They move, react, and desorb according to rates of a form similar to that used in gas-grain models

$$R_x = A \exp\left(-\frac{E_x}{T}\right), \tag{2.4}$$

where E_x is the activation energy for process X, and A is the pre-exponential factor for which a constant number of $\nu \sim kT/h = 2 \times 10^{11}$ s^{-1} is used. The activation energies are not well determined *ab initio* or by experiment. The desorption energies are determined from the binding energy, as explained below, and depend on an energy parameter E. The barriers for reaction are used as a parameter to fit the data. The barrier for hopping (diffusion) from site i to j is assumed to be

$$E_{\mathrm{hop}}(i, j) = \xi E + \frac{\Delta E_{\mathrm{bind}}(i, j)}{2}. \tag{2.5}$$

This expression ensures microscopic reversibility between the different types of sites. The parameter ξ is another input parameter, which is varied between simulations. Little quantitative information is available about diffusion rates on these kind of surfaces, which makes the value of ξ uncertain.

Diffusion into the ice is also considered. Minimum energy path calculations suggest that CO and H can swap position enabling an H atom to penetrate into the CO ice (see Appendix B). The barrier for this process strongly depends on the layer in which the H atom is situated. In the simulations, the barrier for this event is $(350 + 2(z_1 + z_2))$ K for an H atom to swap between layer z_1 and z_2. This compares to a hopping barrier of $E_{\mathrm{hop}}^{\mathrm{H,flat}\rightarrow\mathrm{flat}} = 256$ K and a desorption energy of $E_{\mathrm{bind}}^{\mathrm{H,flat}} = 320$ K (see § 2.4.2). Hiraoka et al. (1998) found that hydrogen atoms can relatively easily diffuse through the CO ice. Moreover, the current experiments show that hydrogen atoms can penetrate into a maximum of four monolayers for 12.0 K. Hydrogen atoms are also allowed to swap with formaldehyde and methanol, but here the initial barrier is chosen to be higher (450 and 500 K) since these species are heavier and are more strongly bound within the ice matrix.

2.4.2 The CO ice layer

Although the experimental CO layers are probably amorphous (Kouchi 1990), crystalline layers are used in the Monte Carlo simulations discussed here. In this way, a lattice-gas Monte Carlo method can be used, which enables far longer simulation times than in off-lattice methods. We expect the crystalline assumption to be reasonable since the local structure of the CO layers is probably close to crystallinity. The energy released during deposition may help the molecules to rearrange slightly, leading to micro-crystalline domains. The α-CO structure (Vegard 1930) is used with layers in the (110) orientation. The dominant faces of a CO crystal will have this crystallographic orientation. The CO surface consists of alternating carbon and oxygen terminated bi-layers. In the bulk configuration, each CO molecule has 14 nearest neighbors: five in layers below, five in layers above, and four in the same layer. The additive energy contribution of these neighbors is $2E$ for the layers below and E for the neighbors in the same layer or of lower z, where z is the depth in layers with respect to the top layer. The different treatment for sites below the particle is to add a contribution for longer range interactions from the ice layer. E is chosen to be 32 K for atomic hydrogen, and 63 K for CO. This leads to a binding energy of $E_{\mathrm{bind}}^{\mathrm{H,flat}}$ = 320 K for H on top of a flat CO ice layer, and $E_{\mathrm{bind}}^{\mathrm{H,layer}}$ = 448 K and $E_{\mathrm{bind}}^{\mathrm{CO,layer}}$ = 882 K for H and CO, respectively, embedded in a CO layer. These values agree very well with binding energies obtained by calculations using accurate H-CO and CO-CO potentials of 320, 440, and 850 K, respectively (see Appendix B).

2.4.3 Comparison to the experiment

The solid lines in Fig. 2.6 represent the results from the Monte Carlo calculations. The exact mechanisms included in these simulations are discussed in more detail in the following sections. The resulting time evolution series are in very good agreement for 12.0 K. The agreement for 13.5, 15.0, and 16.5 K is far less good, probably because of missing mechanisms that promote the penetration into the ice. In the current simulations, only swapping of species is included. Because of the thermal motion of the CO molecules, "real" penetration in which the H atoms penetrate in the CO matrix may also be possible. The shape of the curves is reproduced and only the H_2CO abundance levels off at too low yields.

The main parameters varied to fit the experimental data are the reaction barriers and the diffusion rates. The best-fit model barriers are summarized in Table 2.2. Since the intermediate species HCO and H_3CO are not experimentally detected, the barriers for hydrogenation of these species are significantly lower than for the other two reactions, presumably even zero. The HCO and H_3CO abundances stay below detectable levels in the simulations. The reaction barriers for H + CO and H + H_2CO are temperature dependent and increase with temperature. Our values are in good absolute agreement with the barriers found by Awad et al. (2005), who also found a similar temperature behavior. Their values were obtained using a rate equation analysis for T = 10, 15, and 20 K using the data from Watanabe et al. (2006a). The temperature dependence suggests that there is a clear tunnelling component for the reaction at low temperature. The two barriers for forming H_2CO and CH_3OH show different temperature dependencies. The formation of methanol becomes relatively more important at higher temperature. Note that the Monte Carlo method automatically treats a reaction in competition with desorption and hopping. This is in contrast to gas-grain codes, where it must be included explicitly. To describe the chemical processes properly, one should introduce this competition into the gas-grain model.

The errors in the energy barriers reflect the errors due to the uncertainties in the sticking probability, H-atom flux, diffusion, and exact structure of the CO ice.

Molecular hydrogen is formed on the surface with efficiencies ranging from 3% at $T = 16.5$ K to 70% at $T = 12.0$ K. However, because of the large excess energy of the formation reaction, the majority of the formed H_2 molecules leaves the surface, and the H_2 surface abundance is predominantly determined by impinging H_2 molecules.

Table 2.2 Reaction rates and barriers for CO + H and H_2CO + H for different temperatures.

T	CO + H		H_2CO + H	
	barrier	rate	barrier	rate
(K)	(K)	(s^{-1})	(K)	(s^{-1})
12.0	390 ± 40	2×10^{-3}	415 ± 40	2×10^{-4}
13.5	435 ± 50	2×10^{-3}	435 ± 50	2×10^{-3}
15.0	480 ± 60	3×10^{-3}	470 ± 60	5×10^{-3}
16.5	520 ± 70	4×10^{-3}	490 ± 70	2×10^{-2}

2.4.4 Effect of diffusion

Since the diffusion rates are uncertain, this section discusses the effect of diffusion in more detail. Minimum energy path calculations of the diffusion of a single hydrogen atom on a CO (110) surface (see Appendix B) results in energy barriers ranging from 70 to 170 K ($\xi = 2-5.3$) depending on the direction of diffusion. The Monte Carlo program considers only one type of diffusion between "flat" sites. This corresponds more closely to the isotropic nature of an amorphous surface. Amorphous surfaces are usually more corrugated than crystalline surfaces, increasing the hopping barrier. The second term in Eq. 2.5 ensures microscopic reversibility. Figure 2.10 shows the influence of the diffusion parameter ξ on the H_2CO and CH_3OH production. The simulations are carried out in the presence of H_2 for 12.0 K (*top*) and 15.0 K (*bottom*). The difference in diffusion appears to have a larger effect at 15.0 K than at 12.0 K. Faster diffusion (smaller ξ) clearly results in less CH_3OH and H_2CO production, since the H atoms are more likely to find each other and to react to form H_2. Slower diffusion provides more time for the H atoms per CO encounter to cross the reaction barrier and form HCO. In the simulations presented in Figs. 2.6 and 2.11, we use $\xi = 8$ to reduce the simulation time. This parameter choice results in a ratio $E_{\mathrm{hop}}(\mathrm{flat}, \mathrm{flat})/E_{\mathrm{bind}}(\mathrm{flat})$ of 0.78, which agrees with the experimentally found ratio for H atoms on olivine and amorphous carbon (Katz et al. 1999). The amorphocity of the surface may be responsible for such a high ratio.

2.4.5 Effect of H_2 molecules on the hydrogenation

All simulations include the deposition of both H atoms and H_2 molecules, which results from the undissociated H_2 molecules in the H-beam. If the H_2 molecules are excluded from the simulations, the formation of H_2CO and CH_3OH is affected in only a limited number of cases of both fast diffusion and high temperature. The presence of H_2 appears to have two principle effects: it limits the penetration into the ice and decelerates the H atoms, since they move through a "sea" of H_2. The first effect reduces the production rate, whereas the second depends on the reaction barrier.

The experimental results at temperatures higher than 12.0 K show non-first-order behavior at early times (exponential decay of CO). The H_2CO production rate increases until 30 and 50 minutes of exposure for $T = 13.5$ and 15.0 K, respectively. After this time, the H_2CO and CH_3OH follow the expected first order behavior. None of the simulations in Fig. 2.10 show this trend. The only mechanism capable of describing this phenomenon is an increasing effective H-atom flux with time. This increase in effective flux can be cased by an increase in the sticking of atomic hydrogen to the surface. Since the incoming H atoms are relatively warm, they need to dissipate this extra energy into the surface to stick. Because CO is relatively heavy compared to the H atoms, this energy dissipation will be inefficient, and most of the H atoms will scatter back into the gas phase. Once the surface abundance of the much lighter H_2 molecules increases, the sticking of the H atoms to the surface will increase as well. We assume a 1% sticking for H atoms and H_2 molecules on a bare CO surface and a 65% sticking of H atoms on a surface that is fully covered with H_2. The sticking probability is further assumed to grow linearly with the H_2 coverage. The H_2 surface abundance reaches a constant level of 0.39 ML after a few minutes for T is 12.0 K. This results in a sticking of H atoms to the surface of 26%. For higher temperatures, it is noticeably longer time before to a steady state is reached, explaining the non-linear behavior at early times and inferring a lower final sticking probability. The solid lines in Fig. 2.6 include this mechanism.

As mentioned earlier, Watanabe & Kouchi (2002) concluded that the temperature of the beam has little effect on the hydrogenation process, which seems to contradict our H_2 argument. However, their experiments were carried out at 10 K, where the surfaces are covered with hydrogen atoms early on in the experiment because of the enhanced sticking at low temperatures. They further reported an unknown flux difference between the cold and warm beam, which makes quantifying the sticking probability using these experiments not possible. In conclusion, the temperature of the beam can affect the effective flux of H atoms landing on the surfaces, but it does not introduce additional energetic effects that influence the crossing of the barrier.

2.5 CO hydrogenation under interstellar conditions

Based on the fitting results in the previous section, the Monte Carlo routine can now be used to simulate CO hydrogenation reactions under interstellar conditions. An important ingredient is the H-atom density in the cloud. As in our laboratory beam, the gas in dense clouds consists of a mix of H and H_2. Under steady-state conditions, the balance of the rates of H_2 formation on grains and H_2 destruction by cosmic rays infers an H-atom density of around 1 cm^{-3} (Hollenbach & Salpeter 1971). This H-atom number density is independent of the total density because both the formation and destruction rates scale

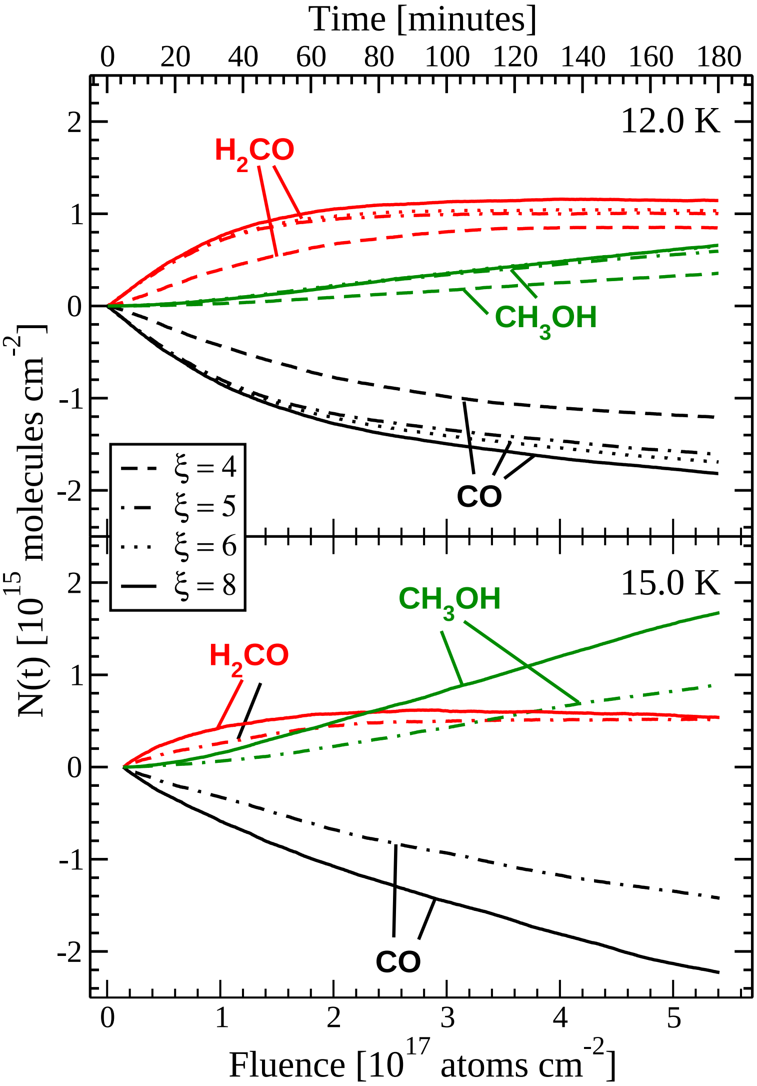

Figure 2.10 Monte Carlo simulations of the time evolution of the surface abundance of CO, H_2CO and CH_3OH during H-atom bombardment of CO ice at 12.0 K (*top*) and 15.0 K (*bottom*). Reaction barriers for H + CO and H + H_2CO can be found in Table 2.2. The diffusion is varied via the parameter ξ (Eq. 5).

with density. Before steady-state is reached, however, the H-atom density may be higher because the timescale for H to H_2 conversion is long ($\sim 10^7$ yr), starting from a purely atomic low-density cloud (Goldsmith et al. 2007). Our model assumes a constant H-atom density of 10 cm^{-3}. Our other model parameters are a gas temperature of 20 K and dust temperatures of 12.0 and 16.5 K. A CO surface is then simulated for 2×10^5 yr, which corresponds to a fluence of 10.8×10^{17} atoms cm^{-2}. Note that half of this fluence was reached in our experiments. Because the H-atom velocities are low, the sticking of H atoms to the CO ice is not varied in the simulations, but remains constant at 100%.

The starting configuration for the simulations is a layer of pure CO ice. This is believed to be representative for the top layers of the grain mantles at the center of a high-density collapsing cloud. Here, the ice layer is observed to consist of predominantly CO ice as the result of "catastrophic" CO freeze-out (Pontoppidan 2006, Pontoppidan et al. 2008). More heterogeneous ice layers are formed at lower densities where CO and H_2O are mixed, or towards the center of proto-stellar envelops or proto-planetary disks where the dust has been heated and CO has desorbed from the top layers.

Figure 2.11 (*top*) shows the resulting time evolution of CO, H_2CO, and CH_3OH ice (thick lines) for 12.0 K. The thin lines in Fig. 2.11 represent the direct scaling of the simulations of the experiment on interstellar timescales. The H_2CO/CH_3OH ratio of the low flux simulation is very different from the scaled experimental simulation. The reason for this is that in the laboratory environment twice as many hydrogen atoms react with each other to form H_2 than are involved in the four CO hydrogenation reactions since the surface density is relatively high. For interstellar conditions, the CO hydrogenation reactions dominate and only <5% of the reacting H atoms are converted into H_2. A second effect that changes the time evolution of the ISM is the difference in sticking. Under laboratory conditions, the sticking probability is much lower since the incoming H atoms at room temperature cannot release their energy very efficiently into the CO ice. The presence of H_2 on the surface may have a positive effect on the sticking probability. In the ISM, the incoming atoms are much colder and energy dissipation will not be a limiting factor for the sticking of H atoms into CO ice. This can be modelled using Monte Carlo simulations but only after deriving the energy barriers by fitting the laboratory data.

The bottom panel in Fig. 2.11 shows similar trends for 16.5 K. Again the onset of H_2CO and CH_3OH formation is at much lower fluences than in the experiment. At the end of the simulation, nearly all H_2CO has been converted into CH_3OH. This is in contrast to the 12.0 K simulations, where a constant non-zero amount of H_2CO remains after 2×10^5 yr. The crossover point from H_2CO-rich to CH_3OH-rich ice occurs at slightly later times at 16.5 K compared to 12.0 K. This can clearly be seen in Fig. 2.12, which plots the H_2CO/CH_3OH ratio for both temperatures. At early times, this ratio is similar for 12.0 and 16.5 K. At $t > 10^3$ yr, the ratio starts to level off at 12.0 K, while it still decreases rapidly at 16.5 K. The noise in the curve for 16.5 K below $t = 5 \times 10^3$ yr is due to the low abundances of H_2CO and CH_3OH.

In space, the H_2CO/CH_3OH ice ratio has been determined directly for only three high-mass young stellar objects (YSOs): W 33A, NGC 7538 IRS9, and AFGL 70009S, with inferred ratios ranging from 0.09 to 0.51 (Keane et al. 2001, Gibb et al. 2004). The laboratory curves for the H_2CO and CH_3OH production show that H_2CO is more or equally abundant during most of our experiments. Thus, values as low as 0.09–0.51 cannot easily be reproduced in the experiments. However, the Monte Carlo simulations for interstellar conditions have a crossover from H_2CO-rich to CH_3OH-rich ice at significantly earlier

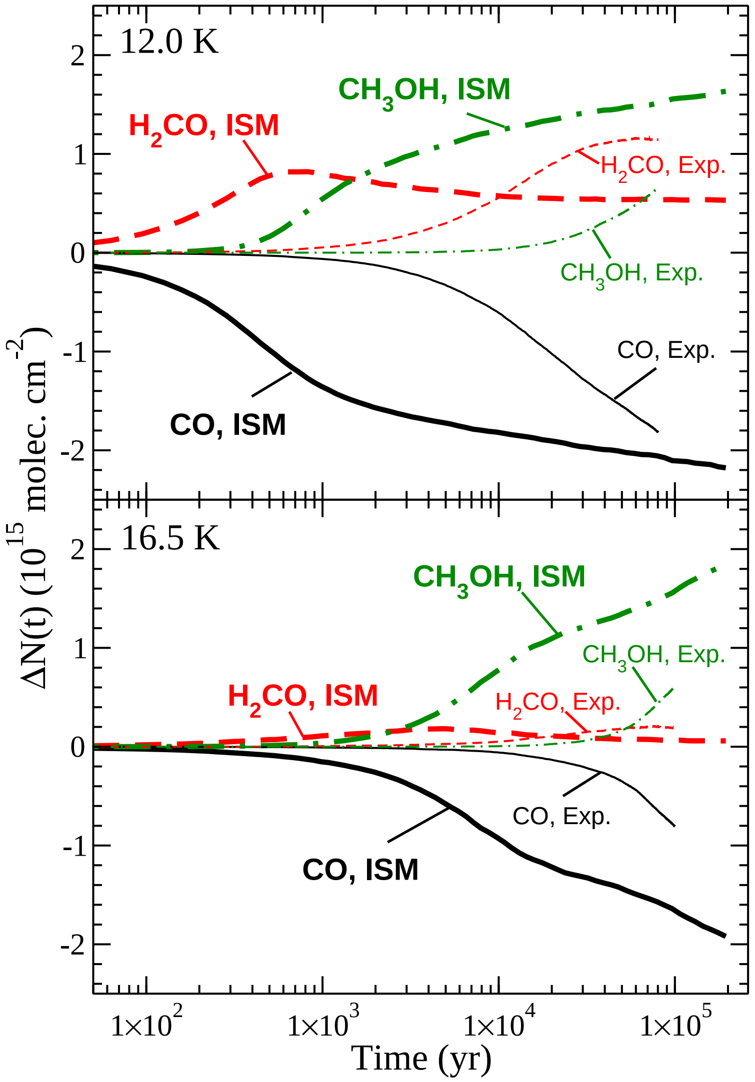

Figure 2.11 Monte Carlo simulations of CO-ice hydrogenation at 12.0 (*top*) and 16.5 K (*bottom*). A constant atomic hydrogen gas phase density of 10 cm^{-3} and a gas temperature of 20 K is assumed. Thick lines represent interstellar conditions, thin lines are the scaled experimental simulations. The results are shown as the change in column density compared with $t = 0$ yr.

times than the experimental curves and a H_2CO/CH_3OH ratio of 0.51 is obtained after 5×10^3 yr at $T_{\mathrm{dust}} = 12$ K. Grains at higher temperatures will have this crossover at even earlier times and for grains with $T_{\rm dust}$ = 16.5 K, a H_2CO/CH_3OH ratio of even 0.09 is obtained after 2×10^4 yr. Thus, the observed ratios are in agreement with the models discussed above for chemical timescales $>2\times10^4$ yr, which is consistent with the estimated ages of these high-mass protostars of a few $10^4 - 10^5$ yr (Hoare et al. 2007).

CH_3OH ice has also been detected toward low-mass YSOs with abundances ranging from <1% to more than 25% of the H_2O ice abundance (Pontoppidan et al. 2003, Boogert et al. 2008). An interesting example is the Class 0 protostar Serpens SMM 4, for which a particularly high CH_3OH abundance of 28% with respect to H_2O ice was deduced for the outer envelope (Pontoppidan et al. 2004). The upper limit to the H_2CO-ice abundance implies a H_2CO/CH_3OH ratio <0.18, implying an age $>1\times10^4$ yr at 16.5 K. This is consistent with the estimated timescale for heavy freeze out in low-mass YSOs of $10^{5\pm0.5}$ yr, including both the pre-stellar and proto-stellar phases (Jørgensen et al. 2005).

Other observational constraints come from sub-millimeter observations of the gas in a sample of massive hot cores, where a constant ratio of H_2CO/CH_3OH of 0.22 ± 0.05 was found (Bisschop et al. 2007c). If both the observed H_2CO and CH_3OH have just evaporated freshly off the grains and if they have not been affected by subsequent gas-phase chemistry, the observed ratio should reflect the ice abundances. This ratio is roughly consistent with the asymptotic value reached by the 12 K model. This remarkably constant abundance ratio implies that very similar physical conditions (*e.g.*, dust temperatures, H-atom abundances) exist during ice formation.

In contrast, since the CH_3OH ice abundance with respect to that of H_2O is known to vary by more than an order of magnitude, both local conditions and timescales appear to play a role. Note, however, that for CH_3OH abundances as large as 25% (columns as large as 10^{18} cm^{-2}), the CH_3OH layer is approximately 25 ML thick ($0.25 \times n(H_2O)/(n_{\rm dust} \times$ <binding sites per grain>) = $0.25\times10^{-4}/(10^{-12}\times10^6)$ = 25 ML), much more than can be produced from just the upper 4 ML of the CO ice. Thus, conversion of CO into CH_3OH ice must in these cases occur simultaneously with the freeze-out and building up of the CO layer. Pure CO ice can also easily desorb as soon as the protostar heats up. This complicates the use of CH_3OH/CO ice as an evolutionary probe. A proper model of interstellar CH_3OH ice formation should therefore include the effects of the variations in CO-ice abundances and dust temperatures in the pre- and protostellar phases, and account for the differences in timescales for CH_3OH-ice formation compared with those of CO adsorption and desorption. This Chapter provides the necessary molecular data to compile such a model.

2.6 Conclusion

The present Chapter shows that the formation of methanol by successive hydrogenation of CO and H_2CO is efficient under various laboratory conditions covering $T_{\rm surf} = 12 - 20$ K, ice thicknesses between 1×10^{15} and 1×10^{16} molecules cm^{-2} equivalent to 1 and 10 ML bulk CO, and H-atom fluxes between 1×10^{12} and 5×10^{13} cm^{-2} s^{-1}. Our results show that the discrepancy between Hiraoka et al. (2002) and Watanabe & Kouchi (2002) was indeed caused mainly by the use of different H-atom fluxes and we agree with the latter

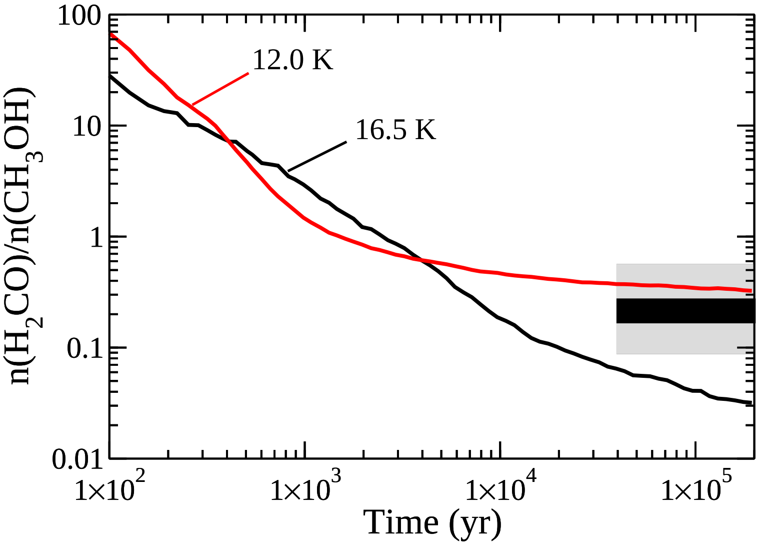

Figure 2.12 The H_2CO/CH_3OH ratio as a function of time obtained from the Monte Carlo simulations of CO hydrogenation at 12.0 and 16.5 K under ISM conditions (see Fig. 2.11). The grey box indicates Spitzer ice observations, the black box gas phase observations.

group of authors that CH_3OH is formed at low temperature. *On the basis of this, the surface hydrogenation of CO can now be safely used to explain the majority of the formed methanol in the interstellar medium*, where it is a key molecule in the synthesis of more complex molecules.

Energy barriers for the H + CO and H_2CO + H reactions are obtained by fitting Monte Carlo simulation results to the experimental data. Using these barriers, the methanol production is simulated for interstellar conditions. The obtained H_2CO and CH_3OH abundances do not scale directly with fluence because of the different relative importance of H_2 production and CO hydrogenation in space compared with the laboratory, as can be clearly seen by comparing the thick and thin lines in Fig. 2.11. However, laboratory experiments are required to derive the necessary rates that serve as input to the Monte Carlo program. The obtained H_2CO/CH_3OH ratios for the interstellar simulations are in closer agreement with observational limits than a direct translation of the experimental observations.

Monte Carlo simulations of the hydrogenation process show that the presence of H_2 has three effects: it promotes the sticking of the warm H atoms, it limits the penetration into the ice, and it slows down the diffusion of H atoms. The first effect will be negligible under interstellar conditions since the incoming H atoms will be cold already and the sticking probability will therefore be high regardless of the substrate. The latter two effects will be important and are similar to the conditions in the laboratory for also a high H_2 abundance.

The experiments show that the hydrogenation process is thickness independent for layers thicker than 4×10^{15} cm^{-2}, and that the active layer, which contains only a limited amount of CO after a steady state is reached, becomes slightly thicker with temperature. For temperatures higher than 15.0 K, a clear drop in the production rate of methanol is observed. This is probably due to two effects: the desorption of H atoms becoming important and the sticking of H atoms being reduced because of the low H_2 surface abundance. Both effects cause the H surface abundance to drop substantially at those temperatures and therefore reduce the probability of hydrogenation reactions occurring in the laboratory. Simulations of CO hydrogenation in space show a strong temperature dependence of the H_2CO/CH_3OH ratio over several orders of magnitude. The CH_3OH abundance changes with time, temperature, and fluence.

Appendix A: Absolute and relative H-atom flux determination

Absolute flux determination

The (accuracy of the) absolute value of the H-atom flux at the ice surface is obtained by estimating lower and upper limits in two independent ways. We exemplify here the H-atom flux determination for the case of our standard values with an H_2 pressure in the chamber of $p_{H_2} = 1 \times 10^{-5}$ mbar and a filament temperature of $T = 2300$ K.

The lower limit to the absolute flux is directly available from the experimental results presented in Chapter 3. That chapter discusses the H_2O_2 and H_2O production from H-atom bombardment of O_2-ice in time using the same setup and settings. During the first hour, H_2O_2 and H_2O are produced with an almost constant production rate of 6.0×10^{12} molecules cm^{-2} s^{-1}. Since both molecules contain two hydrogen atoms, this means that the H-atom flux should be at least twice this value. Assuming a conservative sticking probability of hydrogen atoms at 300 K to O_2-ice between 12 and 28 K of at most 50%, we determine a lower limit to the flux of 2.4×10^{13} cm^{-2} s^{-1}.

The determination of the upper limit to the H-atom flux is more elaborate and involves several steps. Figure 2.1 shows that the hydrogen atoms travel from the source through the atomic-line chamber to a quartz pipe, where the atoms are collisionally cooled and then travel through the main chamber onto the substrate. The final H-atom flux is then determined by

$$\phi_H = \frac{N_{H,source} k_1 k_2 p r}{A}, \tag{2.6}$$

where $N_{H,source}$ is the number of hydrogen atoms leaving the source per second, k_1 is the coupling efficiency between the source and quartz pipe, k_2 is the coupling efficiency between the quartz pipe and the ice surface, p accounts for the pressure drop between the two chambers, r for the loss in H-atoms because of recombinations in the quartz pipe, and A is the surface area that is exposed by the H-atom beam.

Our specific hydrogen source, used in the experiments described here, has been tested prior to delivery at the Forschungszentrum in Jülich where the flux, solid angle, and dissociation rate have been measured for a wide range of H_2 pressures and filament temperatures. The set-up used for these calibration experiments is described in Tschersich & von Bonin (1998). These measurements confirmed that there is little variation between individual instruments, since nearly identical rates were obtained by Tschersich & von Bonin (1998) and Tschersich (2000) and later by Tschersich et al. (2008) for different H-atom sources of the same type. From the flux and dissociation rate measured in Jülich, $N_{\mathrm{H,source}}$ can be obtained as well as k_1 using the solid angle information. In our example case, 4.1×10^{16} H atoms s^{-1} leave the H-atom source and 44% of these atoms enter the quartz pipe, which is located at a distance of 1.5 cm.

The pipe is designed so that the atoms cannot reach the substrate directly and that the number of hydrogen recombinations is kept to a minimum. This is achieved by using a short pipe with a high diameter/length ratio and choosing quartz, which is known to have a low recombination efficiency. Following Walraven & Silvera (1982), a theoretical estimate of the number of recombinations in the pipe can be determined, considering the specific shape and material. This reduces the H-atom flux by another 27 %. The pipe ends in close proximity to the cryogenic surface. The use of a pipe instead of a pinhole or a slit results in a focused H-atom beam for which the flux can be determined to relatively low uncertainty. From geometric considerations, a minimum solid angle can be estimated. This will suffice, since our aim is to obtain an upper limit to the flux. The H-atom beam covers $A = 4.9\ \mathrm{cm}^2$ of the substrate that is located 3 cm behind the quartz pipe. This spot falls completely on the surface and k_2 can readily be assumed to be unity.

Finally, the pressure drop between the source and the main chamber can be determined in two ways: by a calculation using the conductance of the pipe and the pumping speed, and by measuring the pressures in both chambers using undissociated beams. Both results are in reasonable agreement, leading to $p = 3.2 \times 10^{-2}$.

Our upper limit to the flux is now

$$\phi_{\mathrm{H}} = \frac{4.1 \times 10^{16} \cdot 0.44 \cdot 1 \cdot 3.2 \times 10^{-2} \cdot 0.73}{4.9} = 8.6 \times 10^{13} \mathrm{cm}^{-2} \mathrm{s}^{-1}. \qquad (2.7)$$

Deviations from this upper limit are expected to be due to a lower k_1 value, because of misalignments between the source and the entrance of the quartz pipe, an underestimation of the solid angle of the exiting beam from the quartz pipe (lower k_1 and higher A), more recombinations in the pipe or backscattering of atoms from the quartz pipe, to the chamber of the H-atom source.

The value of flux adopted in the present chapter is the resultant intermediate H-atom flux of $5 \times 10^{13}\ \mathrm{cm}^{-2}\ \mathrm{s}^{-1}$, which is within a factor of 2 of the upper and lower limits. It should be noted that this is a conservative error, since the true lower and higher flux limits are likely to be higher and lower, respectively.

Relative flux determination

The accuracy in the relative flux is particularly important to the conclusion presented in this Chapter, more so than the absolute value. For this we use the CO-hydrogenation data obtained from the experiments. Figure 2.13 shows the CO, H_2CO and CH_3OH evolution as a function of fluence for three different fluxes. The fluences are calculated using the flux determination as described above. The three curves clearly overlap, which means that the accuracy of the relative fluxes is well within our error bars. We conclude that the accuracy in the relative flux is substantially higher than the accuracy of the absolute flux, well below 50%. One of the main conclusions of this chapter, that the discrepancy between the two Japanese groups is due to a difference in flux, as envisaged by Hidaka et al. (2004), is therefore robust.

Finally, reproducing the same experiments on different days over the course of several months showed that reproducibility over periods from day-to-day to months is excellent, to within a few percent.

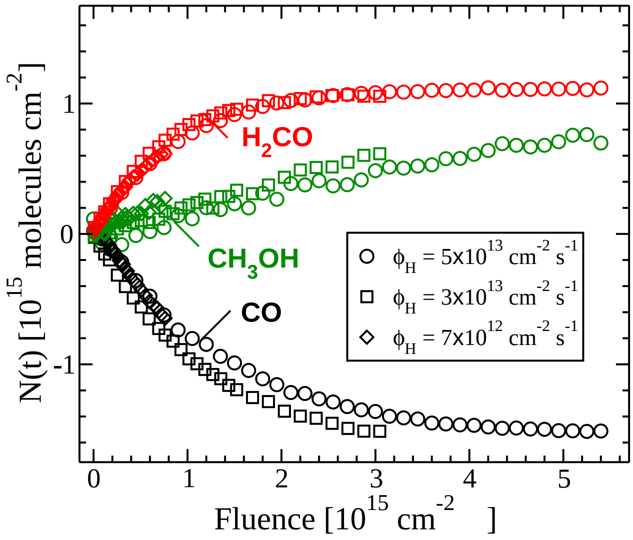

Figure 2.13 Time evolution of the surface abundance (molecules cm^{-2}) of CO, H_2CO and CH_3OH during H-atom bombardment of CO ice at 12.0 K with three different H fluxes of 5×10^{13}, 3×10^{13}, and 7×10^{12} cm^{-2} s^{-1}.

Appendix B: Binding energy calculations

To calculate binding energies and barriers to diffusion, recently-developed CO–CO and H–CO potentials are used. Takahashi and van Hemert (in prep.) have fitted high level electronic structure (coupled cluster) calculations of the CO–CO dimer to an analytic potential consisting of partial charges on the atoms and the centers of mass of the CO molecules, atom-based Lennard-Jones type interactions, and Morse potentials for the intramolecular C–O interaction. In the work by Andersson et al. (in prep.), a potential for the interaction between a hydrogen atom and CO has been calculated by fitting damped dispersion and exponential repulsion potentials to coupled cluster calculations.

Using the CO–CO potential, a CO (110) surface has been created consisting of 528 CO molecules in 11 monolayers in a cell with dimensions 33.8 Å × 31.8 Å in the surface plane. By applying periodic boundary conditions, an infinite surface is created. Binding energies have been calculated by performing energy minimizations for H atoms at different sites on top of and inside the CO surface and by comparing to the energy when the hydrogen is far away from the surface. In the same manner, the binding energy for a CO molecule in the top layer has been calculated. In all instances, the top 3 monolayers of the ice have been allowed to relax.

To calculate the energy barriers to diffusion both on and into the surface, the nudged elastic band (NEB) method (Jónsson et al. 1998) is used initially to map out the minimum energy path (MEP) connecting two potential minima. To fine-tune the barrier height, the Lanczos method is used to optimize the saddle point of the potential energy (Olsen et al. 2004).

CHAPTER 3

Laboratory Evidence for Efficient Water Formation in Interstellar Ices [1]

Even though water is the main constituent in interstellar icy mantles, its chemical origin is not well understood. Three different formation routes have been proposed following hydrogenation of O, O_2, or O_3, but experimental evidence is largely lacking. We present a solid state astrochemical laboratory study in which one of these routes is tested. For this purpose O_2 ice is bombarded by H- or D-atoms under ultra high vacuum conditions at astronomically relevant temperatures ranging from 12 to 28 K. The use of reflection absorption infrared spectroscopy (RAIRS) permits derivation of reaction rates and shows efficient formation of H_2O (D_2O) with a rate that is surprisingly independent of temperature. This formation route converts O_2 into H_2O via H_2O_2 and is found to be orders of magnitude more efficient than previously assumed. It should therefore be considered as an important channel for interstellar water ice formation as illustrated by astrochemical model calculations.

---

[1] Based on: S. Ioppolo, H. M. Cuppen, C. Romanzin, E. F. van Dishoeck, H. Linnartz, 2008, The Astrophysical Journal, volume 686, pages 1474-1479

3.1 Introduction

Solid water ice has been observed on the surfaces of many different astronomical objects. In the Solar System it is found on planets and minor bodies such as comets, trans-Neptunian objects and Centaurs. In dense, cold interstellar clouds, infrared observations show that interstellar dust grains are covered with water-rich ices (*e.g.,* Gillett & Forrest 1973, Gibb et al. 2004, Pontoppidan et al. 2004). The formation of these ice mantles is especially important in the process of star and planet formation, when a large fraction of heavy elements can be depleted onto grains. In the dense cloud phase water layers form on the bare grain surfaces. Then during the gravitational (pre-)collapse, virtually all gas phase species freeze-out on top of these water layers resulting in a CO dominated layer that likely also contains traces of O_2 but very little water.

The observed H_2O ice abundance cannot be explained by direct accretion from the gas phase only. The exact mechanism by which water ice is formed is not understood. The *Herschel Space Observatory*, to be launched in the near future, will provide important new information on gaseous water in interstellar space and will measure quantitatively the water abundance as a function of temperature, UV field and other parameters. Furthermore, the *Photodetector Array Camera and Spectrometer* (PACS) on *Herschel* will cover the 62 μm band of solid H_2O. In this way *Herschel* will provide a unique opportunity to observe the bulk of the water bands that are unobservable from the ground and relate them to *Spitzer* and groundbased mid-IR observations of ices in protostellar envelopes and protoplanetary disks. Understanding the processes by which water forms and why it is not formed under other circumstances will be essential for the interpretation of these data.

Tielens & Hagen (1982) proposed a reaction scheme in which water ice is formed on the surfaces of grains via three different routes: hydrogenation of O, O_2, and O_3. Models predict that water can indeed be formed through such reactions in dense clouds (e.g., Tielens & Hagen 1982, d'Hendecourt et al. 1985, Hasegawa & Herbst 1993, Cuppen & Herbst 2007). Using a Monte Carlo approach Cuppen & Herbst (2007) showed that the contributions of the different formation channels to water ice formation as well as its abundance strongly depend on the local environment. However, the initial reaction scheme with the corresponding rates as proposed by Tielens & Hagen (1982) is based on old, in some cases outdated, gas phase data of the equivalent reactions. Progress has been severely hampered by the lack of realistic experimental simulations of these low-temperature, solid state reactions. Preliminary laboratory studies of water synthesis testing the first reaction channel have been reported by Hiraoka et al. (1998) and by Dulieu et al. (2007). Both groups investigated the products of D- and O- reactions on an ice substrate (N_2O and H_2O, respectively) using temperature programmed desorption (TPD). In experiments exclusively using this technique, it is hard to rule out any H_2O formation during warm up. Furthermore, quantitative interpretation can be tricky because unstable species like H_2O_2 are destroyed in the mass spectrometer upon ionization leading to an artificially enhanced H_2O/H_2O_2 ratio. This chapter focuses on the H + O_2 channel in which O_2 is converted to H_2O via H_2O_2:

$$H + O_2 \rightarrow HO_2 \tag{3.1}$$

$$H + HO_2 \rightarrow H_2O_2 \tag{3.2}$$

$$H + H_2O_2 \rightarrow H_2O + OH \tag{3.3}$$

$$H + OH \rightarrow H_2O \tag{3.4}$$

According to Cuppen & Herbst (2007) this channel is, together with the O_3 channel, responsible for water formation in cold, dense clouds. The exposure of O_2 ice to hydrogen and deuterium atoms is investigated by means of reflection absorption infrared spectroscopy (RAIRS) and TPD. These techniques allow one to determine formation yields and the corresponding reaction rates. The present chapter comprises a study of hydrogenation and deuteration reactions of O_2 ice for different temperatures between 12 and 28 K, *i.e.*, up to the desorption temperature of O_2 (Acharyya et al. 2007). The formation of H_2O and H_2O_2 is observed at all temperatures. An optimum yield is found at 28 K.

3.2 Experiment

Experiments are performed using an ultra-high vacuum set-up ($<5\times10^{-10}$ mbar) which comprises a main chamber and an atomic line unit. The set-up is discussed in more detail in Fuchs et al. (2009). The main chamber contains a gold coated copper substrate (2.5×2.5 cm^2) that is in thermal contact with the cold finger of a 12 K He cryostat. The temperature can be varied with 0.5 K precision between 12 and 300 K. A precision leak valve is used to deposit O_2 (99.999% purity, Praxair) on the substrate. Ices are grown at 45° with a flow of 1×10^{-7} mbar s^{-1} where 1.3×10^{-6} mbar s^{-1} corresponds to 1 Langmuir (L) s^{-1}. In order to compare results from different experiments, the thickness of the O_2 ice is 75 L for all samples studied and the substrate temperature is kept at 15 K during the deposition. An O_2 ice of 75 L consists of roughly 30 monolayers. This thickness is chosen to exclude substrate induced effects. Because a diatomic homonuclear molecule like O_2 is infrared in-active, gas phase O_2 is monitored during the deposition by a quadrupole mass spectrometer (QMS). After deposition at 15 K the ice is slowly cooled down or heated (1 K min^{-1}) until a selected temperature is reached. Systematic studies are performed for different temperatures between 12 and 28 K.

H(D)-atoms are produced in a well-characterized thermal-cracking device (Tschersich & von Bonin 1998, Tschersich 2000). A second precision leak valve is used to admit H_2 (D_2) molecules (99.8% purity, Praxair) into the gas cracking line. In each experiment the H + H_2 (D + D_2) flow through the capillary in the atomic line is 1×10^{-5} mbar s^{-1} and the temperature of the heated tungsten filament, which surrounds the gas cracking pipe, is about 2300 K. The dissociation rate and the atomic flux depend on the pressure and temperature (Tschersich 2000) and are kept constant during all the experiments. A nose-shaped quartz pipe is placed along the path of the atomic beam in order to cool down H(D)-atoms to room temperature before reaching the ice sample by collisions (Walraven

& Silvera 1982). The H(D)-atomic flux nearby the sample is estimated, within 50%, as 5×10^{13} cm^{-2} s^{-1}. At temperatures of 12 K and higher, no blocking of surface processes by the presence of H_2 is expected in the ice.

The newly formed species after hydrogenation (deuteration) of O_2 ice are monitored by RAIRS using a Fourier transform infrared spectrometer (FTIR) running at a spectral resolution of 4 cm^{-1} in the range between 4000 and 700 cm^{-1} (2.5−14 μm). Typically the ice is exposed to the H (or D) beam for 3 (or 2) hours and IR spectra are acquired every few minutes.

Systematic control experiments have been performed in order *(i)* to unambiguously confirm that the products are formed by surface processes and not by gas phase reactions, *(ii)* to check that any water present in the system does not affect the final results and *(iii)* to verify that water and H_2O_2 formation occurs in the solid phase after H(D)-atom bombardment and not by H_2(D_2)-molecules addition. For *(i)* co-deposition experiments are undertaken in which H and O_2 are deposited simultaneously. Water is only formed if the surface temperature is below the desorption temperature of oxygen, confirming that the presence of the oxygen ice is required for this reaction sequence to occur. Point *(ii)* is verified by using inert initial substrates like N_2 ice to estimate the background water contribution, as well as by using different isotopologues ($^{18}O_2$, $^{15}N_2$ and D). Finally *(iii)* is checked by using pure H_2(D_2)-beams, *i.e.*, without any H(D) present.

3.3 Results

The formation of both H_2O_2 and H_2O ice is confirmed by the appearance of their infrared solid state spectral signatures. Figure 3.1 shows typical RAIRS results for hydrogenation and deuteration of O_2 ice at 25 K. From top to bottom a time sequence of four spectra is plotted. These spectra are difference spectra with respect to the initial oxygen ice. However, since our initial oxygen ice only consists of 30 ML, no features due to the intrinsically very weak O_2 feature (Ehrenfreund et al. 1992, Bennett & Kaiser 2005) are observed in the original spectrum. Both the H_2O and H_2O_2 clearly grow in time as the H-fluence (H-flux × time) increases. Similar features appear for the deuteration experiment, although here clearly less D_2O is formed. After fitting the infrared spectra with a straight baseline the column density (molecules cm^{-2}) of the newly formed species in the ice is calculated from the integrated intensity of the infrared bands using a modified Lambert-Beers equation (Bennett et al. 2004). In the range of our spectrometer, water ice has two candidate bands for determining its column density, at 3430 cm^{-1} and 1650 cm^{-1} (3 and 6 μm, respectively). Since the strong 3430 cm^{-1} feature overlaps with the 3250 cm^{-1} band of H_2O_2, the weak feature at 1650 cm^{-1} was chosen to quantify the water column density. Since literature values of transmission band strengths cannot be used in reflection measurements, an apparent absorption strength is obtained from a calibration experiment in which a pure water ice layer desorbs at constant temperature until the sub-monolayer regime (Öberg et al. 2007b). The uncertainty in the band strengths remains within a factor of two. Quantification of H_2O_2 is done using the 1350 cm^{-1} band. As it is experimentally very hard to deposit pure H_2O_2 ice, the apparent absorption strength has to be obtained indirectly by assuming the ratio of the integrated band strengths between the two bands in transmittance to be the same as in reflectance $H_2O/H_2O_2 = 0.57$ (Gerakines et al. 1995, Loeffler et al. 2006). The band modes of solid D_2O and D_2O_2 ices have systematic peak position shifts of ~400 cm^{-1} with respect to the H_2O and H_2O_2 bands. The column density for deuterated species is obtained in a similar way from a calibration experiment, while the absorption strength for D_2O_2 is estimated assuming that $H_2O/H_2O_2 = D_2O/D_2O_2$.

In Fig. 3.2 the column densities of water and H_2O_2 are plotted as a function of the H(D)-fluence (atoms cm^{-2}) for different substrate temperatures. The results for H_2O_2 and D_2O_2 are found to be very reproducible (errors within the symbols). Due to their low column densities the relative errors for H_2O and especially D_2O are larger. The H_2O_2 and D_2O_2 results all show the same initial linear increase followed by a very sharp transition to a steady state column density, with the steady state value increasing with temperature. The water results show similar behavior although the transition is not as sharp and the temperature dependence of the steady-state value is not as clear. The observation that the results for all temperatures show the same initial slope means that the rate of the reaction to H_2O_2 is temperature independent. The final yield is however temperature dependent and this depends on the penetration depth of the hydrogen atoms into the O_2 ices; at higher temperatures H-atoms can penetrate deeper. This is discussed in more detail later.

During the preparation of this manuscript we received a preprint by Miyauchi et al. (2008) who performed a similar experiment for one single temperature (10 K). Our results for 12 K turn out to be close to their results, apart from an absolute scaling due to different assumptions on the band strengths.

3.4 Determining the reaction rates

Reaction rates are obtained by fitting a set of differential equations to the time evolution curves of H_2O (D_2O) and H_2O_2 (D_2O_2). Usually a diffusive mechanism is considered to construct these equations. For H_2O_2 that is formed from oxygen and converted into water as given in Eqs. 3.1-3.4 the rate equation would be

$$\begin{aligned}\frac{\mathrm{d}n_{\mathrm{H_2O_2}}(\mathrm{t})}{\mathrm{dt}} &= (k^{\mathrm{H}}_{\mathrm{hop}} + k^{\mathrm{O_2}}_{\mathrm{hop}})k_1 n_{\mathrm{H}}(t) n_{\mathrm{O_2}}(t) \\ &- (k^{\mathrm{H}}_{\mathrm{hop}} + k^{\mathrm{H_2O_2}}_{\mathrm{hop}})k_3 n_{\mathrm{H}}(t) n_{\mathrm{H_2O_2}}(t) \qquad (3.5)\end{aligned}$$

with $k^{\mathrm{X}}_{\mathrm{hop}}$ and n_{X} the hopping rate and column density of species X and k_1 and k_3 the rate constants of reactions (3.1) and (3.3).

Awad et al. (2005) and Miyauchi et al. (2008) applied similar expressions to determine the rates of the formation of methanol and water, respectively. They solved these equations under the assumption that the atomic hydrogen abundance on the surface remains constant. In this way expressions for the surface abundances of the reaction products were obtained with only the effective reaction rates as fitting parameter

$$n_{\mathrm{H_2O_2}} = n_{\mathrm{O_2}}(0)\frac{\beta_1}{\beta_1 - \beta_3}\left(\exp(-\beta_3 t) - \exp(-\beta_1 t)\right), \qquad (3.6)$$

with

$$\beta_1 = (k_{\mathrm{hop}}^{\mathrm{H}} + k_{\mathrm{hop}}^{\mathrm{O_2}}) k_1 n_{\mathrm{H}}. \tag{3.7}$$

Fitting this expression to the experimental data points in Fig. 3.2 gives a very poor agreement because the model has an exponential behavior whereas the experiments for several temperature values clearly do not. This would moreover result in a different rate for H + O_2 for each temperature whereas the experimental curves show that the rate is independent of temperature. For this reason we decided to use a different model. We consider two regimes. In the first regime ($t < t_t$) the hydrogen atoms get trapped into the ice with an efficiency that is independent of temperature. Once an atom is trapped it can diffuse efficiently and find an oxygen molecule to react with. This results in a zeroth order rate. Once nearly all oxygen molecules within the penetration depth are converted to H_2O_2 ($t > t_t$), diffusion becomes rate limiting and a diffusive mechanism for the reaction to H_2O_2 and H_2O is applied. Since now the ice is changed from an O_2 ice to an H_2O_2 ice the penetration depth of the H-atoms into the ice will change as well. This model is described by the following set of equations

$$\begin{aligned} n_{\mathrm{H_2O_2}} &= \beta_1' t \frac{p_{\mathrm{O_2}} - p_{\mathrm{H_2O_2}}}{p_{\mathrm{O_2}}} + \frac{\beta_1'}{\beta_3} \frac{p_{\mathrm{H_2O_2}}}{p_{\mathrm{O_2}}} \left(1 - \exp(-\beta_3 t)\right) & (3.8) \\ n_{\mathrm{H_2O}} &= \beta_1' \frac{p_{\mathrm{H_2O_2}}}{p_{\mathrm{O_2}}} \left(t - \frac{1 - \exp(-\beta_3 t)}{\beta_3} \right) & (3.9) \end{aligned}$$

for $t < t_t$ and

$$\begin{aligned} n_{\mathrm{H_2O_2}} &= \frac{\beta_1'}{\beta_3} \frac{p_{\mathrm{H_2O_2}}}{p_{\mathrm{O_2}}} \exp(-\beta_3 t) \left(\exp(\beta_3 t_t) - 1\right) \\ &\quad + \frac{n_{\mathrm{O_2}}(t_t)}{\beta_3 - \beta_1} \frac{p_{\mathrm{H_2O_2}}}{p_{\mathrm{O_2}}} \left(\beta_1 \exp(-\beta_3 (t - t_t)) - \beta_3 \exp(-\beta_1 (t - t_t))\right) \\ &\quad - n_{\mathrm{O_2}} - p_{\mathrm{H_2O_2}} + p_{\mathrm{O_2}} & (3.10) \\ n_{\mathrm{H_2O}} &= -\frac{\beta_1'}{\beta_3} \frac{p_{\mathrm{H_2O_2}}}{p_{\mathrm{O_2}}} \exp(-\beta_3 t) \left(\exp(\beta_3 t_t) - 1\right) \\ &\quad - \frac{n_{\mathrm{O_2}}(t_t)}{\beta_3 - \beta_1} \frac{p_{\mathrm{H_2O_2}}}{p_{\mathrm{O_2}}} \left(\beta_1 \exp(-\beta_3 (t - t_t)) - \beta_3 \exp(-\beta_1 (t - t_t))\right) \\ &\quad + p_{\mathrm{H_2O_2}} & (3.11) \end{aligned}$$

for $t > t_t$ with p_{X} the penetration depth of H-atoms into ice X in units of column density, β_1 and β_1' the effective rates of reaction (3.1) and β_3 the rate of reaction (3.3). β_1 and β_3 represent effective diffusive rates that include both the diffusion rate and the reaction rate, whereas β_1' is mainly determined by the hydrogen flux times the efficiency of H trapping into the ice.

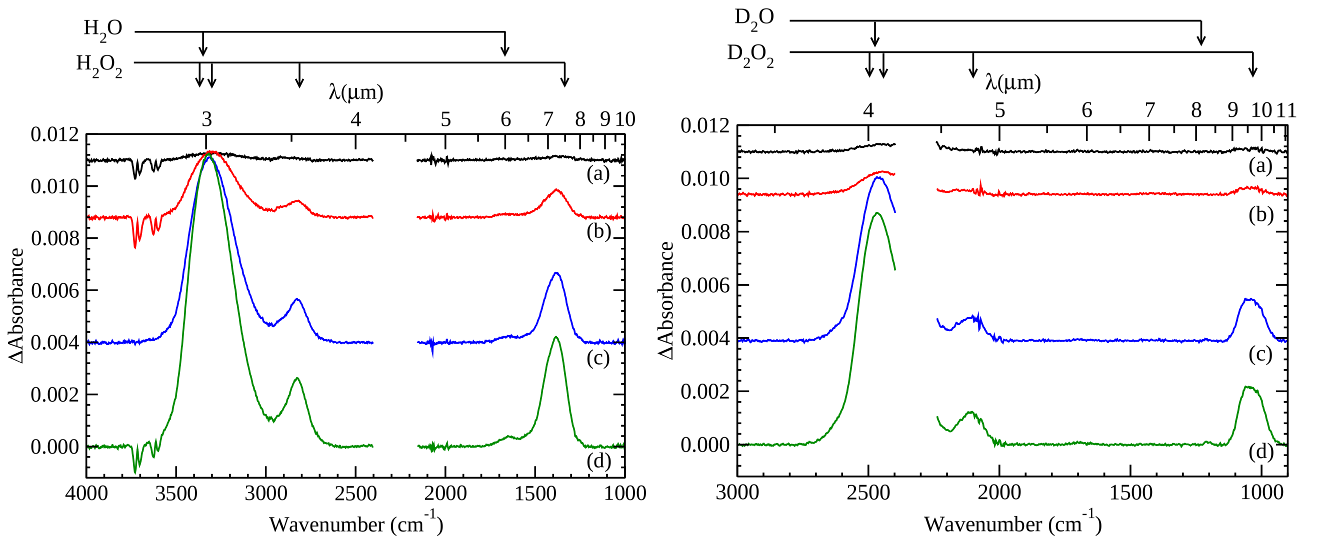

Figure 3.1 RAIR spectral changes of the O_2 ice as a function of H-atom (*left*) and D-atom (*right*) bombardment at 25 K. Spectra at a H(D)-atom fluence of (a) 4×10^{15}, (b) 4×10^{16}, (c) 1×10^{17}, and (d) 2×10^{17} cm^{-2} are given.

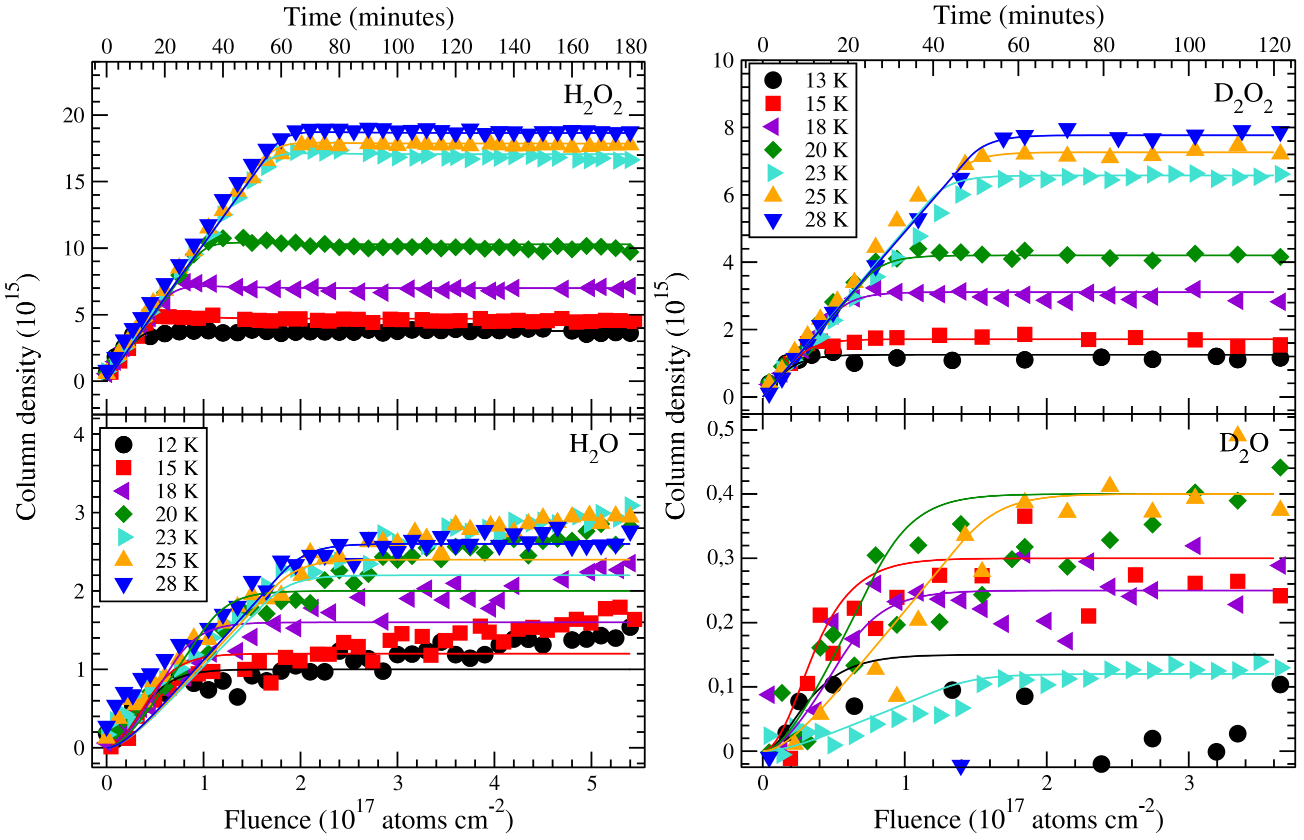

Figure 3.2 The column densities of H_2O_2/D_2O_2 (*top*) and H_2O/D_2O (*bottom*) as a function of time and fluence for different surface temperatures. The symbols indicate experimental data, the solid lines represent the fitted model. The left panel is for hydrogenation, the right for deuteration.

Fitting this model to the data, the three rates are found to be independent of temperature. We therefore apply the same average rate to describe the results at all temperatures and only the two penetration depths are allowed to vary between the experiments. The resulting curves are indicated by the solid lines in Fig. 3.2. The obtained rates are given in Table 3.1. The penetration depths are the steady state values in Fig. 3.2. These clearly increase with temperature to very high values. This suggests that as the O_2 ice reaches its desorption temperature (~30 K) the structure becomes more open and the O_2 molecules more mobile, allowing the hydrogen atoms to penetrate deeply into the ice. The H_2O_2 structure on the contrary is much more dense and rigid and consequently the H(D)-atoms cannot penetrate more than a few monolayers even at the highest temperatures. The temperature effect is also much less prominent in cases where the ice is comfortably below its desorption temperature.

Table 3.1 The reaction rates obtained by fitting the model. For the corresponding uncertainties see the text.

	β_1' [molec cm^{-2}s^{-1}]	β_1 [s^{-1}]	β_3 [s^{-1}]
$H + O_2$	5.4×10^{12}	3.3×10^{-3}	2.7×10^{-3}
$D + O_2$	2.5×10^{12}	3.3×10^{-3}	2.7×10^{-3}

A clear difference in penetration depth between the hydrogenation and deuteration experiments can be observed. For the oxygen penetration depth a difference of a factor of two is found whereas for hydrogen and deuterium peroxide the difference can be even as high as a factor of six.

Like in the models by Awad et al. (2005) and Miyauchi et al. (2008), the rates β_1 and β_3 are the products between the rates of the reactions and the hydrogen surface abundance. The latter is assumed to be constant during the experiment and is the overall result of accretion, desorption and reaction with both H and O_2. A comparison of β_1' and β_1 indicates that the reaction with H only plays a minor role.

The uncertainties in β_1 and β_3 are mainly determined by the fit and are within 50%. The error in β_1' due to the fit is much less, but here the main uncertainty is determined by the layer thickness. The error in the calibration of the layer thickness is a factor of two. Assuming that every hydrogen atom that gets trapped reacts with O_2 and considering that two hydrogen atoms are needed to convert O_2 to H_2O_2, the trapping efficiency can be determined from β_1' and the flux (5×10^{13} cm^{-2} s^{-1}). This results in a trapping efficiency of ~10% for deuterium and ~20% for atomic hydrogen. This is very close to the sticking efficiency of hydrogen atoms to a water ice surface of ~30% under these circumstances (Al-Halabi & van Dishoeck 2007). The high efficiency of reaction (3.1) is consistent with recent theoretical studies of this reaction in the gas phase. Xie et al. (2007) and Xu et al. (2005) found that this reaction can proceed barrierless for certain incoming angles. The rates β_1 and β_3 have very similar values. This suggests that also reaction (3.3) is very efficient and H_2O formation is only limited by the penetration depth of H_2O_2.

The rate of reaction (3.3) shows no significant isotope effect. This is in contrast with the results by Miyauchi et al. (2008) who found a significant isotope effect for this reaction using the diffusive model to fit their 10 K results. If a large barrier is involved in reaction (3.3), barrier crossing would proceed via tunneling and an isotope effect is expected (Watanabe, private communications). The fact that we do not observe a (large) effect at 12−28 K either suggests that the barrier for this reaction is low or that other mechanisms for the formation of water should be taken into account in the model to fit the data. We will address this question in Chapters 4 and 5. For now the conclusion remains that the formation of water from O_2 and H is very efficient.

3.5 Astrophysical discussion and conclusion

The hydrogenation and deuteration experiments presented in this letter show an efficient mechanism to convert O_2 ice to H_2O_2 and ultimately H_2O. In the model that describes these experiments, the rate limiting steps for formation are the trapping of the hydrogen into the O_2 ice and the penetration depth of the hydrogen into the H_2O_2. Astrochemical models take reaction, diffusion and desorption barriers as input. Our data shows that the formation of at least H_2O_2 proceeds via a reaction with a barrier that is much lower than the value of 1200 K previously assumed by Tielens & Hagen (1982). It should therefore be considered as a route for water formation on interstellar grain surfaces.

Care should however be taken when extending these findings from a laboratory environment directly to interstellar ices. The temperature independence of the reaction rate that is observed, for instance, is directly due to the unique property of the O_2 ice that allows hydrogen to penetrate its structure and thereby preventing desorption back into the gas phase. In interstellar clouds the mantle surfaces would not consist of pure O_2 ice but of a mixture of different species with water as its main constituent (Whittet et al. 1998). The structure of these "dirty" ices and the binding energies to it would govern the desorption and diffusion behavior of adsorbates like O_2 and H. Experiments on the binding of atomic hydrogen on water ice surfaces showed that the surface abundance is generally dependent on temperature (Perets et al. 2005, Hornekær et al. 2003, Dulieu et al. 2005). Also hydrogenation experiments of CO showed that the decreasing H coverage for increasing temperature results in lower effective rates (Watanabe et al. 2003, 2006b, Linnartz et al. 2007, Cuppen et al. 2008). Here we discuss the implications of the present work to two different interstellar environments: hydrogenation of an apolar (water-poor) ice mantle after freeze-out and cold cloud conditions where ice is formed from direct deposition of H and O.

Observations show that interstellar ice mantles consist of polar (water-rich) and apolar (water-poor) layers Tielens et al. (1991). Apolar ices are thought to form during freeze-out in the densest parts of the cloud. In dense gas, most of the atomic oxygen has converted to O_2 which can become subsequently a constituent of this polar phase. The lack of observed H_2O_2 and H_2O means that most of the O_2 in the ice does not react to produce H_2O_2 or H_2O. This laboratory work however shows that hydrogen atoms can penetrate deeply into O_2 ices and then react. In apolar interstellar ices the penetration depth is not

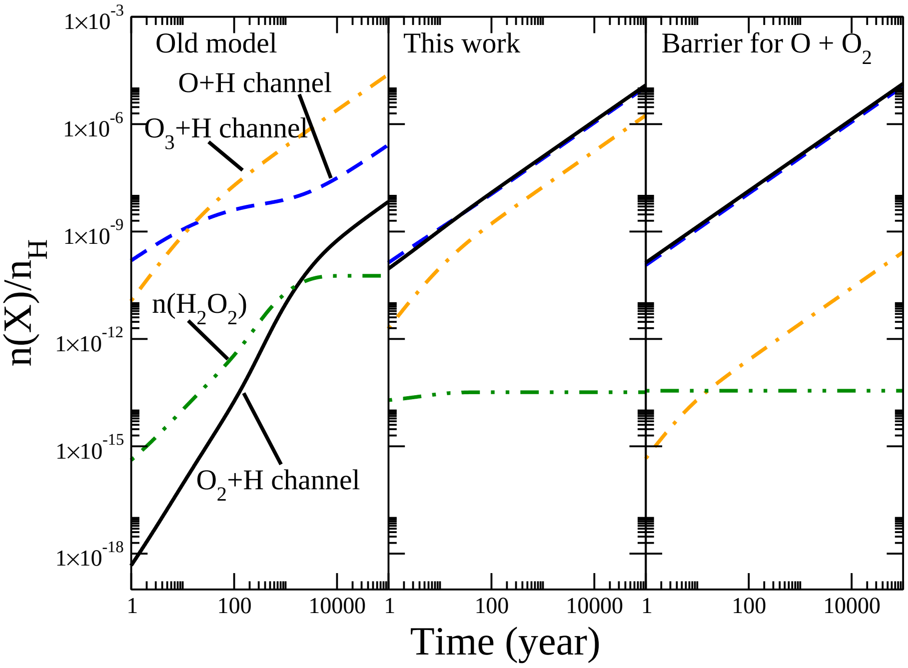

Figure 3.3 The contributions of the three different channels to H_2O formation in three models and the H_2O_2 abundance, $n(H_2O_2)$ from the O_2 + H channel. (*left*) Old network by Tielens & Hagen (1982), (*middle*) new network without barriers for reactions (3.1) and (3.3) and (*right*) new network with barrier for O + O_2 reaction. See text for details.

determined by oxygen ice but by the main constituent of the ice mantle, CO. We therefore have performed additional laboratory experiments in which a mixture of CO and O_2 ice is exposed to H-atoms. These show indeed that only the top few layers are hydrogenated and that the main part of the ice stays intact in agreement with the observations. Details of these experiments are reported in Ioppolo et al. (2010b) (Chapter 7).

In cold and translucent clouds H- and O-atoms deposit onto the grain simultaneously. The species can then react immediately and O_2 is converted all the way to water. Here the penetration depth observed in the laboratory becomes unimportant. What can we learn from the present experiments then? The fast reaction kinetics justify treating H + O_2 and H + HO_2 in a similar way as H + H are treated in astrochemical models, with the difference that probably only hydrogen is mobile for reaction. The results further suggest that the continuing reactions leading to water proceed with high efficiency. The original grain surface network by (Tielens & Hagen 1982) includes two more water formation routes: via OH and via ozone. Under dense cloud conditions the ozone route was proposed to be the most efficient as is shown in the left panel of Fig. 3.3. This figure plots the contributions for the three different H_2O formation channels using a reaction network limited to the three water formation routes and without any dissociation reactions. The model parameters are taken from model M1 by Ruffle & Herbst (2000) and the initial conditions from Tielens & Hagen (1982) are used ($n(H_2) = 5 \times 10^4$, $n(H) = 1.41$ and $n(O) = 2.36\ \mathrm{cm}^{-2}$). These calculations include a barrier for reactions (3.1) and (3.3). The present work shows that these barriers are negligible and the middle panel plots the same model calculation without these barriers. The figure clearly shows that the O_2 channel has a major contribution to the overall water formation rate. Recent laboratory experiments by Sivaraman et al. (2007) on the temperature-dependent formation of ozone by irradiation of oxygen ices by high energy electrons suggest that mobile oxygen atoms prefer the O + O pathway over O + O_2 even though the O/O_2 ratio in the ice is very small. This implies the presence of a barrier for the formation of ozone. The right panel gives the model results when a small barrier of 500 K for this reaction is considered. The contribution of the ozone channel is now further reduced.

Figure 3.3 further shows the H_2O_2 abundance, $n(H_2O_2)$, for all models as produced through the O_2 + H route. Boudin et al. (1998) set an observational constraint of the H_2O_2 ice abundance toward NGC 7538 IRS9 of 5.2% with respect to the H_2O ice abundance. All models are consistent with this number.

CHAPTER 4

Water formation at low temperatures by surface O_2 hydrogenation I: characterization of ice penetration[1]

Water is the main component of interstellar ice mantles, is abundant in the solar system and is a crucial ingredient for life. The formation of this molecule in the interstellar medium cannot be explained by gas phase chemistry only and its surface hydrogenation formation routes at low temperatures (O, O_2, O_3 channels) are still unclear and most likely incomplete. In Chapter 3 we discussed an unexpected zeroth-order H_2O production behavior in O_2 ice hydrogenation experiments compared to the first-order H_2CO and CH_3OH production behavior found in former studies on hydrogenation of CO ice. In this chapter we experimentally investigate in detail how the structure of O_2 ice leads to this rare behavior in reaction order and production yield. In our experiments H atoms are added to a thick O_2 ice under fully controlled conditions, while the changes are followed by means of Reflection Absorption InfraRed Spectroscopy (RAIRS). The H-atom penetration mechanism is systematically studied by varying the temperature, thickness and structure of the O_2 ice. We conclude that the competition between reaction and diffusion of the H atoms into the O_2 ice explains the unexpected H_2O and H_2O_2 formation behavior. In addition, we show that the proposed O_2 hydrogenation scheme is incomplete, suggesting that additional surface reactions should be considered. Indeed, the detection of newly formed O_3 in the ice upon H-atom exposure proves that the O_2 channel is not an isolated route. Furthermore, the addition of H_2 molecules is found not to have a measurable effect on the O_2 reaction channel.

---

[1] Based on: S. Ioppolo, H. M. Cuppen, C. Romanzin, E. F. van Dishoeck, H. Linnartz, 2010, Physical Chemistry Chemical Physics, volume 12, pages 12065-12076

4.1 Introduction

The presence of water is a prerequisite for the origin of life as we know it and, even though the ubiquity and abundance of water ice in space (*i.e.*, dense molecular clouds, protoplanetary disks and solar-like systems) is well established by infrared observations (Gillett & Forrest 1973, Dartois et al. 1998, Whittet 2003, Gibb et al. 2004, Boogert et al. 2008), the chemical origin of water is not yet well understood. Among the various molecules detected in the solid phase in dense molecular clouds, water is the dominant component of interstellar icy grain mantles. In such environments, the observed abundance of water ice cannot be explained by direct accretion from the gas phase only. Indeed, theoretical models predict that grain surface reactions play an essential role in water formation (Tielens & Hagen 1982, d'Hendecourt et al. 1985, Hasegawa et al. 1992, Hasegawa & Herbst 1993, Cuppen & Herbst 2007).

Tielens & Hagen (1982) proposed a reaction scheme in which solid water ice is formed on grain surfaces by hydrogenation of atomic oxygen, molecular oxygen and ozone. Using a Monte Carlo approach, Cuppen & Herbst (2007) showed that the contribution of the different formation channels strongly depends on the local environment in interstellar clouds. They concluded that the atomic oxygen channel is the main route in translucent and diffuse clouds, while the molecular oxygen channel, together with the ozone route, is more efficient in dense cold molecular clouds. However, these theoretical results on surface reactions are largely based on gas phase input data and these data should not be extrapolated directly to the solid phase. A systematic laboratory investigation of water ice formation at interstellar relevant temperatures (~10 K) is therefore highly needed to confirm these reaction routes.

The suggested water formation channel with the smallest number of steps is the hydrogenation of O atoms:

$$H + O \rightarrow OH, \tag{4.1}$$

$$H + OH \rightarrow H_2O, \tag{4.2}$$

and

$$H_2 + OH \rightarrow H_2O + H. \tag{4.3}$$

From gas phase data, it is clear that the radical-radical reactions (4.1) and (4.2) proceed without activation barriers. Recently, Atkinson et al. (2004) reviewed reaction (4.3), assigning it a gas phase barrier of 2100 K, instead of 2600 K as assumed earlier (Schiff 1973). Preliminary investigations on the H + O (D + O) channel in the solid phase have been carried out by Hiraoka et al. (1998) and Dulieu et al. (2010). Both groups reported the formation of D_2O by temperature programmed desorption (TPD) through reactions of D and O atoms on a N_2O matrix and an annealed amorphous H_2O ice, respectively. Since the TPD technique does not allow to distinguish between water formed at low temperature and during heating, a quantitative interpretation of these results is not straight-forward.

The hydrogenation of ozone proceeds through the formation of OH and O_2:

$$H + O_3 \rightarrow OH + O_2. \tag{4.4}$$

The hydroxyl radical can be further hydrogenated via reactions (4.2) and (4.3). Mokrane et al. (2009) reported experimental evidence for water formation via ozone deuteration at 10 K using again TPD for analysis. Also here, the exclusive use of a quadrupole mass spectrometer for the analysis of the surface reaction final products led to a qualitative study. Recently, Romanzin et al. (2010) investigated water formation via ozone hydrogenation/deuteration at different temperatures, combining infrared spectroscopy with mass spectrometry as a probe for the identification of the ongoing surface processes (see Chapter 6).

The hydrogenation of molecular oxygen results in the formation of water through the following steps:

$$H + O_2 \rightarrow HO_2 \tag{4.5}$$

$$H + HO_2 \rightarrow H_2O_2 \tag{4.6}$$

$$H + H_2O_2 \rightarrow H_2O + OH. \tag{4.7}$$

This O_2 channel is the best studied solid-phase route to form water in the literature. Reactions (4.5) and (4.6) have no activation barriers Troe & Ushakov (2008), Keyser (1986) while reaction (4.7) has a gas phase activation energy of ~1800 K (Baulch et al. 1992). Reactions (4.2) and (4.3) are also included in this channel. Several groups have explored the O_2 hydrogenation reaction route independently in the solid phase (Miyauchi et al. 2008, Ioppolo et al. 2008, Matar et al. 2008, Oba et al. 2009) and this channel is also the topic of the present chapter. The experimental procedure used here is similar to the one described in (Miyauchi et al. 2008, and Chapter 3).

In Chapter 3 we exposed 15 ML (1 ML $\sim 10^{15}$ molecules cm^{-2}) of solid O_2 to H/D atoms, covering a large range of ice temperatures from 12 K to 28 K. A comparison between the experimental results presented in Chapter 3 and obtained here, is reported in § 4.3.1 which discusses the temperature dependence. For all investigated temperatures shown in Chapter 3, we observed an initial linear and temperature independent growth of the products, H_2O_2/D_2O_2 and H_2O/D_2O, which corresponds to a zeroth-order formation rate. The final yield was found to be temperature dependent. Surface reactions are usually considered to follow second order dynamics, since they depend on the diffusion of two reactants. Because of the constant H-atom flux in the surface reaction experiments, which results in a constant abundance of one of the reactants, namely H, this will effectively lead to first order behavior. Our observation of zeroth order kinetics therefore came as a surprise. Hence, we decided to use an effective model to fit our results reflecting a zeroth order behavior. We considered two regimes to describe the initial linear temperature independent growth and the temperature dependent final yield, respectively. In the first regime, the H_2O_2/D_2O_2 is formed following a zeroth-order rate, while H_2O/D_2O follows a usual first order rate. In the second regime, both products follow first-order behavior. This method gives the correct functional form to describe the experimental results, whereas a first-order model over the entire regime does not. This is especially apparent at high temperatures. In contrast, Miyauchi et al. (2008) used a diffusive, first-order model to fit their hydrogenation/deuteration results, investigating only experiments at a low temperature of 10 K, where the zeroth-order behavior is less prominent.

Oba et al. (2009) stated that the physicochemical meaning of this model is unclear. However, in Chapter 3, we explained our two phase model by the following scenario. Initially, the incoming H atoms diffuse into the ice with an efficiency that is independent of temperature. Once an H atom is trapped in the ice, it can diffuse efficiently and find an oxygen molecule to react with. When nearly all oxygen molecules within the penetration depth, which is temperature dependent, are converted to H_2O_2/D_2O_2, diffusion becomes rate limiting. According to our model no large isotope effect was found for reaction (4.7). Using their diffusive model, Miyauchi et al. (2008) did find a significant isotope effect for this reaction. Our results, however, suggest that the reaction can proceed with a low barrier or that additional mechanisms for water formation should be taken into account in the model to fit the data.

In order to resolve this issue, we provide here the experimental verification of our scenario for a non-standard behavior, *i.e.*, for an initially linear and temperature independent growth of the reaction products with a final yield that is temperature dependent. For this purpose, the penetration mechanism of H atoms into the O_2 ice is studied experimentally and we discuss in detail the different possible origins for the temperature dependent penetration depth. Our further objective is to study several surface reaction mechanisms leading to H_2O formation under laboratory conditions for different temperatures, thicknesses and structures of the O_2 ice. In Chapter 5 we focus on unravelling the reaction scheme with an emphasis on alternative H_2O formation routes to explain the lacking isotope effect.

In the following sections we present the experimental and data analyzing methods, the results and discussion, which include temperature dependence, thickness dependence, structural effect, penetration mechanism, and H_2 dependence, and – in the last section – we summarize the main conclusions of this study.

4.2 Experimental and data analysis

4.2.1 Experimental

All experiments are performed in an ultra high vacuum setup (SURFRESIDE), which consists of a stainless steel vacuum main chamber and an atomic line. Details are available from Ioppolo et al. (2008), Fuchs et al. (2009). The room temperature base pressure of the vacuum system is in the 10^{-10} mbar regime. A schematic view of the experimental apparatus is shown in Fig. 4.1. The gold coated copper substrate (2.5×2.5 cm^2), placed in the center of the main chamber, is in thermal contact with a cold finger of a close-cycle He cryostat. The substrate temperature is controlled between 12 and 300 K with a precision of 0.5 K. The absolute temperature accuracy is better than 2 K. An all-metal leak valve is used to admit gaseous O_2 (99.999% purity, Praxair) into the chamber, where it condenses onto the substrate for temperatures below ~30 K (Acharyya et al. 2007). Deposition proceeds under an angle of 45° and with a controllable flow between 10^{-8} and 10^{-7} mbar s^{-1}, where 1.3×10^{-6} mbar s^{-1} corresponds to 1 Langmuir (L). According to the measurements presented here 1 ML corresponds to 3 L (see § 4.3.4). Diatomic homonuclear molecules like O_2 are infrared in-active, except when embedded in an ice matrix (Ehrenfreund et al. 1992). Hence, gas phase O_2 is monitored during the deposition mass spectrometrically using a quadrupole mass spectrometer (QMS) with a Faraday cup, which is placed behind the substrate and opposite to the atomic source.

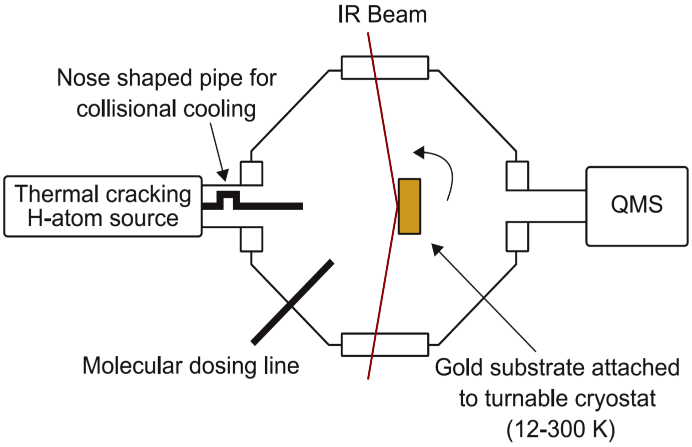

Figure 4.1 Schematic top-view of the solid-state experimental UHV set-up.

A second precision leak valve is used to admit H_2 molecules (99.8% purity, Praxair) into the capillary of a well-characterized thermal cracking source (Tschersich & von Bonin 1998, Tschersich 2000, Tschersich et al. 2008), which is used to hydrogenate our O_2 sample through heating the capillary from 300 to 2250 K by a surrounding tungsten filament. During the experiments the H + H_2 flow through the capillary and the temperature of the tungsten filament are controlled and kept constant. A quartz pipe is placed along the path of the dissociated beam. The nose-shaped form of the pipe is designed to efficiently thermalize all H atoms to room temperature through surface collisions *before* they reach the ice sample. The geometry is designed in such a way that this is realized through at least four collisions of the H-atoms with the walls before leaving the pipe. In this way, hot species (H; H_2) cannot reach the ice directly. Furthermore, previous experiments with liquid nitrogen cooled atomic beams did not show any H/D-atom temperature dependence in the O_2 hydrogenation reaction process (Miyauchi et al. 2008, Oba et al. 2009). It is important to note that the relatively high temperature of 300 K of the incident H atoms in our experiments does not affect the experimental results, since H atoms are thermally adjusted to the surface temperature as has been shown in Chapter 2.

In this work, atomic fluxes are measured at the sample position in the main chamber, following the procedure described in Hidaka et al. (2007). The H-atom flux used for all our experiments is 2.5×10^{13} atoms cm^{-2} s^{-1} for a filament temperature of 2200 K and an atomic chamber pressure of 1×10^{-6} mbar and confirms the value used within the errors in Chapter 2 and 3. The atomic beam is normal to the substrate surface except for the experiment regarding the angle dependence, which is reported in § 4.3.2. Details about

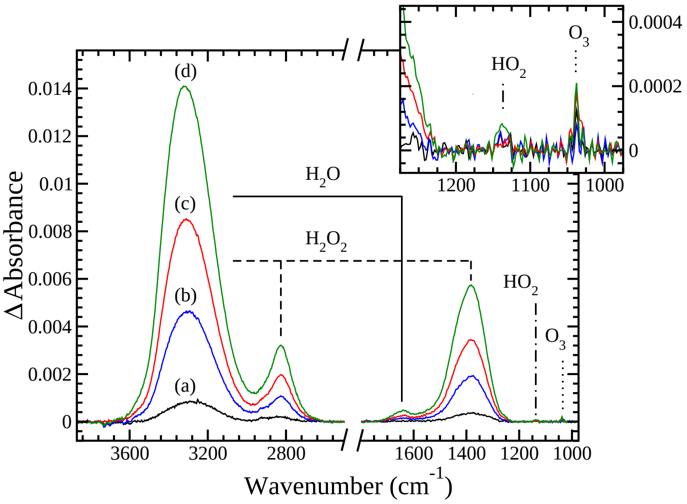

Figure 4.2 RAIR spectral changes of the O_2 ice at 25 K as a function of the H-atom fluence: (a) 4.5×10^{15}, (b) 3.7×10^{16}, (c) 7.5×10^{16}, and (d) 1.5×10^{17} atoms cm^{-2}.

the H- and D-atom flux determination are given in Appendix A.

Ices are monitored by means of RAIRS using a Fourier Transform InfraRed Spectrometer (FTIR), which covers the range between 4000 and 700 cm^{-1} (2.5−14 μm). A spectral resolution of 4 cm^{-1} is used and 512 scans are co-added. RAIR difference spectra ($\Delta Absorbance$) with respect to the initial O_2 ice are acquired every few minutes during H/D exposure. Newly formed solid H_2O/D_2O and H_2O_2/D_2O_2 in hydrogenation/deuteration experiments are detected using RAIRS. Table 4.1 shows an extensive list summarizing different ice thicknesses and temperatures for which the O_2 hydrogenation is investigated. Additional experiments are performed to study the effect of ice structure, the H-atom penetration mechanism into the ice and the role of H_2 in the hydrogenation reaction scheme. Deuteration experiments are also performed for control purposes.

4.2.2 Data analysis

After fitting the infrared spectra with a straight baseline, the column densities (molecules cm^{-2}) of the newly formed species are determined from the integrated intensity of the infrared bands using a modified Lambert-Beer equation (Bennett et al. 2004):

$$N_X = \frac{\int A(\nu)\mathrm{d}\nu}{S_X} \tag{4.8}$$

where $A(\nu)$ is the integrated absorbance and S_X is the corresponding band strength. This equation can however only be used for thin layers. Teolis et al. (2007) showed that the proportionality between the optical depth and the ice abundance breaks down for thick

Table 4.1 List of experiments. The ice thickness is expressed in monolayers (ML); R_{dep} is the O_2 deposition rate; T_{dep} is the substrate temperature during O_2 deposition; $T_{H/D-add}$ is the substrate temperature during H/D-atom addition; P_{AL} is the atomic line pressure during the H/D-atom exposure; T_{AL} is the tungsten filament temperature; H/D-atom fluence is the total fluence at the end of the experiment; t is the time of the H/D-atom addition which includes, in some cases, the ramping time when changing temperature.

O_2 Thickness (ML)	R_{dep} (ML min^{-1})	T_{dep} (K)	$T_{H/D-add}$ (K)	P_{AL} (10^{-6} mbar)	T_{AL} (K)	H/D-atom fluence (10^{17} atoms cm^{-2})	t (min)
Control experiments						(H/D)	
co-deposition(a)	–	60	60	1	2200	1.3	90
25(b)	1.5	15	15	1	2200	2.7	180
35(c)	0.7	15	25	1	2200	2.7	180
25(d)	1.5	15	25	1	300	–	150
100(e)	1.5	15	28	1	2200	4.5	300
15(f)	0.7	15	25	1	2200	1.5	100
Temperature dependence						(H)	
35	0.7	15	15	1	2200	2.2	150
35	0.7	15	18	1	2200	2.2	150
35	0.7	15	20	1	2200	2.2	150
35	0.7	15	23	1	2200	2.2	150
35	0.7	15	25	1	2200	2.2	150
35	0.7	15	26	1	2200	2.7	180
35	0.7	15	27	1	2200	3.3	220
Structural effect							
25(g)	1.5	15	15	1	2200	1.8	125
25(h)	1.5	15	15	1	2200	0.22	125
35(i)	0.7	15	25	1	2200	1.9	130
Penetration mechanism							
25(j)	1.5	15	15→25	1	2200	1.6	130
25(k)	1.5	15	25→15	1	2200	2.1	160
35(l)	0.7	15	25→15	1	2200	2.5	190
Thickness dependence							
1	0.15	15	25	1	2200	2.2	150
3	0.15	15	25	1	2200	2.2	150
5	0.15	15	25	1	2200	2.2	150
8	0.15	15	25	1	2200	1.8	125
12	0.15	15	25	1	2200	2.2	150
25	0.15	15	25	1	2200	2.2	150
35	0.15	15	25	1	2200	2.2	150
70	1.5	15	25	1	2200	1.9	130
90	1.5	15	25	1	2200	3.0	200
H_2 dependence							
25	1.5	15	25	10	1850	2.2	150
25	1.5	15	25	1	2200	2.2	150
25	1.5	15	25	0.5	2250	2.2	150

(a) Simultaneous deposition of O_2 and D atoms. (b) An inert layer of $^{15}N_2$ ice is used instead of solid O_2. (c) D-atom beam. (d) H_2 added to the O_2 ice. (e) H-atom beam. (f) Thin O_2 layer deposited at 15 K on top of 100 ML of compact H_2O ice deposited at 120 K. (g) The ice is annealed at 25 K before H-atom addition. (h) H-atom addition is stopped upon saturation of the H_2O_2. (i) H-atom beam at 45° with respect to the substrate. (j) H-atom addition at 15 K is stopped after 31 minutes; the ice is heated to 25 K with 1 K min^{-1} rate; H atoms are added for 79 minutes. (k) H-atom addition at 25 K is stopped after 31 minutes; the ice is cooled to 15 K with 1 K min^{-1} rate; H atoms are added for 109 minutes. (l) H-atom addition at 25 K is stopped beyond saturation of the H_2O_2 after 100 minutes; the ice is cooled to 15 K with 1 K min^{-1} rate; H atoms are added for 70 minutes.

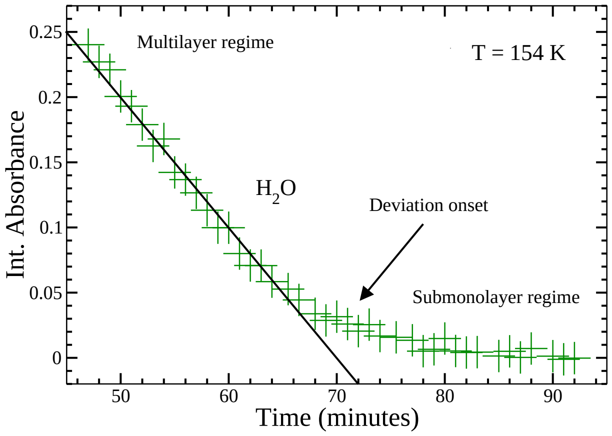

Figure 4.3 Isothermal desorption at 154 K of a thick layer of H_2O ice. The straight line guides the eye to identify the change in the slope of the curve, which corresponds to the transition from zeroth-order to first-order desorption.

layers. The integrated band area oscillates as a function of the layer thickness due to optical interference that is caused by the reflection at both the film-vacuum and film-substrate interfaces. The results presented in this chapter are all in the linear regime, where the modified Lambert-Beer equation still applies. This is verified by depositing pure H_2O ice and checking for non-linearities in the growth rate.

The RAIR difference spectra acquired during an hydrogenation experiment of 35 ML of solid O_2 at 25 K are shown in Fig. 4.2. Both H_2O and H_2O_2 integrated band intensities clearly grow as the H-fluence (H-flux × time) increases. The inset in Fig. 4.2 also shows the presence of ozone in our RAIR spectra upon H-atom exposure. The $\nu_3(O_3)$ stretching mode peaks at 1038 cm^{-1} in our spectra and corresponds to the band position when solid O_3 is formed and mixed in a polar environment like H_2O:O_2 ices (Cooper et al. 2008). The presence of solid ozone formed upon hydrogenation of O_2 ice provides clear experimental evidence for the incompleteness of the H_2O formation routes considered for decades in astrochemical models. In Chapter 5 these models are extended with a more complete reaction scheme. In this chapter, the focus is on the ice penetration mechanism. Ozone hydrogenation is an efficient formation channel and can contribute to the total water amount in our experiments (Mokrane et al. 2009, Chapter 6). Figure 4.2 shows trace amounts of HO_2 trapped in the ice. The $\nu_3(HO_2)$ band mode peaks at 1140 cm^{-1} in our infrared spectra and corresponds to the band position when HO_2 is trapped in H_2O ices (Cooper et al. 2008). Although the $\nu_3(HO_2)$ mode is weaker than the $\nu_2(HO_2)$ mode, the latter is not visible in our infrared spectra, since it overlaps with strong H_2O_2 bending modes. We did not detect OH radicals here. This may have two reasons; they have either reacted further to form H_2O or H_2O_2 or their infrared features in a H_2O:H_2O_2 ice are too broad to be distinguished from the H_2O and H_2O_2 OH-stretching band modes. In

Chapter 5 we present the spectroscopic detection of OH radicals, which have formed in the ice through surface reactions at an early stage in the reaction scheme, using a different experimental approach.

Two vibrational modes of the newly formed H_2O, peaking at 3430 and 1650 cm^{-1}, are above the noise-level in our RAIR spectra (Fig. 4.2). The broad 3430 cm^{-1} OH-stretching modes (ν_1 and ν_3) of H_2O overlap with the 3250 cm^{-1} stretching modes (ν_1 and ν_5) of H_2O_2. The integrated band area of the OH-stretching modes is at the edge of the linear regime for the experiment carried out at 28 K, where the optimum in the final yield is found. Thus, we have chosen the bending modes, peaking at 1650 cm^{-1} (ν_2) and 1350 cm^{-1} (ν_2, ν_6 and $2\nu_4$), to quantify the column densities of solid H_2O and H_2O_2, respectively. The band modes of D_2O and D_2O_2 ices exhibit systematic peak position shifts of ~400 cm^{-1} towards lower wavenumbers with respect to the H_2O and H_2O_2 band modes. The column densities of the deuterated species are obtained in a similar way as described above.

Since literature values of transmission band strengths cannot be used directly in reflectance measurements, an apparent absorption strength of the various species is calculated from calibration experiments. The determination of this apparent absorption strength is set-up specific. The calibration method is described in Chapter 2. In short, a layer of the selected ice is deposited at a temperature lower than its desorption temperature. The sample is then linearly heated, close to its desorption temperature. Infrared spectra are acquired regularly until the desorption of the ice is complete. The transition from zeroth-order to first-order desorption is assumed to occur at the onset to the submonolayer regime and appears in the desorption curve as a sudden change in slope. Figure 4.3 shows the isothermal desorption of a H_2O ice layer at 154 K. The arrow in the graph indicates the onset of the deviation from constant desorption. The apparent absorption strength in cm^{-1} ML^{-1} is then calculated by relating the observed integrated area to 1 ML in the modified Lambert-Beer equation. The largest uncertainty in the band strengths is due to the uncertainty in the onset of the first-order desorption, which can be affected by the non-wetting property of the gold substrate (hydrophobic surface) in the case of H_2O, for instance. We verified our calibration method by repeating the experiments reported by Fraser et al. (2001) who performed several TPD experiments of H_2O ice deposited on a gold substrate for different ice thicknesses, where the deposited amount of H_2O ice was measured using a quartz crystal microbalance. The desorption order and the position of the desorption peak depend on the deposited amount of H_2O ice. We were able to reproduce their results quantitatively using the H_2O band strength obtained from the isothermal desorption experiment. We estimate the uncertainty of the band strength to be within 50%. In this work, this calibration method is applied to both H_2O and D_2O ice, giving the same band strength value for both.

Pure hydrogen peroxide and deuterium peroxide are experimentally difficult to deposit, because of their chemical instability. In Chapter 3 the apparent absorption strengths are obtained indirectly, assuming the ratio of the integrated band strengths in reflectance between H_2O and H_2O_2 (D_2O and D_2O_2) to be the same as in transmittance H_2O/H_2O_2 = D_2O/D_2O_2 = 0.57 (Gerakines et al. 1995, Loeffler et al. 2006). The H_2O bending mode is very sensitive to the local environment in terms of band shape and width and partially overlaps with the H_2O_2 bending mode at lower wavenumbers in a mixture. Thus, we obtained the H_2O band strength from calibration experiments, integrating the H_2O bending mode in the range where it does not overlap with the H_2O_2 bending mode, and we determined the band strength ratio in a H_2O_2-rich environment independently. This is done by assuming mass balance in a H_2O_2 hydrogenation experiment between the formed H_2O and reacted H_2O_2 molecules. The H_2O_2 layer is formed on top of the gold substrate by co-depositing H atoms and O_2 molecules with a ratio $H/O_2 = 20$ and heating the substrate to above the O_2 desorption temperature. Details of this experiment are reported in Chapter 5. We find the ratio of the integrated band strengths between H_2O and H_2O_2 (D_2O and D_2O_2) to be 0.31±0.10.

4.2.3 Control experiments

The list of experiments in Table 4.1 contains a number of control experiments. These are performed

1. to verify that new species are formed in the solid phase by surface reactions and not in the gas phase;
2. to check whether the deposition of background H_2O on the substrate is indeed negligible;
3. to confirm that final products are due to surface reactions involving H/D atoms and not H_2/D_2 molecules;
4. to verify that the maximum penetration depth of the atomic hydrogen into the oxygen ice is not larger than the actual O_2 thickness chosen for each experiment;
5. to verify that the gold substrate does not affect the final results.

Point 1 is investigated by the simultaneous deposition of O_2 molecules and D at 60 K. At this temperature O_2 molecules do not stick to the substrate long enough to form an ice layer, while H_2O and H_2O_2 could still freeze-out onto the substrate if they would be formed via gas phase reactions. After 90 minutes of co-deposition no new solid species are detected on the substrate. Point 2 is estimated by exposing an inert $^{15}N_2$ ice layer instead of solid O_2 to H atoms at 15 K for 180 minutes. In this case no newly formed H_2O and H_2O_2 molecules are detected and the background H_2O contamination does not exceed 0.1 ML after 3 hours of H-addition to $^{15}N_2$ ice. Furthermore, we repeated the standard experiment using D atoms instead of H atoms to confirm that solid H_2O is formed in the ice and does not originate from the background. In this case, as shown in Miyauchi et al. (2008), Ioppolo et al. (2008), only solid deuterium peroxide and heavy water are formed. Point 3 is verified by exposing an O_2 layer to H_2 molecules. After 2.5 hours of H_2 addition at 25 K, no new species are formed.

Concerning point 4, a thick O_2 layer (100 ML) is deposited at 15 K and then exposed to an H-atom beam for 5 hours at 28 K. Acharyya et al. (2007) showed that under ultra high vacuum conditions O_2 thermal desorption starts at ~28 K. Therefore, the O_2 ice thickness can change in time at 28 K upon desorption and experiments at this temperature are not straight-forward. Nevertheless, as in Chapter 3, we find an optimum temperature for the formation of H_2O and H_2O_2 at 28 K. The control experiment performed in this work shows that the O_2 use-up at 28 K, obtained according to reactions (4.7) and (4.2) ($N[O_2] = \frac{1}{2} \times N[H_2O] + N[H_2O_2]$, see § 4.3.4), is ~35 ML. This has to be considered as a lower limit for the maximum penetration depth of the atomic hydrogen into the O_2 ice at 28 K, because of the thermal desorption of the oxygen layer. However, experiments at lower temperatures never reached an O_2 use-up higher than 35 ML. For this reason we decided to use an O_2 ice thickness of 35 ML for most of our experiments and to investigate only temperatures below 28 K, where the O_2 layer does not desorb (see Table 4.1). This thickness is higher than the 15 ML thickness used in Chapter 3 (more details in § 4.3.1). In this work, special care is taken to use low O_2 deposition rates to ensure optimal control of the ice thickness (see Table 4.1). The number of monolayers is calculated assuming a constant O_2 deposition rate. However, during the first minutes of the O_2 deposition the rate is not in a linear regime and, once the deposition valve is closed again, background O_2 molecules still present in the main chamber can still contribute to the total ice thickness. Thus, longer deposition times result in a smaller error in the O_2 ice thickness, because the relative contribution in time of the non-linear deposition rates becomes negligible.

Point 5 is addressed by depositing a thick layer of compact H_2O ice (100 ML) at 120 K and on top a thinner layer of O_2 (15 ML) at 15 K, which is subsequently hydrogenated at 25 K. In this case the O_2 layer will become completely hydrogenated, because the maximum penetration depth of H atoms at 25 K is ~15 ML (see § 4.3.4), but the H atoms cannot reach the gold substrate because of the thick layer of compact H_2O ice (Dulieu et al. 2010, Matar et al. 2008). The result of this experiment is the same as for a similar experiment with the O_2 ice directly deposited on the gold substrate. Thus, the gold substrate is found not to affect the O_2 hydrogenation process within the sensitivity limits of our experiment.

4.3 Results and discussion

In a standard hydrogenation experiment, O_2 ice is deposited at 15 K with a thickness of 35 ML. After deposition the ice is slowly heated to the required temperature, with a rate of 1 K min^{-1}, and subsequently exposed to an H-atom flux of ~2.5×10^{13} atoms cm^{-2} s^{-1} for several hours.

4.3.1 Temperature dependence

Experiments are performed for different temperatures in the range between 15 and 27 K. The aim of this section is to study the effect of the ice temperature on the formation rate of H_2O and H_2O_2 and final yield, investigating in more detail than in Chapter 3 temperatures above 20 K, where an optimum in the final yield was found. Figure 4.4 plots the column

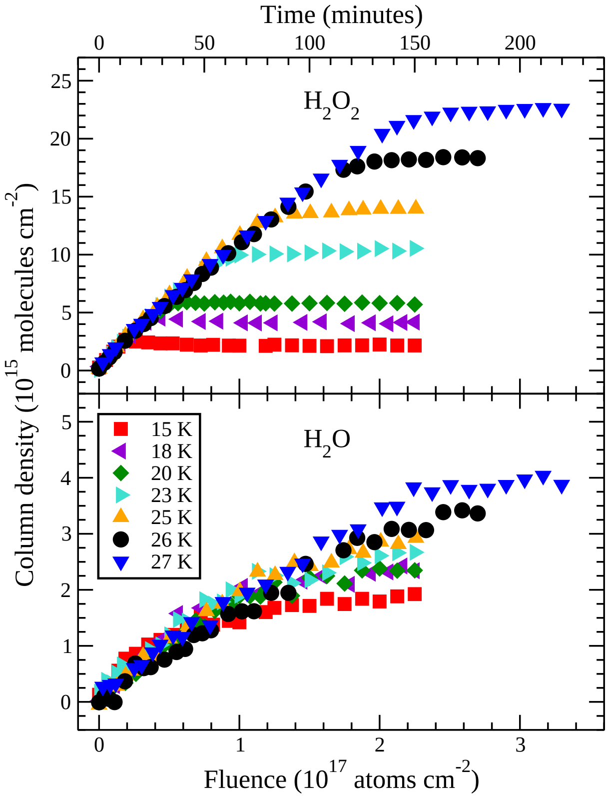

Figure 4.4 Temperature dependence of the H_2O_2 (*top*) and H_2O (*bottom*) column densities as a function of the H-atom fluence and time of H-atom exposure.

densities of H_2O and H_2O_2 as a function of the H-fluence for all the considered substrate temperatures. In each experiment, the final H_2O_2 yield is higher than the H_2O yield resulting in smaller relative errors for the H_2O_2 data. For all temperatures, the solid H_2O_2 column density shows the same initial linear increase followed by a relatively sharp transition to a steady state regime, with the final yield increasing with temperature. The solid H_2O column densities exhibit a similar behavior, but the transition is not as sharp as in the H_2O_2 case and the temperature dependence of the final yield is not as pronounced.

The experimental results presented in this section reproduce those discussed in Chapter 3 for temperatures below 23 K, once results presented in Chapter 3 are scaled with the H_2O_2 band strength value used in this work. For temperatures above 23 K the H_2O and H_2O_2 final yield is found to be higher in this work than in Chapter 3, while the formation rate is the same in both studies for all the investigated temperatures. As discussed above, a different O_2 deposition rate at 15 K in the two studies (1.5 ML min^{-1} Chapter 3 vs. 0.7 ML min^{-1} this chapter) caused an initial different O_2 ice thickness (15 ML in Chapter 3 according to the O_2 use-up vs. 35 ML this chapter). The different O_2 ice thicknesses may explain the discrepancy between the two studies in the H_2O and H_2O_2 final yield for temperatures above 23 K, where the hydrogen can penetrate deeper into the ice than 15 ML. Details are reported in § 4.2.3 and § 4.3.4.

The initial constant formation rate and the high final yield of tens of monolayers (see Fig. 4.4) indicate that the hydrogenation reaction of solid O_2 is a bulk process that does not involve the surface of the ice only. H atoms diffuse into the O_2 ice with a penetration depth which is temperature dependent. This is different from the case of CO hydrogenation, in which only ~4 ML are involved in the reactions and minimal amounts of final products are detected in experiments at temperatures higher than 16 K, due to H-atom desorption at high temperatures (Watanabe et al. 2004, Fuchs et al. 2009). In the case of O_2, however, H atoms penetrate deeper into the ice at high temperatures (>20 K). Moreover, the constant formation rate shows that even at high temperatures the desorption of H atoms from the ice is a negligible process. Thus, H atoms can penetrate deep and stay into the oxygen ice long enough to react with O_2.

The temperature dependence of the penetration depth can have several origins. It is possible that for higher temperatures the O_2 ice is less rigid and the mobility of the O_2 atoms facilitates the penetration into the ice by moving to the side. However, more thermal vibration of O_2 molecules leads to larger effective radii, which may also hinder the H atoms while passing. We would therefore expect the penetration depth to have an optimum temperature (as in the case of CO ice hydrogenation around 15 K) when there is high H-atom mobility but not too much thermal vibration of O_2 molecules, and this has not been found. This is therefore not likely the dominant mechanism responsible for the temperature dependence of the H-atom penetration. A second possibility could be that at higher temperature the oxygen layer slowly converts from amorphous to crystalline which is more effective to penetrate. A third scenario is that the hydrogen atoms do not really penetrate the ice, but that mobile oxygen molecules keep replenishing the top layers. A final possible scenario involves the ratio between the rate of the barrierless reaction between hydrogen and solid O_2, which is temperature independent, and the rate of the thermally activated process of hydrogen diffusion into the ice, which increases with temperature. In this scenario, at each O_2 layer that the H atom passes, it has a probability to react with the O_2 ice or to penetrate deeper into the ice. At low temperature, reaction is favored; at high temperature, penetration. Thus, for this explanation the penetration length of an individual atom is a stochastic process and the average length depends on the temperature of the ice. In the following sections we will discuss in more detail the latter three scenarios proposed here: restructuring of the O_2 ice, replenishing of the top layers and competition between reaction and diffusion. We will experimentally show that the competition between reaction and diffusion is the most likely scenario.

4.3.2 Structural effect

The yield of the final products in the experiments at high temperatures (>20 K) show that hydrogen atoms can penetrate the ice over several monolayers. One possible explanation for the efficient diffusion of H atoms into the ice for higher temperatures is, as mentioned before, a higher crystalline fraction in the structure of the ice at higher temperature. To verify this hypothesis an O_2 layer deposited at 15 K is annealed at 25 K before H-atom addition at 15 K. This experiment is meant to investigate the effects of possible irreversible structural changes, which could take place at temperatures slightly below the desorption temperature of O_2 (Kreutz et al. 2004). Infrared spectroscopy does not allow us to investigate different phases of solid O_2. Nevertheless, if the change in the ice structure would play an important role in the O_2 hydrogenation experiments, one would expect to obtain a higher final yield of the products than in a standard O_2 hydrogenation experiment at 15 K. However, the H_2O and H_2O_2 formation rates and final yield in the annealing and in the standard experiment at 15 K are all comparable within the experimental uncertainties (see Fig. 4.5).

It should be noted that if a structural change from amorphous to crystalline in the ice is present at high temperatures a different incident angle of the H-atom beam could still affect the rate reaction and final yield of the end products. We compared results from a 25 K experiment of H-atom addition with an incident angle of 45° to those obtained from an experiment, where the H-atom beam is normal to the substrate surface. In both cases the geometry of the infrared optics is kept the same, since the H-atom beam was stopped and the sample turned back to 90° to the the H-atom beam each time an infrared spectrum was acquired. The infrared beam is in both cases wider than the projection of the H-atom beam on the substrate. Figure 4.6 shows that formation rate and final yield of the products are the same in both cases. Thus, the higher penetration depth of the H atoms into the ice at high temperatures is most likely due to one of the two remaining scenarios: replenishing or reaction vs. diffusion.

As a further extension, Fig. 4.5 shows also an experiment performed at 15 K in which H-atom addition is interrupted upon saturation of H_2O_2 (*triangle*). This experiment is performed to confirm that the decrease in H_2O_2 after saturation is due to reaction and not to desorption. We will come back to this point later.

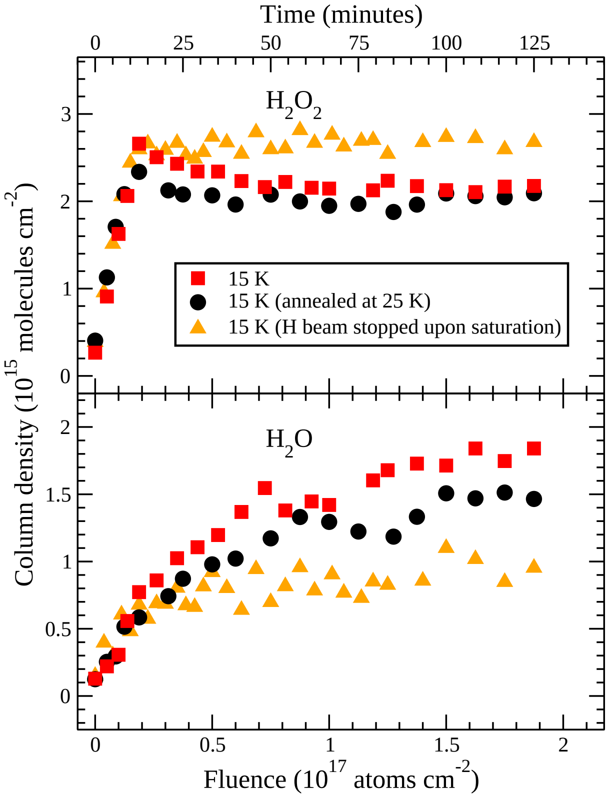

Figure 4.5 The H_2O_2 (*top*) and H_2O (*bottom*) column densities as a function of the H-atom fluence and time of H-atom exposure for a standard experiment performed at 15 K (*square*) compared to an experiment in which an O_2 layer deposited at 15 K is annealed at 25 K before H-atom addition (*circle*). Also shown is an experiment in which the H-atom addition is stopped upon H_2O_2 column density saturation (*triangle*).

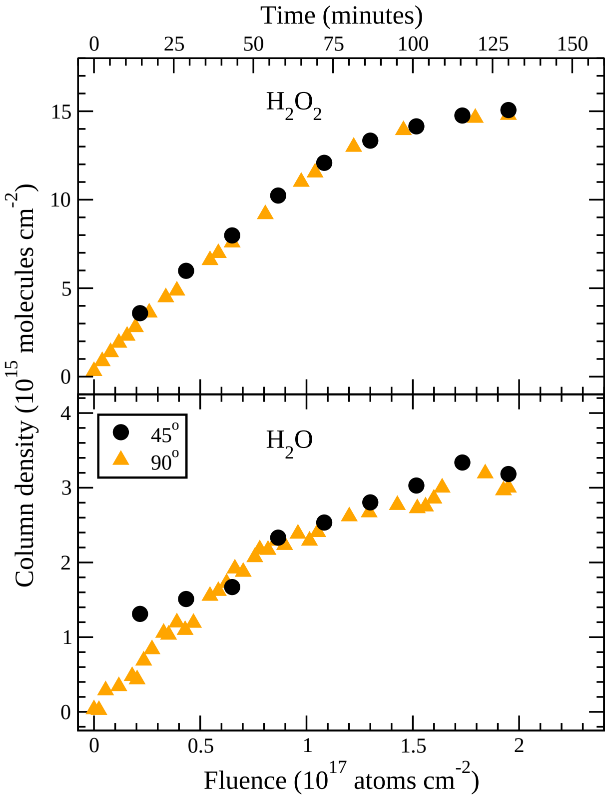

Figure 4.6 H_2O_2 (*top*) and H_2O (*bottom*) column densities as a function of the H-atom fluence and time of H-atom exposure for an experiment performed at 25 K, in which the H-atom beam has an incident angle to the O_2 ice of 45° (*circle*), compared to a similar experiment, in which the H-atom beam is normal to the substrate surface (*triangle*).

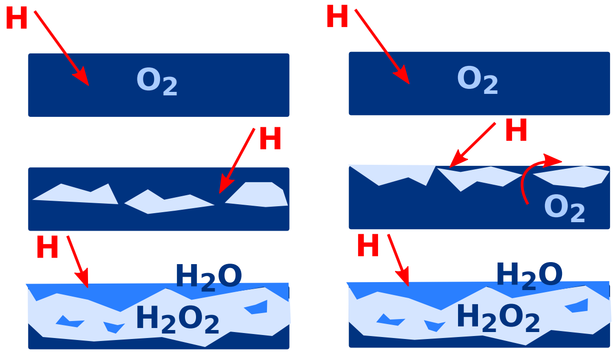

Figure 4.7 Schematic representation of two penetration scenarios: (*left*) competition between reaction and diffusion (*mainly bottom-up*) and (*right*) replenishing of the top layers by O_2 mobility (*top-down*).

4.3.3 Penetration mechanism

In the previous sections we gave experimental evidence for the importance of the hydrogen penetration depth into O_2 ice ruling out two possible mechanisms. The purpose of this section is to investigate whether the high H-atom penetration depth is due to the competition between reaction and diffusion or replenishing of the top layers by mobile O_2 molecules. The two scenarios are schematically depicted in Fig. 4.7. In the first case, O_2 is hydrogenated mainly bottom to top, in the latter top to bottom.

Using thick O_2 ices (see Table 4.1), we performed the experiments shown in Fig. 4.8. In the first experiment we added H atoms to the O_2 ice at 15 K until the column density of the newly formed species was saturated (O_2 use-up = 2.5 ML). After interrupting the hydrogenation we heated the ice to 25 K and added H atoms until a new saturation level was found (total O_2 use-up = 4 ML). We repeated the same experiment hydrogenating an identical ice at a temperature of 25 K, until saturation (O_2 use-up = 13 ML), then we cooled it to 15 K and hydrogenated it for 70 minutes (total O_2 use-up = 13 ML). In the third experiment we hydrogenated another O_2 ice at 25 K, interrupting the H-atom addition before saturation (O_2 use-up = 5.5 ML). Then, we cooled it to 15 K and hydrogenated it for 109 minutes (total O_2 use-up = 6.5 ML).

Figure 4.8 shows that the results from these three experiments differ. The final yield of the newly formed species and the final O_2 use-up are not the same in the first two experiments. The O_2 use-up is ~4 ML for an O_2 ice hydrogenated at 15 K and then at 25 K, while it is ~13 ML for an O_2 ice directly hydrogenated at 25 K. In the competition scenario, the H atoms have to penetrate 2 ML of O_2 molecules already converted into H_2O and H_2O_2, if we hydrogenate an O_2 ice at 25 K, which was previously hydrogenated at 15 K. In this case the final hydrogen penetration depth into the ice is just 4 ML and not 13 ML, because the penetration depth of the H atoms into solid H_2O and H_2O_2 is lower than into pure O_2 ice. This result leads us to hypothesize that the hydrogenation follows

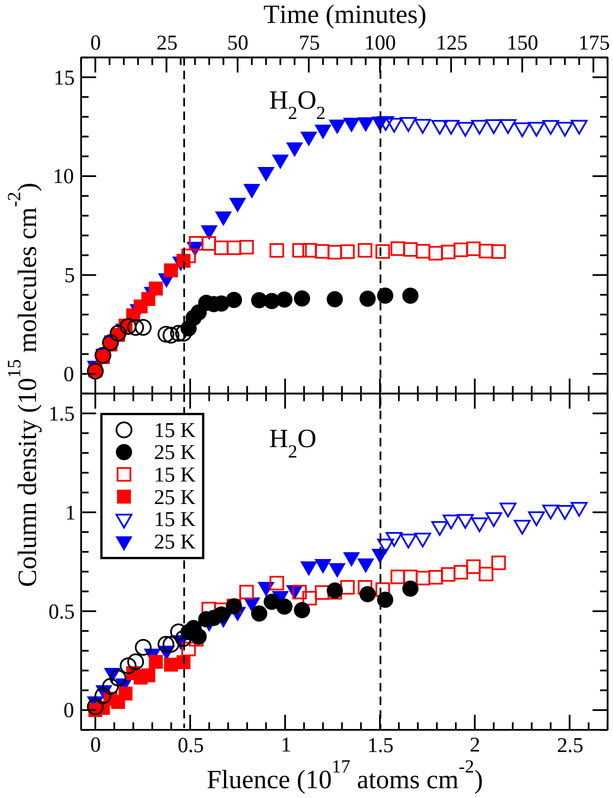

Figure 4.8 The H_2O_2 (*top*) and H_2O (*bottom*) column densities as a function of the H-atom fluence and time of H-atom exposure for an experiment in which H atoms are added to the O_2 ice at 15 K (*open symbols*) until saturation of the column densities and, then, at 25 K (*closed symbols*) until a new saturation level was found (*circle*); the same experiment, inverting the order of the temperatures for the H-atom addition (*triangle*); an experiment in which the hydrogenation of the O_2 ice at 25 K is stopped before saturation and, then, continued at 15 K (*square*).

a distribution that starts mainly from the bottom layers of the ice to the top. If instead the replenishing of the top layers due to a higher O_2 molecules mobility in the ice for higher temperatures would play an important role in the O_2 hydrogenation, we would expect to get the same final yield for both experiments. This is not the case.

In the third experiment we interrupted the hydrogenation process when 5.5 ML of the ice were converted into H_2O and H_2O_2 at 25 K. If the hydrogenation would start straight from the bottom layers to the top, the top layers of the ice would have not yet been hydrogenated and we would expect to hydrogenate up to an extra 2.5 ML of ice at 15 K in the second part of the experiment, whereas we observed the hydrogenation of only 1 ML of ice. The final O_2 use-up is probably not reached because the H atoms are blocked by some of the H_2O and H_2O_2 molecules, which are earlier formed in the upper layer of the ice according to the competition scenario, which involves mainly the bottom layers and partially the top layers of the O_2 ice in the early stage of the hydrogenation.

Thus, all experiments presented so far are in accordance with the following scenario: first, the H atoms penetrate into the ice without desorbing. The penetration depth is determined by a temperature dependent competition between reaction with O_2 molecules and further diffusion into the ice. In this way, the ice is hydrogenated following a distribution that involves mainly the bottom layers and partially the top layers at the beginning. Subsequently, the penetration depth of atoms that enter the ice in a later stage is determined by the competition mechanism until they reach species other than O_2.

4.3.4 Thickness dependence

Different thicknesses are studied in the range between 1 and 35 ML. The O_2 ice is deposited at 15 K with a rate of ~0.3 ML min^{-1} to better control the ice thickness during deposition and then heated to 25 K. The ice layer is subsequently exposed to H atoms, in most of the cases, for 150 minutes with a total H-atom fluence of 2.2×10^{17} atoms cm^{-2}. Figure 4.9 plots the column density of H_2O_2 and H_2O versus the fluence of impinging H atoms on the solid O_2 layer for different thicknesses.

Again, the initial formation rate of H_2O and H_2O_2 is constant and thickness independent, while the final yield is thickness dependent and is affected by the penetration depth of the H atoms into the ice. The O_2 ice is indeed completely converted into H_2O and H_2O_2 for layers thinner than the maximal penetration depth of the H atoms into the ice at 25 K (low oxygen coverage). For layers thicker than the maximal penetration depth of the H atoms into the ice, some O_2 is not hydrogenated (high oxygen coverage). Figure 4.10 shows the final yield for H_2O and H_2O_2 formation as well as the O_2 use-up as a function of the initial O_2 thickness. The O_2 use-up is estimated by adding half of the newly formed H_2O column density to the H_2O_2 column density ($N[O_2] = \frac{1}{2} \times N[H_2O] + N[H_2O_2]$), according to reactions (4.7) and (4.2), where, from each O_2 molecule, two H_2O molecules can be formed. Figure 4.10 shows that the maximal penetration depth at 25 K is reached in the high oxygen coverage regime (>15 ML) and is ~16 ML.

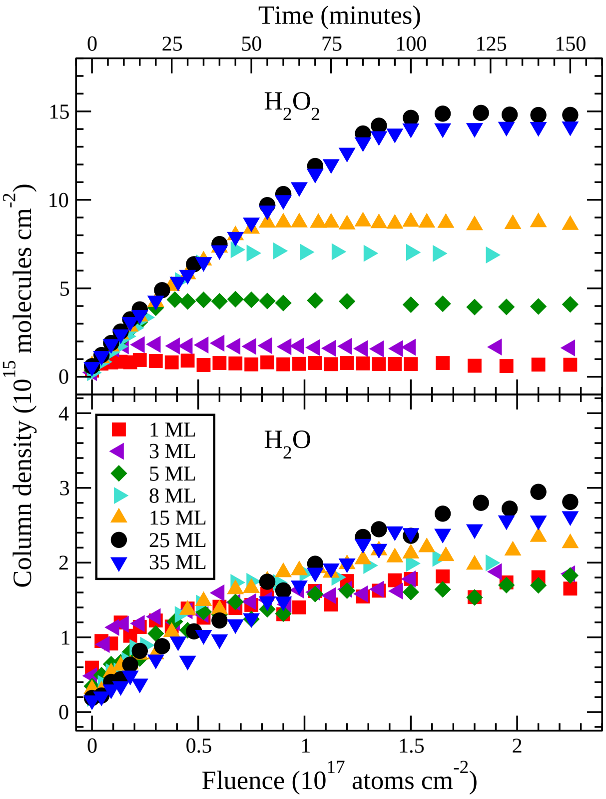

Figure 4.9 Thickness dependence on the H_2O_2 (*top*) and H_2O (*bottom*) column densities as a function of the H-atom fluence and time of H-atom exposure at 25 K.

The O_2 use-up ($N[O_2]$) is fitted with the following function:

$$N[O_2] = \left((a\vartheta)^{-2} + (b)^{-2}\right)^{-\frac{1}{2}} \tag{4.9}$$

where a and b are fitting parameters and ϑ is the initial O_2 thickness. Equation 4.9 is a combination of two linear functions describing the O_2 use-up in the two extreme regimes. For low coverage, the yield is expected to be equal to the coverage $N[O_2] = a\vartheta$, with $a = 1$. At high coverage, the yield will be equal to the maximum penetration depth, b. The fit to the data gives $a = 1$, as we expected, and $b = 16$ ML. The transition between the two linear regimes is not sharp. This can be explained by considering that the penetration length of the H atoms is not one absolute value, but covers a distribution with an average value of 16 ML at 25 K. In the case of a 16 ML thick O_2 ice, the high end of the distribution will be missing, resulting in a lower average value. This is again in agreement with the competition scenario. Results from the control experiment of 15 ML of O_2 deposited on top of a compact H_2O layer, plotted in Fig. 4.10, confirm the scenario described above. In

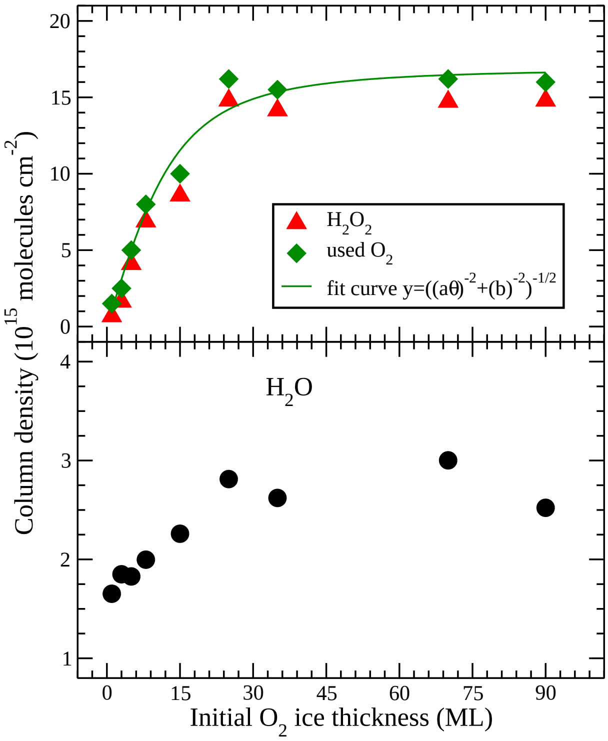

Figure 4.10 Final yields for H_2O_2 (*top*, *triangle*) and H_2O (*bottom*, *circle*) and O_2 use-up (*top*, *diamond*) as a function of the initial O_2 thickness at 25 K. The line is the fit curve to the O_2 use-up data. Data from the control experiment of 15 ML of O_2 deposited on top of a compact H_2O ice are also plotted and included in the fit.

this case less than 15 ML of O_2 are hydrogenated. Correlating the O_2 use-up expressed in monolayers to our O_2 deposition flow in Langmuir, we have an independent estimate of the O_2 ice thickness for all our experiments, which leads to a correspondence of 3 L to 1 ML.

For oxygen films thinner than 5 ML, more H_2O is formed initially and almost all H_2O_2 formed at low fluence is later converted into H_2O. This can be explained by the fact that H atoms are more likely to find H_2O_2 to react with in thin O_2 layers than in thick O_2 layers for the same absolute amount of H_2O_2. This confirms that H_2O formation can proceed with H_2O_2 as a precursor (reaction (4.7)). Figure 4.5 indeed shows that the decrease in H_2O_2 is due to reaction. The figure clearly shows that reaction (4.7) is stopped and H_2O_2 is not converted to form H_2O. In Chapter 5 we will discuss in more detail this reaction channel.

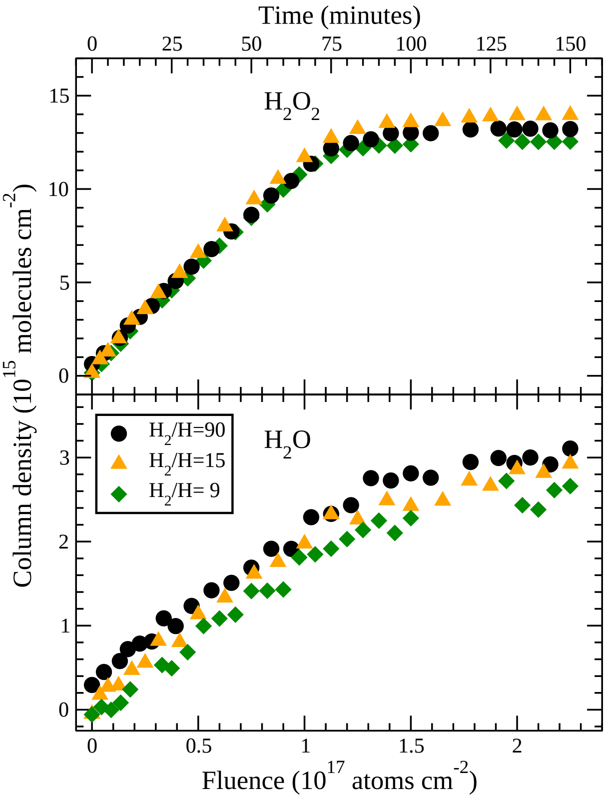

Figure 4.11 The H_2O_2 (*top*) and H_2O (*bottom*) column densities as a function of the H-atom fluence and time of H-atom exposure for different H_2/H ratios at 25 K.

4.3.5 H_2 dependence

Reaction (4.3) could play a role in the solid phase, even though it has a barrier in the gas phase. By controlling the H_2 flow into the thermal cracking source and the filament temperature, different hydrogen fluxes and different H_2/H ratios can be realized. The role of H_2 in surface reactions is investigated comparing the results of three similar experiments at 25 K in which the same H-atom flux, but different H_2/H ratios, are used. The details about these experiments are reported in Table 4.1. From flux measurements (see Appendix A) we estimate the H_2/H ratio to vary between 9 and 90. If reaction (4.3) is important and if a significant amount of OH radicals is present in the ice, the H_2O abundance should be higher in the case of more H_2. Figure 4.11 shows that the formation rate and the final column densities of both H_2O and H_2O_2 are the same in all cases within the experimental errors. This indicates that H_2 molecules, formed through surface reactions in the ice or along the quartz pipe or originating from the not-fully dissociated

H-beam, do not have any measurable effect on the O_2 reaction channel and consequently that reaction (4.3) is not an important route for H_2O formation in our experiments.

4.4 Conclusion

An extensive complementary study of Chapter 3 is presented under ultra high vacuum conditions at temperatures between 15 and 28 K. RAIR spectra are used to analyze the results and calibration experiments are performed to measure atomic fluxes and band strengths of the newly formed species. From this quantitative study we draw the following conclusions:

1. The initial constant H_2O and H_2O_2 formation rate is temperature and thickness independent. The final yield is temperature and thickness dependent and is probably governed by the competition between the reaction of atomic hydrogen with the solid O_2 and the hydrogen diffusion into the ice, which is temperature and thickness dependent.

2. The penetration depth of the H atoms into the ice is affected by the competition between reaction and diffusion and increases with temperature. H atoms penetrate into the bulk of the ice with a penetration depth (up to ~35 ML at 28 K), that is temperature dependent. Once an H atom is trapped into the ice, it diffuses efficiently and finds an oxygen molecule to react with.

3. The ice is hydrogenated initially mainly bottom-up and partially from the top layers. The penetration length of the H atoms covers a distribution of values with an average value which corresponds to the maximum penetration depth measured, which is temperature dependent. Experimental evidence shows that the model used in Chapter 3 and described in the introduction of the present chapter to fit the experimental data not only reproduces the laboratory data, but also has physicochemical meaning; it explains the behavior of the H-atom diffusion into the O_2 ice for the conditions investigated here. This also corrects statements made in Oba et al. (2009).

4. H_2O and H_2O_2 formation via the molecular oxygen channel proposed by Tielens & Hagen (1982) is experimentally proven to be efficient under laboratory conditions. Nevertheless, other reactions should be considered in the reaction route as well. The presence of solid ozone formed in the ice, under the experimental conditions described here, gives a clear experimental evidence for the incompleteness of the H_2O formation routes considered for decades in astrochemical models (more will be presented in Chapter 5).

5. H_2 molecules do not take a relevant part in the reaction scheme at a detectable level, for the temperature range investigated.

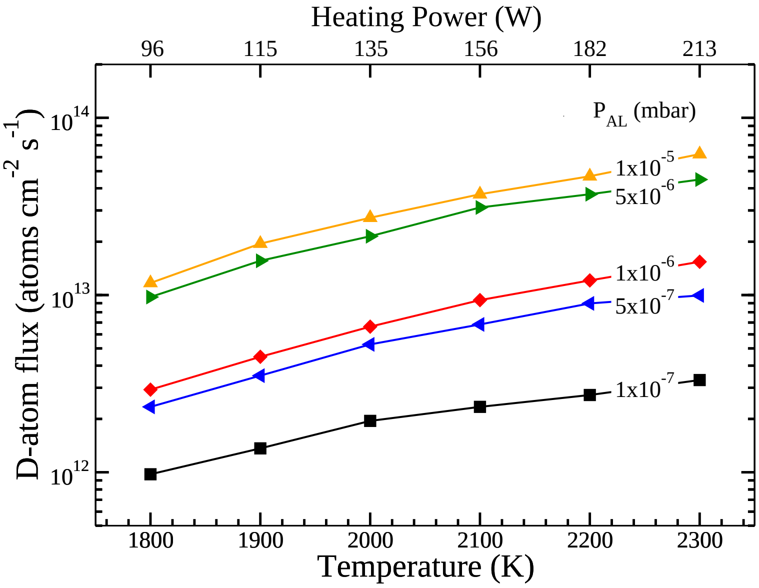

Figure 4.12 The D-atom fluxes at the substrate site plotted versus different parameter settings: temperature of the tungsten filament, heating power and atomic line pressure. The lines connecting data points guide the eye and are not best-fits.

Appendix A: Absolute atomic flux determination

Absolute atomic fluxes are measured in the main chamber, following the procedure described in Hidaka et al. (2007). Since the sensitivity of the standard 1–200 amu QMS does not allow an accurate measurement at mass 1, we decided to measure D-atom fluxes. For this the substrate was removed and the inlet of the QMS was placed at the center of the chamber in sight of the atomic line, exactly at the position where the ice is hydrogenated. Once the source was turned on, the increase in intensity of the D atoms was monitored with the QMS with a Faraday cup. The QMS measurements do not directly give the D-atom flux values, but the increase in intensity of the QMS signal, ΔQ_{D}, is proportional to the increase in pressure in the main chamber, ΔP_{D}:

$$\Delta P_{\mathrm{D}} = a\Delta Q_{\mathrm{D}} \tag{4.10}$$

We measured the proportionality factor a, which is independent of the gas species, introducing D_2 molecules instead of D atoms in the main chamber, since the D-atom beam contains a significant amount of D_2 molecules and an exact measurement of ΔP_{D} is not straight-forward from pressure gauges. A constant factor a was determined for all main chamber and atomic line pressures that were used during the experiments. The absolute D-atom flux is then obtained from the following expression:

$$f_{\mathrm{D}} = \frac{c_{\mathrm{D}} \Delta P_{\mathrm{D}} \langle v \rangle}{4 k_{\mathrm{B}} T} = \frac{c_{\mathrm{D}} a \Delta Q_{\mathrm{D}} \langle v \rangle}{4 k_{\mathrm{B}} T} \tag{4.11}$$

where c_{D} is the calibration factor for the pressure gauge for D atoms taken from the manual, $\langle v \rangle$ is the thermal velocity of the D atoms at 300 K, k_{B} is the Boltzmann constant, and T is the D-atom temperature. By changing the filament temperature and/or the D_2 inlet flow, the D-atom flux can be varied between 10^{12}–10^{14} atoms cm^{-2} s^{-1}. Figure 4.12 shows the D-atom flux values measured at the substrate site for different parameter settings.

The H-atom flux value used in all the experiments presented here, is determined by comparing the H_2O_2 and D_2O_2 formation rate, which is flux dependent, in two identical 25 K experiments with a filament temperature of 2200 K and an atomic chamber pressure of 1×10^{-6} mbar. The resulting H-atom flux at the surface site is a factor of two higher than the D-atom flux measured. This can be explained by the difference in mass between hydrogen and deuterium, which affects the atomic thermal velocity, and the cracking efficiency in the source. The final H-atom flux value of 2.5×10^{13} atoms cm^{-2} s^{-1} confirms the value previously estimated and used in Chapter 2 and 3. The relative error for D-atom fluxes is within 10%, for H-atom fluxes within 50%. The absolute error is within 50%.

CHAPTER 5

Water formation at low temperatures by surface O_2 hydrogenation II: the reaction network[1]

Water is abundantly present in the Universe. It is the main component of interstellar ice mantles and a key ingredient for life. Water in space is mainly formed through surface reactions. Three formation routes have been proposed in the past: hydrogenation of surface O, O_2, and O_3. In Chapter 3 we discussed an unexpected non-standard zeroth order H_2O_2 production behavior in O_2 hydrogenation experiments, which suggests that the proposed reaction network is not complete, and that the reaction channels are probably more interconnected than previously thought. In this chapter we aim to derive the full reaction scheme for O_2 surface hydrogenation and to constrain the rates of the individual reactions. This is achieved through simultaneous H-atom and O_2 deposition under ultra-high vacuum conditions for astronomically relevant temperatures. Different H/O_2 ratios are used to trace different stages in the hydrogenation network. The chemical changes in the forming ice are followed by means of Reflection Absorption Infrared Spectroscopy (RAIRS). New reaction paths are revealed as compared to previous experiments. Several reaction steps prove to be much more efficient (H + O_2) or less efficient (H + OH and H_2 + OH) than originally thought. These are the main conclusions of this work and the extended network concluded here will have profound implications for models that describe the formation of water in space.

---

[1] Based on: H. M. Cuppen, S. Ioppolo, C. Romanzin, H. Linnartz, 2008, 2010, Physical Chemistry Chemical Physics, volume 12, pages 12077-12088

5.1 Introduction

Water is the simplest stable compound of the two most common reactive elements, O and H, and is abundantly present throughout the Universe. It is the main component of interstellar (Whittet et al. 1988, Boogert et al. 2008) and cometary ices (Bockelée-Morvan et al. 2000) and both types of ices are believed to play an important role in the delivery of water to Earth in the early times of our Solar System. Water is considered an essential ingredient for the formation of life but it is surprising that its own formation mechanism is not fully understood.

Water in the interstellar medium (ISM) is predominantly formed through surface reactions on interstellar dust particles. Three reaction routes have been proposed: hydrogenation of atomic oxygen, molecular oxygen and ozone (Tielens & Hagen 1982). These formation routes in the solid phase have been the topic of several laboratory studies in recent years. The hydrogenation routes through atomic oxygen and ozone have been studied by Hiraoka et al. (1998) and Dulieu et al. (2010); and Mokrane et al. (2009) and Romanzin et al. (2010). Here we focus on the hydrogenation of molecular oxygen via the reaction scheme

$$H + O_2 \rightarrow HO_2, \tag{5.1}$$

$$H + HO_2 \rightarrow H_2O_2, \tag{5.2a}$$

$$H + H_2O_2 \rightarrow H_2O + OH, \tag{5.3}$$

and

$$H + OH \rightarrow H_2O, \tag{5.4}$$

as proposed by Tielens & Hagen (1982). Our and other experimental studies of the hydrogenation of O_2 ice indeed showed the formation of hydrogen peroxide and water (Miyauchi et al. 2008, Ioppolo et al. 2008, Matar et al. 2008), but the results also raised several unanswered questions. As discussed in Chapter 4, the formation of H_2O_2 shows zeroth order kinetics, whereas first order kinetics are expected. We hypothesized that penetration of hydrogen atoms into the oxygen ice causes this effect. Molecular oxygen ice has unique properties, as compared to CO and H_2O ice, and allows hydrogen atoms to penetrate deep into the ice, depending on the ice temperature. In Chapter 4 this mechanism was indeed shown to explain the observed zeroth order behavior. Our second puzzling observation was the fact that we did not observe an isotope effect in reaction (5.3) whereas this is expected due to its relatively large barrier. This point is made later by Oba et al. (2009) as well. Reactions with barriers at low temperatures generally proceed via tunnelling and this would here result in a faster hydrogenation than deuteration rate. This was not observed. In Ioppolo et al. (2008) we promised to address this point in a later paper and here we suggest that reactions (5.1)-(5.4) may not be the only reactions involved in the formation of water when hydrogenating O_2 ice and that the incomplete reaction network of the model artificially resulted in an isotope-independent reaction rate. An additional indication for this is the observation that the water ice formation rate does not seem to increase with the amount of H_2O_2 and this is expected if H_2O_2 is its only precursor.

The present chapter focuses on the reactions involved in the hydrogenation of pure oxygen ice. This is done by co-deposition experiments of O_2 molecules and H atoms. This is intrinsically different from the method used in Chapter 4 where the O_2 ice was prepared first and then sequentially exposed to hydrogen atoms. By changing the stoichiometric ratios of O_2 and H, different stages of the formation route through reactions (5.1)-(5.4) become experimentally accessible. This gives us the unique opportunity to probe also the reactive intermediates. In all previous studies only the stable intermediate H_2O_2- and final H_2O-products were recorded. Oba et al. (2009) performed similar co-deposition experiments using a very high H/O_2 ratio with the aim to study the structure of the obtained water ice. This mainly gave information about the final products but not about the individual reaction routes. Since the conditions in the interstellar medium vary and also differ from the laboratory conditions — especially in terms of atom fluxes — it is very important to obtain detailed information about the surface reaction routes. In a Monte Carlo study of water ice formation in diffuse, translucent and dark clouds, Cuppen & Herbst (2007) showed that the dominant water formation route is determined by the environment (temperature and H/H_2 ratio). However, the reaction scheme used in these simulations was based on gas phase data and not tested for surface reactions. In the present chapter, a range of different O_2/H ratios are applied to probe different hydrogenation stages. Three different astronomically relevant surface temperatures of 15, 20 and 25 K are used to check for thermally activated processes. The highest temperature, 25 K, is chosen to be just below the desorption temperature of molecular oxygen (Acharyya et al. 2007). The overall goal is to derive the full reaction network and to constrain reaction rates for the individual reactions. We will show that indeed a number of extra reaction paths should be considered to complete the initially proposed reaction network and that the O_2 hydrogenation channel is interconnected with the O and O_3 production channels.

5.2 Experimental and data analysis

5.2.1 Experimental

All experiments are performed in an ultra high vacuum setup (SURFRESIDE) with a room temperature base pressure in the 10^{-10} mbar regime. A detailed description of the experiment is given in Chapter 4 and here only a brief explanation is given with the focus on the difference in methodology with respect to the previous study in Chapter 4. Hydrogen atoms and molecules and oxygen molecules are deposited simultaneously on a gold coated copper substrate in the center of the main chamber which is temperature controlled by a close-cycle He cryostat. Temperatures as low as 12 K can be reached with a relative precision of 0.5 K and an absolute temperature accuracy better than 2 K. An all-metal leak valve is used to admit O_2 gas (99.999% purity, Praxair) into the chamber. Deposition of O_2 proceeds under an angle of 45° and with a controllable flow between 10^{-8} and 10^{-7} mbar. A pressure of 10^{-7} mbar corresponds to an O_2 flux of 2.5×10^{13} molecules cm^{-2} s^{-1} (see Chapter 4).

A second precision leak valve is used to admit H_2 molecules (99.8% purity, Praxair) into the capillary of a well-characterized thermal cracking source (Tschersich & von Bonin 1998, Tschersich et al. 2008). For a standard flux, this capillary is heated to 2150 K by a surrounding tungsten filament. A stable H + H_2 flow is obtained in this way. The beam enters the main chamber through a nose-shape quartz pipe, which is designed to collisionally cool the H atoms to room temperature while keeping the number of recombinations of H to H_2 to a minimum and is guided to the surface under 90°. The quartz pipe is designed such that atoms and molecules have a minimum of four collisions before impinging on the ice substrate and are therefore fully collisionally cooled. The final H-atom flux at the surface is measured to be 2.5×10^{13} atoms cm^{-2} s^{-1} under our standard conditions within a factor of two. By changing the filament temperature and/or the H_2 inlet flow, the H-atom flux can be varied between 10^{12}–10^{14} atoms cm^{-2} s^{-1}. Absolute vales are determined as described in Chapter 4. Relative flux accuracies are estimated to be within a factor of 50%. Between the experiments the H/O_2 ratio is varied. This is achieved by varying the O_2 inlet flow and keeping the H-atom flux constant.

Ices are monitored by means of RAIRS using a Fourier Transform infrared spectrometer (FTIR) with a spectral coverage between 4000 and 700 cm^{-1}. A resolution of 0.5 cm^{-1} is used and 128 scans are co-added for one spectrum.

5.2.2 Data analysis

Although O_2 as a diatomic homonuclear molecule is infrared in-active and only gives a small contribution in a water-rich environment (Ehrenfreund et al. 1992), deposition of O_2 has an effect on the baseline of the RAIR spectra. This can be seen in Fig. 5.1a which shows a reference spectrum taken after an O_2 and H_2 co-deposition experiment. The spectrum is completely determined by the deposition of O_2 and the experiments indicate that the distortion of the baseline is directly proportional to the amount of O_2 present in the ice.

For the H and O_2 co-deposition experiments, we assume that the resulting ice at low H/O_2 ratios mainly consists of O_2 and that the baseline distortion is similar to the reference experiment with H_2. Figure 5.1b shows an example spectrum before baseline subtraction for H/O_2 = 2 at 20 K. To correct for the influence of O_2, the baseline subtraction consists of two steps for H/O_2 = 1 and 2. For H/O_2 = 10, we assume that most O_2 is converted to H_2O_2 and indeed here the baseline distortion is minimal. First, a reference spectra (Fig. 5.1a) based on the O_2 and H_2 co-deposition spectrum after a similar fluence of O_2 is subtracted. As a second step, which is applied for all H/O_2 ratios, a piecewise straight baseline is subtracted. A resulting spectrum is shown in Fig. 5.1c for a H/O_2 ratio of 2 and a surface temperature of 20 K. This spectrum (with inset) is also shown in the third panel from the top in Fig. 5.2 and clearly consists of a forest of different features. The bands that we have been able to identify are indicated in Fig. 5.2 and summarized in Table 5.1. All intermediate species from the reaction scheme (5.1)-(5.4) are observed as well as O_3 which is not part of this scheme. A small O_2 feature becomes visible due to interactions with water. Two unidentified features appear at 1420 and 1430 cm^{-1}.

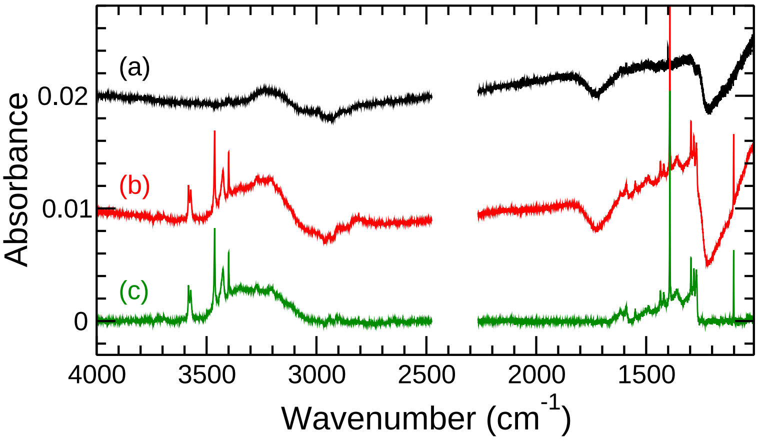

Figure 5.1 RAIR spectra of co-deposited O_2 and H_2 without baseline subtraction (a), co-deposited O_2 and H without baseline subtraction (b), and co-deposited O_2 and H with baseline subtraction (c). H/O_2 or H_2/O_2 is 2 and the surface temperature is 20 K. The spectra (b) and (c) are displaced on the vertical axis by 0.01 and 0.02, respectively.

The formation trends are followed by integrating the corresponding band area as a function time. Because of the overlapping features and because bandstrength information is not available for unstable species like HO_2 and OH, no absolute values are given. The asterisk in Table 5.1 marks the features that have been used for integration and relative quantification. In the case of overlapping bands, Gaussian fits are used to separate the individual contributions.

Table 5.1 Assigned infrared features with their corresponding reference

Position[1] (cm^{-1})	Species	Mode	Reference
1037	O_3	ν_3	Sivaraman et al. (2007)
1100	HO_2	ν_3	Bandow & Akimoto (1985)
1272	H_2O_2	ν_6	Catalano & Sanborn (1963), Lannon et al. (1971)
1282	H_2O_2	ν_6	Catalano & Sanborn (1963), Lannon et al. (1971)
1296	H_2O_2	ν_6	Catalano & Sanborn (1963), Lannon et al. (1971)
1370 (∗)	H_2O_2 (bulk)	ν_2, ν_6, $2\nu_4$	Giguère & Harvey (1959)
1392 (∗)	HO_2	ν_2	Bandow & Akimoto (1985)
1550	O_2	ν_1	Loeffler et al. (2006)
1590 (∗)	H_2O	ν_2	Bandow & Akimoto (1985)
1600 (∗)	H_2O	ν_2	Bandow & Akimoto (1985)
1650 (∗)	H_2O (bulk)	ν_2	Gerakines et al. (1995)
2810	H_2O_2 (bulk)	$2\nu_6$	Giguère & Harvey (1959)
3270	H_2O_2 (bulk)	ν_1, ν_5	Giguère & Harvey (1959)
3240	H_2O (bulk)	ν_1, ν_3	Gerakines et al. (1995)
3400	HO_2	ν_1	Bandow & Akimoto (1985)
3426 (∗)	OH	ν_1(OH-stretch)	Acquista et al. (1968)
3463 (∗)	OH	ν_1(OH-stretch)	Acquista et al. (1968)
3572 (∗)	H_2O_2	ν_5 (OH-stretch)	Catalano & Sanborn (1963), Khriachtchev et al. (2000)
3581 (∗)	H_2O_2	ν_5 (OH-stretch)	Catalano & Sanborn (1963), Khriachtchev et al. (2000)

[1] Asterisks mark the features used to the determine the integrated absorption.

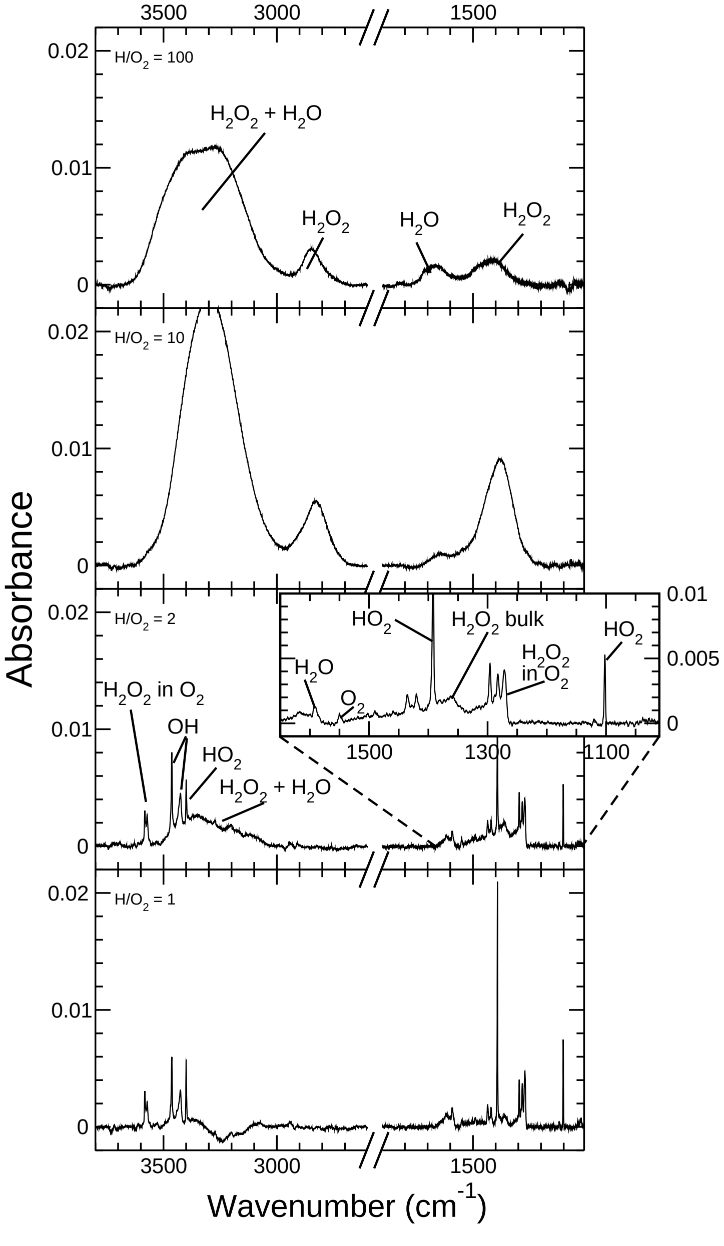

Figure 5.2 RAIR spectra of H and O_2 co-deposition experiments performed for a surface temperature of 20 K and different H/O_2 ratios of 100, 10, 2, and 1 from top to bottom. The H-atom fluence is the same for all spectra.

The spectral appearance of both the H_2O and H_2O_2 bands strongly depends on the environment. In an oxygen-rich environment the bands are narrow. In the remainder of the chapter we will refer to these features as monomer bands, since they are mainly due to single H_2O or H_2O_2 molecules in a hydrophobic environment, in this case the O_2 matrix. By increasing the amount of hydrophilic material in the ice, the bands broaden and the peak positions shift. These we define as bulk bands since they are caused by H_2O or H_2O_2 in an H_2O- or H_2O_2-rich environment. Multiple infrared studies have shown the presence of both bulk and monomer features (Giguère & Harvey 1959, Catalano & Sanborn 1963, Lannon et al. 1971, Bandow & Akimoto 1985, Gerakines et al. 1995, Khriachtchev et al. 2000). For H_2O_2 the bulk and monomer contributions are separated (3572 and 3581 cm^{-1} vs. 1370 cm^{-1}, respectively). The OH-stretch monomer features of H_2O at 3724 and 3732 cm^{-1} are not observed and we therefore conclude that water is not abundantly formed in O_2-rich environments. Only the integrated absorption of the bulk water feature at 1650 cm^{-1} is given for O_2-poor environments. In general the water estimation has the largest error, since the 1550–1700 cm^{-1} range is affected by O_2 baseline distortion and the broad bulk H_2O_2 feature.

5.3 Results

5.3.1 H/O_2 ratio dependence

The ratio between the deposition of H atoms and O_2 molecules determines the hydrogenation grade. Four H atoms are required to fully hydrogenate O_2 to two H_2O molecules. The top panel of Fig. 5.2 shows the RAIR spectrum of the highest H/O_2 ratio that we can reliably reach, which is $H/O_2 = 100$. This spectrum is clearly dominated by broad H_2O and H_2O_2 bands. In this experiment roughly equal amounts of H_2O and H_2O_2 are produced. Oba et al. (2009) produced even more H_2O dominated ices in this way using a higher H/O_2 ratio of 500.

In the present chapter, we are particularly interested in the oxygen dominated regime, where full hydrogenation cannot be reached. Because of the constant supply of O_2, intermediate species are locked in the ice mantle. In this way, all intermediate species listed in Table 5.1 — HO_2, H_2O_2, and OH — can be observed. The first intermediate, HO_2, is clearly present in a very oxygen-rich environment. This is reflected by monomer bands at 1100, 1392, and 3400 cm^{-1} in the spectrum of the bottom panel of Fig. 5.2 for an H/O_2 ratio of 1. In the same spectrum, also H_2O_2 and OH features appear (both monomer features). The presence of the OH features is rather surprising since OH is only formed in reaction (5.3) of the proposed reaction scheme and this reaction is expected to be reached at a higher level of hydrogenation. Furthermore, H_2O, which is formed in the same reaction, is not abundantly present in this spectrum. The third panel of Fig. 5.2 shows a spectrum obtained after exposure of the same H-atom fluence but with an O_2 flow that is reduced by a factor of 2. Here, the HO_2 features shrink, whereas the H_2O_2 and OH signals appear to increase slightly. The H_2O features are small and do not grow and are mostly likely due to background water in the chamber since control experiments of H_2

and O_2 co-deposition result in similar amounts of H_2O. If the oxygen flow is further reduced (second panel, Fig. 5.2), broad bulk water bands can be clearly identified, which are consistent with H_2O formation and in addition the H_2O_2 bands broaden and shift. The spectral features of the intermediates OH and HO_2 disappear entirely.

5.3.2 O_3 detection

For specific conditions, O_3 can be detected as well. Figure 5.3 zooms in on the 1038 cm^{-1} ozone band for three different temperatures and three different H/O_2 ratios. This O_3 band is rather broad and appears to consist of several contributions. As discussed in Sivaraman et al. (2007) it is very sensitive to the local environment and can shift over more than ten wavenumbers. Ozone appears to be predominantly present in the low temperature spectra (15 and 20 K) and for low H/O_2 ratios, or at the opposite conditions: high temperature (25 K) and high H/O_2 ratio. Its presence indicates that oxygen atoms are involved at some stage in the reaction scheme, since ozone is formed from oxygen atoms and oxygen molecules

$$O + O_2 \rightarrow O_3. \tag{5.5}$$

Two possible O-atom formation routes are through the hydrogenation of HO_2

$$H + HO_2 \rightarrow H_2O + O, \tag{5.2c}$$

and the reaction OH with molecular oxygen

$$OH + O_2 \rightarrow HO_2 + O. \tag{5.6}$$

Both reactions are discussed in more detail in § 5.4.1.

Sivaraman et al. (2007) also observed a temperature dependence for O_3 production after electron bombardment of an O_2 ice. They attributed this to O atoms which are more likely to react together to form O_2 than to form O_3 with O_2, even in an O_2 dominated environment. The amount of formed O_3 decreases with temperature in oxygen-rich environments for this reason. At higher temperatures, O atoms become mobile and are more likely to find reactive species like O atoms before reacting with O_2. Similar processes may be at play here and give a similar temperature dependence at low H/O_2 ratios.

For high H/O_2 ratios, reaction (5.5) competes with

$$O + H \rightarrow OH, \tag{5.7}$$

which should proceed without any barrier. We expect that the relative contribution of reaction (5.5) increases with temperature since the lifetime of H atoms on the surface, responsible for the competing reaction, decreases. A second possible mechanism that could be responsible for the detection of ozone at high temperatures is the increased penetration of hydrogen atoms into the O_2 ice with temperature as discussed in Chapter 4. Oxygen atoms are formed through hydrogenation reactions as is addressed in more detail in § 5.4 of the present chapter. At high temperatures H atoms can penetrate deeper into the ice and therefore oxygen atoms form deeper in the ice, which in turn lead to deeply embedded ozone molecules. The chance of hydrogenating species that are positioned deep in the ice is lower than for surface species, even at high temperatures, since newly formed products at the surface and the constant deposition of O_2 can block further penetration. The ozone molecules therefore remain embedded in the ice, whereas at lower temperatures they can react further. Ozone can react with hydrogen atoms to form OH and O_2

$$O_3 + H \rightarrow OH + O_2 \tag{5.8}$$

which both can react further to water. The hydrogenation scheme of pure ozone ice is the topic of a separate paper and confirms water formation upon hydrogenation of a pure O_3 ice (Chapter 6). We expect that the detection of ozone for high H/O_2 ratios and high temperatures is due to a combination of a more effective formation and a less effective destruction at high temperatures.

Ozone is also detected in Chapter 4 upon hydrogenation of a pre-deposited pure O_2 ice and its abundance is observed to increase with ice temperature. The experimental conditions in Chapter 4's experiments can be best compared to the high H/O_2 conditions of the present chapter. We therefore expect that the effect of penetration at high temperatures is the dominant mechanism responsible for the ozone formation.

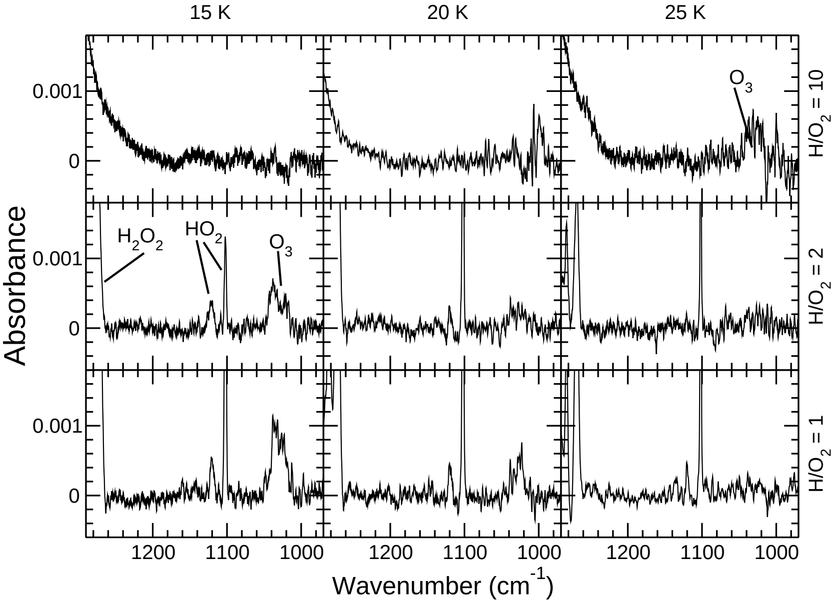

Figure 5.3 RAIR spectra of H and O_2 co-deposition experiments performed for three different surface temperature (15, 20, and 25 K) and three different H/O_2 ratios (10, 2, and 1). The spectra are zoomed in on the 1038 cm^{-1} ozone region.

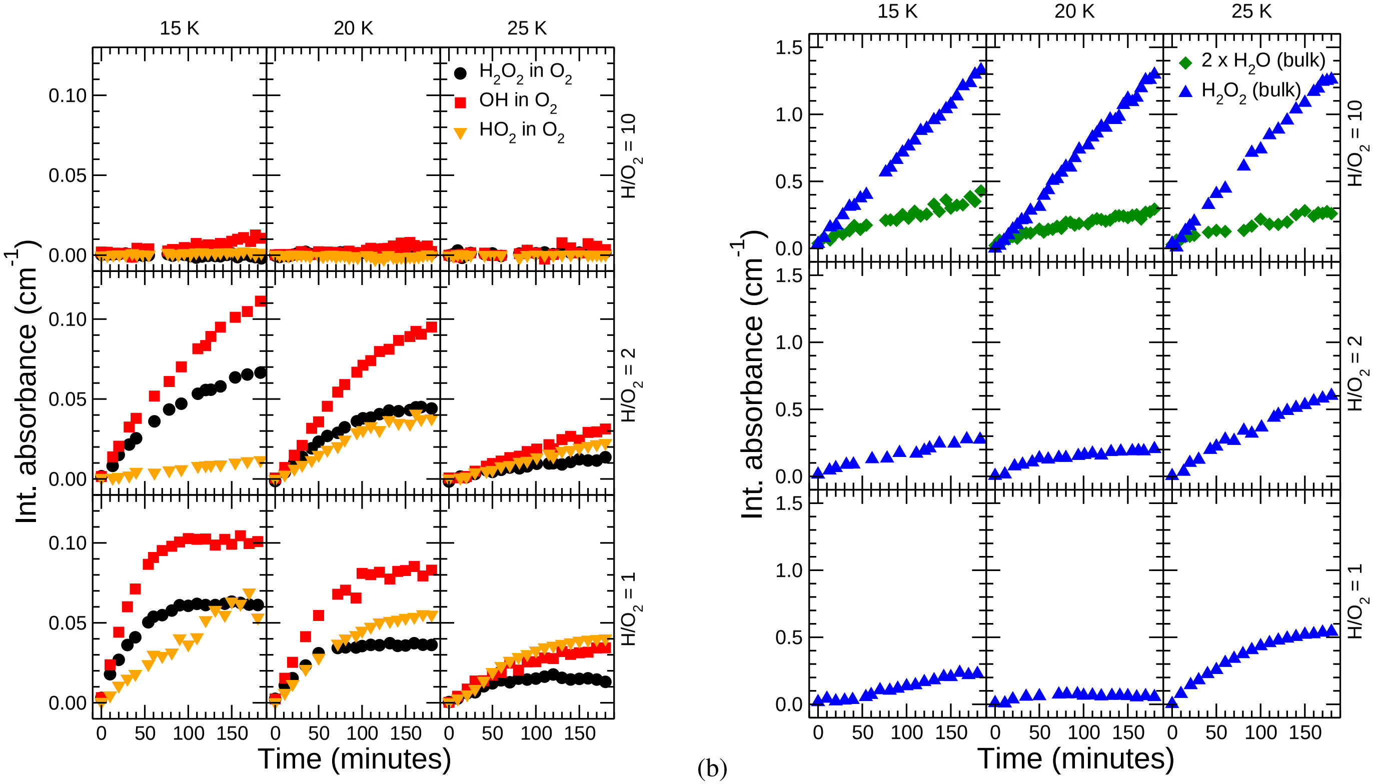

(a)

(b)

Figure 5.4 The integrated absorbance for (a) H_2O_2 in an O_2-rich environment (*circles*), OH (*squares*), and HO_2 (*triangles*) and for (b) the 1370 cm^{-1} H_2O_2 bulk and the 1650 cm^{-1} H_2O bulk features as a function of time for three different surface temperatures and three different H/O_2 ratios. The H_2O bulk integrated absorbance (panel (b)) is multiplied by a factor of two.

5.3.3 Time/fluence dependence

The production of H_2O_2, OH, HO_2 and H_2O is followed by integration of their time resolved infrared features. Figure 5.4a plots the time evolution for the integrated absorbance of the monomer features of H_2O_2, OH, and HO_2 in O_2 at different temperatures (15, 20, and 25 K) and H/O_2 ratios (H/O_2 = 10, 2, and 1). Figure 5.4b shows the corresponding evolution of the H_2O_2 and H_2O bulk features. Note that the latter signals are stronger. As mentioned before, the H_2O features in O_2 are not observed and the bulk water abundance is only shown for H/O_2 = 10, since for the low ratios, the observed water bending features are not distinguishable from the background contributions.

The H_2O_2 monomer features (black diamonds in Fig. 5.4a) follow the same trends and curve shapes as the OH abundance (squares in Fig. 5.4a). Also the H_2O and H_2O_2 bulk features (Fig. 5.4b) seem to follow each other, although not as tightly. The HO_2 abundance has its own distinct behavior. The three different trends are discussed separately below, starting with HO_2. The integrated intensities are plotted as a function of time and not of fluence, since two different species (H and O_2) are simultaneously deposited during these experiments. After 180 minutes an H-atom fluence of 3×10^{17} atoms cm^{-2} is reached; the total O_2 fluence depends on the H/O_2 ratio.

HO_2 monomer features.

The HO_2 abundance is only detectable for low H/O_2 ratios and appears to exhibit only a small temperature dependence, with 20 K as a rough estimate for the optimum temperature. The total production rate of species in general consists of different components and depends on the balance between several formation and destruction reactions. The overall rate of each individual reaction (production rate) is determined by the rate at which the reactants meet (meeting rate) and by the probability that these species react upon meeting each other (reaction rate). The first depends on the diffusion and desorption rates of the reactants; the second on the existence of a reaction barrier and the likelihood to cross this barrier if necessary. The meeting rate first increases with temperature since the species will become more mobile, but once the desorption temperature of (one of) the reactants is reached, it decreases again. The reaction rate is probably independent of temperature when no barrier exists or when the reaction proceeds through tunnelling; in the case of a thermally activated reaction, the reaction rate will increase with temperature. In the present chapter, we will try to disentangle both contributions (meeting vs. reaction rate). For the purpose of astrochemical models, the reaction rates are used as direct input parameters.

Let us consider to the production rate of HO_2. Since the production of H_2O_2 and OH (monomers) is higher at lower temperatures, the reason for the reduced HO_2 abundance at lower temperature lies probably in the more efficient destruction and not in the reduced formation of HO_2. At 25 K, the lifetime of H atoms on the surface is significantly shorter than at 20 K and this is probably the rate limiting factor for HO_2 production at higher temperatures. These arguments suggest that the HO_2 formation rate is actually temperature independent, *i.e.*, the observed temperature dependence of the production rates is because of a temperature-dependent meeting rate. This is in agreement with gas phase calculations of reaction (5.1), where for certain incoming angles no barrier was observed (Sellevag et al. 2008, Troe & Ushakov 2008).

During the co-deposition experiment an ice builds up slowly and surface reactions will predominantly occur in the top layers, determined by the temperature dependent penetration depth as discussed in Chapter 4. If the lower layers of the ice are completely inert, one would expect the absorbance for all species to grow linearly with time. The HO_2 absorbance clearly levels off at later times (Fig. 5.4a), which suggests that some HO_2 is destroyed in the ice. Cooper et al. (2008) suggested a destruction channel via

$$HO_2 + HO_2 \rightarrow H_2O_2 + O_2 \tag{5.9}$$

in H_2O+O_2 UV irradiated ices. The HO_2 radicals, in that study and here, are formed through reaction (5.1). The hydrogen atoms originate from different sources (H-atom beam vs. photolysis). Cooper et al. (2008) found reaction (5.9) to be dominant in the case that HO_2 was formed in confined O_2 clusters where they were in close vicinity of other HO_2 radicals and the radicals did not have to travel over large distances in order to meet. In our O_2 dominated ices, HO_2 radicals are probably formed homogeneously across the ice and the HO_2 will therefore be, for similar densities, at larger average distances from each other and need to diffuse through the ice before they can react together. We do not see evidence for an increase in the destruction of HO_2 with temperature which would correspond to a thermally activated process such as diffusion. Furthermore, the products of reaction (5.9), H_2O_2 and O_2, would result in an increase of the H_2O_2 monomer features at the same time that the HO_2 disappears. However, these features appear to decrease instead of increase. We therefore conclude that HO_2 most likely falls apart in H atoms and oxygen molecules.

In Chapter 4, HO_2 is observed at the end of hydrogenation experiments at high temperatures ($T > 25$ K). We expect that HO_2 under these circumstances is formed deep in the ice and that the destruction of HO_2 by reaction with H atoms is limited in the same way as the destruction of ozone, as explained earlier.

H_2O_2 and OH monomer features.

The H_2O_2 monomer features and the OH abundance follow the same trends and are discussed together. These features are more temperature and H/O_2 ratio dependent than the HO_2 features. For H/O_2 = 1, they initially increase, then decrease and reach a steady state for the investigated temperatures, whereas for H/O_2 = 2, they only increase, although not linearly. Since both features follow each other rather tightly, OH and H_2O_2 are probably formed and destroyed by related processes. This implies that OH is formed earlier in the reaction scheme than through reaction (5.3). We will come back to this later. The decrease of both the OH and H_2O_2 signals (Fig. 5.4a) appears to coincide with the growth of the H_2O_2 bulk and H_2O contributions (Fig. 5.4b). This is a sign typical for segregation and is caused by diffusion of H_2O_2, by O_2 leaving the H_2O_2 matrix ,or a combination of both. Since the interaction between H_2O_2 and the O_2 matrix is rather weak, H_2O_2 may have a higher mobility than usually observed in a hydrophilic environment. The mobility of O_2 is probably also rather high, since the temperature is close to the desorption temperature of O_2. This makes segregation through O_2 diffusion the most plausible scenario (Acharyya et al. 2007). In a similar fashion mobile OH can react with another OH or H_2O_2 to form H_2O_2 or H_2O, respectively, through

$$\mathrm{OH} + \mathrm{OH} \rightarrow \mathrm{H_2O_2} \tag{5.10}$$

and

$$\mathrm{OH} + \mathrm{H_2O_2} \rightarrow \mathrm{H_2O} + \mathrm{HO_2}. \tag{5.11}$$

The first reaction is probably rather inefficient judging from the amount of OH that is present in the co-deposited ices. The hydroxyl radicals are formed in each others vicinity, since they are formed in pairs in the same reaction (see reaction (5.2b) in the next section) and the reaction of the two OH radicals is therefore not diffusion limited, but limited by the reaction probability which does not have a 100% efficiency. Another possibility for mobile OH would be to cluster inside the H_2O_2 bulk aggregates. This will probably lead to a shift and broadening of the OH features causing them to overlap with the broad 3300 cm^{-1} band. The disappearance of the 3426 and 3463 cm^{-1} OH features therefore not necessarily means that OH itself disappears but it may be due to an overlap with the polar bulk features when OH itself is in a more polar environment. Probably a critical amount of OH and H_2O_2 needs to be present before segregation occurs (Öberg et al. 2009a). This would explain why the disappearance of the OH and H_2O_2 monomer features becomes more effective at later times. As mentioned in Cooper et al. (2008), Öberg et al. (2009c) the mobility of OH is thermally activated and only becomes accessible in a water matrix above 80 K. In an oxygen matrix, which is less rigid, this could proceed at lower temperatures. The present data indicates this to be around 25 K. The strong decrease in OH and H_2O_2 monomers and the increase in H_2O_2 bulk and water at 25 K reflects indeed increased mobility of OH and H_2O_2.

Summarizing § 5.3.3, HO_2 forms in a barrierless reaction from H and O_2 and it either reacts further to OH and H_2O_2 or it slowly falls apart in H and O_2. Bulk H_2O and H_2O_2 are mostly formed for a high H/O_2 ratio and they appear to form mostly at later times, which is consistent with their formation in a late stage of the reaction scheme.

5.4 Implications for the reaction network

In this section a consistent reaction scheme is derived that explains the experimental observations described in the previous sections. This scheme is schematically presented in Fig. 5.5. This figure indicates the three initially proposed hydrogenation channels: O, O_2, and O_3 hydrogenation by the black arrows. These three channels run vertically in three columns and have the last step in common: reaction (5.4) or

$$\mathrm{H_2} + \mathrm{OH} \rightarrow \mathrm{H_2O} + \mathrm{H} \tag{5.12}$$

to form H_2O from OH. In this section we add the reactions indicated by the light gray and dark gray arrows to this scheme. The arrow type (*solid, dashed or dotted*) reflects

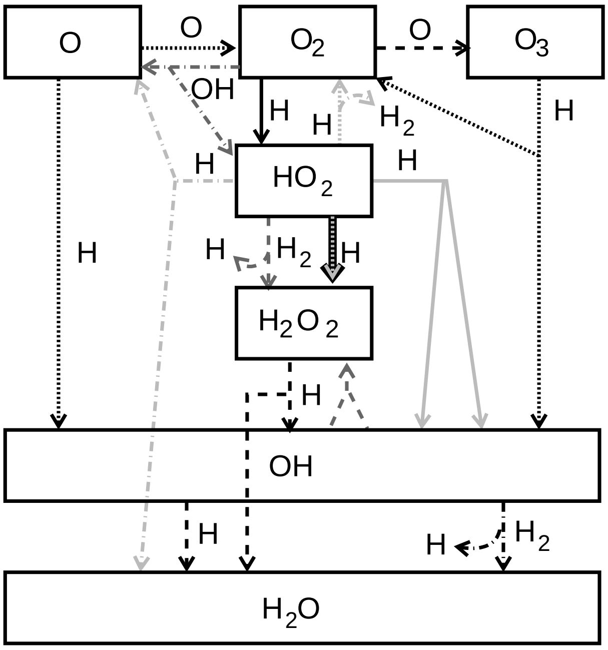

Figure 5.5 A schematic representation of the reaction network as obtained from the present study. Four types of reactions are distinguished: efficient, effectively barrierless, reactions (*solid*), reactions with a barrier but with detectable efficiency (*dashed*), reactions of which the efficiency is below the detection limit (*dash-dotted*), and reactions of which the efficiency could not be determined in this study (*dotted*). The light gray arrows indicate the same entering channel but with different outgoing channels, and the black arrows the reactions which were in the original reaction scheme.

the efficiency of the reaction. The solid arrows in Fig. 5.5 indicate the reactions that are effectively barrierless at low temperatures, the dashed lines proceed with a barrier but have a detectable efficiency, the dash-dotted arrows correspond to reactions that proceed below the detection limit, and the dotted arrows indicate reactions which were observed to proceed, but of which the efficiency could not be determined in this study. In the remainder of this section we will discuss each reaction indicated in Fig. 5.5 separately.

5.4.1 Co-deposition experiments

We first focus on the formation of OH. In the original reaction scheme (black arrows in Fig. 5.5), OH is only formed in the last reaction step. However, as mentioned before, the fact that OH is observed for low H/O_2 ratios and follows the H_2O_2 behavior suggests a common formation route. Indeed in the gas phase, the reaction of atomic hydrogen with

HO_2 is known not only to lead to H_2O_2 through reaction (5.2a)

$$H + HO_2 \rightarrow H_2O_2, \tag{5.2a}$$

but also to result in:

$$H + HO_2 \rightarrow 2OH, \tag{5.2b}$$

$$H + HO_2 \rightarrow H_2O + O, \tag{5.2c}$$

and

$$H + HO_2 \rightarrow H_2 + O_2. \tag{5.2d}$$

In the gas phase branching ratios of 0.90±0.04, 0.08±0.04, and 0.02±0.02 are found for channels (5.2b)-(5.2d), respectively (Keyser 1986). Channel (5.2a) is very unlikely in the gas phase without the presence of a third body. This channel is however allowed in the solid phase. If all four reaction channels would proceed, OH could be formed directly through channel (5.2b) or indirectly through channel (5.2c) after O has reacted to OH or to O_3 which can further react to OH.

In all experiments with $H/O_2 \leq 2$, the ratio between the produced OH and H_2O_2 abundance is constant. This already suggests that OH is mainly formed directly through channel (5.2b), since OH production through subsequent hydrogenation after channel (5.2c) would lead to an OH production as function of time differently from the H_2O_2 production.

Assuming that all detected OH is indeed formed through channel (5.2b), the branching ratios between the OH and H_2O_2 formation channels in the solid phase can be obtained. The 2OH channel (5.2b) is found to be 1.6±0.2 times more likely than the H_2O_2 channel (5.2a), provided that the OH-stretch bandstrength per molecule of H_2O_2 is twice as large as that of an OH radical. Another possibility could be that H_2O_2 is not formed directly through reaction (5.2a) but that in (38±5)% of the cases two OH molecules immediately react and form H_2O_2 (reaction (5.10)). Since OH is still abundantly observed and since most OH is formed through reaction (5.2b) which results in two OH radicals in close vicinity of each other, this reaction will proceed with some barrier. It is therefore indicated by a dashed light gray arrow in Fig. 5.5; the double arrow coming from OH reflects the two OH molecules that are needed in the reaction.

Unfortunately, we cannot quantify channel (5.2d) (H_2+O_2) since both products are not infrared detectable and the change in the water-induced O_2 feature at 1550 cm^{-1} caused by this reaction will be too small to derive a reliable branching ratio.

The branching ratio of the channel leading to H_2O and O (channel (5.2c)) is also hard to quantify, since O atoms can only be detected indirectly by the production of ozone. In the low H/O_2 regime, the OH-stretch modes which are used to quantify the branching ratios for the 2OH and H_2O_2 channels cannot be used for H_2O, since the OH-stretch modes for water in O_2 are below the detection limit. However, using this detection limit, the reactive rate for channel (5.2c) can be constrained to an upper limit of 0.2 times the value of the H_2O_2 channel. This upper limit is 0.08 with respect to combined rate of channels (5.2a) and (5.2b), close to the gas phase branching ratio. The low upper limit further justifies our assumption that OH is mostly formed through channel (5.2b), since only a limited amount of atomic oxygen, needed for the O and O_3 routes, is formed through channel (5.2c).

The light gray arrows in Fig. 5.5 indicate the four different channels for the H + HO_2 reaction. In § 5.3.3 we have argued that reaction (5.1) is barrierless. This reaction is therefore represented by solid arrows. Since in Chapter 4, HO_2 is not observed for $T < 25$ K, the reaction of H + HO_2 is probably effectively barrierless as well, which is in agreement with gas phase data where no barrier is observed between 245−300 K (Keyser 1986). The main channel, (5.2b), is therefore also represented by solid light gray arrows. Channels (5.2a) and (5.2d) cannot be measured directly as discussed above and are therefore represented by dotted arrows. For channel (5.2c) only an upper limit is determined and is therefore represented by a dash-dotted light gray arrow.

Ozone is formed through reaction (5.5) and proceeds with a barrier as discussed earlier. This reaction is therefore indicated by a dashed black arrow in Fig. 5.5. The fact that O_3 is observed, means that O atoms are involved in the reaction network. One O-atom formation route is through reaction (5.2c). The reaction

$$OH + O_2 \rightarrow HO_2 + O, \tag{5.6}$$

which has a gas phase barrier of 220 kJ/mol (Tsang & Hampson 1986), is another likely candidate, if it could proceed through tunnelling which has little temperature dependence. As discussed earlier, the OH features are observed to disappear mostly through a thermally activated diffusion process and reaction (5.6) is therefore thought not to have a large effect on the total OH abundance. In conclusion, the O atoms are probably formed through two relatively inefficient reactions: reactions (5.2c) and (5.6). The observed OH is therefore mainly formed by reaction (5.2b). Since reaction (5.6) is uncertain it is indicated by dash-dotted dark gray arrows in Fig. 5.5.

5.4.2 Hydrogenation of H_2O_2

Water is likely to be formed through a number of different reaction paths in the network: by the hydrogenation of HO_2, OH or H_2O_2. The first, reaction (5.2c), is relatively inefficient as discussed in § 5.4.1. Leaving the other two as as the dominant routes. In this subsection we discuss the specific contribution of H_2O_2 hydrogenation to the overall H_2O production. This route proceeds via reactions (5.3) and (5.4). The first has a barrier in the gas phase of 14.97 kJ/mol (Baulch et al. 1992) and consequently a lower efficiency is expected for H_2O formation through this reaction. The most straightforward way of testing this reaction would be to deposit a pure H_2O_2 ice and subsequently expose this to H atoms. However, since the deposition of H_2O_2 without simultaneous H_2O deposition is not experimentally feasible in our set-up, pure H_2O_2 ice is produced in a different way. At the end of a co-deposition experiment with an H/O_2 ratio of 10, the ice is dominated by H_2O_2 and O_2 (see Fig. 5.2). By heating the ice to 40 K, all the O_2 desorbs from the top, reactive layers, and the resulting bulk H_2O_2 ice can be used for a hydrogenation experiment in which the last part of the reaction scheme (reactions (5.3) and (5.4)) can be studied. In this specific case the ice is exposed to H atoms after it is formed, as in Chapter 4 (in

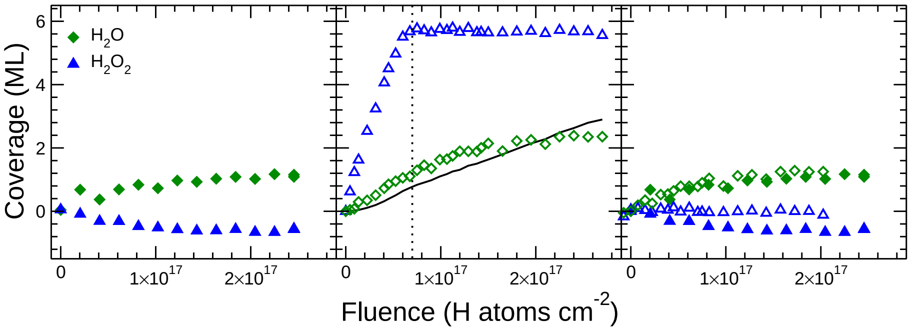

Figure 5.6 The H_2O and H_2O_2 surface coverage in monolayers at 20 K for a H_2O_2 hydrogenation experiment (*filled symbols*) and O_2 hydrogenation experiment (*open symbols*). The right panel compares the H_2O_2 and the O_2 hydrogenation experiment after a fluence of 7×10^{16} atoms cm^{-2} (*dotted line in middle panel*). The solid curve in the middle panel indicates the calculated contribution of water formation from reaction (5.3) (Eq. 5.13).

contrast to the experiments discussed in the rest of the present chapter where H atoms and O_2 molecules are co-deposited). The left panel of Fig. 5.6 plots the H_2O and H_2O_2 surface coverage with respect to the initial H_2O_2 ice for a temperature of 20 K. Hydrogen peroxide is used up whereas H_2O is formed. To obtain the absolute quantities from the integrated absorbances, the apparent bandstrength for water (0.02 cm^{-1}ML^{-1}) as determined in Chapter 4 is used. The corresponding value for H_2O_2 is obtained from this experiment by assuming mass balance. A H_2O(1580−1800 cm^{-1})/H_2O_2(1200−1580 cm^{-1}) ratio of 0.31 is obtained in accordance with Loeffler et al. (2006).

This experiment can be directly compared to the hydrogenation experiments of solid O_2 as reported in Chapter 4. Both the deposition technique (sequential deposition of the ice and H atoms instead of simultaneous) and the experimental conditions in terms of surface temperature and H-atom flux are the same. The middle panel plots the H_2O and H_2O_2 surface coverage as a function of time for an O_2 hydrogenation experiment, again at 20 K. The efficiency of the destruction reaction (5.3) can be determined by comparison of the combined formation reactions (5.1) and (5.2a). In the middle panel $(5.3\pm0.7)\times10^{-17}$ monolayers of H_2O_2 are formed per deposited H atom per cm^2 (slope of the first part of the curves with triangles). It takes two H atoms to form one H_2O_2 molecule. In the left panel $(2.8\pm0.7)\times10^{-18}$ monolayers of H_2O_2 are destroyed per deposited H atom per cm^2 (slope at zero fluence of the curves with triangles). It takes also two H atoms to destroy one H_2O_2 molecule. The H_2O_2 destruction reaction (reaction (5.3)) is the rate limiting step in the formation of water — reaction (5.4) is more efficient. The rate of reaction (5.3) can therefore be quantified with respect to the rate of reaction (5.2a), $k_{5.2a}$, which is $(2.8\pm0.7)\times10^{-18}/(5.3\pm0.7)\times10^{-17} = (0.05\pm0.01)k_{5.2a}$. This lower efficiency with respect to $k_{5.2a}$ indicates that there is a barrier for reaction (5.3) and it is therefore indicated by a dashed black arrow in Fig. 5.5.

The water formed in the O_2 hydrogenation reactions (*middle panel*) can be formed through several reaction routes. The most important two are reactions (5.3) and (5.4). The solid line in the middle panel of Fig. 5.6 shows the contribution of reaction (5.3). This line is obtained from

$$N_{\mathrm{reaction\,(5.3)}}(\mathrm{H_2O}) = 2 \cdot 2.8 \times 10^{-18} F \frac{N(\mathrm{H_2O_2})}{N_{\mathrm{max}}(\mathrm{H_2O_2})} \tag{5.13}$$

with F the hydrogen fluence in atoms cm^{-2}. The factor of 2 accounts for the stoichiometric ratio in O atoms between H_2O and H_2O_2, the rate of 2.8×10^{-18} ML cm^{-2} is taken from the H_2O_2 hydrogenation experiment and the last term in this expression accounts for the probability of an H atom to meet H_2O_2 where the maximum amount of formed H_2O_2 corresponds to the starting condition of the H_2O_2 hydrogenation experiment. Reaction (5.3) accounts for (30±5)% of the formed H_2O in the beginning of the O_2 hydrogenation experiment by comparing the slope of the solid line and the slope of the experimental water abundance (*open diamonds*) at the beginning of the experiment. After 7×10^{16} atoms cm^{-2}, when the maximum amount of H_2O_2 is reached (*vertical dotted line*), the route accounts for roughly 70% of the formed water as is shown in both the middle and the right panel of Fig. 5.6. In the right panel the results of the H_2O_2 hydrogenation experiment are overplotted by the O_2 hydrogenation results after 7×10^{16} atoms cm^{-2}. The H_2O_2 production has reached its maximum at that fluence and the resulting ice is probably similar to the initial condition of the H_2O_2 hydrogenation experiment. The hydrogen peroxide use-up in the O_2 hydrogenation experiment is roughly half of the case where H_2O_2 is hydrogenated (comparison open and closed triangles in right panel) while an equal amount of water is formed (comparison open and closed diamonds in right panel). Part of this is within the error.

Let us now return to the beginning of the O_2 hydrogenation experiment when (30±5)% of the formed H_2O is formed via reaction (5.3). The remaining (70±5)% is most likely formed through reaction (5.4) as discussed earlier. From the co-deposition experiments we know that the reaction of H and HO_2 leads to 3.2 times more OH than H_2O_2, however, only a small amount of water is formed from all these hydroxyl radicals. If OH does not react to H_2O_2, $3.2 \times 5.8 = 19$ ML OH should have formed during the first part of the O_2 hydrogenation experiment. Only $0.70 \times 1.2 = 0.8$ ML of water has been formed from these OH radicals, which amounts to (4±1)%. Since reaction (5.4) is barrierless, this low efficiency is rather surprising. A reason for this could be that the majority of the OH radicals reacts together in the bulk of the ice and would be responsible for part of the H_2O_2 contribution. However, as discussed earlier, we would not expect this to happen in large quantities based on the co-deposition experiments. Another possibility could be that H atoms are not able to reach all OH radicals in the ice. An argument against this is that O_2 still reacts, which means that the ice is not impenetrable. However, it could be that only H-atom approaches under specific incoming angles to OH are reactive, whereas the number of reactive configurations for H reacting with O_2 is much larger. To reflect the relatively low efficiency of this reaction, this reaction is indicated with a dashed black arrow in Fig. 5.5.

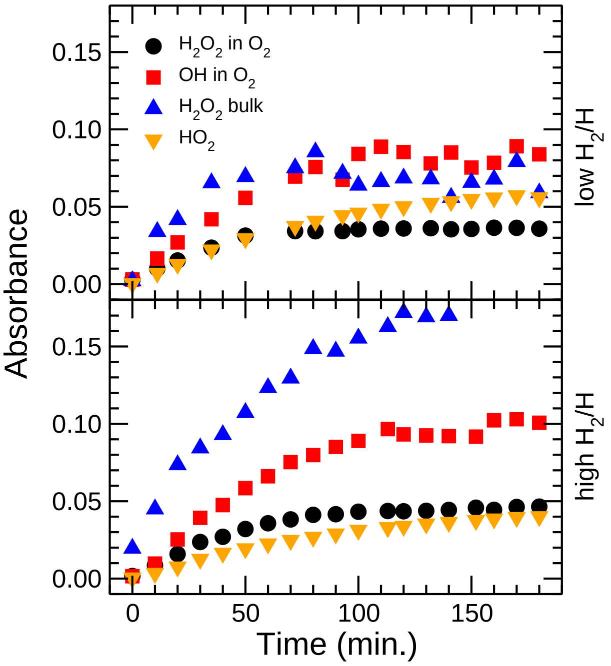

Figure 5.7 RAIRS integrated intensities for $H/O_2 = 1$ and at 20 K with two different H/H_2 ratios. The standard, low, H_2/H ratio results are plotted in the upper panel; the high H_2/H ratio results in the lower panel.

5.4.3 The role of H_2

All reactions discussed in the previous sections ignore the presence of H_2 in the atom beam. However, H_2 will also be present on the surface, mostly from direct deposition of cold molecules from the atom beam, since formed H_2 on the surface is likely to desorb upon formation. If H_2 and O_2 are co-deposited, no reactions are observed, only background deposition of H_2O. However, in the presence of H atoms new reactive species are formed that can react with H_2, in particular OH to form H_2O (reaction (5.12)) or HO_2

$$H_2 + HO_2 \rightarrow H_2O_2 + H. \tag{5.14}$$

By changing the temperature of the filament in the H-atom source and the H_2 pressure in the atomic line, we can keep the H-atom flux constant while increasing the H_2 flux. Figure 5.7 plots the resulting integrated intensities for such an experiment in the lower part. Here the H_2 flux is roughly ten times higher than in the regular experiments ($H/H_2 = 90$ vs. $H/H_2 = 9$ in the standard experiments). The difference in H_2 abundance is therefore definitely due to a change in the cold molecule abundance, since the contribution of formed H_2 molecules remains the same. If reaction (5.12) were efficient, the OH radicals that are formed would react further to H_2O in the high H_2/H experiment and we would be able to observe a significant decrease in the OH surface abundance in the bottom panel with respect to the top panel. At the same time we would expect to be able to detect H_2O in the high H_2/H spectra. Figure 5.7 does however not show such a decrease in OH abundance and also H_2O monomer features were not detected in the IR spectra. We therefore conclude that reaction (5.12) is not very efficient (dash-dotted black arrow in Fig. 5.5). Gas phase experiments show a barrier of 12.69 kJ/mol in the low temperature limit (Orkin et al. 2006).

In the surface abundances of HO_2 and H_2O_2 on the other hand a change can be observed. The abundance of HO_2 decreases in the high H_2/H regime whereas H_2O_2 increases. This is in accordance with reaction (5.14) and this reaction is therefore indicated by a dashed dark gray arrow in Fig. 5.5. The fact that reaction (5.14) proceeds at such low temperatures, is rather surprising since a high gas phase barrier of 109 kJ/mol was reported for this reaction (Tsang & Hampson 1986). An explanation for this is not available.

5.5 Conclusions

The present study shows that the water formation reaction network as originally proposed by Tielens & Hagen (1982) is not complete but that several new reaction paths should be added. The solid state hydrogenation of O_2 exhibits a complex network of reactions as schematically presented in Fig. 5.5. The original reactions are indicated in black. The dark gray and light gray reactions are added in the present study. Through this effort we have shown that the O_2 hydrogenation channel is connected to the O and O_3 hydrogenation channels and we have therefore been able to also draw conclusions on some reactions which are part of the other two hydrogenation channels. We could furthermore quantify the reaction rates of several reactions.

The solid arrows in Fig. 5.5 indicate the reactions that are effectively barrierless at low temperatures. These consist of two reactions

$$H + O_2 \rightarrow HO_2, \tag{5.1}$$

and the reaction of HO_2 and H atoms, indicated in dark gray. The latter has probably four different product channels:

$$H + HO_2 \rightarrow \begin{cases} H_2O_2 & k_{5.2a}, \\ 2OH & (1.6 \pm 0.2)k_{5.2a}, \\ H_2O + O & (< 0.2)k_{5.2a}, \\ H_2 + O_2 & \end{cases} \tag{5.2}$$

where the last product channel cannot be quantified by the methods used in this experimental study.

The reactions which are indicated by the dashed lines proceed with a barrier but have a detectable efficiency. These reactions include:

$$H + H_2O_2 \rightarrow H_2O + OH \qquad (0.05 \pm 0.01)k_{5.2a}, \tag{5.3}$$

$$\mathrm{H} + \mathrm{OH} \rightarrow \mathrm{H_2O}, \tag{5.4}$$

$$\mathrm{H_2} + \mathrm{HO_2} \rightarrow \mathrm{H_2O_2} + \mathrm{H}, \tag{5.14}$$

and

$$2\mathrm{OH} \rightarrow \mathrm{H_2O_2}. \tag{5.10}$$

The dash-dotted arrows indicate reactions that have been proposed but which are not observed to proceed in this study, either because the reaction is too slow or because the experimental method did not allow us to detect this reaction. The reactions

$$\mathrm{H_2} + \mathrm{OH} \rightarrow \mathrm{H_2O} + \mathrm{H}, \tag{5.12}$$

$$\mathrm{H} + \mathrm{HO_2} \rightarrow \mathrm{H_2O} + \mathrm{O} \qquad (< 0.2)k_{5.2a}, \tag{5.2c}$$

and

$$\mathrm{OH} + \mathrm{O_2} \rightarrow \mathrm{HO_2} + \mathrm{O} \tag{5.6}$$

were found to proceed with efficiencies below our detection limit. The reaction

$$\mathrm{H} + \mathrm{HO_2} \rightarrow \mathrm{H_2} + \mathrm{O_2} \tag{5.2d}$$

cannot be detected by the methods used in this experimental study. The same is true for the direct channel of

$$\mathrm{H} + \mathrm{HO_2} \rightarrow \mathrm{H_2O_2} \tag{5.2a}$$

which could proceed with 2OH as intermediates.

The dotted arrows indicate reactions that were found to proceed, but of which the efficiency could not be determined in this study. The reaction

$$\mathrm{H} + \mathrm{O} \rightarrow \mathrm{OH} \tag{5.7}$$

is most likely barrierless. From the the present study we can conclude that it is more efficient than the formation of ozone from oxygen atoms. Since the amount of formed ozone cannot be quantified, the efficiency of the reaction

$$\mathrm{H} + \mathrm{O_3} \rightarrow \mathrm{O_2} + \mathrm{OH} \tag{5.8}$$

could not be determined from this study. Studies of the hydrogenation of ozone indicate this reaction to be efficient.

This studies shows that in the O_2 hydrogenation experiments performed in Chapter 3 and 4, and Miyauchi et al. (2008) water is formed through different reaction paths. Especially in the early stage of experiment, H_2O is not predominantly formed through the hydrogenation of H_2O_2 but through the reaction with OH. By not considering the latter route in the model to fit to the experimental data, an artificial, isotope-independent reaction rate has been obtained for the H + H_2O_2 reaction as explained in the introduction.

This newly determined reaction scheme will have profound implications for models that model the formation of water under interstellar conditions. Clearly several new reaction paths should be considered through this study. Moreover, several reactions proved to be much more efficient (H + O_2) or less efficient (O + OH and H_2 + OH) than originally thought. A dedicated study in which this new scheme will be the input of a new model needs to be applied to tell us how this will affect the formation of interstellar water under different interstellar conditions exactly.

CHAPTER 6

Water formation by surface O_3 hydrogenation[1]

Three solid state formation routes have been proposed in the past to explain the observed abundance of water in space: the hydrogenation reaction channels of atomic oxygen (O + H), molecular oxygen (O_2 + H) and ozone (O_3 + H). New data are presented here for the third scheme with a focus on the reactions O_3 + H, OH + H, and OH + H_2, which were difficult to quantify in previous studies. A comprehensive set of H/D-atom addition experiments is presented for astronomically relevant temperatures. Starting from the hydrogenation/deuteration of solid O_3 ice, we find experimental evidence for H_2O/D_2O (and H_2O_2/D_2O_2) ice formation using Reflection Absorption InfraRed Spectroscopy (RAIRS). The temperature and H/D-atom flux dependence are studied and this provides information on the mobility of ozone within the ice and possible isotope effects in the reaction scheme. The experiments show that the O_3 + H channel takes place through stages that interact with the O and O_2 hydrogenation reaction schemes. It is also found that the reaction OH + H_2 (OH + H), as an intermediate step, plays a prominent (less efficient) role. The main conclusion is that solid O_3 hydrogenation offers a potential reaction channel for the formation of water in space.

---

[1] Based on: C. Romanzin, S. Ioppolo, H. M. Cuppen, E. F. van Dishoeck, H. Linnartz, 2010, submitted to Journal of Chemical Physics

6.1 Introduction

Water is ubiquitous throughout the Universe and belongs to the more abundant species in the interstellar medium. Since gas phase formation rates are not efficient at low temperatures, the formation of H_2O ice in cold dense quiescent interstellar clouds (~10 K) is expected to take place in the solid state on the surface of dust grains through H-atom addition reactions. Three different hydrogenation channels have been proposed in the past: O + H, O_2 + H and O_3 + H (Tielens & Hagen 1982). Several laboratory studies investigated the formation of solid H_2O through the hydrogenation of atomic oxygen (Hiraoka et al. 1998, Dulieu et al. 2010) and molecular oxygen (Miyauchi et al. 2008, Ioppolo et al. 2008, Matar et al. 2008, Oba et al. 2009, Ioppolo et al. 2010, Cuppen et al. 2010). However, only a single study (Mokrane et al. 2009) investigated the third channel so far, showing that the deuteration of O_3 ice on an amorphous H_2O substrate leads to the formation of D_2O by detecting HDO molecules during desorption of the ice using Quadrupole Mass Spectrometry (QMS). We give here further experimental evidence for H_2O/D_2O ice formation, presenting for the first time a comprehensive set of H/D-atom addition experiments on solid O_3 for astronomically relevant temperatures, using Reflection Absorption InfraRed Spectroscopy (RAIRS).

Solid O_3 can be formed in space through energetic processing (ions, photons, electrons) of O-bearing ices at astronomically relevant temperatures (*e.g.*, Famá et al. 2002, Loeffler et al. 2006, Cooper et al. 2008, Schriver-Mazzuoli et al. 1995, Gerakines et al. 1996, Lacombe et al. 1997, Bennett & Kaiser 2005, Sivaraman et al. 2007). Tielens & Hagen (1982) proposed the formation of O_3 ice through the subsequent oxidation of atomic oxygen on the surface of the interstellar grains at low temperature and in absence of UV irradiation. Ozone ice has been observed on the surface of small bodies in the Solar System, like Ganymede, Rhea and Dione (Noll et al. 1996, 1997, Hendrix et al. 1999), but it has not been observed in the interstellar medium. The non-detection of solid ozone in dense molecular clouds is consistent with an efficient use-up through hydrogenation, in the case that O_3 + H is an efficient process under interstellar conditions.

Figure 6.1 is taken from Chapter 5 and shows how the three hydrogenation channels ($O/O_2/O_3$ + H) can interact. Specifically, the hydrogenation of solid O_3 comprises the following solid-state reactions

$$O_3 + H \rightarrow OH + O_2 \tag{6.1}$$

$$OH + H \rightarrow H_2O, \tag{6.2}$$

and

$$OH + H_2 \rightarrow H_2O + H. \tag{6.3}$$

Cuppen & Herbst (2007) and Cazaux et al. (2010) showed in their astrochemical models that the efficiency of this reaction channel strongly depends on the astronomical environment (*e.g.*, diffuse clouds, dense clouds and photon-dominated regions). The experimental results presented in Chapters 4 and 5 showed that the O + H and the O_3 + H channels are connected *via* the O_2 + H route through common reactive intermediates (see Fig. 6.1).

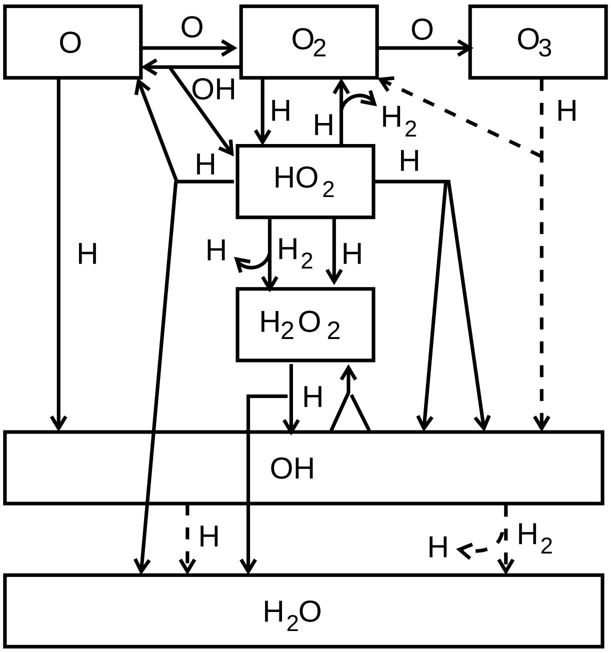

Figure 6.1 A schematic representation of the reaction network as obtained from Chapters 4, 5 and 6. The dashed arrows represent the surface reactions investigated here.

The latter channel involves the reactions

$$HO_2 + H \rightarrow H_2O + O \tag{6.4}$$

and

$$O_2 + OH \rightarrow HO_2 + O, \tag{6.5}$$

which both lead to the formation of O atoms. These can then react with O_2 to form O_3

$$O_2 + O \rightarrow O_3. \tag{6.6}$$

Indeed, O_3 has been found as a reaction product in hydrogenation experiments of pure O_2 ice (Chapters 4 and 5).

In the following sections we investigate the O_3 + H scheme under interstellar analog conditions. We focus in particular on the first reaction step O_3 + H as well as the formation of H_2O from OH through reactions (6.2) and (6.3). For this purpose, most experiments are carried out at elevated temperatures in order to instantaneously desorb the O_2 formed through reaction (6.1).

6.2 Experimental procedure

Experimental details

The experiments are performed using an ultra high vacuum set-up, which has been described in detail elsewhere (Chapters 2 and 4). It consists of an atomic beam line and a main chamber ($\sim 10^{-10}$ mbar), in which ices are grown on a (12−300 K) cryogenically cooled gold-coated copper substrate by depositing gas under an angle of 45°. A fresh O_3 sample is prepared before each experiment in a high-vacuum glass line, following the procedure as described in Berkley et al. (1988). The O_3 sample is prepared in a commercial ozone generator (Fischer-model 502, O_2 99.995% of purity, Praxair) and collected in a liquid nitrogen trap, which is used to purify the sample from O_2 pollution. O_2 deposition originating from the dissociation of O_3 in the main chamber is kept to a minimum by maintaining the substrate temperature at 40 K, well above the O_2 desorption temperature ($T_{\mathrm{des}}(O_2) \sim 30$ K, Acharyya et al. 2007). The ice is monitored by means of RAIRS, using a Fourier Transform InfraRed spectrometer (FTIR). The FTIR covers the range between 4000 and 700 cm^{-1} (2.5−14 μm) with a spectral resolution of 1 cm^{-1}. A co-addition of 256 scans yields one spectrum. RAIR difference spectra (ΔA) with respect to the deposited O_3 ice spectrum are acquired every few minutes during the hydrogenation experiment. According to Sivaraman et al. (2007), shape and position of the $\nu_3(O_3)$ stretching mode is sensitive to the ozone environment. Therefore, the presence of other molecules should affect this infrared band, but the observed $\nu_3(O_3)$ band in our spectra after deposition is typical for a rather pure O_3 ice (Sivaraman et al. 2007, Chaabouni et al. 2000, Misochko et al. 1999), instead of O_3 molecules mixed with O_2 (Schriver-Mazzuoli et al. 1995).

After deposition the ice is subsequently hydrogenated/deuterated at different temperatures (25, 40 and 50 K). H/D atoms are supplied by a well-characterized thermal cracking source (Tschersich & von Bonin 1998, Tschersich 2000, Tschersich et al. 2008). H_2/D_2 molecules are cracked in a capillary pipe surrounded by a tungsten filament, which is heated to 2200 K. During the H/D-atom exposure, the pressure in the atomic line is kept constant. Hot H/D atoms are cooled to room temperature via collisions by a nose-shaped quartz pipe, placed in the H/D-atom beam path towards the substrate. The geometry of the pipe is designed in such a way that hot species (H/D; H_2/D_2) cannot reach the ice directly (more details in Chapters 2 and 4). The H/D-atom fluxes used in our experiments are set by changing the H_2/D_2 pressure in the capillary pipe while the filament temperature is kept constant. The final flux values (2×10^{13} and 8×10^{13} atoms cm^{-2} s^{-1} for H atoms and 1×10^{13} and 4×10^{13} atoms cm^{-2} s^{-1} for D atoms) are measured at the substrate position in the main chamber using a quadrupole mass spectrometer for the D-atom flux. The method is described in the Appendix A of Chapter 4. The relative error in the D-atom flux determination is within 10%, while the relative H-atom flux determination is within 50%. The absolute error for both is estimated to be within 50%.

Several control experiments have been carried out. Deuteration experiments have been performed to estimate the maximum H_2O contamination, *i.e.*, H_2O contributions other than those induced in the ice upon H-atom impact. This is essential as H_2O is the prime target of this study. The pollution may originate from H_2O background in the UHV setup and/or from H_2O in the HV gas line. The contamination is found to increase with time and to be less $\sim$1 ML at the end of all experiments. Results presented in § 6.3 are corrected for this contamination. In the deuteration experiments, naturally, this contamination does not play a role. Also, a pure O_3 ice has been exposed to a D_2 beam (at 40 K) to ensure that the D_2 molecules do not chemically react with the O_3 or physically change the surface through sputtering. Finally, an unprocessed O_3 ice grown at 40 K and subsequently heated to 50 K with a rate of 1 K min^{-1}, shows no substantial O_3 loss because of thermal desorption ($T_{\rm des}(O_3)$ ~63 K, Famá et al. 2002) over a three hour period, the length of a typical experiment.

Data analysis

After subtracting the infrared spectra with a piece-wise straight baseline, the column densities (molecules cm^{-2}) of the newly formed species are calculated using the modified Lambert-Beer equation: $N_X = \int A(\nu)d\nu/S_X$, where $A(\nu)$ is the wavelength dependent absorbance. Since literature values of transmission band strengths cannot be used directly in reflection measurements, an apparent absorption band strength, S_X of species X, is determined by individual calibration experiments. This procedure has been described in detail elsewhere (for the H_2O/D_2O and H_2O_2/D_2O_2 band strength determination see Chapters 4 and 5). Briefly, a layer of the selected ice is deposited at a temperature lower than its desorption temperature. The sample is then linearly heated, close to its desorption temperature. Infrared spectra are acquired regularly until the desorption of the ice is complete. Such an isothermal desorption experiment has been performed to determine the apparent absorption band strength of O_3 by recording the transition from zeroth-order to first-order desorption. This is assumed to occur at the onset of the submonolayer regime and appears in the desorption curve as a sudden change in slope. The apparent absorption strength in cm^{-1} ML^{-1} is then calculated by relating the observed integrated area to 1 ML in the modified Lambert-Beer equation. We estimate the uncertainty of the band strength to be within 50%. The noise in the infrared spectra introduces an extra uncertainty in the H_2O/D_2O, H_2O_2/D_2O_2 and O_3 column densities, which is found to be within ±0.5 ML for all the considered species.

The assignment of the spectral features observed in our experiments is listed in Table 6.1. The band modes peaking at 1650/1210 cm^{-1} (ν_2) and 1390/1050 cm^{-1} (ν_2, $2\nu_4$ and ν_6) are chosen to quantify the column densities of the newly formed species upon H/D-atom exposure (solid H_2O/D_2O and H_2O_2/D_2O_2, respectively). The O_3 band peaking at 1050 cm^{-1} (ν_3) is used to quantify the amount of O_3 deposited on the cold substrate, and, subsequently, the O_3 consumed in the surface reactions during H/D-atom addition. The 1050 cm^{-1} D_2O_2 band overlaps with the $\nu_3(O_3)$ band in our infrared spectra. Thus, a multi-Gaussian fit is used to separate the contributions and determine the area of the individual bands.

Table 6.1 Assigned infrared features in the 4000−700 cm^{-1} region.

Mode	Position^a (cm^{-1})	Species	Position^a (cm^{-1})	Species	Reference
libration	830	H_2O			1, 2
ν_3	888	H_2O_2	884	D_2O_2	1, 3
$\nu_2, 2\nu_4, \nu_6$	1390(∗)	H_2O_2	1050(∗)	D_2O_2	1, 3
ν_2	1650(∗)	H_2O	1210(∗)	D_2O	1, 2
$2\nu_6$	2840	H_2O_2	2100	D_2O_2	1, 3
ν_1, ν_5	3290	H_2O_2	2465	D_2O_2	1, 3
ν_3	3260	H_2O	2440	D_2O	1, 2
ν_3	1050	O_3			4-6
ν_1	1107	O_3			4-6
$\nu_1 + \nu_3$	2110	O_3			4-6

^{a} Asterisks mark the features used to determine the integrated absorbance.

(1) Giguère & Harvey (1959); (2) Hornig et al. (1958); (3) Lannon et al. (1971); (4) Bennett & Kaiser (2005); (5) Chaabouni et al. (2000); (6) Brosset et al. (1993).

6.3 Results and discussion

Figure 6.2 shows the RAIR difference spectra acquired during an hydrogenation (*left panel*) and a deuteration (*right panel*) experiment of solid O_3 at 25 K. Both H_2O/D_2O and H_2O_2/D_2O_2 integrated band intensities clearly grow as the H/D-fluence (H/D-flux × time) increases. Neither species like OH, HO_2, and HO_3, nor the partially deuterated species, like HDO and HDO_2, are detected in our infrared spectra during H/D-atom addition to the O_3 ice. The presence of fully deuterated species gives experimental evidence for surface formation of water ice in the solid phase with O_3 ice as a precursor. The negative peak shown in Fig. 6.2 indeed reflects the O_3 use-up.

6.3.1 Temperature dependence

Figure 6.3 shows the H_2O/D_2O (*square*) and H_2O_2/D_2O_2 (*triangle*) column densities for the three investigated temperatures (25, 40, and 50 K) as a function of the H/D-atom fluence. The solid/open symbols correspond to the low/high H/D-atom flux used in our experiments. The amount of O_3 use-up (*circle*) during H/D-atom addition changes with the substrate temperature from ~1 ML at 25 K to ~10 ML at 50 K. This is consistent with the increase of the H/D-atom penetration depth in the O_3 ice at higher temperatures, since the mobility of O_3 molecules in the ice is expected to improve with increasing temperature, even though the penetration depth of H atoms involves only the surface of the ice and not the bulk. A similar temperature dependence has been observed for the penetration depth of H atoms in CO ice (Chapter 2). Another mechanism may also affect the final amount

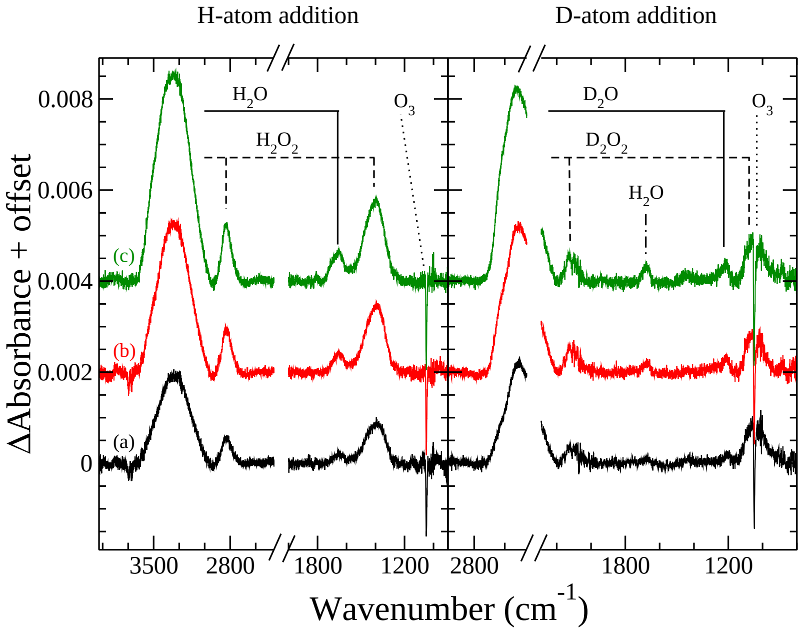

Figure 6.2 Difference infrared spectra of solid O_3 ice, with respect to the spectrum before H/D-atom addition, upon hydrogenation/deuteration at 25 K for three different H/D-atom exposures: (a) 2.4×10^{16}, (b) 7.2×10^{16}, (c) 2.0×10^{17} H/D atoms cm^{-2} s^{-1} (*left/right panel, respectively*). Spectra are offset for clarity. The water pollution is visible in the deuteration experiment (*right panel*).

of O_3 use-up: the erosion of the ice. Each time an H/D atom reacts with an O_3 molecule through reaction (6.1) an O_2 molecule is formed. Whether the O_2 molecule remains on the surface of the ice or desorbs, depends on the temperature of the ice. Below 30 K, the O_2 molecules will be further hydrogenated/deuterated according to the scheme shown in Fig. 6.1 (see also Chapters 4 and 5). At higher temperatures (above 30 K, see Acharyya et al. 2007) the desorption of the O_2 formed through reaction (6.1) will leave the deeper O_3 layers exposed for H/D-atom addition, increasing the final O_3 use-up. The H_2O/D_2O and H_2O_2/D_2O_2 column density ratios are also affected by this desorption behavior. Below 30 K, H_2O/D_2O will be formed through both the hydrogenation/deuteration of O_2 ice and reactions (6.2) and (6.3). A significant amount of H_2O_2/D_2O_2 will be formed through the O_2 channel as well (Chapters 4 and 5). For increasing temperature, the O_2 channel becomes less important and as a consequence the amount of H_2O_2/D_2O_2 decreases, while H_2O/D_2O formation through reactions (6.2) and (6.3) becomes the dominant process.

As a side-effect of the erosion/restructuring of the ice, the H_2O pollution diluted in the O_3 ice, may rearrange in islands. Consequently, the narrow H_2O bands seen after deposition of the O_3 ice in the region of the H_2O bending mode (1650 cm^{-1}) will broaden

Table 6.2 Amounts of O_3 use-up, and formed H_2O/D_2O and H_2O_2/D_2O_2 in ML after an exposure of 1.1×10^{17} H/D atoms cm^{-2} and 4.2×10^{17} H/D atoms cm^{-2} (low and high fluxes, respectively) at the three different substrate temperatures investigated. See §6.2 for the determination of the errors. The O_{budget} corresponds to the mass-balance of O atoms in ML: $O_{budget} = -3O_3 + H_2O + 2H_2O_2$, or the equivalent for deuteration.

H/D-flux (cm^{-2} s^{-1})	T (K)	O_3	H_2O	H_2O_2	O_{budget}	O_3	D_2O	D_2O_2	O_{budget}
				(ML)				(ML)	
2/1 $\times 10^{13}$	25	0.8	1.5	4.9	8.9	1.5	1.0	2.7	1.9
	40	2.7	1.8	2.3	-1.7	3.0	1.1	0.6	-6.7
	50	7.4	1.2	0.7	-19.6	8.8	1.8	0.5	-23.6
8/4 $\times 10^{13}$	25	0.8	3.1	4.6	9.9	1.5	1.6	2.2	1.5
	40	2.9	2.9	2.6	-0.6	2.7	1.6	1.4	-3.7
	50	8.1	3.7	1.8	-17.0	8.5	2.2	0.5	-22.3

upon ice restructuring. This effect increases with time and contributes to the total H_2O bulk feature peaking at 1650 cm^{-1}. This effect is shown in the right panel of Fig. 6.2. The contribution of this effect, which is estimated to be ~1 ML at the end of all the deuteration experiments, is taken into account for all the H-atom addition experiments, as mentioned in §6.2.

6.3.2 H/D-atom flux dependence

Figure 6.3 also indicates the influence of the H/D-atom flux on the amount of reaction products. The H_2O/D_2O and H_2O_2/D_2O_2 column densities follow the same trend for high and low H/D-atom flux and for all investigated temperatures within the experimental uncertainties. This observation is in agreement with a scenario in which a reactive system is limited only by the number of H/D atoms that reaches the ice surface. The O_3 column density follows the same behavior for high and low H/D-atom flux at temperatures below 40 K and at 50 K for a maximum H/D-atom fluence of 1×10^{16} H/D atoms cm^{-2}. However, at higher H/D-atom fluence the O_3 column density profile differs for high and low H/D-atom flux at 50 K. This is most likely caused by the transition between two different regimes: in the first regime, reaction (6.1) is limited by the number of H/D atoms, in the second regime, this reaction is limited by the supply of O_3 molecules, since the formed H_2O/D_2O and H_2O_2/D_2O_2 prevent the incoming H/D atoms to reach the O_3 molecules in the lower layers. Further conversion into H_2O/D_2O and H_2O_2/D_2O_2 is then only possible after replenishing of the top layers by fresh O_3. This process is governed by the diffusion of O_3 in the ice, which increases with temperature and is independent of H/D-atom flux. Thus, this effect is stronger at 50 K than at 40 K and indeed the O_3 use-up follows the same trend for low and high H/D-atom fluxes when plotted as a function of exposure time instead of fluence for $>1\times10^{16}$ H/D atoms cm^{-2}. The two regimes are schematically depicted in Fig. 6.4.

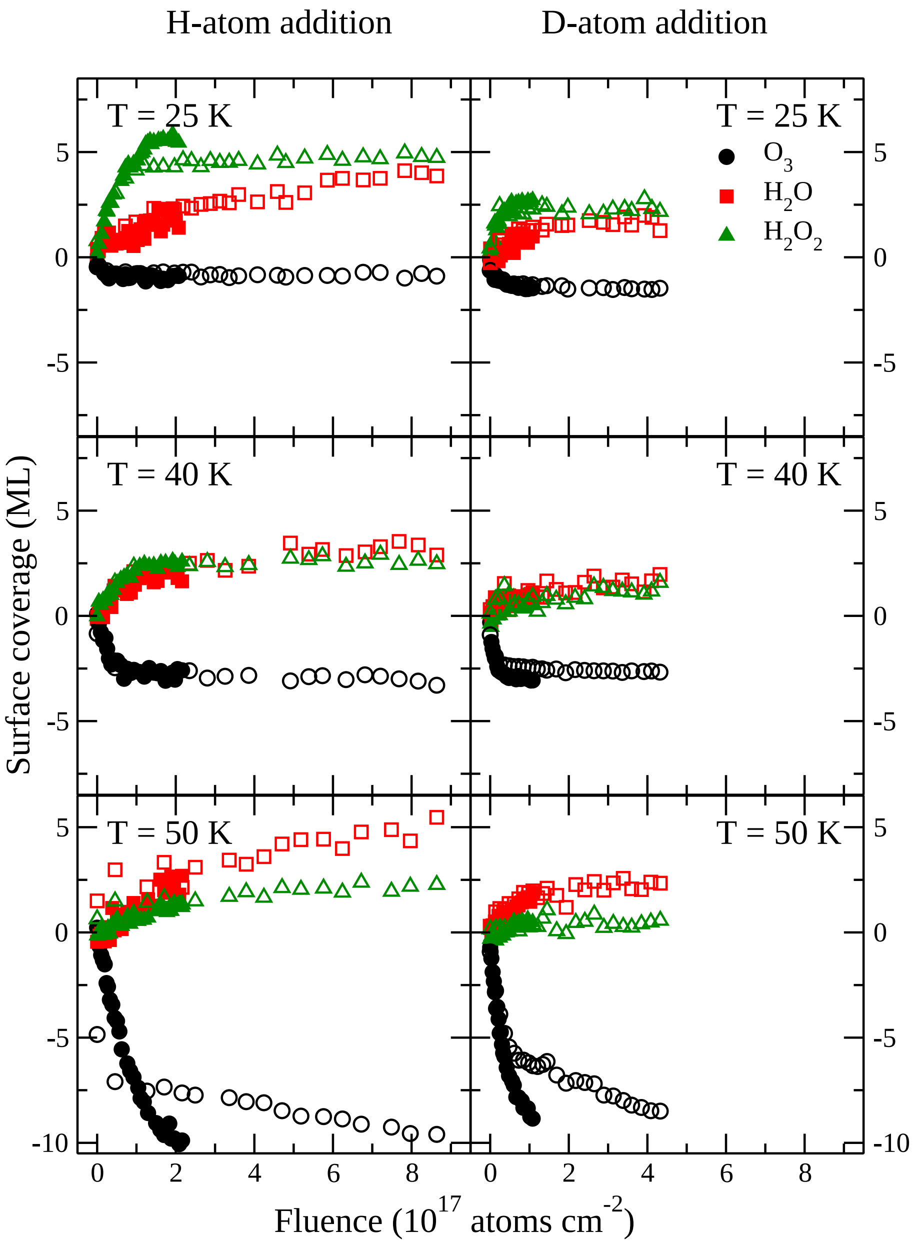

Figure 6.3 Column densities for H_2O/D_2O (*square*), H_2O_2/D_2O_2 (*triangle*) and O_3 (*circle*) for the three temperatures investigated (25, 40, and 50 K) as a function of the H/D-atom fluence. The hydrogenated species are plotted in the left panel, and the deuterated species in the right panel. The solid and open symbols correspond to the lower and higher H/D-atom flux (2×10^{13} and 8×10^{13} atoms cm^{-2} s^{-1} for H atoms, 1×10^{13} and 4×10^{13} atoms cm^{-2} s^{-1} for D atoms), respectively.

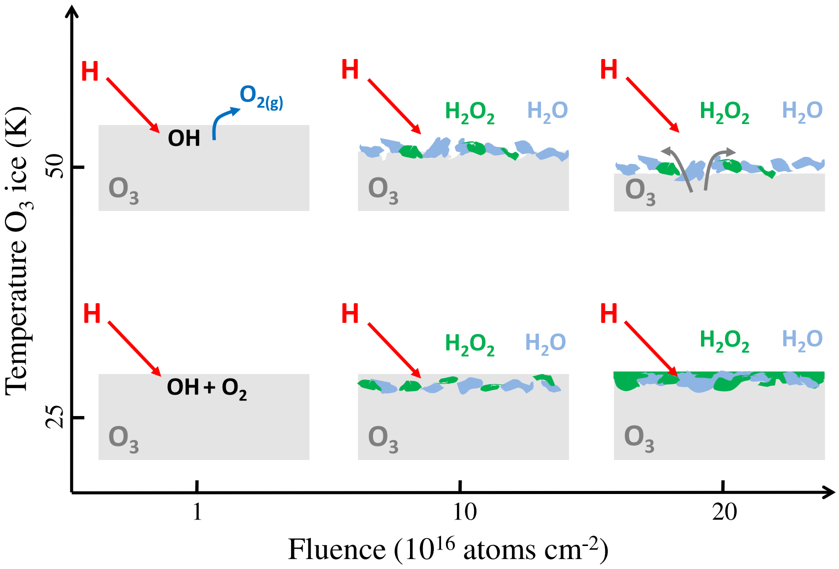

Figure 6.4 Schematic representation of the hydrogenation of O_3 ice as a function of the temperature and H-atom fluence: at temperatures below 40 K (*bottom*) reaction (6.1) is limited by the number of H/D atoms, at higher temperatures (*top*) this reaction is limited by the supply of O_3 molecules. The replenishing of the top layers is induced by diffusion of O_3 in the ice. The erosion of the ice at 50 K is also shown (*top*).

6.3.3 Possible reaction pathways

The investigation of the mass balance between the formed and consumed species in our ice after H/D-atom addition allows identifying the most likely reaction channel responsible for the formation of solid H_2O ice. The mass balance for oxygen atoms can be determined looking at the number of O atoms present in each species (O_{budget} = -3O_3 + H_2O + 2H_2O_2). From the comparison of the results listed in Table 6.2 we summarize three relevant results: (i) the O atoms are found in excess only at 25 K (O_{budget} = 9.9/8.9 ML for higher/lower H-atom flux and 1.5/1.9 ML for both higher/lower D-atom flux); (ii) part of the O use-up is not converted into H_2O/D_2O and H_2O_2/D_2O_2 at 40 and 50 K (negative O_{budget}); and (iii) there appears to be a strong isotope effect in the formation of H_2O/D_2O and H_2O_2/D_2O_2 (more H_2O and H_2O_2 than D_2O and D_2O_2).

Point (i) can be explained by the presence of an extra O_2 poisoning layer deposited on top of the O_3 ice at 25 K. The extra O_2 originates from background deposition, while the substrate was cooled from 40 K to 25 K with a rate of 1 K min^{-1}. This effect is already minimized by lowering the surface temperature only after the main chamber pressure has substantially dropped towards the standard value of 10^{-10} mbar. However, the deposition of a maximum of 5 ML of O_2 on top of the O_3 ice cannot be prevented for the 25 K experiments (5 ML of O_2 correspond to 10 ML of O atoms). The higher value for the

O_{budget} in the 25 K hydrogenation experiment with respect to the deuteration experiment is consistent with a higher penetration depth of H atoms in the O_2 ice compared to D atoms (Chapter 3).

Point (ii) is addressed by the fact that most of the O_2 produced through reaction (6.1) is lost at temperatures higher than the O_2 ice desorption temperature. OH/OD and H_2O/D_2O can desorb upon reaction as well. We will discuss this issue in more detail in the next paragraph, which deals with point (iii).

Roughly the same amount of O_3 is used-up for the hydrogenation and deuteration experiments. This indicates that the observed isotope effect (point (iii)) is not due to a different rate for hydrogenation and deuteration of O_3, but that it is probably caused by a different desorption probability upon reaction. Table 6.2 suggests that D_2O and D_2O_2 are more likely to desorb than H_2O and H_2O_2. Thermal desorption, however, would lead to the reverse and therefore this effect has to come from the reaction energetics. We will first consider H_2O/D_2O, which is formed in two steps. In the first step, reaction (6.1), most of the excess energy will be released in the form of ro-vibrational excitation of OH/OD or in translational energy. Gas phase calculations show that this translational energy is 5.4% higher for deuteration than for hydrogenation (Yu & Varandas 1997), which would lead to a slightly higher desorption probability for D + O_3 than for H + O_3 and may explain at least part of the observed effect. If H_2O/D_2O is then mainly formed from OH/OD through reaction (6.2) (see left side of Fig. 6.5), the large overall difference in desorption probability still cannot be fully explained. It can however be explained if H_2O/D_2O is mainly formed through reaction (6.3). In this case, the kinetic energy is distributed over the products according to the inverse mass which means that D_2O will have nearly twice the kinetic energy of H_2O after reaction (6.3). Since the total excess energy of ~1 eV is close to the desorption energy of H_2O (0.9 eV, Andersson et al. 2006), this difference in kinetic energy will have a substantial effect on the desorption probability. Therefore, in this case more D_2O will desorb from the ice.

The observed isotope effect for H_2O/D_2O can thus be explained by reaction (6.3) instead of reaction (6.2). On first glance one would however expect reaction (6.2) to be more efficient than reaction (6.3), since the first is barrierless, with an excess of 5.3 eV, and the second has a barrier of 0.234 eV (Yang et al. 2001), with an excess of 1 eV. The problem with reaction (6.2) is that one needs to dissipate 5.3 eV of excess energy with just one product. Part of this could be absorbed by the ice surface, but the weak interactions between the product and the ice limits the full dissipation. A reaction where only 1 eV of excess energy is released over two products is therefore more likely, especially since H_2 is abundantly present in our experiment, because the H-atom beam entering the main chamber contains a large fraction of cold H_2.

Furthermore, gas phase experiments indicate that tunneling becomes important for OH + H_2 below 250 K. The reaction rate at 25−50 K will therefore be substantially increased through tunneling. This also leads to an extra isotope effect where OH + H_2 has probably a higher rate than D_2 + OD. In addition, OH/OD is formed “hot” and this energy can also be used to overcome the reaction barrier. Reaction (6.3) may therefore be more relevant than reaction (6.2). These two reactions were previously included in the complete reaction network for O_2 surface hydrogenation investigated in Chapter 5, although no experimental evidence was found for reaction (6.3). However, the method used there was not very sensitive to the detection of this particular reaction. Therefore, extra dedicated studies specifically on the OH + H_2 reaction are needed to determine the absolute efficiency of this reaction, especially in light of the present study, which indicates that this reaction may be crucial as a final step in all three water formation channels ($O/O_2/O_3$ + H).

Similar arguments can be used for the formation of H_2O_2/D_2O_2 from HO_2/DO_2 by

$$HO_2 + H \rightarrow H_2O_2 \tag{6.7}$$

or

$$HO_2 + H_2 \rightarrow H_2O_2 + H, \tag{6.8}$$

where the latter can again lead to an isotope effect with more D_2O_2 than H_2O_2 desorption and a lower rate of reaction for D_2 + DO_2 through tunneling (see right side of Fig. 6.5). HO_2 + H_2 has a high barrier of 1.1 eV and is endothermic by -0.6 eV. However, in the aforementioned study we have observed this reaction to proceed (Chapter 5). The exothermicity of O_2 + H may help to overcome the barrier and the endothermicity, since the total reaction

$$O_2 + H_2 \rightarrow H_2O_2 \tag{6.9}$$

composed of

$$O_2 + H \rightarrow HO_2, \tag{6.10}$$

and

$$HO_2 + H_2 \rightarrow H_2O_2 + H, \tag{6.11}$$

is exothermic by 1.3 eV.

To summarize, the observed isotope effect between H_2O/H_2O_2 and D_2O/D_2O_2 in the O_3 hydrogenation channel can be explained by a combination of effects. First, OD will get more translational energy than OH in reaction (6.1). Then, if H_2O_2 and H_2O are formed through reactions with H_2, tunneling leads to a higher rate for hydrogenation than deuteration and, secondly, the distribution of excess energy can lead to more D_2O/D_2O_2 than H_2O/H_2O_2 desorption. O_3 is destroyed equally for H and D, which indicates that reaction (6.1) proceeds without substantial tunneling effect.

Finally, all the results discussed here are obtained under laboratory conditions, which in some cases differ order of magnitudes from interstellar conditions (*e.g.*, time scale to reach the same H-atom fluence). Therefore, the use of excess energy to allow further reaction steps, which can proceed under laboratory conditions, might not be favorable under interstellar conditions. For instance, the excess energy of the OH radical formed through reaction (6.1) can be dissipated in the ice before H_2 would reach this OH on interstellar timescales. However, two reaction steps might still apply to the ISM at low temperature (10 K), if an H_2 layer is available on the surface of the ice for further reactions.

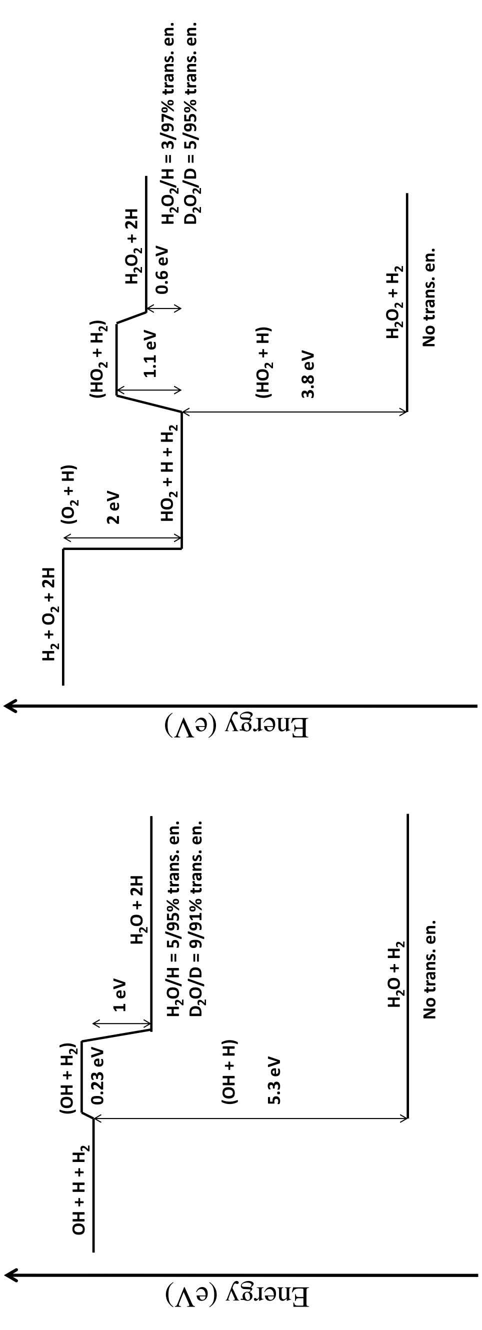

Figure 6.5 Proposed reaction mechanism for the formation of H_2O (*left side*) and H_2O_2 (*right side*) from hydrogenation of O_3 ice. Reactions are shown in brackets.

6.4 Conclusion

The present study shows that the water formation through hydrogenation of solid O_3 ice as proposed by Tielens & Hagen (1982) takes place under interstellar ice analog conditions. Hydrogenation of O_3 ice exhibits a similar temperature dependency as seen for CO ice (Chapter 2): the mobility of O_3 molecules increases with the temperature, while the penetration depth of H atoms into the ice involves only the first monolayers. For temperatures above the O_2 desorption temperature, hydrogenation of O_3 leads to erosion of the ice, since O_2 formed in the reaction O_3 + H desorbs. The remaining OH can further react to H_2O and H_2O_2. The erosion occurs until a layer of H_2O and H_2O_2 layer covers the ice and prevents the incoming H atoms from reaching the underlying O_3 ice. It is found that at high surface temperature (50 K) O_3 is mobile enough to slowly diffuse through the H_2O and H_2O_2 layer and to become available for further hydrogenation on the surface of the ice.

Experimental evidence is found for the connection of the O_3 hydrogenation channel to the O + H and O_2 + H channels, as summarized in Fig. 6.1. As a result it has become possible to draw conclusions on several reactions that are part of the other two hydrogenation channels. The results indicate that the reaction OH + H_2 is most likely more efficient than the reaction OH + H: reaction OH + H_2 could proceed through tunneling, while reaction OH + H needs to dissipate 5.3 eV of excess energy with just one product, which could be difficult. Our experimental results complete the reaction scheme initially proposed in Tielens & Hagen (1982) to explain surface water formation in space. The conclusion that the three channels ($O/O_2/O_3$ + H) are strongly linked, is of importance for astrochemical models focusing on water formation under interstellar conditions.

CHAPTER 7

Competition between CO and O_2-ice hydrogenation channels and surface formation of CO_2 at low temperatures[1]

In the past decade astrochemical laboratory studies have focused on the investigation of isolated surface reaction schemes, starting from the hydrogenation of simple and pure ices, like solid CO or O_2. The reaction products observed for CO hydrogenation are H_2CO and CH_3OH, while after O_2 hydrogenation H_2O_2 and H_2O are formed. We present here the first systematic laboratory study focusing on H-atom addition to a mixed CO:O_2 ice. Mixed ices are more relevant from an astrochemical point of view and can elucidate reactions with radicals that are not readily studied otherwise. The aim of this chapter is to investigate the competition between CO and O_2 hydrogenation, and the corresponding surface formation of CO_2 for astronomically relevant temperatures. Mixtures of CO:O_2 = 4:1, 1:1 and 1:4 are deposited on a substrate in an ultra high vacuum setup at low temperatures (15 and 20 K) and subsequently hydrogenated. The ice is monitored by means of Reflection Absorption InfraRed Spectroscopy (RAIRS). The results show that the contemporary presence of CO and O_2 molecules in the ice influences the final product yields of the separate CO + H and O_2 + H channels, even though the formation rates are not significantly affected. CO_2 is efficiently formed through dissociation of the HO-CO intermediate complex in all studied CO:O_2 mixtures and within the experimental uncertainties no dependency on temperature or ice composition is observed. Moreover, the CO + O and HCO + O channels are not efficient at low temperature under our experimental conditions. The laboratory results demonstrate that CO_2 can be formed in interstellar ices at low temperatures in the absence of UV radiation and show a correlation between the formation of CO_2 and H_2O, which is consistent with the astronomical observation of solid CO_2 in water-rich environments.

---

[1] Based on: S. Ioppolo, Y. van Boheemen, H. M. Cuppen, E. F. van Dishoeck, and H. Linnartz, 2010, submitted to Monthly Notices of the Royal Astronomical Society

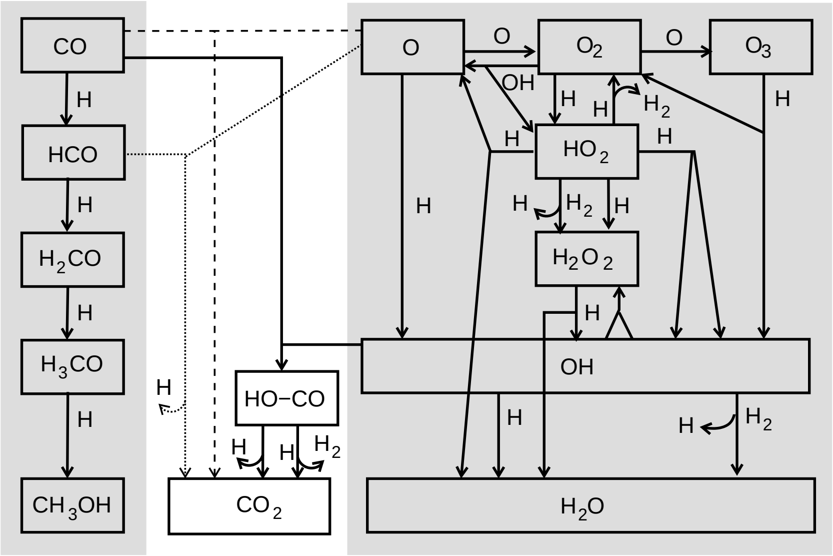

Figure 7.1 A schematic representation of the reaction network as discussed in the present study. The CO + H channel (Chapter 2) is shown on the left-side of the figure, while the $O/O_2/O_3$ + H channels are plotted as presented in Chapter 5 on the right-side. The possible CO_2 formation routes are shown in between the CO + H and $O/O_2/O_3$ + H channels: the dissociation of the HO-CO intermediate (*solid arrow*) is one of the topics of this work; the hydrogenation of the HO-CO complex (*solid arrow*) is presented in Chapter 8; the suggested CO + O (*dashed arrow*) and HCO + O (*dotted arrow*) routes are not experimentally confirmed at low temperature (Tielens & Hagen 1982, Ruffle & Herbst 2001).

7.1 Introduction

Infrared Space Observatory and *Spitzer Space Telescope* observations have shown that H_2O, CO, CO_2, and, in some cases, CH_3OH represent the bulk of solid-state species in dense molecular clouds and star-forming regions. Other ice components, such as CH_4, NH_3, OCN^-, H_2CO, HCOOH, SO_2, and OCS have abundances <5% relative to H_2O (*e.g.*, Gibb et al. 2004, Boogert et al. 2008, Pontoppidan et al. 2008, Öberg et al. 2008, Zasowski et al. 2009, Bottinelli et al. 2010). Several of these species are assumed to be formed in solid state reactions on the surfaces of icy dust grains, first outlined by Tielens & Hagen (1982). Although these reactions have been postulated nearly 30 years ago, few have been measured in the laboratory at low temperatures and UHV conditions until recently. Over the past decade, detailed laboratory studies have started to investigate isolated surface reaction schemes, starting from the hydrogenation of simple and pure ices, like solid CO or O_2.

Several groups proved that the hydrogenation of CO ice at low temperatures (12−20 K) leads to the subsequent formation of H_2CO and CH_3OH (*e.g.*, Watanabe et al. 2004, 2006a, Fuchs et al. 2009). The experiments showed that this hydrogenation process involves only the upper monolayers (4 ML, where 1 ML corresponds to 10^{15} molecules cm^{-2}) of the CO ice and formation rates drop at temperatures higher than 15 K, since the desorption of H atoms becomes important at these temperatures. The hydrogenation of CO to CH_3OH proceeds in four steps,

$$\mathrm{CO} \xrightarrow{\mathrm{H}} \mathrm{HCO} \xrightarrow{\mathrm{H}} \mathrm{H_2CO} \xrightarrow{\mathrm{H}} \mathrm{H_3CO} \xrightarrow{\mathrm{H}} \mathrm{CH_3OH}, \tag{7.1}$$

where the first step from CO to HCO and the third step from H_2CO to H_3CO have a barrier.

The other surface reaction channel that has been well investigated is the hydrogenation of O_2 ice, which leads to the formation of H_2O_2 and H_2O (*e.g.*, Miyauchi et al. 2008, Ioppolo et al. 2008, 2010, Cuppen et al. 2010). This hydrogenation process

$$\mathrm{O_2} \xrightarrow{\mathrm{2H}} \mathrm{H_2O_2} \xrightarrow{\mathrm{2H}} \mathrm{2H_2O} \tag{7.2}$$

behaves differently compared to the hydrogenation of CO ice (reaction scheme 7.2 shows the simplified version of this route, as discussed by Tielens & Hagen 1982). In this case, the penetration depth of H atoms in the O_2 ice increases with temperature, even at values close to the desorption temperature of the O_2 layer, involving the bulk of the ice (tens of monolayers). Thus, H atoms trapped in the ice can diffuse and eventually react up to much higher temperatures. Moreover, at least the formation of H_2O_2 does not exhibit any noticeable barrier.

The present work is a further step towards a laboratory investigation of surface reactions in a more complex and realistic interstellar ice analogue by studying the competition between the two hydrogenation channels in a binary $CO:O_2$ ice mixture as well as the inherent formation of solid CO_2. The latter is not found as a reaction product for the separate channels. CO_2 is one of the most common and abundant ices, yet its formation routes are still very uncertain. Figure 7.1 shows a schematic representation of all the reaction networks investigated in this work (*solid arrows*) and links the previously studied CO + H and O_2 + H channels through the observed CO_2 formation. The dashed and dotted arrows represent suggested CO_2 formation routes in the networks of Tielens & Hagen (1982) and Ruffle & Herbst (2001), that are not experimentally confirmed at low temperature in our studies. As discussed in § 7.4.4, CO_2 is formed under our experimental conditions through the reaction CO + OH. Here OH radicals are formed through the hydrogenation of O_2 ice, while in space they can also result from the O + H reaction or from photodissociation of H_2O ice. Our experiments are designed to test the interaction of the aforementioned individual surface reaction channels rather than simulate a complete realistic interstellar ice evolution. Hence, our experiments show that OH radicals can get further hydrogenated, leading to H_2O formation, or, alternatively, can react with the CO present in the ice, forming solid CO_2. These results give the experimental evidence for the correlation of H_2O and CO_2 formation. Indeed, observations by the *Infrared Space Observatory* (*e.g.*, Gerakines et al. 1999, Nummelin et al. 2001, Gibb et al. 2004) and the

Spitzer Space Telescope (*e.g.*, Boogert et al. 2004, Bergin et al. 2005, Pontoppidan et al. 2005, 2008, Whittet et al. 2007) show that roughly $\frac{2}{3}$ of the solid CO_2 observed in quiescent molecular clouds and star-forming regions is found in water-rich environments, suggesting that the formation routes of these two molecules are linked. The remaining CO_2 ice is predominantly found in a H_2O-poor, CO-rich environment (Pontoppidan et al. 2008). The origin of this common ice mantle component remains uncertain.

It is widely accepted that CO_2 is not formed efficiently in the gas phase, with subsequent accretion onto the grains ($CO_2^{gas}/CO_2^{ice} \ll 1$; van Dishoeck et al. 1996, Boonman et al. 2003). Therefore, the observed CO_2 most likely has to be formed in the solid phase. Several reaction mechanisms have been proposed with a relevance depending on astronomical environment. Energetic processing, such as UV and ion irradiation of interstellar ice analogues, has been investigated in various laboratories and proposed as an efficient CO_2 formation mechanism (Chapter 9 and references therein). Furthermore, in the absence of UV irradiation several cold solid-phase reaction channels have been reported in the past decades as an alternative formation mechanism to explain the CO_2 abundance observed in cold clouds (*e.g.*, Tielens & Hagen 1982, Ruffle & Herbst 2001, Stantcheva & Herbst 2004, Fraser & van Dishoeck 2004, Goumans et al. 2008, Goumans & Andersson 2010). The most straightforward surface reaction channel is the addition of an O atom to solid CO ice. The reaction CO + O → CO_2 has been experimentally investigated only by temperature programmed desorption experiments using thermal O atoms below 160 K (Roser et al. 2001) and by energetic O atoms (Madzunkov et al. 2006). This surface reaction channel has a high reaction barrier, because the $CO(^1\Sigma)$ + $O(^3P)$ reactants do not correlate directly with the singlet ground state $CO_2(^1\Sigma)$ (2970 K in the gas phase; Talbi et al. 2006). Ruffle & Herbst (2001) found in their astrochemical model that they were only able to reproduce the CO_2 abundances observed towards the cold (10 K) cloud Elias 16, if they artificially lowered the barrier to 130 K. Recently, Goumans & Andersson (2010) used harmonic quantum transition state theory to conclude that whilst quantum mechanical tunneling through the activation barrier increases the classical reaction rate for reaction CO + O at low temperatures (10−20 K), the onset of tunneling is at too low temperatures for the reaction to efficiently contribute to CO_2 formation in quiescent clouds.

Solid CO_2 is further suggested to be formed through the surface reaction HCO + O, which presents two exit channels (CO_2 + H and CO + OH; Ruffle & Herbst 2001). Alternatively, solid CO_2 can be formed through the surface reaction CO + OH, which yields a HO-CO intermediate. This complex can directly dissociate, forming solid CO_2 and leaving a H atom, or can be stabilized by intramolecular energy transfer to the ice surface and eventually react with an incoming H atom in a barrierless manner to form CO_2 and H_2 (Goumans et al. 2008). Oba et al. (2010) investigated the reaction CO + OH depositing CO molecules on a cold substrate (10 and 20 K) together with H_2O fragments (OH, H, O and H_2) produced by dissociating H_2O molecules in a microwave source. They confirmed the formation of solid CO_2 at low temperature by using CO and OH beams to initiate surface reactions on a cold substrate. However, their experiments differ from ours. In the present work we hydrogenate CO:O_2 ices and OH radicals are produced in the ice through the O_2 + H channel. Therefore, our experiments give also hints on the interaction between different surface reaction channels. In chapter 8 we investigated experimentally the hydrogenation of the HO-CO complex, which presents three exit channels ($CO_2 + H_2$, HCOOH, H_2O + CO) with a branching ratio purely statistical as suggested by density functional theory models and in agreement with our experimental results (Goumans et al. 2008, Ioppolo et al. 2010a). In the present study the HO-CO complex itself is not observed in the ices under our experimental conditions, since it is efficiently dissociated to form CO_2. More details are reported in § 7.4. First, in § 7.2 and 7.3 the experimental method and data analysis are discussed.

7.2 Experimental details

The experiments are performed using an ultra high vacuum setup (SURFRESIDE), which consists of a main chamber (10^{-10} mbar) and an atomic beam line. Details are available in Chapters 2 and 4. The ice is grown on a gold coated copper substrate (12−300 K) that is mounted on the cold head of a close-cycle He cryostat. Deposition of selected $^{12}C^{16}O$:$^{16}O_2$ mixtures (4:1, 1:1 and 1:4) proceeds under an angle of 45° and with a rate of 0.7 ML min^{-1}. The interstellar solid CO:O_2 mixing ratio is observationally constrained to >1:1 (Pontoppidan et al. 2003). After deposition the ice mixture is exposed to a cold H-atom beam. H_2 molecules are dissociated into the capillary of a well-characterized thermal cracking source (Tschersich & von Bonin 1998, Tschersich 2000, Tschersich et al. 2008), which is used to hydrogenate the sample. A quartz pipe with a nose-shaped form is placed along the path of the dissociated beam to efficiently thermalize all H atoms to room temperature through surface collisions before they reach the ice sample. In this way, hot species (H; H_2) cannot reach the ice directly. Furthermore, the relatively high temperature of 300 K of the incident H atoms in our experiments does not affect the experimental results, since H atoms are thermally adjusted to the surface temperature as has been shown in Chapter 2. The final H-atom flux (2.5×10^{13} atoms cm^{-2} s^{-1}) is measured at the substrate position in the main chamber using a quadrupole mass spectrometer, following the procedure as described in the Appendix A of Chapter 4. The absolute error in the H-atom flux determination is within 50%. Ices are monitored by means of Reflection Absorption InfraRed Spectroscopy (RAIRS) using a Fourier Transform InfraRed spectrometer (FTIR), which covers the range between 4000 and 700 cm^{-1} (2.5−14 μm). A spectral resolution of 1 cm^{-1} is used and 128 scans are co-added. RAIR difference spectra (ΔA) relative to the initial unprocessed CO:O_2 ice are acquired every few minutes during H-atom exposure.

We performed a control experiment at 15 K in which a CO:O_2 ice is exposed to an H_2 molecular beam (*i.e.*, without H atoms) to show that the products detected in the hydrogenation experiments are formed on the surface and do not originate from background deposition. Only H_2O is detected in this experiment, which gives us an estimate for the background contamination, that is negligible. None of the other products are detected in this way. It should be noted that we use in the present experiments the same H-atom flux as used in Chapters 2 and 4. Therefore, the hydrogenation of our mixtures involves effectively a lower H-atom flux per (CO and O_2) channel.

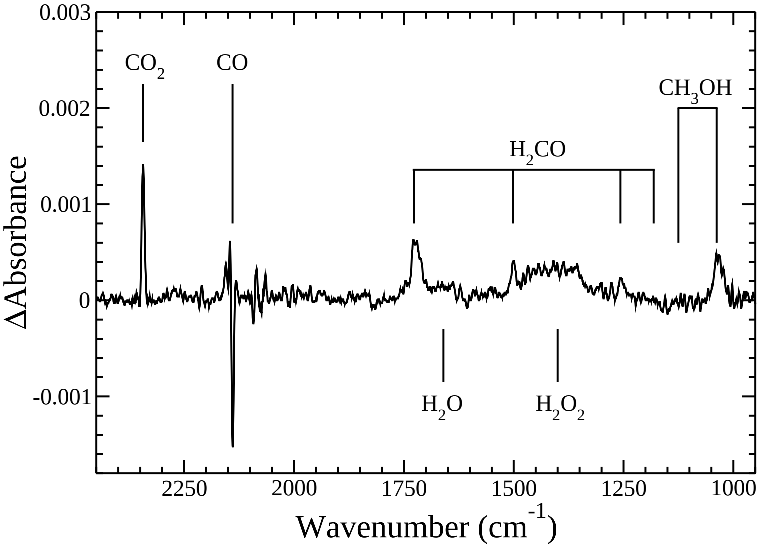

Figure 7.2 RAIR difference spectrum of the CO:O_2=1:4 ice, with respect to the spectrum before H-atom addition, at 15 K after a H-atom fluence of 1.3×10^{17} atoms cm^{-2}.

7.3 Data analysis

Figure 7.2 shows a RAIR difference spectrum of a CO:O_2 = 1:4 mixture acquired after a H-atom fluence (flux × time) of 1.3×10^{17} atoms cm^{-2}. The negative peak shown in Fig. 7.2 is caused by the CO use-up in surface reaction processes. O_2 is infrared in-active, and therefore cannot be observed in the infrared spectrum. All the final reaction products obtained from the hydrogenation of a pure CO ice (H_2CO and CH_3OH; *e.g.*, Watanabe et al. 2004, 2006a, Chapter 2) and a pure O_2 ice (H_2O and H_2O_2; *e.g.*, Miyauchi et al. 2008, Chapters 3 and 4) are present. Neither the intermediate species from the separate CO and O_2 channels, like HCO, H_3CO, HO_2, OH, and O_3, nor more complex species, like the stabilized HO-CO intermediate, HCOOH, and H_2CO_3[1], are observed. However, a new feature appears at ~2344 cm^{-1}, which belongs to the asymmetrical stretching mode of CO_2 ice. This molecule is formed in all our performed experiments at 15 and 20 K, with different CO:O_2 mixing ratios, but was not found in the previous CO + H or O_2 + H experiments.

The infrared spectra are reduced to obtain the column densities of the newly formed species. As a first step in the infrared data analysis, a straight baseline is subtracted from all spectra. Some absorption features, like the H_2O bending mode (~1650 cm^{-1}) and the H_2CO ν(C=O) stretching mode (~1720 cm^{-1}) suffer from spectral overlap. Here a multi-Gaussian fit is used to determine the area of the selected bands. Since the asymmetric 1440 cm^{-1} H_2O_2 band overlaps with the 1500 cm^{-1} H_2CO band, a spectrum of pure H_2O_2

---

[1] Solid H_2CO_3 is observed only in control experiments presented in Chapter 8.

ice is fitted in addition to a Gaussian to our infrared spectrum. The spectrum of solid H_2O_2 is obtained as discussed in Chapter 5, by co-depositing H atoms and O_2 molecules with a ratio of $H/O_2 = 20$ and subsequently heating the ice to a temperature higher than 30 K, which is just above the O_2 desorption temperature (Acharyya et al. 2007).

The column density N_X (molecules cm^{-2}) of species X in the ice is calculated using: $N_X = \int A(\nu)\mathrm{d}\nu / S_X$, where $A(\nu)$ is the wavelength dependent absorbance. Since literature values of transmission band strengths cannot be used in reflection measurements, an apparent absorption band strength, S_X of species X is determined by individual calibration experiments. These have been described in detail in Chapters 2, 4 and 5. Like for CO, CH_3OH and H_2O, an isothermal desorption experiment has been performed to determine the apparent absorption band strength of CO_2 by determining the transition from zeroth-order to first-order desorption. This is assumed to occur at the onset to the submonolayer regime and appears in the desorption curve as a sudden change in slope. Since pure H_2CO and H_2O_2 are experimentally difficult to deposit, because of their chemical instability, the values for S_{H_2CO} and $S_{H_2O_2}$ are obtained by assuming mass balance as reported in Chapters 2 and 5, respectively.

7.4 Results and discussion

7.4.1 Hydrogenation of O_2 molecules

Figure 7.3 shows the H_2O_2 (*top panels*) and H_2O (*bottom panels*) column densities as a function of the H-atom fluence for the three different mixing ratios ($CO:O_2$ = 4:1 *circles*, 1:1 *squares* and 1:4 *triangles*) and two temperatures investigated (15 K *left panels* and 20 K *right panels*). For comparison, results from the hydrogenation of pure O_2 ice (Chapter 4) are also plotted (*diamonds*). Note that the top-right panel has a different scale for the column density than the other three diagrams. Formation rate and final yield of H_2O_2 and H_2O for all the investigated mixtures are lower than those from the pure O_2 ice hydrogenation. The differences in the final yield are more evident at higher temperature, where the yield for the mixed ices only moderately increases, whereas it increases with several monolayers for the pure O_2 experiments. This cannot be explained only by a low effective H-atom flux for the O_2 channel. Hence, the presence of CO in the mixture influences the final results. In Chapter 2 we showed that H atoms can penetrate only a few layers of CO ice. Therefore, the presence of CO in the mixture most likely diminishes the penetration depth of H atoms into the ice compared to O_2 + H, and, therefore, desorption of H atoms from the ice can become important at higher temperatures. This explains the difference in the H_2O_2 and H_2O final yields compared to those from the pure O_2 ice, which increases with temperature.

The formation rates of H_2O and H_2O_2, which are reflected by the initial slopes of the curves, is also altered by the presence of CO in the ice. In the O_2-rich ice (1:4) the H_2O_2 column density shows the same behavior as seen in pure O_2 ices: a constant formation rate is followed by a sharp transition toward saturation (Chapter 4). For high concentration of CO in the ice, the H_2O_2 column density increases with a much lower rate and does not

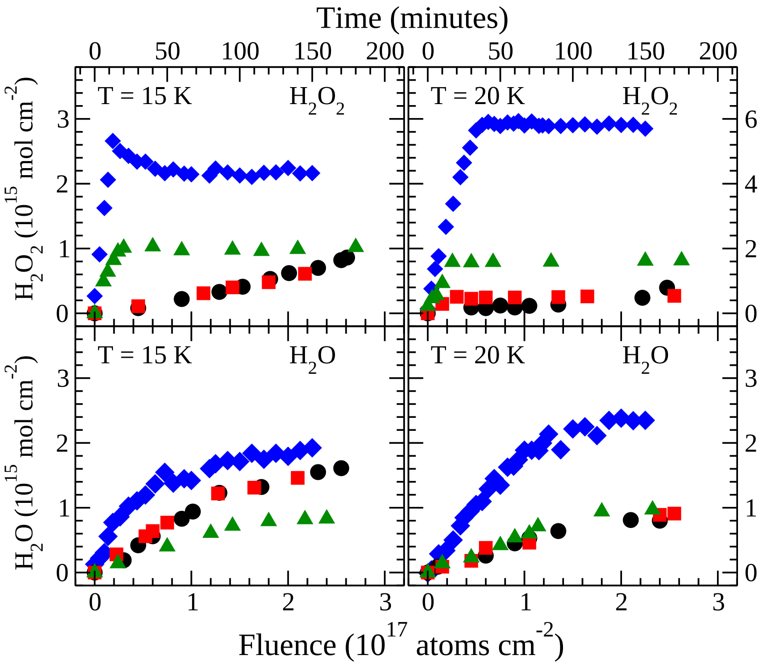

Figure 7.3 H_2O_2 (*top panels*) and H_2O (*bottom panels*) column densities as a function of the H-atom fluence and time of H-atom exposure at 15 K (*left panels*) and 20 K (*right panels*) for the three mixtures studied: CO:O_2 = 4:1 (*circle*), 1:1 (*square*), and 1:4 (*triangle*). For comparison, results from the hydrogenation of pure O_2 ice are plotted (*diamond*). Note different vertical scale for upper right panel.

appear to reach a steady state, even at the highest fluence. The H_2O_2 final yield increases with temperature, like for hydrogenation experiments of pure O_2 ice. The amount of H_2O_2 formed in the ice is inversely proportional to the amount of CO in the mixture, as expected.

In the case of CO-rich ice (4:1), a more efficient conversion of H_2O_2 ice into H_2O ice can explain the high H_2O final yield with respect to the O_2-rich ice experiment. In chapter 4 we showed that H_2O_2 is more effectively formed in the bulk of the ice (Chapter 4). However, the presence of CO in the ice limits the hydrogenation reactions to the surface of the ice. This means that a larger percentage of H_2O_2 formed at the surface of the ice is easily converted into H_2O. This may also explain the lower effective synthesis of H_2O_2 with the increase of the number of CO molecules in the ice. In addition, H_2O can be formed from OH radicals (see Fig. 7.1 and Chapter 5), which can also react to form CO_2 in our ices. The H_2O column density is constant through almost all our experiments. This is also the case for CO_2 as we will show in § 7.4.4 and indicative for a correlation between the formation channels of these two species.

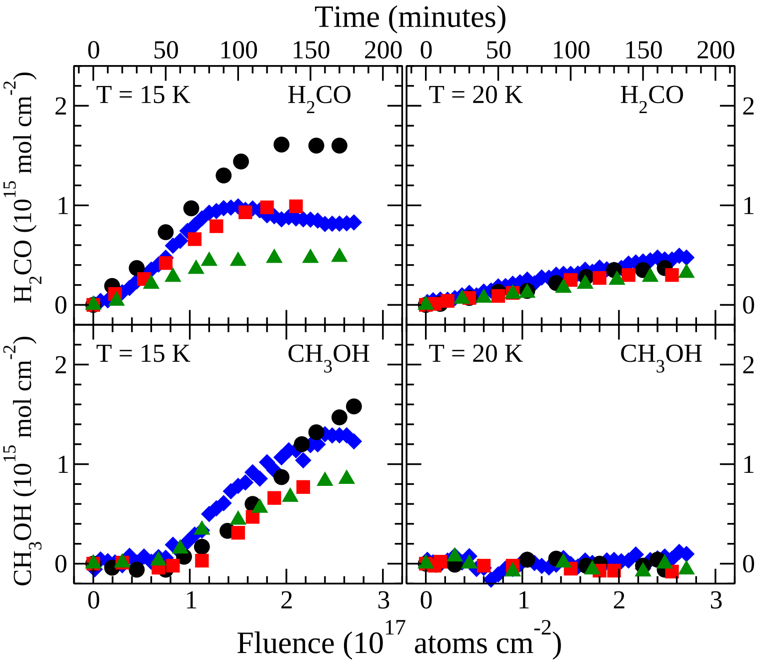

Figure 7.4 H_2CO (*top panels*) and CH_3OH (*bottom panels*) column densities as a function of the H-atom fluence and time of H-atom exposure at 15 K (*left panels*) and 20 K (*right panels*) for the three mixtures studied: CO:O_2 = 4:1 (*circle*), 1:1 (*square*), and 1:4 (*triangle*). For comparison, results from the hydrogenation of pure CO ice are plotted (*diamond*).

7.4.2 Hydrogenation of CO molecules

Figure 7.4 shows the H_2CO (*top panels*) and CH_3OH (*bottom panels*) column densities as a function of the H-atom fluence for the three different mixing ratios (CO:O_2 = 4:1 *circles*, 1:1 *squares* and 1:4 *triangles*) and two temperatures investigated (15 K left panels and 20 K right panels). For comparison, results from the hydrogenation of pure CO ice (Chapter 2) are also plotted (*diamonds*). For the hydrogenation of pure CO ice, the H-atom fluence is corrected according to recent H-atom flux measurements (Chapter 4), which improve the original H-atom flux estimation derived in Chapter 2. The hydrogenation of CO molecules in our mixtures shows the same behavior seen for pure CO ice in terms of temperature dependence (Chapter 2). An optimum in the final yield for H_2CO and CH_3OH is found at 15 K, while at 20 K no CH_3OH is formed and H_2CO has a low formation rate. The H_2CO and CH_3OH formation rates are hardly affected by the presence of O_2 in the ice (within the experimental uncertainties). The higher final yield for H_2CO and CH_3OH in the CO:O_2 = 4:1 experiment at 15 K compared to the pure CO ice cannot be explained by only a difference in the effective H-atom flux. In this case, the presence of O_2 in the ice, as a minor component, increases the penetration depth of H atoms in the ice compared to pure CO and, therefore, the probability that the H atoms get trapped and react in the ice. However, if the O_2 concentration is increased in the 15 K ice, the final yield decreases for both H_2CO and CH_3OH molecules. Clearly, the formation of H_2CO is more sensitive to the O_2 concentration in the ice than CH_3OH. As we saw for the hydrogenation of O_2 ice, the intermediate products (H_2O_2 and H_2CO respectively) are more efficiently converted in the final products (H_2O and CH_3OH, respectively), when the ices are mixed.

7.4.3 Competition between the CO and O_2 channel

The results presented in the former sections reflect the competition between the two channels CO vs. O_2, as shown in the left and right part of Fig. 7.1. It is clear from the experimental results that the presence of one component in the ice influences the reactivity of the other component. The formation rate of the CO hydrogenation reaction products is less affected by the presence of O_2 than the O_2 hydrogenation reaction products are affected by the presence of CO. This can be explained by the lower penetration depth of H atoms in CO ice and by the formation of CO_2 as an additional product, since OH radicals, formed through the O_2 channel, are used to yield CO_2 instead of H_2O and H_2O_2.

In a CO-rich environment at 15 K, the presence of O_2 molecules enhances the production of H_2CO and CH_3OH, since H atoms can penetrate deeper in the ice than in the pure CO ice experiment. However, the formation rate of the final products seems not to be affected by the presence of the O_2 molecules in the ice. Moreover, in a CO-rich ice the formation of H_2O_2 is limited by the small amount of O_2 molecules in the ice, by the amount of OH radicals used to form CO_2 and by the lower penetration depth of H atoms in the ice, caused by the presence of CO molecules. H_2O_2 ice is also more efficiently converted to H_2O on the surface of the ice. This explains the high final yield for H_2O in a CO-rich environment at 15 K.

In a O_2-rich environment at 15 K, the formation of H_2CO and CH_3OH is limited by the small amount of CO molecules, which limits the formation of H_2O_2 and H_2O, since the penetration depth of H-atoms is lower than in the pure O_2 ice experiment.

At 20 K, the CO channel is not efficient, although the H atoms penetrate deep in the ice; at this temperature H atoms prefer to react with O_2 molecules. Also in this case the final yields for H_2O_2 and H_2O are lower than those in the pure O_2 ice experiment.

7.4.4 Formation of solid CO_2

Figure 7.5 shows the CO_2 column density as a function of the H-atom fluence, confirming the CO_2 formation for the three different mixing ratios and two temperatures investigated. Neither the CO_2 formation rate nor its final yield depend significantly on either temperature or mixing ratio for the values studied here. Such a behavior is unexpected, since the

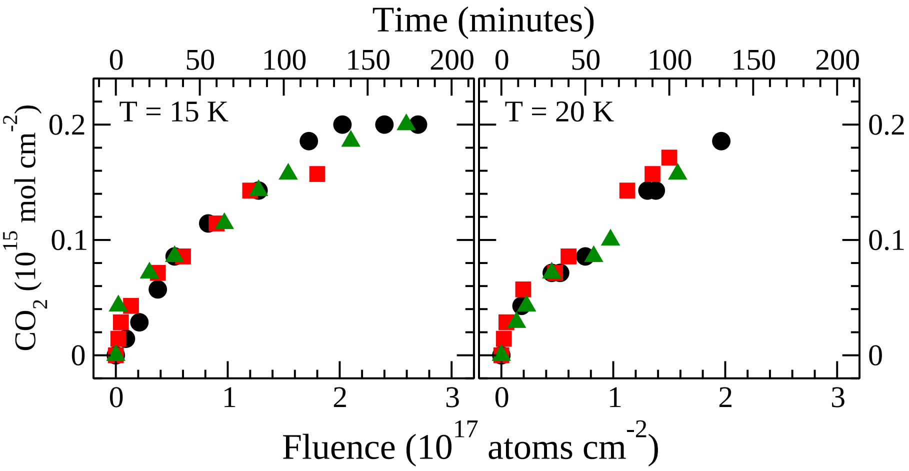

Figure 7.5 CO_2 column density as a function of the H-atom fluence and time of H-atom exposure at 15 K (*left*) and 20 K (*right*) for the three mixtures studied: CO:O_2 = 4:1 (*circle*), 1:1 (*square*), and 1:4 (*triangle*).

separate reaction routes CO + H and O_2 + H clearly depend on temperature, as shown in Chapters 2 and 4. The limiting factor for the CO_2 synthesis in our experiments is, therefore, the amount of ice that can be penetrated by H atoms, which is only a few monolayers. This is caused by the presence of CO molecules affecting the penetration depth of the H atoms in the ice (Chapter 2). Thus, the amount of CO_2 formed in all our experiments is always less than a monolayer. CO_2 subsequently does not contribute to further molecular synthesis in the ice upon ongoing hydrogenation. Bisschop et al. (2007b) showed experimentally that CO_2 does not react with H atoms and is a stable molecule under interstellar ice analogue conditions.

Figure 7.1 summarizes schematically the reaction network which leads to the formation of solid CO_2 starting from the combination of the CO + H and O_2 + H channels. Analyzing the species present in our ice after H-atom addition we can identify which reaction channel is most likely responsible for the formation of solid CO_2 ice. The hydrogenation of the HO-CO intermediate (*black arrow* in the center of Fig. 7.1) should not occur in our experiments, since HCOOH is not detected in the infrared spectra. Density functional calculations (Goumans et al. 2008), confirmed by our previous experimental results (Chapter 8), suggest that the final products from the hydrogenation of the HO-CO complex have a purely statistical branching ratio. Therefore, HCOOH should be detected in the ice as well if CO_2 would be produced through this route, and this is not the case.

The oxidation of solid CO (*dashed arrow*) is also not likely to be the main formation reaction channel, since O_3, which would indirectly prove the presence of abundant O atoms in the ice, is not observed. O_3 ice has been detected in pure O_2 hydrogenation experiments only for temperatures higher than 25 K, when the penetration depth of the H atoms is higher than a few monolayers and the O_2 molecules are most likely more mobile (Chapter 4). The hydrogenation of O_3 ice (Chapter 6) is therefore not considered here. Furthermore, Roser et al. (2001) tentatively observed CO_2 formation through this channel only during the warm up of the ice and when CO molecules and O atoms were covered by a thick layer of H_2O ice, which allows the reactants to remain trapped in the ice for $T > 100$ K. The CO + O reaction contributes at best at high temperatures. Reaction HCO + O (*dotted arrow*) should also be ruled out, since HCO radicals prefer to react in a barrierless manner with H atoms forming H_2CO rather than with O atoms, as shown in Chapter 2 and 8. Furthermore, O atoms are not abundant in our ices.

At low temperatures CO_2 is therefore formed through the direct dissociation of the HO-CO complex in the ice (*black arrow*). The HO-CO complex is efficiently dissociated and, therefore, is not detected in our infrared spectra as a stable species. In chapter 4 we observed this complex only in a water-rich environment. H-bonding should, indeed, improve coupling and heat dissipation through the ice, which stabilizes the HO-CO complex more easily in a polar environment than in an apolar one. Our ice is mainly composed of CO and O_2, with a polar component on the surface of the ice. The amount of the HO-CO intermediate stabilized in the polar ice is also under the detection limit. Therefore, in a water-poor ice the competition between dissociation and further hydrogenation of the HO-CO complex is in favor of the dissociation. H_2O is also formed through hydrogenation of the OH radicals. Hence, the formation of CO_2 is linked to the formation of H_2O in the ice. This is consistent with the presence of CO_2 in polar interstellar ice mantles.

7.5 Astrophysical implications

Recently, results from *Spitzer Space Telescope* observations (Whittet et al. 2007, Pontoppidan 2006, Pontoppidan et al. 2008) have shown that the formation of CO_2 in dark quiescent clouds occurs in two distinct phases. In the early stages, CO_2 forms together with H_2O on the surface of the interstellar dust grains, creating a polar ice mantle. A second phase in the CO_2 formation occurs during the heavy freeze-out of CO. During this second phase, a H_2O-poor ice is formed.

Our experimental results indeed make it likely that CO_2 and H_2O are formed together in the early stages of the clouds through surface reactions assuming that both CO and OH are present in sufficiently high abundances. H_2O ice forms from continued hydrogenation of OH radicals formed on the surface of the dust grains. Alternatively, OH radicals can react with nearby CO molecules, which are present in small amounts in the ice before the strong CO freeze-out phase, forming CO_2 ice through the direct dissociation of the HO-CO intermediate. CO_2 can be also formed at low temperatures through the hydrogenation of the HO-CO complex, which can lead to the formation of HCOOH and H_2O + CO as well as CO_2 + H_2. The concentration of CO in the ice with respect to H atoms determines the probability of OH to react with a CO molecule or with another H atom.

In the second stage, during the heavy CO freeze-out, the gas density is $>10^5$ cm^{-3} and the CO accretion rate could be as high as, or even higher than, the H-atom accretion rate, which makes CO more abundant on the surface than H atoms. OH radicals will therefore more likely react with a nearby CO molecule than with H atoms. CO_2 can thus be efficiently formed through the dissociation or further hydrogenation of the HO-CO complex, while just little H_2O ice formed.

Energetic processing (UV irradiation and cosmic ray-induced photons) of polar and apolar ices is also an efficient mechanism for CO_2 formation for specific environments (Hagen et al. 1979, Mennella et al. 2004, Mennella et al. 2006, Loeffler et al. 2005, Ioppolo et al. 2009). All these channels could contribute to the total CO_2 column density component observed in quiescent clouds.

The experiments presented here are designed to test a possible CO_2 formation route (thermal CO + OH) under interstellar ice analogue conditions rather than simulate a complete realistic interstellar ice evolution. Although our experiments do not exclude other possible CO_2 formation mechanisms, they show that the dissociation of the HO-CO complex is efficient and can contribute to explain the presence of CO_2 in polar and apolar interstellar ices at low temperatures in absence of UV irradiation.

7.6 Conclusions

The present laboratory study shows that the CO and O_2 channels influence each others final product yields, when CO and O_2 molecules are mixed and hydrogenated at low temperature (15 and 20 K). The formation rate for all the final products is found to be less sensitive on the mixture composition than the final yield. The penetration depth of the incoming H atoms is the main limiting factor. It depends on the composition of the ice and decreases when the amount of CO in the ice increases. Our results show that the formation rates found for H_2CO, CH_3OH, H_2O_2 and H_2O are similar within the experimental uncertainties to those found studying the isolated CO and O_2 hydrogenation channels corrected for the reduced effective H-atom fluxes. Therefore, the formation rates found in the isolated studies of the CO + H and O_2 + H channels are still valid for use in astrochemical models.

The formation of CO_2 from the reaction CO + OH is found here. CO_2 is efficiently formed under our laboratory conditions and no dependence on temperature or ice composition is found. The formation of CO_2 is linked to the formation of H_2O and, therefore, competes with the O_2 hydrogenation channel in our experiments. The competition of these two channels, together with the composition of the ice and the penetration depth of H atoms into the ice, explains the differences in the H_2O_2 and H_2O formation rate between our results and the hydrogenation of pure O_2 ice.

Figure 7.1 shows how the H_2O formation through the $O/O_2/O_3$ + H channels is linked to the CO_2 formation. Here we investigated only the O_2 + H channel, even though OH radicals can be efficiently formed on dust grains through all H_2O formation channels as well as through the photodissociation of H_2O and CH_3OH ice. Thus, our experimental result on the efficiency of the CO + OH channel at low temperature has important astrophysical implications on the formation of solid CO_2 in cold dense molecular clouds shielded from strong UV fields and are consistent with the observation of solid CO_2 in H_2O-rich environments.

CHAPTER 8

Surface formation of HCOOH at low temperature [1]

The production of formic acid (HCOOH) in cold and hot regions of the interstellar medium is not well understood. Recent gas-phase experiments and gas-grain models hint at a solid-state production process at low temperatures. Several surface reaction schemes have been proposed in the past decades, even though experimental evidence for their efficiency was largely lacking. The aim of this work is to give the first experimental evidence for an efficient solid-state reaction scheme providing a way to form HCOOH under astronomical conditions. Several surface reaction channels have been tested under fully controlled experimental conditions by using a state-of-the-art ultra high vacuum setup through co-deposition of H atoms and CO:O_2 mixtures with 4:1, 1:1 and 1:4 ratios. During deposition spectral changes in the ice are monitored by means of a Fourier Transform InfraRed (FTIR) spectrometer in Reflection Absorption InfraRed (RAIR) mode. After co-deposition a Temperature Programmed Desorption (TPD) experiment is performed and gas-phase molecules are detected by a Quadrupole Mass Spectrometer (QMS). Formation of HCOOH is observed at low temperatures mainly through hydrogenation of the HO-CO complex, while reactions with the HCO radical as intermediate are found to be inefficient. The HO-CO complex channel, which was previously not considered as an important HCOOH formation route, can explain the presence of HCOOH in dense cold clouds, at the beginning of the warm-up phase of a protostar, and, therefore, is likely to be astrochemically relevant.

---

[1] Based on: S. Ioppolo, H. M. Cuppen, E. F. van Dishoeck, H. Linnartz, 2010, accepted for publication in Monthly Notices of the Royal Astronomical Society

8.1 Introduction

Formic acid (HCOOH), the smallest organic acid, has been observed in the past decades toward high and low mass star forming regions and quiescent clouds in the gas phase (*e.g.*, Zuckerman et al. 1971, Winnewisser & Churchwell 1975, van Dishoeck et al. 1995, Gibb et al. 2000a, Ikeda et al. 2001, Liu et al. 2001, 2002, Requena-Torres et al. 2006, Bottinelli et al. 2007, Bisschop et al. 2007c), and likely also in the solid phase (*e.g.*, Schutte et al. 1998, 1999, Gibb et al. 2000b, 2004, Boogert et al. 2004, 2008, Knez et al. 2005).

Despite the detection of HCOOH in a variety of interstellar environments, its astrochemical origin is still unclear. Leung et al. (1984) discussed in their gas-phase model that HCOOH can be formed in dense interstellar clouds through the dissociative recombination of protonated formic acid ($HCOOH_2^+$), which forms by radiative association of HCO^+ and H_2O. Irvine et al. (1990) reported a detection of HCOOH in L134N with a relative abundance with respect to H_2 of 10^{-10}. They attributed the formation of HCOOH in this cold dark cloud to the ion-molecule gas-phase reaction $CH_4 + O_2^+$ followed by a dissociative recombination of protonated formic acid. According to Vigren et al. (2010), who combined a laboratory study and a gas-phase model, dissociative recombination of protonated formic acid is not as efficient as previously thought and the branching ratio of the channel leading to HCOOH has a maximum of only $\sim$13%. Therefore, they suggested that HCOOH is *predominantly* formed in dense interstellar clouds through surface reactions on grains, even though experimental evidence for the efficiency of surface reactions is largely lacking.

Several solid-phase reaction channels have been proposed in the past decades. Tielens & Hagen (1982) included in their astrochemical model the formation of solid HCOOH on grain surfaces through successive addition of H, O, and H to CO ice:

$$CO + H \rightarrow HCO \xrightarrow{O} HCO_2 \xrightarrow{H} HCOOH. \tag{8.1}$$

As suggested by Garrod et al. (2006), HCOOH could also be formed through the solid-state reaction:

$$HCO + OH \rightarrow HCOOH. \tag{8.2}$$

In a recent laboratory study, Öberg et al. (2009b) investigated, among others, reactions (8.1) and (8.2) experimentally by UV processing of CH_3OH-rich containing ices in which both HCO and OH are produced. However, only upper limits on HCOOH are found in this study. The alternative route of direct hydrogenation of solid CO_2 was tested by Bisschop et al. (2007b), who did not detect any HCOOH formation at low temperatures (below 15 K).

In this work an alternative formation route is studied in detail. Goumans et al. (2008) investigated the formation of CO_2 on a carbonaceous surface representing a model grain with density functional theory. According to their calculations the surface reaction CO + OH can yield a HO-CO complex, stabilised by intramolecular energy transfer to the surface. This intermediate can subsequently react, in a barrierless manner, with an H atom to form $CO_2 + H_2$, $H_2O + CO$ or HCOOH. Which of these three schemes is followed appeared to depend only on the orientation of the HO-CO intermediate and the incoming hydrogen atom. Therefore, the authors postulated that statistically about one third of the events will form HCOOH. We will experimentally focus on solid HCOOH formed through the latter route:

$$CO + OH \rightarrow HO\text{-}CO \xrightarrow{H} HCOOH. \qquad (8.3)$$

This chapter is organized according to the following experimental procedure. Starting from hydrogenation of simple molecules, like CO and O_2, we investigate efficiency and branching ratios of this surface reaction route. Simultaneous deposition (co-deposition) of H atoms and CO:O_2 mixtures with a selected ratio allows us to control the hydrogenation level and composition of the ice. Therefore, under our experimental conditions, radicals trapped in a CO:O_2 matrix are available for further reactions upon heating of the ice (§ 8.2). Infrared spectroscopy and mass spectrometry are combined to constrain the experimental results and to detect the formed and intermediate species (§ 8.3). Our experiments are not designed to simulate a realistic interstellar ice, but to test the above reactions. They provide information which can subsequently be included in astrochemical models of interstellar clouds. Specifically, we discuss the astrophysical importance of this reaction as an efficient channel for HCOOH formation at low temperatures (10 – 20 K) in the dense interstellar clouds (§ 8.4).

8.2 Experimental procedure

The experimental set-up (SURFRESIDE) has been described in detail elsewhere (Chapters 2 and 4). Here we give a brief description of the apparatus, focussing more on the experimental procedure. H atoms are deposited together with CO and O_2 molecules (co-deposition) on a gold coated copper substrate, placed in the centre of the ultra high vacuum main chamber (10^{-10} mbar). CO:O_2 mixtures with a ratio of 4:1, 1:1 and 1:4 are prepared in a high vacuum glass line, which comprises a liquid nitrogen trap to prevent water pollution. During the co-deposition the substrate is kept at a temperature of 15 K by a close-cycle He cryostat with a relative temperature precision of 0.5 K and an absolute accuracy better than 2 K. Deposition of the mixtures occurs under an angle of 45° with a flow of 5×10^{-8} mbar, while the H-atom beam is normal to the sample.

H atoms are supplied by a well-characterized thermal cracking source (Tschersich & von Bonin 1998, Tschersich 2000, Tschersich et al. 2008). H_2 molecules are cracked in a capillary pipe surrounded by a tungsten filament, which is heated to 2200 K. During the H-atom exposure, the pressure in the atomic line is kept constant at 1×10^{-6} mbar. Hot H atoms are cooled to room temperature via collisions by a nose-shaped quartz pipe, placed in the H-atom beam path. The geometry of the pipe is designed in such a way that each H atom has at least four collisions with the walls before leaving the pipe. In this way, hot species (H; H_2) cannot reach the ice directly. Furthermore, previous experiments with liquid nitrogen cooled atomic beams did not show any H/D-atom temperature dependence in hydrogenation reaction processes (*e.g.*, Watanabe et al. 2006a, Miyauchi et al. 2008, Oba et al. 2009). The final H-atom flux (2.5×10^{13} atoms cm^{-2} s^{-1}) is measured at the substrate position in the main chamber using a quadrupole mass spectrometer, as described in the Appendix A of Chapter 4. The absolute error in the H-atom flux determination is within 50%.

The ice is monitored by means of reflection absorption infrared spectroscopy, using a Fourier transform infrared spectrometer. The FTIR covers the range between 4000 and 700 cm^{-1} (2.5−14 μm) with a spectral resolution of 1 cm^{-1} and a co-addition of 128 scans. RAIR difference spectra (ΔA) with respect to the bare 15 K gold substrate spectrum are acquired every few minutes during the experiment. The QMS that monitors gas-phase species is placed behind the substrate and in line with the HABS. Following all our co-deposition experiments a temperature programmed desorption is performed by heating linearly the co-deposited ice to 200 K with a rate of 0.5 K min^{-1}. Each separate experiment is performed twice to link the RAIRS to the QMS data: during the first experiment the sample is kept in the IR optical line also during the TPD phase; in the second experiment the sample is turned 180° to face directly the QMS after co-deposition.

The main goal of this work is to improve our qualitative picture of possible reaction schemes and to search for an efficient HCOOH formation channel that may be responsible for the observed abundances of HCOOH in quiescent clouds. To enhance the detection of intermediates in the reaction schemes, we carry out a so-called co-deposited experiment in which hydrogenation occurs while the mixture is deposited. Moreover, since a beam of OH radicals and a H-dominated environment is difficult to produce, we use a mixture of CO with O_2, because hydrogenation of O_2 ice is known to lead to efficient OH production (Chapter 4 and 5). The ratio between H atoms and CO:O_2 mixtures during co-deposition at 15 K determines the hydrogenation grade in our experiments. We are interested in the CO and O_2 dominated regime, where full hydrogenation is not reached and radicals are trapped in the ice. Thus, the same H/[CO:O_2] = 2 ratio is applied to all the H and CO:O_2 co-deposition experiments, resulting in a deposited ice mainly consisting of CO and O_2 molecules. RAIRS and QMS results from the co-deposition experiments are compared to those from selected control experiments in order to give experimental evidence for the unambiguous solid HCOOH formation under our laboratory conditions. For this purpose, pure HCOOH and H_2CO ices and mixtures of H_2O:HCOOH and H_2O:H_2CO (10:1 and 3:1, respectively) are used as control experiments. The HCOOH containing ices are deposited at 30 K, while the H_2CO containing ices are formed *in situ* by hydrogenation of several thin layers (1 ML per step) of pure CO ice or H_2O:CO mixtures at 12 K. The hydrogenation is stopped once almost all the CO is converted into H_2CO ice: the H_2CO formation yield has reached its maximum at this point and only traces of CH_3OH ice are formed, as shown in Chapter 2.

8.3 Results and discussion

8.3.1 Formation of solid HCOOH

Figure 8.1 shows the normalized TPD curves obtained by the QMS with a rate of 0.5 K min^{-1} for the 46 amu (HCOOH) and 30 amu (H_2CO) mass signals from the H-atom

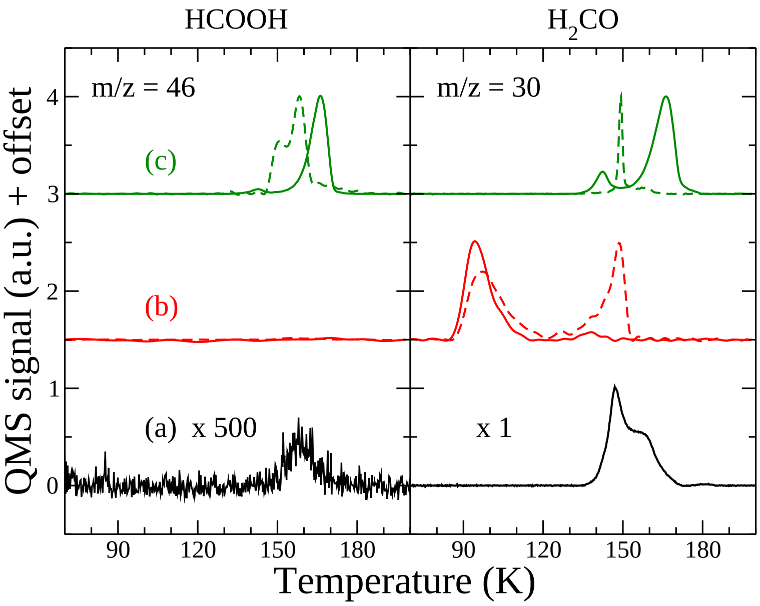

Figure 8.1 The 46 amu (HCOOH, *left column*) and 30 amu mass QMS signals (H_2CO, *right column*) from the TPD of a H-atom and $CO:O_2$ = 4:1 co-deposition experiment (a), compared to TPDs of the following experiments: solid H_2CO (b, *solid line*), $H_2O:H_2CO$ = 3:1 mixture (b, *dashed line*), and HCOOH ice (c, *solid line*), H_2O:HCOOH = 10:1 mixture (c, *dashed line*). Spectra are offset for clarity.

and $CO:O_2$ = 4:1 co-deposition experiment compared to the normalized and offset TPD curves of selected control experiments to prove unambiguously the formation of HCOOH ice. Mass 46 amu (*left column*) from the co-deposition experiment has a broad desorption peak at ~160 K in the TPD curve with a low signal to noise ratio, due to the weakness of this peak before normalization (Fig. 8.1a). Desorption of pure HCOOH occurs at 142 and 166 K under our experimental conditions (*solid line*, Fig. 8.1c), while HCOOH in H_2O desorbs together with H_2O between 150 and 160 K (*dashed line*, Fig. 8.1c). This is the desorption temperature range found in the co-deposition experiment for mass 46 amu (Fig. 8.1a). Similar TPD experiments using pure H_2CO ice (*solid line*, Fig. 8.1b) and H_2CO in H_2O ice (*dashed line*, Fig. 8.1b) reveal no desorption peaks for mass 46 amu. For this we conclude that the signal from mass 46 amu detected during the TPD of the co-deposition experiment corresponds to HCOOH desorption from a polar ice and that all detected HCOOH originates from surface reactions.

The 30 amu mass signal (*right column*) in the TPD curve from the co-deposition experiment presents a double peak at 147 and 160 K (Fig. 8.1a). Desorption of pure H_2CO occurs at 95 K (*solid line*, Fig. 8.1b), while H_2CO in H_2O desorbs at 97 and 148 K (*dashed line*, Fig. 8.1b), which is close to one of the desorption temperatures found in the co-deposition experiment (Fig. 8.1a). In a TPD experiment of pure HCOOH (*solid line*, Fig. 8.1c), the 30 amu mass signal is detected at the same temperature found for mass 46 amu, showing that HCOOH can be fragmented into H_2CO by the electron-emitting filament in the ionization chamber of the QMS. In the TPD curve of solid HCOOH in H_2O (*dashed line*, Fig. 8.1c), the 30 amu mass signal peaks at 148 K, which is the same desorption temperature of H_2CO in H_2O (*dashed line*, Fig. 8.1b). Hence, when HCOOH ice is diluted in H_2O, some of it is already dissociated in the solid phase to form H_2CO at high temperatures.

In conclusion, we find that HCOOH is formed in the solid phase for temperatures between the co-deposition of H atoms and $CO{:}O_2$ mixtures at 15 K and its desorption at $\sim$160 K. In the following sections we will use infrared data to constrain the temperature of HCOOH formation and its reaction pathway.

8.3.2 Formation temperature

As a first step in the infrared data analysis, a straight baseline is subtracted from all spectra. HCOOH ice presents several absorption features in the spectral range from $2000-1000$ cm^{-1}, among which ν(C=O) stretching mode at $\sim$1700 cm^{-1} is the strongest one. Shape and position of the HCOOH infrared spectral features are sensitive to temperature and ice composition as was shown by Bisschop et al. (2007a). In order to further investigate the temperature at which HCOOH ice is formed, we have compared the infrared spectra acquired during the TPD of the co-deposition experiments to selected laboratory spectra in the range between 1000 and 2000 cm^{-1}. We will start close to the HCOOH desorption temperature since the QMS recorded TPD results gave a positive identification of HCOOH there and we will then go down in temperature to detect the first occurrence of HCOOH. The top-left side of Fig. 8.2 shows the RAIR spectrum at 150 K of a H-atom and $CO{:}O_2$ = 4:1 co-deposition experiment. The broad 1720 cm^{-1} HCOOH stretching mode overlaps with the 1650 cm^{-1} H_2O bending mode. Solid H_2O_2 appears also in the investigated spectral range as a strong and broad absorption. The top-right side of Fig. 8.2 shows the zoom-in of the RAIR spectrum in the range between 1450 and 1850 cm^{-1}. In the same panel a broad component at 1720 cm^{-1} from the $HCOOH{:}H_2O$ = 1:10 mixture at 50 K is plotted (*dotted line* with an offset). This feature not only reproduces the band profile and peak position of the HCOOH stretching mode, but also indicates that HCOOH is mixed with H_2O in the ice at temperatures slightly below the HCOOH desorption temperature, confirming the mass spectrometry analysis presented in § 8.3.1. A $H_2CO{:}H_2O$=1:3 mixture spectrum at 50 K (*dashed line*) is also plotted to show how shape and position of H_2CO ν(C=O) stretching mode differ from the 1720 cm^{-1} spectral feature.

The bottom-left panel of Fig. 8.2 shows the infrared spectrum at 50 K of the same H-atom and $CO{:}O_2$ = 4:1 co-deposition experiment, while the bottom-right panel of Fig. 8.2 plots the zoom-in of the aforementioned spectrum and the 1740 cm^{-1} feature from a pure HCOOH ice at 30 K (*dotted line*), compared to a spectrum of pure H_2CO at 50 K (*dashed line*). The HCOOH feature present in our infrared spectrum at 50 K is narrow and shifted to higher wavenumbers with respect to the 1650 cm^{-1} H_2O bending mode. Again,

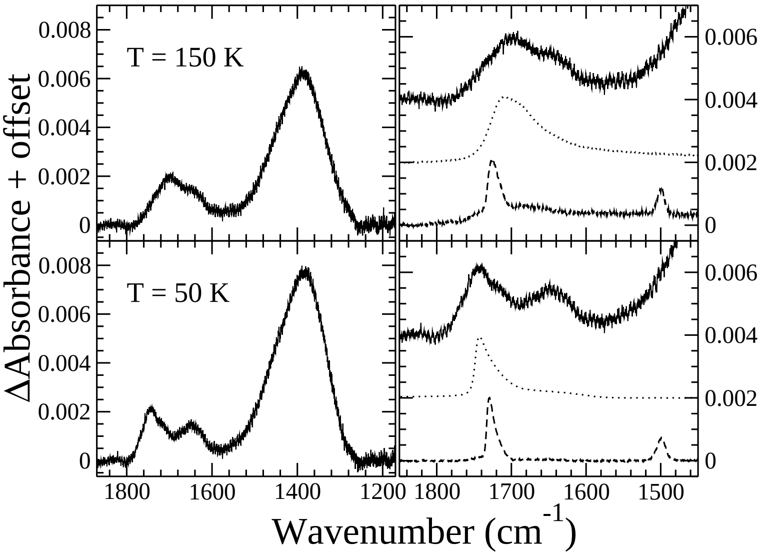

Figure 8.2 Infrared spectra at 150 K (*top panels*) and 50 K (*bottom panels*) from the H-atom and $CO:O_2$ = 4:1 co-deposition experiment (*solid lines*). The left side of the figure shows the spectra in the range between 1000 and 2000 cm^{-1}, while the right side shows a zoom-in of the 1700 cm^{-1} region. For comparison two spectra of mixed H_2O:HCOOH = 10:1 (*dotted line*) and $H_2O:H_2CO$ = 3:1 (*dashed line*) are shown in the top-right panel, and two spectra of pure HCOOH (*dotted line*) and H_2CO (*dashed line*) are plotted in the bottom-right panel. Spectra are offset for clarity.

shape and peak position are better reproduced by the HCOOH than by H_2CO, since the H_2CO band peaks at 1730 cm^{-1} and is more narrow than the HCOOH feature. This result indicates that HCOOH is present in the ice at 50 K and is most likely formed at lower temperatures. It is also less mixed with H_2O ice than at high temperatures. Hence, at high temperatures HCOOH molecules can better diffuse in the ice and get mixed with H_2O_2 and H_2O ice above 100 K, when H_2O ice starts restructuring.

Figure 8.3a shows the infrared spectrum of the ice after co-deposition of H atoms and $CO:O_2$ = 4:1 at 15 K, when the ice is hydrogenated but not yet heated. At this stage of the experiment the HCOOH stretching mode is around our detection limit and a feature at 1815 cm^{-1} is detected. The identification of this feature will be discussed in § 8.3.3. The first clear detection of solid HCOOH in the $CO:O_2$ = 4:1 experiment is shown in Fig. 8.3b at ~30 K, when CO and O_2 are not completely desorbed yet from the ice (Öberg et al. 2005, Acharyya et al. 2007). At this temperature the 1815 cm^{-1} intensity decreases and the band broadens and shifts to 1820 cm^{-1}, while the HCOOH stretching mode appears at ~1750 cm^{-1}. The HCOOH peak position and band shape are in agreement with those from a CO:HCOOH = 100:1 mixture shown in Fig. 8.3c. Solid HCOOH is detected at 15 K in the co-deposition experiments of H atoms and $CO:O_2$ = 1:1, and 1:4

(spectra not shown). However, the feature at 1815 cm^{-1} is detected only in the H-atom and CO:O_2 = 1:1 co-deposition experiment, where an increase of the HCOOH stretching mode is observed at 30 K, in agreement with the results from the CO:O_2 = 4:1 mixture shown in Fig. 8.3. In the case of the CO:O_2 = 1:4 mixture we do not observe the feature at 1815 cm^{-1} at 15 K and the increase of the HCOOH stretching mode at 30 K. Thus, the 1815 cm^{-1} feature requires the presence of CO in the mixture. Fig. 8.3d and e will be discussed in the next section.

As the previous discussion showed, the HCOOH feature changes strongly in shape and position as a function of temperature. This is generally true for the entire spectrum. Figure 8.4 shows this clear temperature dependence in the morphology of the ice in a CO:O_2 = 4:1 co-deposition experiment after an H-atom fluence of 2.7×10^{17} atoms cm^{-2}. In a CO- and O_2-*rich* environment, like the ice at 15 K of our co-deposition experiments, the H_2O_2 and H_2O infrared bands are present in both hydrophobic and hydrophilic contributions (monomer and bulk, respectively; see Fig. 8.4a. For feature assignments see Chapter 5 and references therein). By increasing the temperature of the sample, the amount of hydrophobic material decreases and the H_2O_2 and H_2O bands broaden and shift. Thus, the 50 K infrared spectrum presents several broad bulk features originating from species like H_2O_2, H_2O, and bands due to CO_2, HCOOH and traces of CO, still trapped in the mixture (Fig. 8.4b). In the 150 K spectrum (Fig. 8.4c) the CO stretching mode has disappeared, traces of solid CO_2 are present in the ice, since a very weak stretching mode band is still visible, and the HCOOH 1740 cm^{-1} feature has broadened and shifted towards lower wavenumbers (1700 cm^{-1}), overlapping with the 1650 cm^{-1} H_2O bending mode. The HCOOH feature decreases in the RAIR spectra at the same temperature where the signal of mass 46 amu increases in the mass spectrometer (~160 K; see Fig. 8.1a).

In conclusion, the results presented here show that HCOOH ice is formed during co-deposition experiments at low temperature (~15 K) and that its formation increases at a temperature close to the desorption temperature of volatile species like CO, O_2, when radicals produced by the hydrogenation of the ice are more mobile (~30 K). In the next section we describe the possible reaction mechanism.

8.3.3 Possible reaction pathways

Infrared spectroscopy is used to identify the possible reaction intermediates: HCO according to reactions (8.1) and (8.2) or HO-CO according to reaction (8.3).

As mentioned in § 8.2, the deposited ice mainly consists of CO and O_2 molecules. This is reflected by the saturated CO stretching band mode present in Fig. 8.4a and a very weak O_2 absorption band peaking at 1550 cm^{-1} (the presence of O_2 in the ice causes also distortions in the infrared spectrum, as discussed in Chapter 5). The infrared spectrum at 15 K presents a forest of bands in absorption due to newly formed species upon hydrogenation of O_2 ice, like H_2O_2, H_2O, HO_2, OH (see Chapter 5). CO ice is not hydrogenated in our experiments, since neither HCO, H_2CO nor CH_3OH features appear in the RAIR spectra at 15 K (Fig. 8.4a). This is consistent with a previous conclusion that

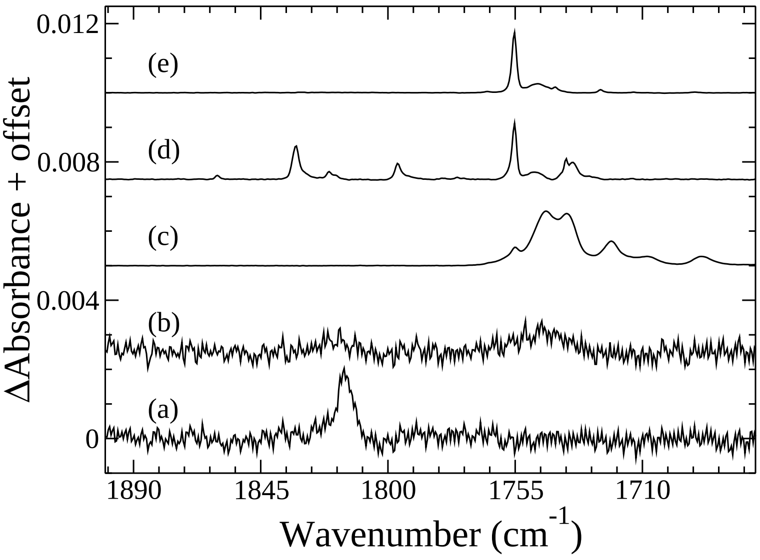

Figure 8.3 Infrared spectra from a H-atom and CO:O_2 = 4:1 co-deposition experiment at 15 K (a), and 30 K (b) compared to a spectrum of CO:HCOOH = 100:1 at 15 K (c), a spectrum from a CO:O_2 = 100:1 co-deposition experiment at 15 K (d), and a spectrum of CO:HCOOH = 1000:1 at 15 K (e) using higher H-atom flux (2 × 10^{14} cm^{-2} s^{-1}) and CO:O_2 flow (1 × 10^{14} cm^{-2} s^{-1}). Spectra are offset for clarity.

CO + H is less efficient than O_2 + H (Chapter 2, 4 and 5). Therefore, since HCO and H_2CO never form in the other co-deposition experiments, reactions (8.1) and (8.2), with HCO as intermediate, are likely not to take place during our co-deposition experiments.

We performed a control co-deposition experiment, using higher H-atom flux (2 × 10^{14} cm^{-2} s^{-1}) and higher CO:O_2 = 100:1 deposition rate (~1×10^{14} cm^{-2} s^{-1}), with the intention to give an assignment to the low temperature 1815 cm^{-1} feature. This experiment allows to observe more reactions products, but with similar matrix properties to the other co-deposition experiments. During this control experiment several species, like OH, HO_2, H_2O, H_2O_2, O_3, CO_2, CO_3, HO-CO, HCOOH, HCO, H_2CO are formed in the ice at 15 K. Table 1 lists the assignments of the features present in the spectral region between 1700 and 1900 cm^{-1}, also shown in Fig. 8.3d. The band position and shape of solid HCOOH formed at low temperature in the control experiment corresponds to the HCOOH feature in a CO matrix (CO:HCOOH = 1000:1) as shown in Fig. 8.3e. The *cis* and *trans*-HO-CO complexes appear in the control experiment spectrum in both environments: polar (in H_2O matrix at 1775 and 1820 cm^{-1}, respectively) and apolar ice (in CO matrix at 1796 and 1833 cm^{-1}, respectively). The peak at 1815 cm^{-1} is detected in our standard co-deposition experiments and can now be assigned by comparison with the control experiment results to the stabilized *trans*-HO-CO complex in a polar environment. The *cis*-HO-CO complex absorption strength, which is normally weaker than that

Table 8.1 Assigned infrared features with their corresponding reference in the range between 1700-1900 cm^{-1} as found in a control co-deposition experiment.

Species	Position (cm^{-1})	Reference	Matrix
HCO	1860	Milligan & Jacox (1964)	Ar
trans-HO-CO	1833	Milligan & Jacox (1971)	CO
trans-HO-CO	1820	Zheng & Kaiser (2007)	H_2O
cis-HO-CO	1796	Milligan & Jacox (1971)	CO
cis-HO-CO	1775	Zheng & Kaiser (2007)	H_2O
HCOOH	1755	this work	CO
HCOOH	1748	this work	CO
H_2CO	1737	Nelander (1980)	N_2
H_2CO	1734	Nelander (1980)	N_2

from the *trans*-HO-CO, is around the detection limit.

Solid HCOOH is therefore most likely formed through reaction (8.3), which can also lead to the formation of CO_2 + H_2 and H_2O + CO (Goumans et al. 2008). The presence of CO_2 ice and the stabilized *trans*-HO-CO complex at 1815 cm^{-1} (Fig. 8.4), suggests indeed that CO ice can react with OH-bearing species produced by hydrogenation of O_2 ice, since this bond is only present after hydrogenation of CO and O_2 containing ices. As previously discussed, the HO-CO complex is only detected in a water-*rich* environment. However, our ice is mainly composed of CO and O_2, with traces of other polar species. Therefore, we would expect to detect the HO-CO complex also in a water-*poor* environment. Moreover, the amount of solid HCOOH detected at 15 K is close to the detection limit for all the mixtures investigated, while CO_2 is on average 10 times more abundant than HCOOH in the ice at low temperature. These experimental results suggest that the HO-CO complex formed in a CO and O_2 matrix is mainly used to form CO_2 by direct dissociation of the complex, and only a small fraction of CO_2 comes from reaction (8.3) at 15 K. Furthermore, the HO-CO complex appears to be stabilized and shielded from hydrogenation in a water-*rich* environment at low temperatures. It is indeed likely that H-bonding improves coupling and heat dissipation through the ice, which would stabilize the HO-CO complex more easily in a water-*rich* environment than in a CO and O_2 ice (T. P. M. Goumans, private communication). The HO-CO intermediate formed in a polar ice is then available again to react at higher temperatures, when it is more mobile and hydrogen can still be present in the ice. In our experiments also solid H_2CO_3 can be formed from the same HO-CO complex through the reaction:

$$\mathrm{CO + OH \rightarrow HO\text{-}CO \xrightarrow{OH} H_2CO_3}, \qquad (8.4)$$

as shown by Oba et al. Oba et al. (2010). Moreover, reaction (8.4) can also lead to the formation of CO_2 + H_2O and H_2O_2 + CO. At temperatures below 100 K the HCOOH ν(C=O) stretching mode overlaps with the H_2CO_3 one, hindering a spectral assignment of solid H_2CO_3 in the infrared spectra. However, the different desorption temperatures of these molecules allows an identification, since HCOOH desorbs at ~160 K and H_2CO_3 at ~250 K.

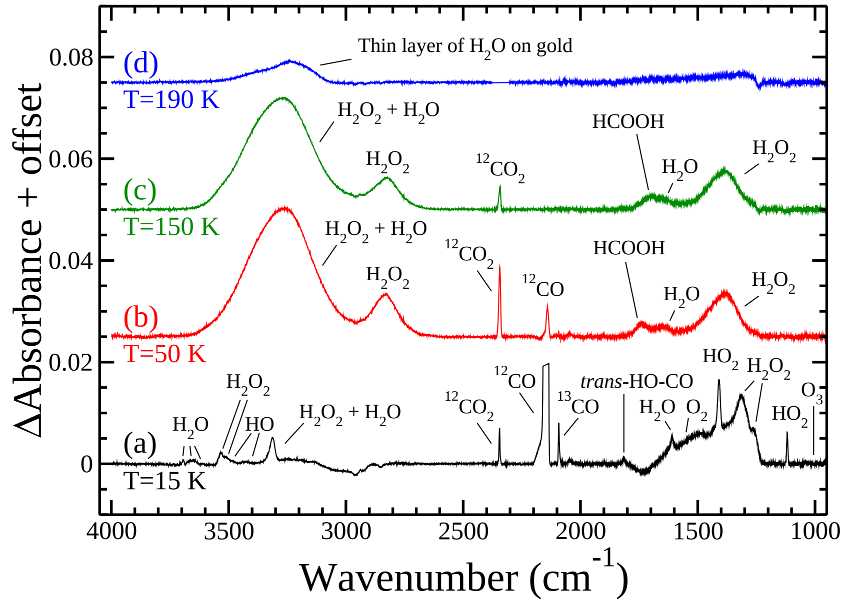

Figure 8.4 The 15 K (a), 50 K (b), 150 K (c), and 190 K (d) infrared spectra of the H-atom and CO:O_2 = 4:1 co-deposition experiment after an H-atom fluence of 2.7×10^{17} atoms cm^{-2}. Spectra are offset for clarity.

Figure 8.4d shows the 190 K RAIR spectrum from the co-deposition experiment, in which all the absorption bands have disappeared. Distortions at low wavenumbers in the difference RAIR baseline spectrum are caused by the high temperature of the gold substrate. This result excludes the presence of formed solid H_2CO_3 in the ice in our co-deposition experiments, since H_2CO_3 desorbs at temperatures above 220 K (*e.g.*, Zheng & Kaiser 2007) and should therefore still be present at 190 K.

Oba et al. (2010) studied the formation of solid CO_2 through surface reactions between carbon monoxide and non-energetic OH radicals, produced by dissociating H_2O molecules in microwave-induced plasma. According to their results H_2CO_3 was formed through reaction (8.4), but no HCOOH was detected. The difference in the experimental results between Oba et al. (2010) and this work can be found in a different flux composition. In their case, H_2O is dissociated and a combination of OH radicals and H atoms gives the final flux, most likely one to one. In the present work we use an H-atom flux. The OH radicals present in the ice are formed via surface reactions. Hence, the HO-CO complex has a higher probability to find and react with a H atom instead of a OH radical, which is less abundant in the ice.

8.3.4 Branching ratio of reaction HO-CO + H

As shown in the previous sections, solid CO_2 and H_2O, which are also observed in our infrared spectra, can be formed together with HCOOH by reaction HO-CO + H (Goumans et al. 2008). However, the determination of the branching ratios for this reaction is not straightforward, since CO_2 can also be formed during co-deposition by direct dissociation of the complex HO-CO (Oba et al. 2010), and H_2O through hydrogenation of molecular oxygen (Miyauchi et al. 2008, Ioppolo et al. 2008, Oba et al. 2009, Ioppolo et al. 2010, Cuppen et al. 2010). Here we make an attempt to estimate the branching ratios of reaction HO-CO + H at higher temperatures, when the other reaction routes to form CO_2 and H_2O are less efficient. At 50 K the three reaction products are all formed but have not yet desorbed from the ice. In order to calculate the branching ratios based on our experimental results, we assume that:

1. solid HCOOH is formed only through reaction (8.3);
2. the CO_2 formed at 15 K comes mainly through direct dissociation of the complex HO-CO in a water-*poor* environment and, therefore, is subtracted to the CO_2 column density obtained at 50 K;
3. H_2O can be formed through hydrogenation of O_2 and, therefore, the contribution of this channel is estimated by comparing the results presented here to those from a similar experiment ($H/O_2 = 10$) shown in Chapter 5 and then subtracted to the H_2O column density obtained in our 50 K spectrum.

Since literature values of transmission band strengths cannot be used directly in reflectance measurements, an apparent absorption strength of HCOOH, CO_2, and H_2O is calculated from calibration experiments. The determination of this apparent absorption strength is set-up specific. The calibration method is described in Chapter 2 and 4.

The values for the branching ratios obtained here after subtracting the contributions from other possible reaction channels are in agreement with those presented by Goumans et al. (2008), who suggested that the branching ratio is purely statistical:

$$\mathrm{CO + OH} \xrightarrow{\mathrm{H}} \begin{cases} \mathrm{HCOOH} & k \\ \mathrm{CO_2 + H_2} & (0.7\pm0.3)k \\ \mathrm{H_2O + CO} & \leq k, \end{cases} \tag{8.5}$$

where k is the branching ratio of the channel leading to HCOOH. We conclude from the 50 K infrared spectrum that the amount of solid HCOOH and CO_2 formed in our standard H-atom and $CO:O_2 = 4:1$ co-deposition experiment is ~1±0.1 ML, while the amount of H_2O is roughly the same as that produced after the same H-atom fluence in the H-atom and O_2 co-deposition experiment ($H/O_2 = 10$) shown in Chapter 5 (~10±1 ML). Therefore, H_2O ice is mainly formed through hydrogenation of O_2 and the amount of H_2O formed through reaction HO-CO + H could be equal to that of CO_2 and HCOOH within the experimental uncertainties. Results using the $CO:O_2 = 1:1$ and 1:4 mixtures confirmed the branching ratio values shown above.

8.4 Astrophysical implications

The origin of the observed HCOOH in the interstellar medium has been unclear. Both gas-phase reactions and grain-surface processes have been suggested for producing the HCOOH column densities observed in star forming regions. Results from a two-stage hot-core gas-grain chemical model (stage 1: collapse; stage 2: warm-up phase) proposed by Garrod et al. (2006) suggested that HCOOH is mainly formed in the gas phase during the warm-up phase. According to the authors, at early times of the warm-up, HCOOH is most likely formed in the gas phase through the dissociative recombination of protonated formic acid, which forms by radiative association of HCO^+ and H_2O or by reaction $CH_4 + O_2^+$. However, as mentioned in the introduction, recent gas-phase laboratory experiments showed that the dissociative recombination channel is less efficient than considered before. In the case of L134N for instance, it is found to be 8 times less efficient than in models using the latest release of the UMIST database for astrochemistry (Woodall et al. 2007), and a factor of 4 less than the observed value. Hence, the observed HCOOH abundances in cold regions cannot be explained by gas-phase reactions only, and, therefore, surface reactions should be taken into account for the formation of HCOOH, even at low temperatures. Especially, since solid HCOOH may be destroyed by energetic processing or in reaction with NH_3 to lead to $HCOO^-$ and NH_4^+ (*e.g.*, Hudson & Moore 1999, Schutte et al. 1999). HCOOH ice was shown in the laboratory to be stable against further hydrogenation (Bisschop et al. 2007b).

The model used by Garrod et al. (2006) includes only surface reaction (8.2). At low temperatures, the formation of formaldehyde and methanol through subsequent hydrogenation of solid CO (Chapter 2) is favored over the formation of HCOOH through reaction (8.2). We can roughly estimate the efficiency of reaction (8.2) at low temperatures considering the abundance of H atoms and OH radicals over CO molecules at the end of the cloud collapse phase. If we assume that one H_2O molecule is formed on the grain surface from one OH radical, which gives a ratio one-to-one between H_2O and OH, CO ice is 4 times less abundant on average in dense regions than OH radicals (*e.g.*, Gibb et al. 2004). However, H atoms are orders of magnitude more abundant than OH radicals in this environment and H atoms are more mobile on the surface. Therefore, the probability that an HCO radical finds an OH to react with before it is hydrogenated is almost negligible. Garrod et al. (2006) found an optimum in HCOOH formation through reaction (8.2) at ~40 K, when H_2CO resides in the gas phase, but can also accrete again on the grains and re-evaporate quickly. This allows for reaction with OH radicals in the solid phase to form HCO available for reaction (8.2). However, grain-surface reaction (8.2) was never considered as a dominant process in their model during the warm-up phase, since HCOOH can still be formed in the gas phase at these temperatures (>40 K) through the reaction $OH + H_2CO$.

The experiments presented here are designed to test the possible reaction channels and not necessarily to simulate a realistic interstellar ice. In particular, they show a low efficiency of reaction (8.2) under our laboratory conditions, and even though we do not exclude that reactions (8.1) and (8.2) can occur under interstellar conditions, our experiments show unambiguously the formation of HCOOH through reaction (8.3) in the solid phase at low temperatures, giving roughly the same branching ratio for the final reaction products (HCOOH, CO_2 + H_2 and H_2O + CO). These results are in agreement with density functional theory models, which suggest that there could be equal branching ratio between the three possible channels. Under interstellar conditions, the HO-CO complex is expected to be even more stabilized in the H_2O-*rich* ices, than in our apolar laboratory analogues. Furthermore, the HO-CO complex channel should be considered an important HCOOH formation route, since it could explain the presence of HCOOH in dense molecular clouds and at the beginning of the warm-up phase of the protostar in low and high mass star forming regions.

CHAPTER 9

Formation of interstellar solid CO_2 after energetic processing of icy grain mantles[1]

Space infrared observations with ISO-SWS and Spitzer telescopes have clearly shown that solid carbon dioxide (CO_2) is ubiquitous and abundant along the line of sight to quiescent clouds and star forming regions. Due to the CO_2 low gas-phase abundance, it is suggested that CO_2 is synthesized on grains after energetic processing of icy mantles and/or surface reactions. We study quantitatively the abundance of carbon dioxide synthesized from ice mixtures of astrophysical relevance induced by ion irradiation at low temperature. We compare the CO_2 stretching and bending-mode band profiles observed towards some young stellar objects (YSOs) for which infrared spectra exist. Using a high vacuum experimental setup, the effects induced by fast ions (30−200 keV) on several ice mixtures of astrophysical interest are investigated. Chemical and structural modifications of the ice samples that form new molecular species are analyzed using infrared spectroscopy. The formation cross section of solid CO_2 is estimated from the increase in column density as a function of the dose fitting of experimental data with an exponential curve. Our laboratory experiments showed that carbon dioxide is formed after irradiation of ice mixtures containing C- and O- bearing molecules. Furthermore, when the same amount of energy is released into the icy sample, a larger amount of CO_2 is formed in H_2O-rich mixtures in agreement with previous studies. We also found that the CO_2 stretching and bending mode band profiles depend on the mixture and temperature of the ice sample. We found that the amount of carbon dioxide formed after ion irradiation can account for the observed carbon dioxide towards YSOs. Furthermore, we discovered that laboratory spectra are a good spectroscopic analogue of the interstellar features. Even if the comparison between laboratory and observed spectra presented here cannot be considered unique and complete, our results quantitatively support the hypothesis that interstellar solid CO_2 forms after ion irradiation and UV photolysis of icy mantles.

---

[1] Based on: S. Ioppolo, M. E. Palumbo, G. A. Baratta, V. Mennella, 2009, Astronomy & Astrophysics, volume 493, pages 1017-1028

9.1 Introduction

An unanswered question concerning the astrophysics of the interstellar medium is the origin of solid CO_2 observed along the line of sight to embedded young stellar objects (YSOs) and field stars obscured by dense molecular clouds. Solid CO_2 absorption bands are detected in those regions by the *Infrared Space Observatory* (*ISO*; *e.g.*, Gerakines et al. 1999, Gibb et al. 2004, Nummelin et al. 2001) and by the *Spitzer Space Telescope* (*e.g.*, Boogert et al. 2004, Pontoppidan et al. 2005, 2008, Whittet et al. 2007). Since there is a small abundance of gas phase CO_2 in the interstellar medium, about a factor of 100 less than in the solid state (van Dishoeck et al. 1996, Boonman et al. 2003), which is in agreement with chemical models that predict low CO_2 production efficiency by gas phase reactions (Bergin et al. 1995), it is generally assumed that this molecule is synthesized onto grains. Solid CO_2 could be produced in-situ by means of surface reactions (*e.g.*, Tielens & Hagen 1982, Stantcheva & Herbst 2004, Fraser & van Dishoeck 2004), although this chemical pathway remains controversial. The reaction $CO + O \rightarrow CO_2$ was found to have a prohibitively high barrier in at least one study (Grim & D'Hendecourt 1986), while, according to Roser et al. (2001), it proceeds with a small barrier or even barrierless. Extensive laboratory studies of these surface reaction schemes are required. Energetic processing such as UV and ion irradiation of ices containing C- and O- bearing molecules is another possible formation mechanism. Laboratory experiments demonstrated that CO_2 is formed after energetic processing of pure CO ice and icy mixtures containing CO and H_2O (*e.g.*, D'Hendecourt & Allamandola 1986, Moore et al. 1991, Gerakines et al. 1996, Ehrenfreund et al. 1997, Palumbo et al. 1998, Watanabe & Kouchi 2002, Loeffler et al. 2005). Interstellar grains are being continuously exposed to energetic processes such as cosmic ion irradiation and UV photolysis. Fast ions passing through molecular solids release their energy into the target material. As a consequence, many molecular bonds are broken along the ion-track and, in a short time (less than one picosec), and the molecular fragments recombine to produce a rearrangement of the chemical structure that leads to the formation of new molecular species. In the case of UV photolysis, the energy is released into the target material by a single photodissociation or photoexcitation event. In this particular case, new molecular species are also formed (Strazzulla & Palumbo 2001, Palumbo 2005). Mennella et al. (2004), Mennella et al. (2006) suggested that in cold dark clouds, solid CO and CO_2 can be formed by energetic processing of carbon grains with a water ice cap, and they quantitatively evaluated the amount of CO and CO_2 formed. In this scenario, polar CO_2 would be produced mainly on carbon grains when water ice mantles are formed and nonpolar CO_2 would be formed when freeze-out of gas-phase CO takes place. These results represent a different chemical pathway with respect to the grain-surface reaction routes proposed by Bergin et al. (2005). Both mechanisms could contribute to the total solid CO_2 column density detected along the line of sight to dense clouds. Nevertheless, a comprehensive quantitative analysis of the amount of CO_2 formed after irradiation of ice mixtures and a direct comparison with observations is still lacking.

We present results of a quantitative analysis of the CO_2 abundance synthesized by ion irradiation of several ice mixtures at low temperature. In particular, we studied ice mixtures containing carbon monoxide, and ice mixtures that do not contain carbon monoxide but comprise C- and O- bearing molecules. These data and those obtained by Mennella et al. (2004), Mennella et al. (2006) are used to fit the CO_2 stretching and bending-mode band profiles observed towards some YSOs. The fits presented here support quantitatively the hypothesis that the formation of interstellar solid CO_2 after energetic processing of icy mantles is an efficient mechanism.

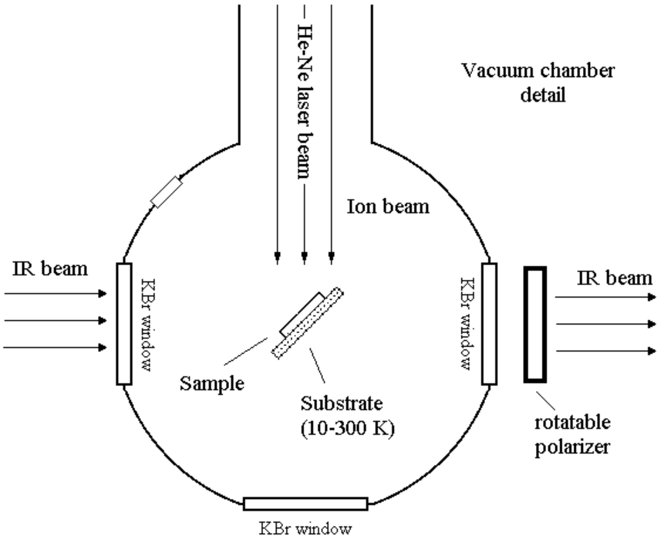

Figure 9.1 Schematic top view of the vacuum chamber.

9.2 Experimental procedure

The experiments are conducted at the Laboratory for Experimental Astrophysics, INAF-Catania Astrophysical Observatory (Italy). A schematic view of the experimental apparatus is shown in Fig. 9.1. Experiments are carried out in a stainless steel vacuum chamber with base pressure of about 10^{-7} mbar. Inside the vacuum chamber, a crystalline silicon (or KBr) substrate is placed in thermal contact with a cold finger, whose temperature can be varied within the 10−300 K range. A needle valve is used to admit pure gases (or mixtures) into the chamber, where they freeze onto the substrate. Ices are monitored using an FTIR spectrometer (Bruker Equinox 55) at a resolution of 1 cm^{-1}. A He-Ne laser is used to monitor the thickness of the icy film during deposition. The vacuum chamber is connected to an ion implanter (200 kV; Danfysik) from which ions of energy up to 200 keV (400 keV for double ionizations) can be obtained. The ion beam produces a spot on the target larger than the area probed by the IR beam. Current densities range from 100 nA cm^{-2} up to a few μA cm^{-2}. In this set-up, IR spectra can be obtained before and after ion irradiation without tilting the sample. The icy samples studied are deposited and irradiated at 12−16 K. Spectra are acquired before and after irradiation at low temperature and after warm-up at higher temperatures up to 80−90 K. A different procedure is used for only one pure CO deposit. In this case, the sample is grown and is irradiated at 16 K. It is then heated to 70 K and irradiated. It is subsequently cooled to 16 K and irradiated again. This enabled us to study whether the profile of the CO_2 bands changes after further irradiation at higher temperature and after CO sublimation.

At all the examined irradiation doses and temperatures for each sample two spectra, P and S, are taken. With a polarizer placed in the path of the IR beam (Fig. 9.1), it is possible to select and analyze the P and S component of the IR beam separately. The P polarized component has the electric vector parallel to the plane of incidence (the plane of the figure), while the S polarized component has the electric vector perpendicular to the plane of incidence. The corresponding spectrum of the background acquired before deposition is subtracted from all spectra for a given polarization (Baratta & Palumbo 1998). As shown by Baratta et al. (2000), spectra taken at oblique incidence in S polarization are equivalent to spectra taken at normal incidence.

In all examined cases, the penetration depth of impinging ions is larger than the thickness of the sample as verified using the TRIM code (Ziegler 2003). The ions used are H^+ or He^+ at energies of 200 keV and 30 keV, respectively. Results do not depend on the ion used but on the deposited energy, i.e. dose (eV/16 amu), which is calculated from knowledge of the stopping power (energy loss per unit path length) of the ions and measurement of the number of impinging ions per unit of area, fluence (ions cm^{-2}). Some characteristics of the analyzed samples are listed in Table 9.1. In a few instances, the energy deposited is not uniform throughout the samples. Then the mean stopping power is calculated as $\int S\ dx/\int dx$, where $\int dx$ is the film depth and S is the stopping power calculated by TRIM. The doses are given in eV/16 amu to compare the results of experiments performed with different mixture concentrations and/or using species of different molecular weight.

To estimate the abundance of solid molecules in both laboratory samples and along the line of sight to molecular clouds, it is essential to convert the transmittance spectra (I_f) into optical depth units $\tau(\nu) = \ln(I_o/I_f)$, where I_o is the normalization continuum. We also needed to know the integrated absorbance (cm molecule^{-1}) of their IR bands. For the integrated absorbance, we assumed 20×10^{-17} cm mol^{-1} (Allamandola et al. 1988) for the 3 μm H_2O stretching mode, 7.6×10^{-17} cm mol^{-1} (Yamada & Person 1964) for the CO_2 asymmetric stretching mode, 1.1×10^{-17} cm mol^{-1} (Gerakines et al. 1995) for the CO_2 bending mode, 1.1×10^{-17} cm mol^{-1} (Jiang et al. 1975) for the CO stretching mode, 0.64×10^{-17} cm mol^{-1} (Schutte et al. 1993, Mulas et al. 1998) for the C-H deformation mode of CH_4, 1.7×10^{-17} cm mol^{-1} (Lacy et al. 1998) for the umbrella mode of NH_3, and 1.3×10^{-17} cm mol^{-1} (Palumbo et al. 1999) for the C−O stretching mode of CH_3OH. After fitting a straight baseline, the band area $\int\tau(\nu)d\nu$ is calculated and divided by the integrated absorbance to derive the column density for each considered species.

Table 9.1 Characteristics of the studied samples. All ice mixtures are irradiated at 12−16 K and then heated to 80−90 K.

Ices	Energy (keV)	Ion	Thickness (nm)	Stopping Power (eV/Å)	Dose max (eV/16 amu)
CO	200	H^+	220	6.177	18
CO	200	H^+	990	6.440	32
$CO^{(a)}$	200	H^+	1120	6.585	40
$CO:N_2 = 8:1$	200	H^+	2000	6.800	23
$CO:N_2 = 1:1$	200	H^+	2000	6.900	23
$CO:N_2 = 1:8$	200	H^+	2000	7.100	27
$H_2O:CO = 1:10$	200	H^+	750	7.311	28
$H_2O:{}^{13}CO^{(b)} = 6:1$	200	H^+	160	9.500	4
$H_2O:CO = 8:1$	30	He^+	90	8.842	57
$H_2O:CO:N_2 = 1:3:3$	30	He^+	300	7.381	49
$N_2:CH_4:CO = 1:1:1$	30	He^+	300	8.190	54
$CO:NH_3 = 2:1$	30	He^+	300	7.925	19
CH_3OH	30	He^+	110	10.477	80
$CH_3OH:N_2 = 1:1$	200	H^+	250	9.446	21
$H_2O:CH_4 = 4:1$	30	He^+	90	9.902	180
$H_2O:CH_4 = 1:1$	30	He^+	300	9.078	60
$H_2O:CH_4:N_2 = 1:1:1$	30	He^+	300	8.328	50

(a) Sample irradiated at 16 K; heated to 70 K and irradiated; cooled to 16 K and irradiated. (b) The ${}^{13}CO_2$ band is analyzed.

Table 9.2 Best-fit parameters for Eq. (9.1) to the experimental data regarding samples containing CO ice.

Ices	$A^{(a)}$	$\sigma_{tot}{}^{(b)}$ (16 amu/eV)
$CO^{(c)}$	0.074 ± 0.002	0.242 ± 0.009
$CO:N_2$ = 8:1	0.092 ± 0.002	0.106 ± 0.005
$CO:N_2$ = 1:1	0.162 ± 0.002	0.090 ± 0.002
$CO:N_2$ = 1:8	0.108 ± 0.004	0.203 ± 0.027
$H_2O:CO$ = 1:10	0.121 ± 0.003	0.125 ± 0.009
$H_2O:^{13}CO$ = 6:1	0.922 ± 0.128	0.107 ± 0.018
$H_2O:CO$ = 8:1	0.567 ± 0.016	0.103 ± 0.013
$H_2O:CO:N_2$ = 1:3:3	0.246 ± 0.004	0.198 ± 0.009
$N_2:CH_4:CO$ = 1:1:1	0.072 ± 0.001	0.105 ± 0.005
$CO:NH_3$ = 2:1	0.131 ± 0.005	0.094 ± 0.007

(a) The asymptotic value for CO_2 column density divided by the initial column density of CO before the irradiation. (b) The total cross section. (c) Sample with a thickness of 990 nm (see Table 9.1).

9.3 Results

9.3.1 Irradiation of CO bearing mixtures

The formation of solid carbon dioxide is investigated in different mixtures that contain CO ices irradiated at low temperature. All samples considered are listed in Table 9.2. Among the samples containing CO, pure CO ice is discussed first. The most important product upon irradiation of pure CO ice is solid carbon dioxide. For all samples listed in Table 9.2, the column density of solid CO_2 (N_{CO_2}) is estimated as a function of irradiation dose:

$$N_{CO_2}/N^0_{CO} = A[1 - e^{-(\sigma_{tot} \times D)}], \tag{9.1}$$

where $A = A_0/N^0_{CO}$ is the asymptotic value for CO_2 column density (A_0) divided by the initial column density of CO in the sample before the irradiation (N^0_{CO}), σ_{tot} is the total cross section and D is the dose. The best-fit functions fitted to the experimental data are shown in Figs. 9.2, 9.3, and 9.4, while the values found for A and σ_{tot} are listed in Table 9.2. It is interesting to note that the column density of CO_2 increases rapidly at low doses and then reaches a saturation value, indicating that a steady state is reached between the formation and destruction mechanisms as discussed by Mennella et al. (2004), Loeffler et al. (2005). In the case of a pure CO sample, the percentage of CO_2 with respect to the initial CO is in agreement with Loeffler et al. (2005). In the top-left panel of Fig. 9.2, the results obtained from two different samples of thickness 220 nm and 990 nm are plotted. To evaluate the amount of CO_2 formed by energetic processing, the pure CO

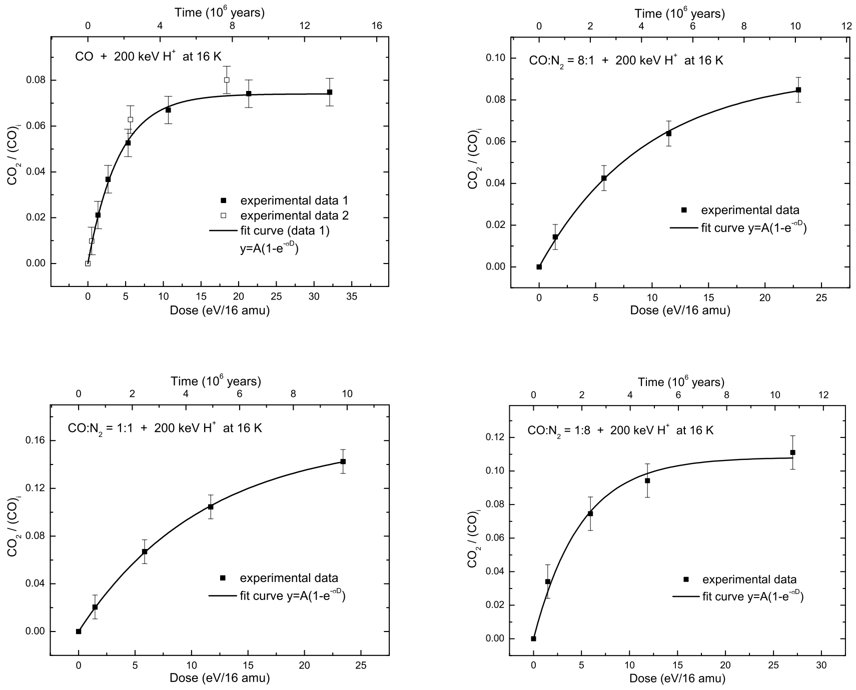

Figure 9.2 Column density of CO_2 divided by the initial column density of CO before irradiation for pure CO ice and CO:N_2 mixtures. The column density ratio is plotted as a function of dose. The dose is transferred to interstellar timescales as indicated on the top x-axis. Experimental data are fitted to an exponential curve (Eq. (9.1)): $y = A[1-e^{-(\sigma\ D)}]$, where A is the asymptotic value for CO_2 column density divided by the initial column density of CO, σ is the total cross section, and D is the dose. Only the points indicated by data 1 (990 nm thick sample) are used for the fit in the top-left panel. Data 2 (220 nm thick sample) is plotted for comparison.

sample of thickness 990 nm is fitted with Eq. (9.1). A larger amount of CO_2 is formed in H_2O-rich mixtures, comparing the results reported in Figs. 9.2, 9.3, and 9.4, and considering the same amount of energy released to the icy sample, in agreement with previous studies (*e.g.*, D'Hendecourt & Allamandola 1986, Moore et al. 1991, Ehrenfreund et al. 1997, Palumbo et al. 1998, Watanabe & Kouchi 2002). Figure 9.3, furthermore, plots the results obtained from four mixtures containing CO and H_2O in different proportions. CO_2 molecules formed after ion irradiation in the H_2O:CO = 1:10 mixture represent ~12% of the initial CO and this value is close to the percentage obtained after irradiation of pure CO, while the column density of CO_2 in a H_2O:CO = 8:1 mixture is about 60% of the initial CO. In the case of the H_2O:^{13}CO = 6:1 mixture, the fit of experimental data provides

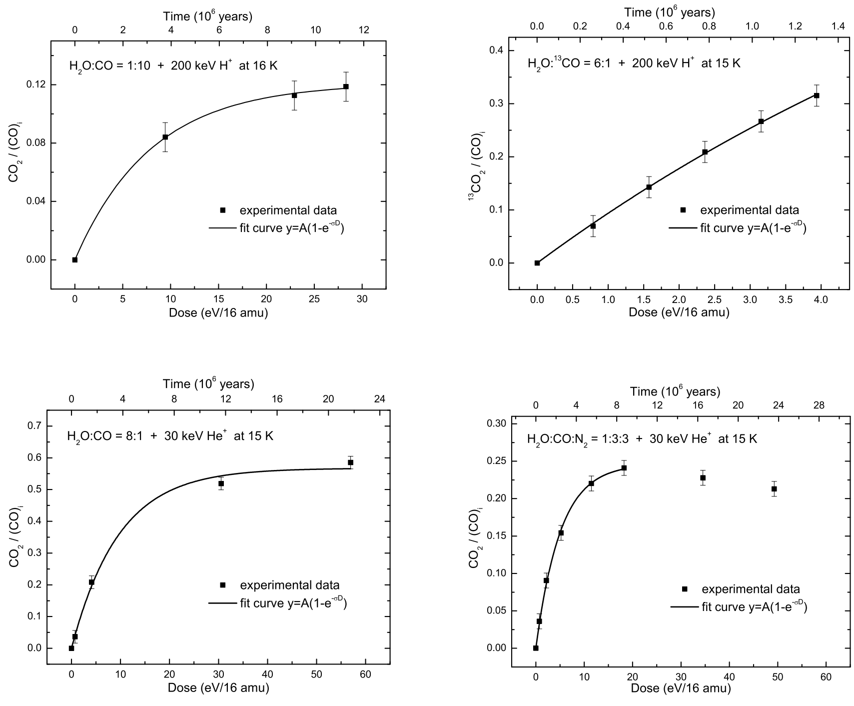

Figure 9.3 Column density of CO_2 divided by the initial column density of CO before irradiation for H_2O:CO = 1:10, H_2O:^{13}CO = 6:1, H_2O:CO = 8:1, and H_2O:CO:N_2 = 1:3:3 ice mixtures. The column density ratio is plotted as a function of dose. The dose is transferred to interstellar timescales as indicated on the top x-axis. Experimental data are fitted to an exponential curve (Eq. (9.1)): $y = A[1 - e^{-(\sigma\ D)}]$, where A is the asymptotic value for CO_2 column density divided by the initial column density of CO, σ is the total cross section, and D is the dose.

higher A value (0.92) than in the other considered cases. We note that this is unrealistic. The experimental data points are far from the saturation value and follow an almost linear trend, since irradiation is halted after a dose of ~4 eV/16 amu, which is lower than those used for the other considered samples. After a dose of ~30 eV/16 amu, the CO_2 column density in the H_2O:CO:N_2 = 1:3:3 mixture decreases because CO_2 molecules, like other species (Baratta et al. 2002), are destroyed after their formation by ion irradiation. We therefore decided to fit the data up till the dose of ~20 eV/16 amu, which corresponds to the maximum CO_2 formation level reached in this experiment.

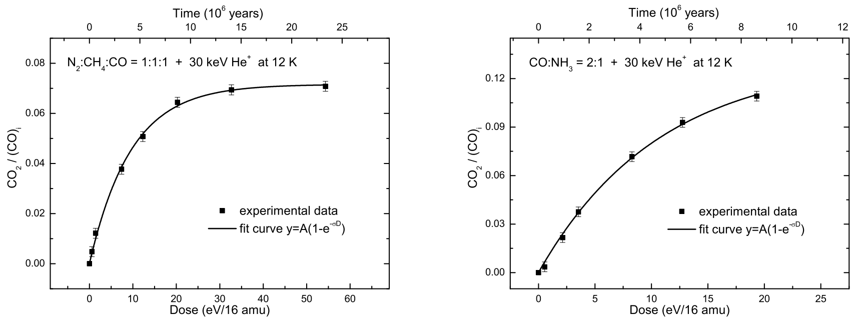

Figure 9.4 Column density of CO_2 divided by the initial column density of CO before irradiation for N_2O:CH_4:CO = 1:1:1 and CO:NH_3 = 2:1 ice mixtures. The column density ratio is plotted as a function of dose. The dose is transferred to interstellar timescales as indicated on the top x-axis. Experimental data are fitted to an exponential curve (Eq. (9.1)): $y = A[1 - e^{-(\sigma\ D)}]$, where A is the asymptotic value for CO_2 column density divided by the initial column density of CO, σ is the total cross section, and D is the dose.

9.3.2 Irradiation of ice mixtures without CO

Solid CO and CO_2 are the foremost molecules formed at low temperature after processing of C- and O- bearing ices, which do not contain CO ice initially.

The effects of ion irradiation in a sample of pure solid CH_3OH and in a mixture of H_2O and CH_4 with a ratio 4:1 are quantified. Notice that it is impossible to reproduce the trend of the CO and CO_2 column density with one exponential curve. For both of the aforementioned mixtures, the experimental column densities of formed CO and CO_2 divided by the initial column densities of CH_3OH and CH_4, respectively, are fitted by two exponential curves with a threshold dose (D_0) to take into account the change in the CO and CO_2 production rate. In the case of CO_2 and for $D \leq D_0$:

$$N_{CO_2}/N_X^0 = A_1[1 - e^{-(\sigma_{tot}^1 \times D)}], \tag{9.2}$$

while for $D > D_0$:

$$N_{CO_2}/N_X^0 = A_1[1 - e^{-(\sigma_{tot}^1 \times D)}] + A_2[1 - e^{-[\sigma_{tot}^2 \times (D - D_0)]}], \tag{9.3}$$

where A_1 and A_2 are the asymptotic values of CO_2 column density divided by the initial column density of CH_3OH and CH_4 (N_X^0), for the deposit of pure solid CH_3OH, and, for the 4:1 mixture of H_2O and CH_4 respectively, σ_{tot}^1 and σ_{tot}^2 are the total cross sections, D is the dose and D_0 is the threshold dose. Equations (9.2) and (9.3) are also used to quantify the CO column density obtained in both of the aforementioned mixtures by energetic processing at low temperature. The best-fits to experimental data for CO and CO_2 column density divided by N_X^0 as a function of the dose are shown in Fig. 9.5, while the asymptotic values of CO and CO_2 column density divided by N_X^0 and the total cross sections are listed in Tables 9.3 and 9.4 respectively.

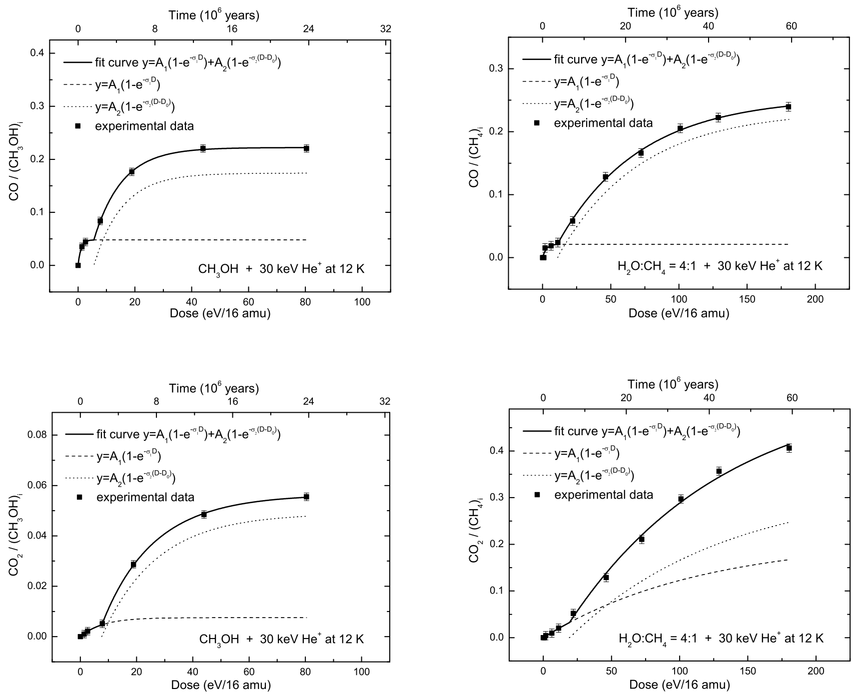

Figure 9.5 Column density of CO and CO_2 divided by the initial column density of CH_3OH and CH_4 for the deposit of pure CH_3OH ice and of H_2O:CH_4 = 4:1 mixture, respectively. CO and CO_2 are formed after ion irradiation of icy samples containing C- and O- bearing molecules. The column density ratios are plotted as a function of dose. The dose is transferred to interstellar timescales as indicated on the top x-axis. Experimental data are fitted to two exponential curves with a threshold dose (Eqs. (9.2) and (9.3)). For $D \leq D_0$: $y = A_1[1 - e^{-(\sigma_1 \times D)}]$, while for $D > D_0$: $y = A_1[1 - e^{-(\sigma_1 \times D)}] + A_2[1 - e^{-[\sigma_2 \times (D - D_0)]}]$, where A_1 and A_2 are the asymptotic values for CO and CO_2 column density divided by the initial column density of CH_3OH and CH_4, σ_1 and σ_2 are the total cross sections, D is the dose, and D_0 is the threshold dose.

During irradiation, the column density of methanol, water, and methane decreases, while the column density of newly formed species, such as CO, CO_2, and H_2CO, increases. We note that at low doses the trend of CO and CO_2 production differs from that at higher doses. Furthermore, at low doses, the main molecules formed are hydrocarbons (Baratta et al. 2002), whose column density decreases at higher doses as the CO and CO_2

column densities increase. First and second generation molecules therefore exist. The presence of newly formed solid CO in the mixture supports the CO_2 synthesis, because reactions with CO as a precursor, such as CO + OH, must be important. In addition, CO_2 could be formed by reactions that do not have CO as a precursor.

9.3.3 Carbon grains with a water ice cap

According to observations, the ratio of solid CO_2 to H_2O abundance is almost constant (varying from 15% to 40%) toward field stars as well as embedded objects, while the abundance of solid CO with respect to water ice is strongly cloud-density dependent (*e.g.*, Gerakines et al. 1999, Whittet et al. 1998, Nummelin et al. 2001, Bergin et al. 2005, Pontoppidan et al. 2008). This suggests that solid water and carbon dioxide may be formed under similar conditions. During the continuous cycling of dust between diffuse and dense regions in the interstellar medium, an H_2O-rich ice layer covers hydrogenated carbon grains as they enter in dense clouds. A standard cosmic-ray field and UV field induced by cosmic-ray fluorescence of molecular hydrogen can process carbon grains covered by mantles of water ice, leading to the formation of new solid species. Laboratory studies show that formation of CO and CO_2 molecules occurs when hydrogenated carbon grains with a water ice cap are irradiated at low temperature. The experimental results for ion irradiation and UV photolysis of H_2O ice covered carbon grains are described by Mennella et al. (2004), Mennella et al. (2006) and represent an alternative efficient formation route with respect to that proposed by Bergin et al. (2005). Nevertheless, we emphasize that both energetic processing and surface reactions are not mutually exclusive and could rather contribute to the total solid CO_2 observed along the line of sight to dense clouds.

Mennella et al. (2004), Mennella et al. (2006) derived the formation cross section of CO and CO_2 molecules from the increase in intensity of the CO and CO_2 stretching modes as a function of the ion and UV fluences, and estimated that after $t = 3 \times 10^7$ yr, column densities are:

$$N_{CO} = 7.0 \times 10^{15} A_V, \tag{9.4}$$

and

$$N_{CO_2} = 9.3 \times 10^{15} A_V, \tag{9.5}$$

where A_V is the visual extinction of the cloud.

These laboratory data will be added to our sample and discussed in the following sections.

Table 9.3 Best-fit parameters for Eqs. (9.2) and (9.3) to the experimental CO column density regarding samples without CO.

Ices	$D_0(CO)^{(a)}$ (eV/16 amu)	$A_1(CO)^{(b)}$	$\sigma^1_{tot}(CO)^{(c)}$ (16 amu/eV)	$A_2(CO)^{(b)}$	$\sigma^2_{tot}(CO)^{(c)}$ (16 amu/eV)
CH_3OH	5.5 ± 0.3	0.048 ± 0.004	0.150 ± 0.150	0.174 ± 0.004	0.101 ± 0.004
$H_2O:CH_4 = 4:1$	10.8 ± 2.9	0.021 ± 0.011	0.376 ± 0.376	0.233 ± 0.013	0.017 ± 0.002

(a) The threshold dose for the exponential curves. (b) The asymptotic values for CO column density divided by the initial column density of CH_3OH and CH_4 before irradiation. (c) The total cross sections.

Table 9.4 Best-fit parameters for Eqs. (9.2) and (9.3) to the experimental CO_2 column density regarding samples without CO.

Ices	$D_0(CO_2)^{(a)}$ (eV/16 amu)	$A_1(CO_2)^{(b)}$	$\sigma^1_{tot}(CO_2)^{(c)}$ (16 amu/eV)	$A_2(CO_2)^{(b)}$	$\sigma^2_{tot}(CO_2)^{(c)}$ (16 amu/eV)
CH_3OH	7.6 ± 1.1	0.008 ± 0.006	0.126 ± 0.126	0.049 ± 0.006	0.051 ± 0.007
$H_2O:CH_4 = 4:1$	19.2 ± 3.0	0.211 ± 0.033	0.009 ± 0.002	0.327 ± 0.033	0.009 ± 0.001

(a) The threshold dose for the exponential curves. (b) The asymptotic values for CO_2 column density divided by the initial column density of CH_3OH and CH_4 before irradiation. (c) The total cross sections.

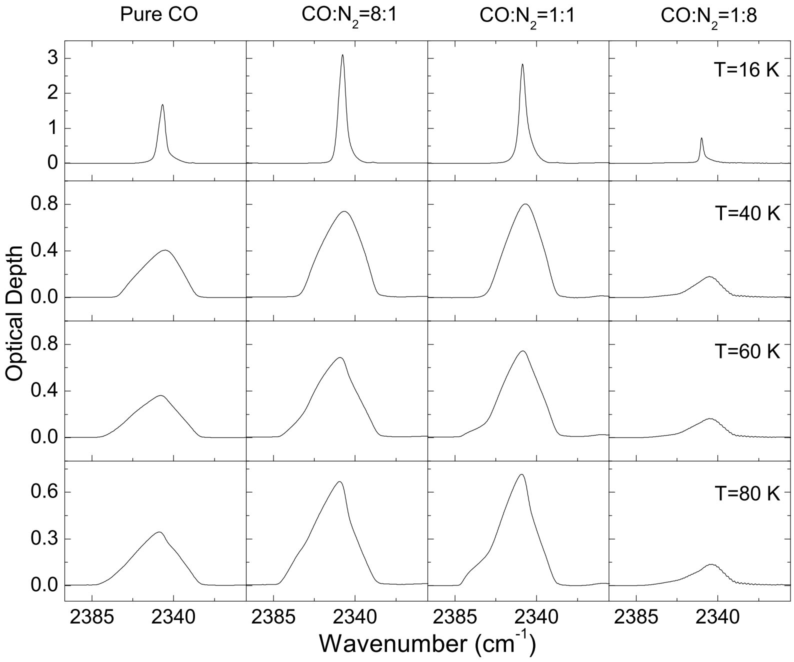

Figure 9.6 The band profile of the CO_2 stretching mode at about 2340 cm^{-1} formed after ion irradiation of four different mixtures: (from the left to the right side) pure CO ice, $CO:N_2$ = 8:1, $CO:N_2$ = 1:1, and $CO:N_2$ = 1:8. The top side of the figure shows the spectrum taken for each experiment after ion irradiation at 16 K. The following rows show the spectra taken after irradiation at 16 K and heated at 40, 60, and 80 K, respectively.

9.3.4 Band profiles

In Figs. 9.6 and 9.7, we present the band profile of the CO_2 stretching and bending mode (at about 2340 cm^{-1} and 660 cm^{-1} respectively) formed after ion irradiation of four different mixtures. From the left hand side to the right hand side of Figs. 9.6 and 9.7, the case of pure CO ice, $CO:N_2$ = 8:1, $CO:N_2$ = 1:1, and $CO:N_2$ = 1:8 are shown. From top to bottom of Figs. 9.6 and 9.7, the spectra taken at 16, 40, 60, and 80 K for each experiment, after irradiation at 16 K, are shown. Comparing the band profile of the CO_2 stretching mode for the spectra taken at 16 K with those taken at 80 K it becomes apparent that, after heating the sample, the feature becomes broad and asymmetric. Some differences in peak positions and band widths can also be discerned by comparing the spectra of dif-

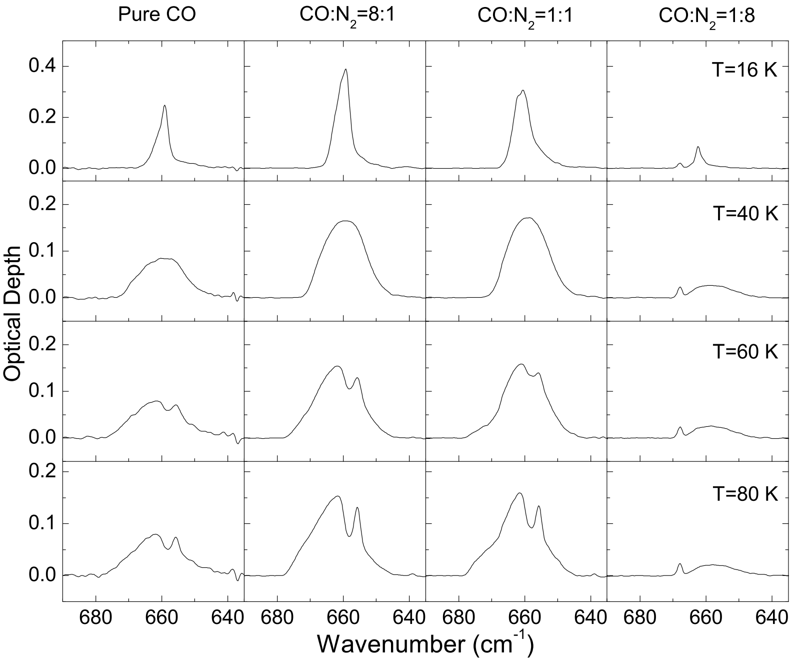

Figure 9.7 Similar to Fig. 6 for the CO_2 bending mode at about 660 cm^{-1}.

ferent samples taken at the same temperature. The bending mode appears more sensitive to temperature variations than the stretching mode. If the sample is heated, the bending mode feature changes drastically: a double peak appears at about 655 cm^{-1} and 660 cm^{-1} and the band becomes broader. The double peak shifts in position and changes in intensity for different N_2 abundance in the mixtures, until it effectively disappears in the spectra for the $CO:N_2$ = 1:8 mixture. At all the investigated temperatures, the spectra of the $CO:N_2$ = 1:8 sample present a peak due to the KBr substrate at about 670 cm^{-1}. The infrared spectra show that, due to the different volatility, after irradiation, CO sublimes at about 30 K, while CO_2 remains in the solid phase up to about 90 K. The band profile of the CO_2 bending mode also depends on the N_2 concentration. In general, the results presented here agree with the study of the CO_2 band profile by Ehrenfreund et al. (1997).

Figures 9.8 and 9.9 show the band profile of the CO_2 stretching and bending mode formed after energetic processing at low temperature of other samples. From top to bottom of Figs. 9.8 and 9.9, we present the spectrum of CH_3OH ice irradiated at 16 K, a mixture of $H_2O:CO$ = 1:10 irradiated at 16 K and heated to 90 K, and irradiated water ice deposited on hydrogenated amorphous carbon grains called ACARL_H (Mennella et al.

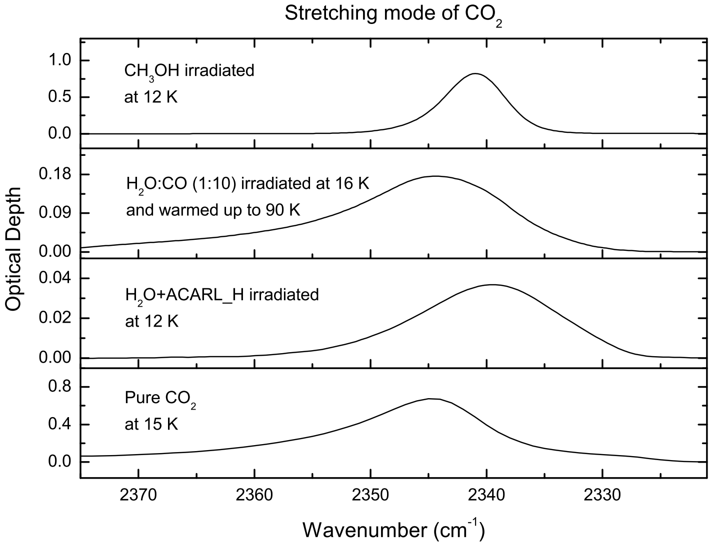

Figure 9.8 The band profile of the CO_2 stretching mode at about 2340 cm^{-1} formed after energetic processing at low temperature of some samples: (from top to bottom) CH_3OH ice irradiated at 12 K, H_2O:CO = 1:10 irradiated at 16 K and heated to 90 K, water ice deposited on hydrogenated amorphous carbon grains ACARL_H (Mennella et al. 2006) and irradiated at 12 K. The band profile of the stretching mode of pure CO_2 ice at 15 K is also shown for comparison.

2006). The stretching and bending mode band profiles of pure CO_2 ice are also shown for comparison. It is interesting to note that, although the peak position changes in each spectrum for both the stretching and bending modes, the bending mode appears more sensitive to mixture variations.

9.4 Comparison with observations

9.4.1 CO_2 towards massive YSOs

Along the line of sight to embedded young stellar objects (YSO), icy mantles could have been exposed to energetic processing and warming. The observed band profiles due to solid CO_2 indicate the presence of different components along the line of sight. We considered the following YSOs: S140 IRS 1, AFGL 2136, NGC 7538 IRS 9, NGC 7538 IRS 1, and W33A (Gerakines et al. 1999). A list of the considered young infrared source param-

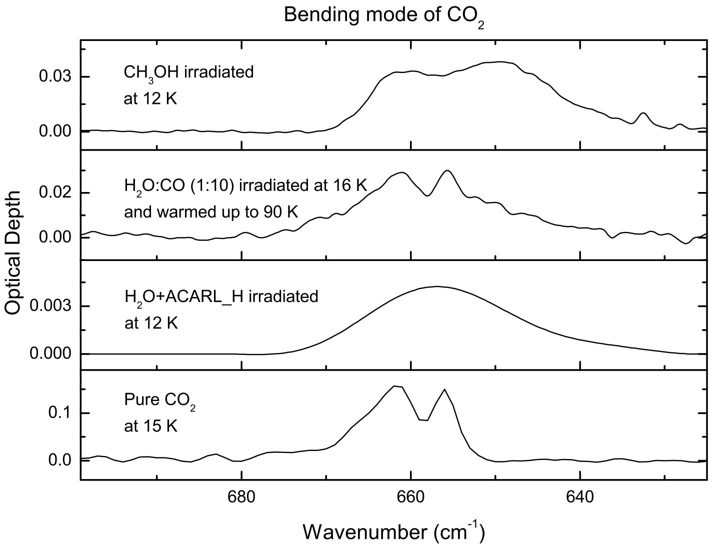

Figure 9.9 Similar to Fig. 8 for the CO_2 bending mode at about 660 cm^{-1}.

eters is reported in Table 9.5.

S140 is an H II region of both high and low mass star formation located 0.9 kpc behind about 23 mag of visual extinction. AFGL 2136 is associated with a bipolar reflection nebula. Along most of the line of sight to AFGL 2136, the dust and the gas temperature is about 30 K. NGC 7538 IRS 9 is an embedded, luminous, and compact infrared source. NGC 7538 IRS 1 is a pre-main-sequence object, which is the most luminous in the NGC 7538 complex. W33A is a massive, luminous source. Along the line of sight to this source, there is evidence for energetic processing provided by the presence of abundant XCN (Gibb & Whittet 2002). In all the considered sources water, carbon monoxide, carbon dioxide and methanol are detected in the solid phase (Gibb et al. 2004).

9.4.2 The fitting procedure

Gerakines et al. (1999) considered three categories of laboratory mixtures in attempting to reproduce qualitatively the CO_2 stretching and bending mode of the observed, aforementioned spectral features: polar, nonpolar, and annealed ices. In the cases of polar and nonpolar ices, they applied particle shape corrections to the laboratory data using different grain models derived from the real and imaginary parts of the ice's refractive index (*n* and *k* values).

In this chapter, we have attempted to analyze quantitatively the formation of CO_2

Table 9.5 Young infrared source parameters: distance (d), luminosity (l), visual extinction (A_V), and cold component of CO column density detected in gas phase along the line of sight to some YSOs ($N_{gas(cold)}CO$), solid CO_2 column density observed along the line of sight to some YSOs ($N_{solid}CO_2$).

Sources	d (kpc)	l ($L_\odot$)	A_V (mag)	$N_{gas(cold)}CO$ (10^{19} mol cm^{-2})	$N_{solid}CO_2$ (10^{17} mol cm^{-2})	reference
S140 IRS 1	0.9	2000	23	0.45	4.2(0.1)	1, 4
AFGL 2136	2	7×10^4	94	1.08	7.8(0.3)	1, 3
NGC 7538 IRS 9	2.7	4×10^4	84	1.44	16.3(1.8)	1, 2, 3
NGC 7538 IRS 1	2.8	1.3×10^5	119	1.30	5.1(0.2)	1, 4
W33A	4	1.1×10^5	150	1.96	14.5(1.3)	1, 3

(1) Gibb et al. (2004). (2) Chiar et al. (1998). (3) Tielens et al. (1991). (4) Mitchell et al. (1990).

in dense clouds. We have therefore compared the band profiles of CO_2 stretching and bending mode, observed towards embedded YSOs, with laboratory spectra of selected ion-irradiated samples, to assess the effect of energetic processing on interstellar icy mantles.

According to Baratta et al. (2000, 2002), the P polarized component of the spectrum can show additional features that are not due to absorption (k) but to the increased reflectivity of the region across the absorption band where $n<1$. The difference between the P and S polarized components of the spectra depends on the optical constants of the ice. Additionally, for a given sample, it depends on the thickness, being higher for thinner films. Baratta et al. (2000) also demonstrated that if P and S polarized components differ, then band profiles are unrepresentative of small particle extinction spectra and cannot be compared with observed interstellar spectra. Figure 9.10 shows the band profile of the stretching and bending mode for CO_2 formed after irradiation of the CO ice, indicating that the P and S components are similar. We verified that this is true for all band profiles used in the fits. Given that the signal-to-noise ratio of P spectra is higher than for S spectra, the former are used to fit the observed data. Since P and S spectra are similar, small particle extinction cross section calculations are in our case unnecessary. For this reason, we used the laboratory spectra in optical depth units for the fitting procedure.

Looking at the observed interstellar spectra, the 4.27 μm feature due to the CO_2 stretching mode is clearly saturated for NGC 7538 IRS 9 and W33A (Fig. 9.11). AFGL 2136 exhibits a shallow shoulder on the long wavelength side of the 4.27 μm feature. It is suspected that this is the result of an unidentified, broad, underlying component (Gerakines et al. 1999). The shallow absorption shoulders on the short and long wavelength sides of the stretching mode are due to the unresolved P and R branches of gas-phase CO_2, which are consistent with the strong gas-phase CO_2 absorptions detected at 14.97 μm toward these sources. Spurious structures also exist in the troughs of the 4.27 μm feature of NGC 7538 IRS 1, which may be close to saturation. The observed CO_2 15.2 μm bending mode for all the sources can be divided into three components: a feature at 14.97 μm due to gas-phase CO_2 absorption, a pair of sharp peaks at about 15.15 and 15.27 μm that highlight CO_2 segregation induced by thermal processing along the line of sight, and a shoulder close to 15.4 μm assigned to the acid-base interaction between CO_2 and alcohols

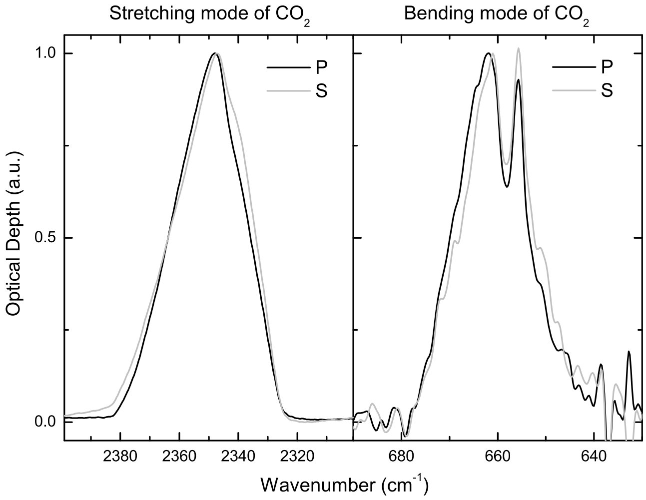

Figure 9.10 The band profile of the CO_2 stretching and bending modes formed after irradiation at 16 K and heating to 80 K of pure CO ice. The comparison between the P (*black line*) and S (*light gray line*) component of the IR beam is plotted, see text in § 9.2.

(Ehrenfreund et al. 1998, Dartois et al. 1999).

Using home-written software, all spectra for samples listed in Table 9.1 are compared systematically with the observed YSOs data. The software selected spectra of laboratory mixtures that fitted simultaneously the CO_2 bending and stretching mode band profile of the source considered. The best results are reported in Fig. 9.11.

We note that three or four components are needed to fit simultaneously the bending and stretching mode band profile of each object. The fit components and percentages are shown in Table 9.6. The spectra used to fit the observed CO_2 band profiles are available in the Catania database (http://www.oact.inaf.it/weblab/).

The profile of CO_2 formed after irradiation of a pure CO or a H_2O:CO = 1:10 mixture heated to 70 K is required to reproduce the sharp peaks of the bending mode profile at 15.15 and 15.27 μm. The profile of CO_2 formed after irradiation of methanol is required to fit the shoulder at 15.4 μm. This component is due to an acid-base interaction between the C atom of CO_2 and the oxygen atom of a polar molecule. When CO_2 molecules are in the presence of alcohol, they act as a Lewis acid (Ehrenfreund et al. 1998, Dartois et al. 1999). The most abundant alcohol detected in dense clouds is methanol. For this reason, we considered a sample of methanol deposited and irradiated at low temperature. The profile of CO_2 bending and stretching modes formed after irradiation of H_2O on carbon grains are broad and smooth (Figs. 9.8 and 9.9), and these are also required to fit the observed bands.

Table 9.6 Contributions in percentage for each listed fit component to the total CO_2 column density observed along the line of sight to the considered sources as obtained from the fitting procedure (Fit columns) and as estimated from Eqs. (9.5), (9.6), (9.7), and (9.8) which give the maximum possible contribution by each component to the total observed CO_2 (Eq. columns).

Spectra	S140 IRS 1		AFGL 2136		NGC 7538 IRS 9		NGC 7538 IRS 1		W33A		
	Fit (%)	Eq. (%)	Fit (%)	Eq. (%)	Fit (%)	Eq. (%)	Fit (%)	Eq. (%)	Fit (%)	Eq. (%)	[Eq.]
$CO^{(a)}$	38	71	-	-	-	-	-	-	-	-	[6]
$CO^{(b)}$	33	71	-	-	41	59	-	-	-	-	[6]
$H_2O:CO^{(c)} = 1:10$	28	100	66	100	44	100	72	100	23	100	[6]
$CO:NH_3{}^{(d)} = 2:1$	-	-	-	-	-	-	2	2	-	-	[8]
$CH_3OH^{(d)}$	1	83	19	78	15	43	20	92	44	100	[7]
ACARL_H$^{(d)}$	-	-	15	100	-	-	6	100	33	96	[5]

(a) Irradiated at 16 K; heated to 70 K and irradiated. (b) Irradiated at 16 K; heated to 70 K and irradiated; cooled to 16 K and irradiated. (c) Irradiated at 16 K and heated to 90 K. (d) Irradiated at 12 K.

In the case of NGC 7538 IRS 1, the fit improves if we consider a small contribution (2%) from CO_2 formed after irradiation of a $CO:NH_3 = 2:1$ mixture. An upper limit to the abundance of ammonia ($<3.7 \times 10^{17}$ cm^{-2}) is indeed derived along the line of sight to NGC 7538 IRS 1 (Gibb et al. 2001).

Finally, it is noted that the considered sample of laboratory spectra is by no means complete and should be regarded only as a starting point for the analysis of the composition of the icy grain mantles. Future studies of the composition of the CO_2 ices should include other laboratory samples of a range of ion and UV irradiation doses, temperatures, and mixture ratios.

From Fig. 9.11, it is clear that while the bending mode profile is always well reproduced by laboratory spectra, the fit of the stretching mode is not always satisfactory. This could be due to the fact that the optical depth of the stretching mode band is very large and our approach could be no longer applicable.

Pontoppidan et al. (2008) performed a fitting analysis of the CO_2 ice bending mode profile for a large sample of low mass embedded young stars. They used five components to reproduce the profile of the considered feature. A $CO_2:H_2O \sim 1:7$ mixture and a $CO_2:CO \sim 1:1$ mixture, which are named the red and blue component respectively, generally dominate the bending mode profile and the total CO_2 column density observed. The other three components are needed to reproduce subtle differences due to trace constituents. All components considered by Pontoppidan et al. (2008) correspond to interstellar relevant ice analogues and can be divided into polar and nonpolar ices. Our fitting results presented here are similar to those of Pontoppidan et al. (2008), although we emphasize that our fitting components are obtained after energetic processing of interstellar ice analogues and both stretching and bending modes are fitted simultaneously without any particle-shape correction.

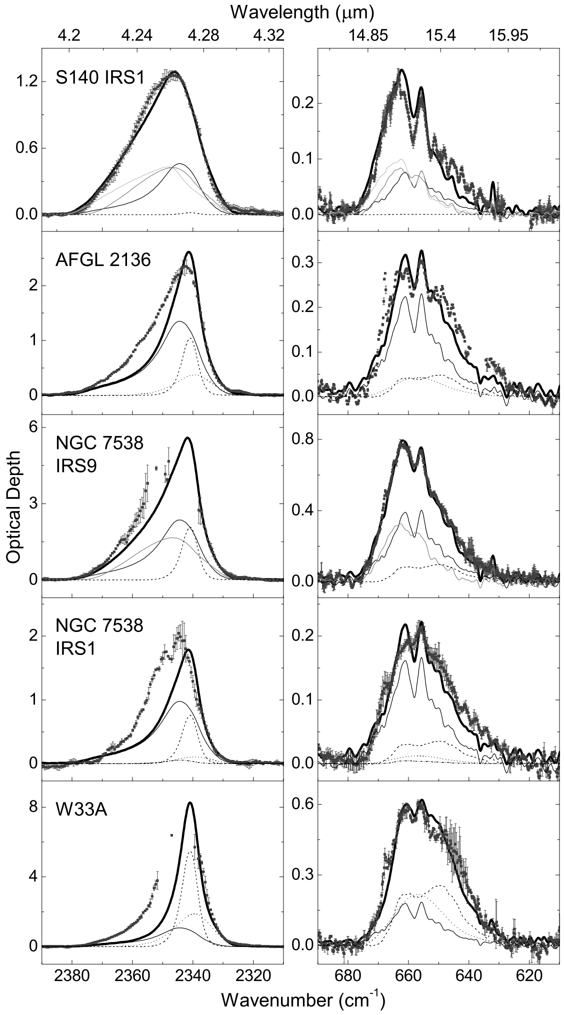

Figure 9.11 The CO_2 stretching and bending mode band profile of selected YSO sources are fitted (*thick black line*) at the same time using different laboratory spectra: CO ice irradiated at 16 K, heated to 70 K and irradiated (*light gray line*); CO ice irradiated at 16 K, heated to 70 K and irradiated, cooled to 16 K and irradiated (*gray line*); H_2O:CO = 1:10 mixture irradiated at 16 K and heated to 90 K (*black line*); CO:NH_3 = 2:1 irradiated at 12 K (*dash-dot line*); methanol ice irradiated at 12 K (*dash line*); water ice on hydrogenated carbon grains irradiated at 12 K (*dot line*). The spectra used to fit the observed CO_2 band profiles are available in the Catania database (http://www.oact.inaf.it/weblab/).

9.5 Discussion

Deriving a reliable fit is insufficient to prove the validity of a model; reasonable physical arguments are also required. We have performed a quantitative study of the CO_2 formed in laboratory C- and O- bearing samples upon energetic processing, and we extended our results to the interstellar medium by considering the lifetime in solid phase of species irradiated in dense cores, and the temperature gradient along the line of sight.

In Figs. 9.2, 9.3, 9.4, and 9.5 the top ordinate axes indicate an estimation of the time (years) required to achieve the same effect on interstellar ices as observed in the laboratory. To estimate this time, we considered the approximation of effective monoenergetic 1 MeV protons assuming that in dense interstellar regions the effective 1 MeV proton flux is equal to 1 proton cm^{-2} s^{-1} (Mennella et al. 2003). The laboratory results are extrapolated to the interstellar medium conditions by deriving the formation cross section due to 1 MeV protons from that obtained in the irradiation experiments with 30 keV He^+ and 200 keV H^+ using the ratio of the corresponding stopping power as a scaling factor.

As reported by Greenberg (1982), a dense cloud lifetime ranges between 3×10^7 and 5×10^8 yr. Assuming a density of $n_0 \sim 10^4$ cm^{-3}, the gas takes $10^9/n_0 \simeq 10^5$ yr to condense onto grains (Tielens & Allamandola 1987a). Icy grain mantles therefore undergo cosmic ion irradiation for about 10^5–10^8 yr. The first estimate refers to the case of icy mantles that sublime as soon as they form (which could be the case for volatile species such as CO), the latter estimate refers to the limit case of icy mantles that survive throughout the cloud lifetime (which could be the case for less volatile species such as H_2O). The lifetime of molecules in the solid phase is related to the volatility of each species. The results of the fits discussed in § 9.4 and summarized in Table 9.6, indicate that a significant percentage of the CO_2 band profiles is reproduced by the spectra of CO_2 formed after ion irradiation of pure CO or H_2O:CO = 1:10 ice mixtures. To justify this result, we should assume that all the CO molecules that we observe today in the gas phase along the line of sight to YSOs are frozen onto grains during the cloud collapse phase and have been processed by ion irradiation for about 8×10^6 yr. Then, as indicated by laboratory experiments, when the temperature of the grains increases, CO molecules sublimate, while CO_2 molecules formed after ion irradiation remain. Thus, the profile of the bending mode shows the pair of sharp peaks required to fit the observed band profile. To estimate the amount of solid CO_2 that can form after ion irradiation of CO-rich icy mantles, we therefore use the following equation:

$$N_{CO_2} = N(CO)_{Obs,gas} \times [N(CO_2)/N(CO)]_{Lab,\ solid}, \tag{9.6}$$

where $N(CO)_{Obs,\ gas}$ is the CO column density detected in gas phase along the line of sight to the considered sources, while $[N(CO_2)/N(CO)]_{Lab,\ solid}$ is the ratio of the CO_2 to CO column density obtained in laboratory spectra.

Solid CO is also observed along the line of sight to YSOs and we then expect that the spectrum of solid CO_2 at low temperatures, formed after ion irradiation of pure CO, should also be considered in the fit of the CO_2 observed band profile. As already discussed by Loeffler et al. (2005), this component accounts for 1–6% of the observed solid CO_2. We included this component in the fitting procedure and found that the quality of the fit is equivalent to that obtained by considering the mixtures listed in Table 9.6 and shown in Fig. 9.11. This result agrees with the result obtained by Pontoppidan et al. (2008), who found that the contribution of the CO_2:CO ~ 1:25 mixture is almost negligible.

To estimate the amount of solid CO_2 formed after ion irradiation of methanol, we used the following equation:

$$N_{CO_2} = N(CH_3OH)_{Obs,\ solid} \times [N(CO_2)/N(CH_3OH)]_{Lab,\ solid}, \tag{9.7}$$

where the time considered is the lifetime of dense clouds (3×10^7 yr), $N(CH_3OH)_{Obs,\ solid}$ is the methanol detected in solid phase along the line of sight to the considered sources, and $[N(CO_2)/N(CH_3OH)]_{Lab,\ solid}$ is the ratio of the CO_2 to CH_3OH column density measured in the laboratory spectrum used for the fit. We point out that this ratio is not the $CO_2/(CH_3OH)_i$ ratio reported in Fig. 9.5.

To estimate the amount of CO_2 formed after ion irradiation of CO:NH_3 = 2:1 mixture we used the following equation:

$$N_{CO_2} = N(NH_3)_{Obs,\ solid} \times [N(CO_2)/N(NH_3)]_{Lab,\ solid}, \tag{9.8}$$

where $N(NH_3)_{Obs,\ solid}$ is the column density of NH_3 observed along the line of sight to the sources and $[N(CO_2)/N(NH_3)]_{Lab,\ solid}$ is the CO_2 and NH_3 column density ratio measured in the laboratory spectrum used for the fit. In this calculation, we assumed that all solid ammonia observed along the line of sight is mixed with CO.

Following Mennella et al. (2006), and considering clouds for which visual extinction (A_V) is known, we used Eq. (9.5) to evaluated the contribution of CO_2, which is produced by energetic irradiation of carbon grains with a water ice cap, to the observed column density.

In Table 9.6, the percentages of the CO_2 column density calculated by Eqs. (9.5), (9.6), (9.7), and (9.8) are compared to the percentages obtained by fits for all young infrared sources considered. These percentages indicated by "Eq" represent the maximum possible contribution by each component. It is relevant to note that the percentages for the fit components of each YSOs considered agree with the percentages of the CO_2 column density calculated by Eqs. (9.5), (9.6), (9.7), and (9.8). In all cases analyzed, the percentage values for the fit components are indeed lower than the values derived from Eqs. (9.5), (9.6), (9.7), and (9.8). Even though the fits presented here are not unique, they are supported by reasonable astrophysical hypotheses as discussed above.

By assuming that in dense clouds all CO molecules detected in the gas phase (CO_{tot}) are frozen onto grains during the cloud collapse phase, it is possible to evaluate, using Table 9.7, the contribution, due to irradiation, of pure CO ice to the observed CO_2 column density. For the other ice mixtures listed in Table 9.7, CO_{in} is the amount of interstellar solid CO originally present in icy grain mantles and mixed with other species. For those lines of sight along which visual extinction are known, it is possible to calculate the contribution to the solid CO_2 due to irradiation of carbon particles covered by amorphous water ice.

Table 9.7 Contribution of CO_2 produced by energetic irradiation of laboratory samples to the observed column density for those clouds of which the visual extinction and the CO gas-phase abundance are known.

Icy samples	N_{CO_2} (upper limits) (mol cm^{-2})
CO	$0.07 \times CO_{tot}$
$CO:N_2$ = 8:1	$0.09 \times CO_{in}$
$CO:N_2$ = 1:1	$0.16 \times CO_{in}$
$CO:N_2$ = 1:8	$0.11 \times CO_{in}$
$H_2O:CO$ = 1:10	$0.12 \times CO_{in}$
$H_2O:CO$ = 8:1	$0.57 \times CO_{in}$
$H_2O:CO:N_2$ = 1:3:3	$0.25 \times CO_{in}$
$N_2:CH_4:CO$ = 1:1:1	$0.07 \times CO_{in}$
$CO:NH_3$ = 2:1	$0.13 \times CO_{in}$
ACARL_H	9.3×10^{15} A_V

9.6 Conclusions

Abundant amount of solid CO_2 is detected towards embedded YSOs (both low mass and high mass protostars) and field stars. Observations towards high mass star-forming regions indicate that some of the observed carbon dioxide is segregated (Ehrenfreund et al. 1998). On the other hand, observations along the line of sight to field stars indicate that most solid CO_2 is mixed with water ice (Bergin et al. 2005). As shown in this article, CO and CO_2 are formed easily after energetic processing of ice mixtures containing C- and O- bearing molecules and carbon grains covered by water ice. Furthermore, given the same amount of energy released to the icy sample, a larger amount of CO_2 is formed in H_2O-rich mixtures. It has been found that the band profile of the CO_2 stretching and bending modes depends on the mixture and temperature of the ice sample. On the basis of the present laboratory results, it is possible to estimate the contribution of CO_2, produced after energetic processing, to the observed carbon dioxide column densities for several YSOs. Laboratory results presented account not only quantitatively for the column density of observed interstellar CO_2 but also provide a good spectroscopic analogue of the interstellar features supporting the hypothesis that interstellar solid CO_2 is formed after ion irradiation and UV photolysis of icy mantles. This however does not exclude the possibility that other formation routes, such as grain surface reactions, contribute to the production of the observed interstellar solid CO_2.

Bibliography

Acharyya, K., Fuchs, G. W., Fraser, H. J., van Dishoeck, E. F., & Linnartz, H. 2007, A&A, 466, 1005

Acquista, N., Schoen, L. J., & Lide, Jr., D. R. 1968, J. Chem. Phys., 48, 1534

Al-Halabi, A. & van Dishoeck, E. F. 2007, MNRAS, 382, 1648

Allamandola, L. J., Sandford, S. A., & Valero, G. J. 1988, Icarus, 76, 225

Allen, M. & Robinson, G. W. 1977, ApJ, 212, 396

Andersson, S., Al-Halabi, A., Kroes, G., & van Dishoeck, E. F. 2006, J. Chem. Phys., 124, 064715

Atkinson, R., Baulch, D. L., Cox, R. A., et al. 2004, Atmospheric Chemistry & Physics, 4, 1461

Awad, Z., Chigai, T., Kimura, Y., Shalabiea, O. M., & Yamamoto, T. 2005, ApJ, 626, 262

Bally, J. 2007, Ap&SS, 311, 15

Bandow, H. & Akimoto, H. 1985, J. Phys. Chem., 89, 845

Baratta, G. A., Leto, G., & Palumbo, M. E. 2002, A&A, 384, 343

Baratta, G. A. & Palumbo, M. E. 1998, Journal of the Optical Society of America A, 15, 3076

Baratta, G. A., Palumbo, M. E., & Strazzulla, G. 2000, A&A, 357, 1045

Barzel, B. & Biham, O. 2007, ApJ, 658, L37

Baulch, D. L., Cobos, C. J., Cox, R. A., et al. 1992, J. Phys. Chem. Ref. Data, 21, 411

Bennett, C. J., Jamieson, C., Mebel, A. M., & Kaiser, R. I. 2004, Phys. Chem. Chem. Phys., 6, 735

Bennett, C. J. & Kaiser, R. I. 2005, ApJ, 635, 1362

Bennett, C. J. & Kaiser, R. I. 2007, ApJ, 661, 899

Bergin, E. A., Langer, W. D., & Goldsmith, P. F. 1995, ApJ, 441, 222

Bergin, E. A., Melnick, G. J., Gerakines, P. A., Neufeld, D. A., & Whittet, D. C. B. 2005, ApJ, 627, L33

Bergin, E. A. & Tafalla, M. 2007, ARA&A, 45, 339

Berkley, D. D., Johnson, B. R., Anand, N., Beauchamp, K. M., & Conroy, L. E. 1988, Appl. Phys. Lett., 53, 1973

Bisschop, S. E. 2007, PhD thesis, Leiden Observatory, Leiden University

Bisschop, S. E., Fraser, H. J., Öberg, K. I., van Dishoeck, E. F., & Schlemmer, S. 2006, A&A, 449, 1297

Bisschop, S. E., Fuchs, G. W., Boogert, A. C. A., van Dishoeck, E. F., & Linnartz, H. 2007a, A&A, 470, 749

Bisschop, S. E., Fuchs, G. W., van Dishoeck, E. F., & Linnartz, H. 2007b, A&A, 474, 1061

Bisschop, S. E., Jørgensen, J. K., van Dishoeck, E. F., & de Wachter, E. B. M. 2007c, A&A, 465, 913

Bockelée-Morvan, D., Lis, D. C., Wink, J. E., et al. 2000, A&A, 353, 1101

Boogert, A. C. A., Pontoppidan, K. M., Knez, C., et al. 2008, ApJ, 678, 985

Boogert, A. C. A., Pontoppidan, K. M., Lahuis, F., et al. 2004, ApJS, 154, 359

Boonman, A. M. S., van Dishoeck, E. F., Lahuis, F., & Doty, S. D. 2003, A&A, 399, 1063

Bottinelli, S., Boogert, A. C., Bouwman, J., et al. 2010, ApJ, 718, 1100

Bottinelli, S., Ceccarelli, C., Williams, J. P., & Lefloch, B. 2007, A&A, 463, 601

Boudin, N., Schutte, W. A., & Greenberg, J. M. 1998, A&A, 331, 749

Bouwman, J., Ludwig, W., Awad, Z., et al. 2007, A&A, 476, 995

Brosset, P., Dahoo, R., Gauthierroy, B., Abouafmarguin, L., & Lakhlifi, A. 1993, Chem. Phys., 172, 315

Cami, J., Bernard-Salas, J., Peeters, E., & Malek, S. E. 2010, Science, 329, 1180

Catalano, E. & Sanborn, R. H. 1963, J. Chem. Phys., 38, 2273

Cazaux, S., Cobut, V., Marseille, M., Spaans, M., & Caselli, P. 2010, A&A in press

Chaabouni, H., Schriver-Mazzuoli, L., & Schriver, A. 2000, Low Temp. Phys., 26, 712

Chang, Q., Cuppen, H. M., & Herbst, E. 2007, A&A, 469, 973

Charnley, S. B. 2001, ApJ, 562, L99

Charnley, S. B., Rodgers, S. D., & Ehrenfreund, P. 2001, A&A, 378, 1024

Charnley, S. B., Tielens, A. G. G. M., & Millar, T. J. 1992, ApJ, 399, L71

Charnley, S. B., Tielens, A. G. G. M., & Rodgers, S. D. 1997, ApJ, 482, L203

Chiar, J. E., Adamson, A. J., Kerr, T. H., & Whittet, D. C. B. 1995, ApJ, 455, 234

Chiar, J. E., Pendleton, Y. J., Geballe, T. R., & Tielens, A. G. G. M. 1998, ApJ, 507, 281

Collings, M. P., Anderson, M. A., Chen, R., et al. 2004, MNRAS, 354, 1133

Collings, M. P., Dever, J. W., Fraser, H. J., & McCoustra, M. R. S. 2003, Ap&SS, 285, 633

Cooper, P. D., Moore, M. H., & Hudson, R. L. 2008, Icarus, 194, 379

Cuppen, H. M., Fuchs, G. W., Ioppolo, S., et al. 2008, in IAU Symposium, Vol. 251, IAU Symposium, ed. S. Kwok & S. Sandford, 377

Cuppen, H. M. & Herbst, E. 2007, ApJ, 668, 294

Cuppen, H. M., Ioppolo, S., Romanzin, C., & Linnartz, H. 2010, Phys. Chem. Chem. Phys., 12, 12077

Cuppen, H. M., van Dishoeck, E. F., Herbst, E., & Tielens, A. G. G. M. 2009, A&A, 508, 275

Dartois, E., Cox, P., Roelfsema, P. R., et al. 1998, A&A, 338, L21

Dartois, E., Schutte, W., Geballe, T. R., et al. 1999, A&A, 342, L32

D'Hendecourt, L. B. & Allamandola, L. J. 1986, A&AS, 64, 453

d'Hendecourt, L. B., Allamandola, L. J., & Greenberg, J. M. 1985, A&A, 152, 130

Draine, B. T. 2009, in Astronomical Society of the Pacific Conference Series, Vol. 414, Astronomical Society of the Pacific Conference Series, ed. T. Henning, E. Grün, & J. Steinacker, 453

Dulieu, F., Amiaud, L., Baouche, S., et al. 2005, Chem. Phys. Lett., 404, 187

Dulieu, F., Amiaud, L., Congiu, E., et al. 2010, A&A, 512, A30

Dulieu, F., Amiaud, L., Fillion, J.-H. ., et al. 2007, in Molecules in Space and Laboratory

Eddington, A. S. 1937, The Observatory, 60, 99

Ehrenfreund, P., Boogert, A. C. A., Gerakines, P. A., Tielens, A. G. G. M., & van Dishoeck, E. F. 1997, A&A, 328, 649

Ehrenfreund, P., Breukers, R., D'Hendecourt, L., & Greenberg, J. M. 1992, A&A, 260, 431

Ehrenfreund, P., Dartois, E., Demyk, K., & D'Hendecourt, L. 1998, A&A, 339, L17

Evans, II, N. J. 1999, ARA&A, 37, 311

Famá, M., Bahr, D. A., Teolis, B. D., & Baragiola, R. A. 2002, Nucl. Instrum. and Methods in Phys. Res. B, 193, 775

Fraser, H. J., Collings, M. P., McCoustra, M. R. S., & Williams, D. A. 2001, MNRAS, 327, 1165

Fraser, H. J. & van Dishoeck, E. F. 2004, Advances in Space Research, 33, 14

Fuchs, G. W., Cuppen, H. M., Ioppolo, S., et al. 2009, A&A, 505, 629

Garrod, R., Park, I. H., Caselli, P., & Herbst, E. 2006, Faraday Disc., 133, 5

Garrod, R. T., Weaver, S. L. W., & Herbst, E. 2008, ApJ, 682, 283

Geppert, W. D., Thomas, R. D., Ehlerding, A., et al. 2005, J. Phys.: Conf. Ser., 4, 26

Gerakines, P. A., Schutte, W. A., & Ehrenfreund, P. 1996, A&A, 312, 289

Gerakines, P. A., Schutte, W. A., Greenberg, J. M., & van Dishoeck, E. F. 1995, A&A, 296, 810

Gerakines, P. A., Whittet, D. C. B., Ehrenfreund, P., et al. 1999, ApJ, 522, 357

Gibb, E., Nummelin, A., Irvine, W. M., Whittet, D. C. B., & Bergman, P. 2000a, ApJ, 545, 309

Gibb, E. L. & Whittet, D. C. B. 2002, ApJ, 566, L113

Gibb, E. L., Whittet, D. C. B., Boogert, A. C. A., & Tielens, A. G. G. M. 2004, ApJ Suppl., 151, 35

Gibb, E. L., Whittet, D. C. B., & Chiar, J. E. 2001, ApJ, 558, 702

Gibb, E. L., Whittet, D. C. B., & Schutte et al, W. A. 2000b, ApJ, 536, 347

Giguère, P. A. & Harvey, K. B. 1959, J. Mol. Spec., 3, 36

Gillett, F. C. & Forrest, W. J. 1973, ApJ, 179, 483

Goldsmith, P. F., Li, D., & Krčo, M. 2007, ApJ, 654, 273

Goumans, T. P. M. & Andersson, S. 2010, MNRAS, 406, 2213

Goumans, T. P. M., Uppal, M. A., & Brown, W. A. 2008, MNRAS, 384, 1158

Green, N. J. B., Toniazzo, T., Pilling, M. J., et al. 2001, A&A, 375, 1111

Greenberg, J. M. 1982, in IAU Colloq. 61: Comet Discoveries, Statistics, and Observational Selection, ed. L. L. Wilkening, 131

Grim, R. J. A. & D'Hendecourt, L. B. 1986, A&A, 167, 161

Hagen, W., Allamandola, L. J., & Greenberg, J. M. 1979, Ap&SS, 65, 215

Hasegawa, T. I. & Herbst, E. 1993, MNRAS, 263, 589

Hasegawa, T. I., Herbst, E., & Leung, C. M. 1992, ApJ Suppl., 82, 167

Hendrix, A. R., Barth, C. A., & Hord, C. W. 1999, J. Geophys. Res., 104, 14169

Herbst, E. & van Dishoeck, E. F. 2009, ARA&A, 47, 427

Hidaka, H., Kouchi, A., & Watanabe, N. 2007, J. Chem. Phys., 126, 204707

Hidaka, H., Watanabe, N., Shiraki, T., Nagaoka, A., & Kouchi, A. 2004, ApJ, 614, 1124

Hiraoka, K., Miyagoshi, T., Takayama, T., Yamamoto, K., & Kihara, Y. 1998, ApJ, 498, 710

Hiraoka, K., Sato, T., Sato, S., et al. 2002, ApJ, 577, 265

Hoare, M. G., Kurtz, S. E., Lizano, S., Keto, E., & Hofner, P. 2007, in Protostars and Planets V, ed. B. Reipurth, D. Jewitt, & K. Keil, 181

Hogerheijde, M. 1998, PhD thesis, Dept. of Astronomy, University of California, Campbell Hall, Berkeley, CA 94720, USA

Hollenbach, D. & Salpeter, E. E. 1971, ApJ, 163, 155

Hornekær, L., Baurichter, A., Petrunin, V. V., Field, D., & Luntz, A. C. 2003, Science, 302, 1943

Hornig, D. F., White, H. F., & Reding, F. P. 1958, Spectrochim. Acta, 12, 338

Hudson, R. L. & Moore, M. H. 1999, Icarus, 140, 451

Hudson, R. L. & Moore, M. H. 2000, A&A, 357, 787

Ikeda, M., Ohishi, M., Nummelin, A., et al. 2001, ApJ, 560, 792

Ioppolo, S., Cuppen, H. M., Romanzin, C., van Dishoeck, E. F., & Linnartz, H. 2008, ApJ, 686, 1474

Ioppolo, S., Cuppen, H. M., Romanzin, C., van Dishoeck, E. F., & Linnartz, H. 2010, Phys. Chem. Chem. Phys., 12, 12065

Ioppolo, S., Cuppen, H. M., van Dishoeck, E. F., & Linnartz, H. 2010a, accepted for publication in MNRAS

Ioppolo, S., Palumbo, M. E., Baratta, G. A., & Mennella, V. 2009, A&A, 493, 1017

Ioppolo, S., van Boheemen, Y., Cuppen, H. M., van Dishoeck, E. F., & Linnartz, H. 2010b, submitted to MNRAS

Irvine, W. M., Friberg, P., Kaifu, N., et al. 1990, A&A, 229, L9

Jiang, G. J., Person, W. B., & Brown, K. G. 1975, J. Chem. Phys., 62, 1201

Jónsson, H., Mills, G., & Jacobsen, K. W. 1998, Nudged Elastic Band Method for Finding Minimum Energy Paths of Transitions, ed. B. J. Berne, G. Ciccotti, & D. F. Coker (Singapore: World Scientific), 385

Jørgensen, J. K., Schöier, F. L., & van Dishoeck, E. F. 2005, A&A, 435, 177

Katz, N., Furman, I., Biham, O., Pirronello, V., & Vidali, G. 1999, ApJ, 522, 305

Keane, J. V., Tielens, A. G. G. M., Boogert, A. C. A., Schutte, W. A., & Whittet, D. C. B. 2001, A&A, 376, 254

Keyser, L. F. 1986, J. Phys. Chem., 90, 2994

Khriachtchev, L., Pettersson, M., Jolkkonen, S., Pehkonen, S., & Räsänen, M. 2000, J. Chem. Phys., 112, 2187

Knez, C., Boogert, A. C. A., Pontoppidan, K. M., et al. 2005, ApJ, 635, L145

Kouchi, A. 1990, J. Cryst. Growth, 99, 1220

Kreutz, J., Serdyukov, A., & Jodl, H. J. 2004, Journal of Physics Condensed Matter, 16, 6415

Lacombe, S., Cemic, F., Jacobi, K., et al. 1997, Phys. Rev. Lett., 79, 1146

Lacy, J. H., Faraji, H., Sandford, S. A., & Allamandola, L. J. 1998, ApJ, 501, L105

Lannon, J. A., Verderame, F. D., & Anderson, Jr., R. W. 1971, J. Chem. Phys., 54, 2212

Leung, C. M., Herbst, E., & Huebner, W. F. 1984, ApJS, 56, 231

Linnartz, H., Acharyya, K., Awad, Z., et al. 2007, in Molecules in Space and Laboratory

Liu, S., Girart, J. M., Remijan, A., & Snyder, L. E. 2002, ApJ, 576, 255

Liu, S., Mehringer, D. M., & Snyder, L. E. 2001, ApJ, 552, 654

Loeffler, M. J., Baratta, G. A., Palumbo, M. E., Strazzulla, G., & Baragiola, R. A. 2005, A&A, 435, 587

Loeffler, M. J., Raut, U., Vidal, R. A., Baragiola, R. A., & Carlson, R. W. 2006, Icarus, 180, 265

Madzunkov, S., Shortt, B. J., Macaskill, J. A., Darrach, M. R., & Chutjian, A. 2006, Phys. Rev. A, 73, 020901

Matar, E., Congiu, E., Dulieu, F., Momeni, A., & Lemaire, J. L. 2008, A&A, 492, L17

Mennella, V., Baratta, G. A., Esposito, A., Ferini, G., & Pendleton, Y. J. 2003, ApJ, 587, 727

Mennella, V., Baratta, G. A., Palumbo, M. E., & Bergin, E. A. 2006, ApJ, 643, 923

Mennella, V., Palumbo, M. E., & Baratta, G. A. 2004, ApJ, 615, 1073

Milligan, D. E. & Jacox, M. E. 1964, J. Chem. Phys., 41, 3032

Milligan, D. E. & Jacox, M. E. 1971, J. Chem. Phys., 54, 927

Misochko, E. Y., Akimov, A. V., & Wight, C. A. 1999, J. Phys. Chem. A, 103, 7972

Mitchell, G. F., Maillard, J., Allen, M., Beer, R., & Belcourt, K. 1990, ApJ, 363, 554

Miyauchi, N., Hidaka, H., Chigai, T., et al. 2008, Chem. Phys. Lett., 456, 27

Modica, P. & Palumbo, M. E. 2010, A&A, 519, A22

Mokrane, H., Chaabouni, H., Accolla, M., et al. 2009, ApJ, 705, L195

Moore, M. H., Khanna, R., & Donn, B. 1991, J. Geophys. Res., 96, 17541

Mulas, G., Baratta, G. A., Palumbo, M. E., & Strazzulla, G. 1998, A&A, 333, 1025

Nagaoka, A., Watanabe, N., & Kouchi, A. 2005, ApJ Suppl., 624, L29

Nelander, B. 1980, J. Chem. Phys., 73, 1034

Noll, K. S., Johnson, R. E., Lane, A. L., Domingue, D. L., & Weaver, H. A. 1996, Science, 273, 341

Noll, K. S., Roush, T. L., Cruikshank, D. P., Johnson, R. E., & Pendleton, Y. J. 1997, Nature, 388, 45

Nummelin, A., Whittet, D. C. B., Gibb, E. L., Gerakines, P. A., & Chiar, J. E. 2001, ApJ, 558, 185

Oba, Y., Miyauchi, N., Hidaka, H., et al. 2009, ApJ, 701, 464

Oba, Y., Watanabe, N., Kouchi, A., Hama, T., & Pirronello, V. 2010, ApJ, 712, L174

Öberg, K. I. 2009, PhD thesis, Leiden Observatory, Leiden University, P.O. Box 9513, 2300 RA Leiden, The Netherlands

Öberg, K. I., Boogert, A. C. A., Pontoppidan, K. M., et al. 2008, ApJ, 678, 1032

Öberg, K. I., Bottinelli, S., Jørgensen, J. K., & van Dishoeck, E. F. 2010a, ApJ, 716, 825

Öberg, K. I., Fayolle, E. C., Cuppen, H. M., van Dishoeck, E. F., & Linnartz, H. 2009a, A&A, 505, 183

Öberg, K. I., Fraser, H. J., Boogert, A. C. A., et al. 2007a, A&A, 462, 1187

Öberg, K. I., Fuchs, G. W., Awad, Z., et al. 2007b, ApJ Lett, 662, L23

Öberg, K. I., Garrod, R. T., van Dishoeck, E. F., & Linnartz, H. 2009b, A&A, 504, 891

Öberg, K. I., Linnartz, H., Visser, R., & van Dishoeck, E. F. 2009c, ApJ, 693, 1209

Öberg, K. I., van Broekhuizen, F., Fraser, H. J., et al. 2005, ApJ Suppl., 621, L33

Öberg, K. I., van Dishoeck, E. F., & Linnartz, H. 2009d, A&A, 496, 281

Öberg, K. I., van Dishoeck, E. F., Linnartz, H., & Andersson, S. 2010b, ApJ, 718, 832

Olsen, R. A., Kroes, G. J., Henkelman, G., Arnaldsson, A., & Jónsson, H. 2004, J. Chem. Phys., 121, 9776

Orkin, V. L., Kozlov, S. N., Poskrebyshev, G. A., & Kurylo, M. J. 2006, J. Phys. Chem. A, 110, 6978

Palumbo, M. E. 2005, in IAU Symposium, Vol. 227, Massive Star Birth: A Crossroads of Astrophysics, ed. R. Cesaroni, M. Felli, E. Churchwell, & M. Walmsley, 37

Palumbo, M. E., Baratta, G. A., Brucato, J. R., et al. 1998, A&A, 334, 247

Palumbo, M. E., Baratta, G. A., Fulvio, D., et al. 2008, Journal of Physics Conference Series, 101, 012002

Palumbo, M. E., Castorina, A. C., & Strazzulla, G. 1999, A&A, 342, 551

Palumbo, M. E. & Strazzulla, G. 1993, A&A, 269, 568

Perets, H. B., Biham, O., Manicó, G., et al. 2005, ApJ, 627, 850

Pontoppidan, K. M. 2006, A&A, 453, L47

Pontoppidan, K. M., Boogert, A. C. A., Fraser, H. J., et al. 2008, ApJ, 678, 1005

Pontoppidan, K. M., Dartois, E., van Dishoeck, E. F., Thi, W.-F., & d'Hendecourt, L. 2003, A&A, 404, L17

Pontoppidan, K. M., Dullemond, C. P., van Dishoeck, E. F., et al. 2005, ApJ, 622, 463

Pontoppidan, K. M., van Dishoeck, E. F., & Dartois, E. 2004, A&A, 426, 925

Requena-Torres, M. A., Martín-Pintado, J., Rodríguez-Franco, A., et al. 2006, A&A, 455, 971

Romanzin, C., Ioppolo, S., Cuppen, H. M., van Dishoeck, E. F., & Linnartz, H. 2010, submitted to J. Chem. Phys.

Roser, J. E., Vidali, G., Manrico, G., & Pirronello, V. 2001, ApJ, 555, L61

Ruffle, D. P. & Herbst, E. 2000, MNRAS, 319, 837

Ruffle, D. P. & Herbst, E. 2001, MNRAS, 322, 770

Sandford, S. A., Allamandola, L. J., Tielens, A. G. G. M., & Valero, G. J. 1988, ApJ, 329, 498

Schiff, H. I. 1973, in ASSL Vol. 35: Physics and Chemistry of Upper Atmospheres, ed. B. M. McCormac (Dordrecht: Reidel), 85

Schriver-Mazzuoli, L., de Saxcé, A., Lugez, C., Camy-Peyret, C., & Schriver, A. 1995, J. Chem. Phys., 102, 690

Schutte, W. A., Allamandola, L. J., & Sandford, S. A. 1993, Icarus, 104, 118

Schutte, W. A., Boogert, A. C. A., Tielens, A. G. G. M., et al. 1999, A&A, 343, 966

Schutte, W. A., Greenberg, J. M., van Dishoeck, E. F., et al. 1998, Ap&SS, 255, 61

Sellevag, S. R., Georgievskii, Y., & Miller, J. A. 2008, J. Phys. Chem. A, 112, 5085

Sellgren, K., Werner, M. W., Ingalls, J. G., et al. 2010, ApJ, 722, L54

Shu, F. H., Ruden, S. P., Lada, C. J., & Lizano, S. 1991, ApJ, 370, L31

Sivaraman, B., Jamieson, C. S., Mason, N. J., & Kaiser, R. I. 2007, ApJ, 669, 1414

Stantcheva, T. & Herbst, E. 2004, A&A, 423, 241

Stantcheva, T., Shematovich, V. I., & Herbst, E. 2002, A&A, 391, 1069

Strazzulla, G. & Palumbo, M. E. 2001, Advances in Space Research, 27, 237

Talbi, D., Chandler, G. S., & Rohl, A. L. 2006, Chemical Physics, 320, 214

Teolis, B. D., Loeffler, M. J., Raut, U., Famá, M., & Baragiola, R. A. 2007, Icarus, 190, 274

Tielens, A. G. G. 2005, The Physics and Chemistry of the Interstellar Medium (New York: Cambridge University Press)

Tielens, A. G. G. M. & Allamandola, L. J. 1987a, in ASSL Vol. 134: Interstellar Processes, ed. D. J. Hollenbach & H. A. Thronson, Jr. (Dordrecht: Kluwer), 397

Tielens, A. G. G. M. & Allamandola, L. J. 1987b, in NATO ASIC Proc. 210: Physical Processes in Interstellar Clouds, ed. G. E. Morfill & M. Scholer, 333

Tielens, A. G. G. M. & Charnley, S. B. 1997, Orig. Life Evol. Biosph., 27, 23

Tielens, A. G. G. M. & Hagen, W. 1982, A&A, 114, 245

Tielens, A. G. G. M., Tokunaga, A. T., Geballe, T. R., & Baas, F. 1991, ApJ, 381, 181

Troe, J. & Ushakov, V. G. 2008, J. Chem. Phys., 128, 204307

Tsang, W. & Hampson, R. F. 1986, J. Phys. Chem. Ref. Data, 15, 1087

Tschersich, K. G. 2000, J. Appl. Phys., 87, 2565

Tschersich, K. G., Fleischhauer, J. P., & Schuler, H. 2008, J. Appl. Phys., 104, 034908

Tschersich, K. G. & von Bonin, V. 1998, J. Appl. Phys., 84, 4065

van Broekhuizen, F. A., Pontoppidan, K. M., Fraser, H. J., & van Dishoeck, E. F. 2005, A&A, 441, 249

van de Hulst, H. C. 1996, in IAU Symposium, Vol. 178, Molecules in Astrophysics: Probes & Processes, ed. E. F. van Dishoeck, 13

van Dishoeck, E. F. 2004, ARA&A, 42, 119 van Dishoeck, E. F., Blake, G. A., Jansen, D. J., & Groesbeck, T. D. 1995, ApJ, 447, 760

van Dishoeck, E. F., Helmich, F. P., de Graauw, T., et al. 1996, A&A, 315, L349

van Dishoeck, E. F. & Jørgensen, J. K. 2008, Ap&SS, 313, 15

Vegard, I. 1930, Z. Physik, 61, 185

Vigren, E., Hamberg, M., Zhaunerchyk, V., et al. 2010, ApJ, 709, 1429

Visser, R. 2009, PhD thesis, Leiden Observatory, Leiden University, P.O. Box 9513, 2300 RA Leiden, The Netherlands

Walraven, J. T. M. & Silvera, I. F. 1982, Rev. Sci. Instr., 53, 1167

Watanabe, N., Hidaka, H., & Kouchi, A. 2006a, in AIP Conf. Ser., Vol. 855, Astrochemistry - From Laboratory Studies to Astronomical Observations, ed. R. I. Kaiser, P. Bernath, Y. Osamura, S. Petrie, & A. M. Mebel, 122

Watanabe, N. & Kouchi, A. 2002, ApJ Lett., 571, L173

Watanabe, N., Nagaoka, A., Hidaka, H., et al. 2006b, Planet. Space Sci., 54, 1107

Watanabe, N., Nagaoka, A., Shiraki, T., & Kouchi, A. 2004, ApJ, 616, 638

Watanabe, N., Shiraki, T., & Kouchi, A. 2003, ApJ Lett., 588, L121

Whittet, D. C. B. 2003, Dust in the Galactic Environment (Bristol: Institute of Physics)

Whittet, D. C. B., Bode, M. F., Longmore, A. J., et al. 1988, MNRAS, 233, 321

Whittet, D. C. B., Gerakines, P. A., Tielens, A. G. G. M., et al. 1998, ApJ, 498, L159

Whittet, D. C. B., Shenoy, S. S., Bergin, E. A., et al. 2007, ApJ, 655, 332

Winnewisser, G. & Churchwell, E. 1975, ApJ, 200, L33

Woodall, J., Agúndez, M., Markwick-Kemper, A. J., & Millar, T. J. 2007, A&A, 466, 1197

Xie, D., Xu, C., Ho, T.-S., et al. 2007, J. Chem. Phys., 126, 4315

Xu, C., Xie, D., Zhang, D. H., Lin, S. Y., & Guo, H. 2005, J. Chem. Phys., 122, 244305

Yamada, H. & Person, W. B. 1964, J. Chem. Phys., 41, 2478

Yang, M., Zhang, D. H., Collins, M. A., & Lee, S. 2001, J. Chem. Phys., 115, 174

Yu, H. G. & Varandas, A. J. C. 1997, J. Chem. Soc., Faraday Trans., 93, 2651

Zasowski, G., Kemper, F., Watson, D. M., et al. 2009, ApJ, 694, 459

Zheng, W. & Kaiser, R. I. 2007, Chemical Physics Letters, 450, 55

Ziegler, J. F. 2003, Stopping and Range of Ions in Matter SRIM2003 (available at www.srim.org)

Zuckerman, B., Ball, J. A., & Gottlieb, C. A. 1971, ApJ, 163, L41

Nederlandse Samenvatting

De ruimte tussen de sterren is zeer ijl, ijler dan het beste vacuüm dat we op Aarde kunnen genereren, maar de ruimte is niet leeg. Waterstof en helium gas en resten van zwaardere elementen (~99 %) evenals micrometer grote stofdeeltjes (~1 %) zijn waargenomen in de ruimte tussen de sterren. Dit mengsel van gas en stof wordt het interstellaire medium (ISM) genoemd. Omdat het ISM ook nog eens zeer koud is (enkele tientallen graden boven het absolute nulpunt) werd lange tijd aangenomen dat in het ISM geen chemische processen plaats vinden die kunnen leiden tot de vorming van moleculen. In de jaren dertig van de afgelopen eeuw werden echter in donkere interstellaire wolken de eerste twee-atomige moleculen CN, CH en CH^+ waargenomen. Een nieuwe wetenschap ontstond: de astrochemie. Vandaag de dag, tachtig jaar later, zijn meer dan 150 verschillende moleculen in de ruimte geïdentificeerd, zowel in de gasfase als in de vaste stof, door laboratorium spectra en astronomische waarnemingen te vergelijken. Het betreft kleine 'alledaagse' moleculen zoals CO, keukenzout en water, maar ook exotische radicalen, bv. $HC_{11}N$ en C_6H^-, en organische moleculen, zoals ethanol, dimethylether en ethyleen-glycol, die een mogelijke rol spelen als prebiotische bouwstenen. Een deel van deze moleculen ontstaat in gasfase reacties, een ander deel in de vaste stof, en ook de wisselwerking tussen de gasfase en de vaste stof speelt een belangrijke rol. De onderliggende chemische processen zijn sterk afhankelijk van de evolutionaire levensfase waarin een ster en het haar omringende materiaal zich bevinden.

De nadruk in dit proefschrift ligt op reacties die plaatsvinden in de vaste stof, om precies te zijn in de dunne ijslaagjes op interstellaire stofdeeltjes. Dergelijke ijzige stofdeeltjes ontstaan rond nieuwe sterren wanneer gasfase atomen en moleculen vastvriezen en ze werken als een soort kosmische katalysator. De dichtheid van deeltjes op het oppervlak is aanzienlijk hoger dan in de gasfase - het ijs functioneert als een reservoir - en bovendien biedt het oppervlak een mogelijkheid om overtollige reactie-energie af te voeren. Reacties worden thermisch geïnitieerd, door interactie met energierijke straling, bv. hard UV licht, of deeltjes zoals snelle ionen of waterstofatomen. Om het belang van deze reacties in de ruimte te begrijpen, is het noodzakelijk vergelijkbare reacties op aarde in een laboratorium en onder gecontroleerde omstandigheden na te bootsen.

Experimentele studies van simulaties van ruimte ijs hebben een lange traditie in Leiden. In de 80- en 90-er jaren van de afgelopen eeuw werd m.b.v. hoog-vacuüm (HV) op-

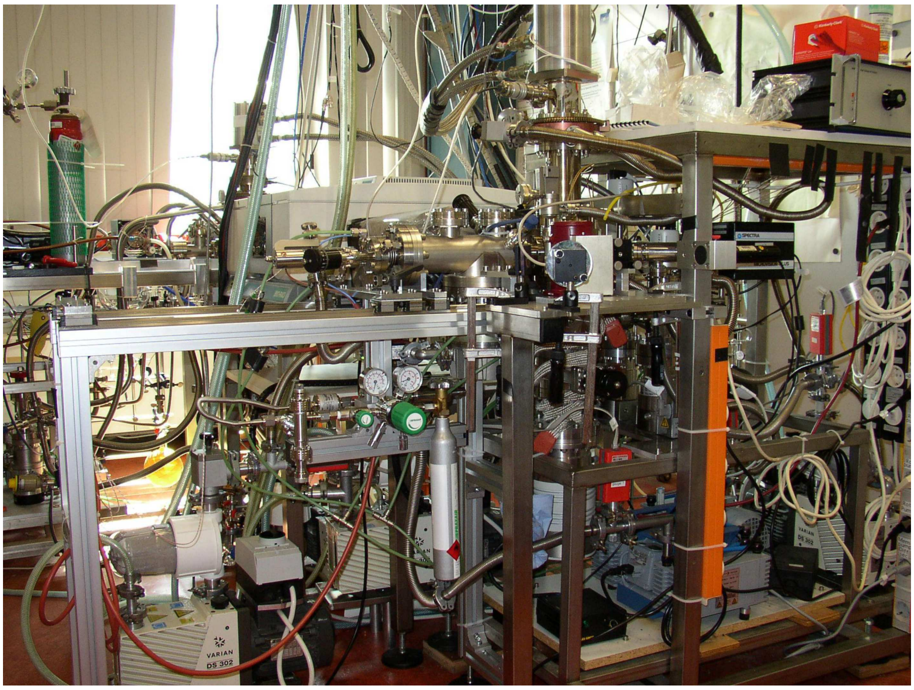

Figure 1 SURFRESIDE (zie ook voorkant proefschrift).

stellingen ($p > 10^{-7}$ mbar, een tienmiljardste van de normale luchtdruk) voor astronomisch relevante temperaturen onderzocht of in realistische (en complexe) ijsmengsels organische moleculen kunnen ontstaan, bv. door dagenlange UV bestraling van een ijs. Inderdaad liet een infrarode en massa spectrometrische analyse van het ijs en van het ijs residu een opmerkelijk scala aan complexe moleculen zien. Het was echter niet mogelijk om individuele reacties te bestuderen en hun afhankelijkheid van relevante parameters zoals bv. de ijs temperatuur. Dit werd mogelijk rond de millennium wisseling door de introductie van ultra-hoog vacuüm (UHV) experimenten ($p > 10^{-11}$ mbar), waarin de mogelijke vervuiling van een ijs door achtergrond gas (voornamelijk H_2; in HV is dit voornamelijk H_2O) een aanzienlijk geringere rol speelt. Interstellaire ijs analogen kunnen tegenwoordig met de precisie van een enkele monolaag worden bereid in het laboratorium en astrofysisch relevante processen worden nagebootst door het ijs te bombarderen met atomen, ionen en electronen of te bestralen met hard UV-licht. Hiermee kan een aantal processen experimenteel worden gekarakteriseerd, zoals diffusie, segregatie, thermische en niet-thermische desorptie, en vooral de vorming van nieuwe moleculen in het ijs. Veranderingen in het ijs worden bestudeerd met UHV detectie technieken, zoals RAIRS (Reflection Absorption InfraRed Spectroscopy), een spectroscopische analysemethode die het mogelijk maakt in-situ, dus in het ijs, signaal sterktes om te rekenen in molecuulabundanties en TPD (Temperature Programmed Desorption), een massaspectrometrische methode waarmee in de gasfase gedesorbeerde moleculen kunnen worden gedetecteerd.

In dit proefschrift ligt de nadruk op ijs reacties van moleculen met individuele waterstof atomen. Gezien de hoeveelheid waterstof in de ruimte, spelen dergelijke reacties een belangrijke rol bij het ontstaan van nieuwe moleculen. In de hoofdstukken 2-8 worden vaste-stofreactieschema's ($CO + H$, $O_2 + H$ en $CO{:}O_2 + H$) besproken, die resulteren in de vorming van H_2CO, CH_3OH, H_2O, CO_2 en HCOOH. Een recentelijk geconstrueerde UHV-opstelling, SURFRESIDE, met daaraan gekoppeld een waterstof atoom bron (HABS) is in deze experimenten gebruikt (zie hoofdstuk 1). Het merendeel van de resultaten dat hier wordt beschreven is met deze Leidse opstelling gerealiseerd en RAIRS en TPD zijn gebruikt om reacties en reactieproducten in het ijs zichtbaar te maken. In hoofdstuk 9 wordt een hoog-vacuum experiment beschreven waarin wisselwerkingen van energierijke ionen met een ijs worden gepresenteerd. De betreffende opstelling bevindt zich in het laboratorium voor experimentele astrofysica in Catania (Italië).

De volgende paragrafen vatten het onderzoek per hoofdstuk kort samen en geven een overzicht van de belangrijkste conclusies.

De vorming van CH_3OH in de vaste stof (hoofdstuk 2)

Hoofdstuk 2 beschrijft de vorming van formaldehyde (H_2CO) en methanol (CH_3OH) door opeenvolgende hydrogenatie reacties in puur CO-ijs ($CO \overset{H}{\longrightarrow} HCO \overset{H}{\longrightarrow} H_2CO \overset{H}{\longrightarrow} H_3CO \overset{H}{\longrightarrow} CH_3OH$). Methanol ijs is waargenomen in de ruimte en een scenario waarin CH_3OH vooral in de vaste stof wordt gevormd is recentelijk flink in de belangstelling gekomen door het inzicht dat gasfasereacties van ionen en neutrale moleculen niet efficiënt genoeg zijn om de waargenomen methanol abundanties in de ruimte te verklaren (Geppert et al. 2005). Eerdere CO + H experimenten (Hiraoka et al. 2002, Watanabe & Kouchi 2002) resulteerden echter in conflicterende conclusies. De ene onderzoeksgroep rapporteerde alleen de vorming van H_2CO, terwijl de andere groep ook de vorming van CH_3OH constateerde. In hoofdstuk 2 wordt bewezen, dat dit een expliciet gevolg was van de verschillende H-atoom fluxen die door beide groepen werden gebruikt en dat methanol inderdaad wordt aangemaakt, zelfs bij zeer lage temperaturen. De vorming van zowel H_2CO als CH_3OH is daarnaast bevestigd m.b.v. massa spectrometrie in een TPD experiment. Verder zijn in hoofdstuk 2 m.b.v. RAIRS de reactie snelheden bepaald voor verschillende ijstemperaturen, ijsdiktes en H-atoom fluxen. Monte Carlo simulaties van de nieuw verkregen experimentele data leveren waarden voor de energiebarrieres van de reacties CO + H en $H_2CO + H$, waarmee het mogelijk wordt om de vorming van methanol te bestuderen onder interstellaire omstandigheden en over astronomische tijdsschalen (Cuppen et al. 2009). De conclusie is dat hydrogenatie reacties van CO-ijs een effectief mechanisme vormen waarmee de astronomisch waargenomen methanolabundanties kunnen worden verklaard. Dit is een belangrijke uitkomst, omdat recentelijk is aangetoond (Öberg et al. 2009b) dat de UV-fotolyse van puur CH_3OH-ijs resulteert in de vorming van een substantieel aantal van de organische moleculen, die reeds in de ruimte zijn geïdentificeerd.

De vorming van H_2O in de vaste stof (hoofdstukken 3-6)

De vorming van water in oppervlakte reacties wordt uitvoerig behandeld in de hoofdstukken 3 t/m 6. In 1982 werd het idee geopperd dat interstellair water ontstaat op stof deeltjes, door hydrogenatie van atomair zuurstof (O), van moleculair zuurstof (O_2) en van ozon (O_3) (Tielens & Hagen 1982). De astrofysische relevantie van deze individuele reactiekanalen is afhankelijk van de plek in de ruimte waar ze plaatsvinden. Cuppen & Herbst (2007) en Cazaux et al. (2010) concludeerden op basis van Monte-Carlo-simulaties dat het eerste kanaal belangrijk is in diffuse wolken, terwijl de beide andere kanalen vooral in dichte en koude interstellaire wolken een rol spelen. Pas recentelijk is het mogelijk gebleken de reactie schema's O + H, O_2 + H en O_3 + H ook experimenteel te realiseren. Het blijkt dat voor astronomisch lage temperaturen alle drie vaste stof kanalen inderdaad resulteren in de vorming van water (Dulieu et al. 2010). Vooral de hydrogenatie van moleculair-zuurstof ijs is intensief bestudeerd in de afgelopen jaren (Miyauchi et al. 2008, Ioppolo et al. 2008, Matar et al. 2008, Ioppolo et al. 2010, Cuppen et al. 2010). In hoofdstuk 3 wordt het reactie mechanisme $O_2 \xrightarrow{2H} H_2O_2 \xrightarrow{2H} 2H_2O$ beschreven voor een reeks van temperaturen onder de thermische desorptie temperatuur van O_2. Vergelijking met de hydrogenatie van CO (hoofdstuk 2) leert dat de efficiëntie waarmee waterstofperoxide (H_2O_2) en water vormen veel minder temperatuur afhankelijk is dan in het geval van formaldehyde en methanol. Ook blijkt O_2-hydrogenatie te resulteren in een aanzienlijk hogere conversie dan de paar monolayers in een vergelijkend CO-hydrogenatie-experiment. De uiteindelijke opbrengst is wel temperatuurafhankelijk. Deze verschillen zijn een direct gevolg van het feit dat de diffusie van H-atomen in een O_2-ijs gemakkelijker plaatsvindt dan in een CO-ijs. Dit is het onderwerp van hoofdstuk 4, waar de reactie O_2 + H wordt onderzocht voor verschillende ijsdiktes, ijstemperaturen, ijsstructuren en waterstofconcentraties in de H-atoom bundel. Hoofdstuk 5 gaat vervolgens in op het onderliggende reactieschema, met het doel om de reactiekanalen en hun relatieve efficiëntie te bepalen. In hoofdstuk 6 wordt tenslotte de hydrogenatie van ozon ijs besproken. O_3 + H is een experimenteel moeilijk te bestuderen reactie, omdat bij de depositie van ozon ervoor gezorgd moet worden, dat het ijs vrij is van moleculair zuurstof. Dit wordt gerealiseerd door het ozon te deponeren bij een temperatuur die hoger is dan de desorptie temperatuur van O_2, maar lager dan die van O_3. Zuurstof moleculen die tijdens de hydrogenatie van ozon ontstaan, desorberen meteen en nemen niet deel in het reactieschema. Op deze wijze is het mogelijk gebleken om de vorming van water via de vervolgreactie van OH met H of H_2 te bestuderen. De reactie O_3 + H lijkt op de hydrogenatie van CO-ijs; alleen de bovenste lagen nemen deel in het reactieschema. Verder lijkt de tunnelreactie OH + H_2 efficiënter te zijn dan de reactie OH + H en deze reacties verdienen in de toekomst zeker een diepergaande studie. De experimentele resultaten tonen aan, dat het oorspronkelijk model met separate O + H, O_2 + H en O_3 + H reactiekanalen te eenvoudig was en dat de drie kanalen in feite sterk onderling gekoppeld zijn door gemeenschappelijke tussenproducten. Dit is van belang voor astrochemische modellen die de vorming van water verklaren voor interstellaire omstandigheden. De data die in deze hoofdstukken worden gepresenteerd zijn belangrijk om in de nabije toekomst astronomische waarnemingen van water (HIFI-Herschel en ALMA) met meer diepgang te interpreteren.

De vorming van CO_2 in de vaste stof: O_2 + H vs. CO + H (hoofdstuk 7)

De resultaten in de hoofdstukken 2-6 zijn gebaseerd op H-atoom interacties met puur ijs (CO, O_2 en O_3). Astronomische waarnemingen laten zien, dat de interstellaire ijs samenstelling aanzienlijk complexer is. Dus hoe gedraagt zich een ijs, dat bv. bestaat uit een mengsel van CO en O_2? In hoeverre beïnvloeden de beide bestanddelen elkaars chemie - ze zijn nu in competitie om met een H-atoom te kunnen reageren - en ontstaan daarbij nieuwe moleculen, die niet worden gevormd in een hydrogenatie-experiment van een enkelvoudig ijs? Deze vragen worden beantwoord in hoofdstuk 7. De gelijktijdige hydrogenatie van CO en O_2 resulteert in de productie van koolstofdioxide (CO_2) door de reactie van OH met CO. Hoofdstuk 7 laat zien, dat het CO en O_2 ook elkaars reactiviteit beïnvloeden. Dit is te verwachten, gezien H-atoom diffusie en penetratie in CO- en O_2-ijs zo verschillend zijn. De reactiesnelheid blijkt daarbij minder afhankelijk te zijn van de mengverhouding als de uiteindelijke productie. De beperkende factor daarbij is vooral de penetratiediepte van de invallende H-atomen. Deze hangt af van de ijs compositie en neemt af voor een toenemende hoeveelheid CO in het ijs. De reactie snelheden voor de vorming van H_2CO, CH_3OH, H_2O_2 en H_2O (gecorrigeerd voor de gereduceerde H-atoom flux) blijven vergelijkbaar binnen de experimentele onzekerheid met de waardes gevonden voor puur CO- en O_2-ijs. De belangrijke conclusie is dat CO_2 ijs gevormd kan worden via een thermische CO + OH reactie.

De vorming van HCOOH in de vaste stof (hoofdstuk 8)

Hoofdstuk 8 behandelt de vorming van mierezuur (HCOOH) in de vaste stof. HCOOH wordt zowel in koudere als warmere gebieden in het ISM aangetroffen, maar het is niet duidelijk hoe dit organisch zuur ontstaat. Als alternatief voor gasfase reactie schema's is een aantal mogelijke reacties in de vaste stof geponeerd; de opeenvolgende toevoeging van H-, O- en H-atomen aan CO ijs (Tielens & Hagen 1982), via de reactie HCO + OH (Garrod et al. 2006) of uitgaande van de hydrogenatie van een HO-CO complex (Goumans et al. 2008), dat in het ijs door intramoleculaire energieoverdracht stabiliseert. De reactie HO-CO + H resulteert vervolgens in een van de reactie producten $CO_2 + H_2$, H_2O + CO of HCOOH. Het doel van hoofdstuk 8 is om te laten zien dat de hydrogenatie van het HO-CO complex een effectieve methode is om bij lage temperatuur mierezuur te vormen. Daartoe wordt met RAIRS en TPD gekeken naar ijs dat ontstaat door gelijktijdig waterstof atomen en een CO:O_2-gasmengsel te deponeren op het cryogeen gekoelde substraat. Na co-depositie wordt inderdaad HCOOH gemeten, wanneer de temperatuur wordt verhoogd tot een waarde onder die van de CO- en O_2-desorptietemperatuur (<30 K). Voor dergelijke temperaturen kunnen H-atomen in de ijsmatrix reageren met het gestabiliseerde HO-CO complex. Voor lage temperaturen blijkt de reactie HCO + OH langzaam te zijn. De conclusies van dit onderzoek zijn in dit hoofdstuk in een astronomische context geplaatst. Hieruit volgt, dat HCOOH-productie uit HO-CO-hydrogenatie een mogelijke verklaring biedt voor de mierezuur dichtheden, die in dichte interstellaire wolken ten tijde van de opwarmings fase van de protoster zijn waargenomen.

De vorming van CO_2 in de vaste stof door ion beschieting (hoofdstuk 9)

In hoofdstuk 7 werd besproken hoe CO_2 ontstaat in een astronomisch relevant temperatuur bereik, door de reactie van CO met OH. In hoofdstuk 9 wordt een alternatieve route besproken, waarbij chemische reacties worden gestart door beschieting met energierijke (30−200 keV) ionen. Voor verschillende ijs samenstellingen worden veranderingen zichtbaar gemaakt m.b.v. infrarood transmissie spectroscopie en de resulterende data worden rechtstreeks vergeleken met astronomische waarnemingen. Het laboratorium werk laat zien dat op deze wijze CO_2 wordt gevormd in ijs dat bestaat uit C- en O-houdende moleculen. De efficiëntie waarmee CO_2 vormt, neemt toe in waterrijke mengsels. Het profiel van de CO_2 strek- en buigvibratie blijkt daarbij afhankelijk te zijn van ijsmengsel en ijstemperatuur (zie ook hoofdstuk 1). De conclusie is, dat ook dit productie proces resulteert in een efficiënte manier om CO_2 onder interstellaire omstandigheden te produceren en dat het reactiemechanisme de hoeveelheid waargenomen CO_2 bij protosterren kan verklaren.

Publications

Refereed papers

- *Water formation by surface O_3 hydrogenation*
  Romanzin, C., **Ioppolo, S.**, Cuppen, H. M., van Dishoeck, E. F., Linnartz, H. 2010, submitted to Journal of Chemical Physics (Chapter 6)

- *Competition between CO and O_2-ice hydrogenation channels and surface formation of CO_2 at low temperatures*
  Ioppolo, S., van Boheemen, Y., Cuppen, H. M., van Dishoeck, E. F., Linnartz, H. 2010, submitted to Monthly Notices of the Royal Astronomical Society (Chapter 7)

- *The influence of temperature on the synthesis of molecules on icy grain mantles in dense molecular clouds*
  Garozzo, M., La Rosa, L., Kanuchova, Z., **Ioppolo, S.**, Baratta, G. A., Palumbo, M. E., Strazzulla, G. 2010, accepted for publication in Astronomy & Astrophysics

- *Surface formation of HCOOH at low temperature*
  Ioppolo, S., Cuppen, H. M., van Dishoeck, E. F., Linnartz, H. 2010, accepted for publication in Monthly Notices of the Royal Astronomical Society (Chapter 8)

- *Water formation at low temperatures by surface O_2 hydrogenation II: The reaction network*
  Cuppen, H. M., **Ioppolo, S.**, Romanzin, C., Linnartz, H. 2010, Physical Chemistry Chemical Physics, 12, 12077-12088 (Chapter 5)

- *Water formation at low temperatures by surface O_2 hydrogenation I: Characterization of ice penetration*
  Ioppolo, S., Cuppen, H. M., Romanzin, C., van Dishoeck, E. F., Linnartz, H. 2010, Physical Chemistry Chemical Physics, 12, 12065-12076 (Chapter 4)

- *Hydrogenation reactions in interstellar CO ice analogues. A combined experimental/theoretical approach*
  Fuchs, G. W., Cuppen, H. M., **Ioppolo, S.**, Romanzin, C., Bisschop, S. E., Andersson, S., van Dishoeck, E. F., Linnartz, H. 2009, Astronomy & Astrophysics, 505, 629-639 (Chapter 2)

- *Formation of interstellar solid CO_2 after energetic processing of icy grain mantles*
  Ioppolo, S., Palumbo, M. E., Baratta, G. A., Mennella V. 2009, Astronomy & Astrophysics, 493, 1017-1028 (Chapter 9)

- *Laboratory evidence for efficient water formation in interstellar ices*
  Ioppolo, S., Cuppen, H. M., Romanzin, C., van Dishoeck, E. F., Linnartz, H. 2008, Astrophysical Journal, 686, 1474-1479 (Chapter 3)

Conference Proceedings

- *Formation of alcohols on ice surfaces*
  Cuppen, H. M., Fuchs, G. W., **Ioppolo, S.**, Bisschop, S. E., Öberg, K. I., van Dishoeck, E. F., Linnartz, H. 2008, Organic Matter in Space, International Astronomical Union Symposium, 251, 377-382

- *Laboratory study of CO ice hydrogenation*
  Ioppolo, S., Fuchs, G. W., Bisschop, S. E., van Dishoeck, E. F., Linnartz, H. 2007, Molecules in Space and Laboratory

- *Solid state astrophysics and chemistry: four questions - four answers*
  Linnartz, H., Acharyya, K., Awad, Z., Bisschop, S. E., Bottinelli, S., Bouwman, J., Cuppen, H. M., Fuchs, G. W., **Ioppolo, S.**, Öberg, K. I., van Dishoeck, E. F. 2007, Molecules in Space and Laboratory

- *Ion irradiation of TNO surface analogue ice mixtures: the chemistry*
  Baratta, G. A., Brunetto, R., Caniglia, G., Fulvio, D., **Ioppolo, S.**, Leto, G., Palumbo, M. E., Spinella, F., Strazzulla, G. 2007, Memorie della Società Astronomica Italiana Supplementi, 11, 185-189

Curriculum Vitae

Originally from Italy, I was born on November 17, 1980 in the city of Catania. In 1994 I began my high school education at the Liceo Scientifico Galileo Galilei, a school for science. I graduated in five years with the highest possible grades. During these years I developed passion for physics and mathematics and I decided to continue my education at the University of Catania at the department of Physics; there I began my specialization in Astrophysics. My master thesis constituted of experimental investigations of the formation of interstellar solid CO_2 after energetic processing of icy grain mantles. The research was carried out in the LASp (Laboratory for Experimental Astrophyiscs) in Catania, under the supervision of Dr. Maria Elisabetta Palumbo and Prof. Giovanni Strazzulla and resulted in a publication.

My following doctoral studies began after receiving an invitation from the Raymond and Beverly Sackler Laboratory for Astrophysics in Leiden, the Netherlands. Supervised by Prof. Harold Linnartz, Prof. Ewine van Dishoeck, and Dr. Herma Cuppen (daily supervisor) my PhD project dedicated to the experimental investigation of surface formation routes of interstellar molecules took shape. All experiments were performed using SURFRESIDE which consists of an ultra-high vacuum main chamber and a hydrogen/deuterium atomic line and allows to study H-atom addition reactions in interstellar ice analogs under astronomically relevant conditions. The doctoral research resulted in seven publications using SURFRESIDE, which are presented in this thesis. In addition, the project required the construction and implementation of a second atomic beam line on SURFRESIDE. I have worked together with Dr. Guido Fuchs and Dr. Claire Romanzin in the development of the new system. Along with my research, I also supervised the work of two bachelor students from the Leiden University and one graduate student from the University of Catania, Italy. Furthermore, I had the opportunity to spend one month as a visiting researcher at the Laboratory for Experimental Astrophysics (LASp). During my PhD studies, I took part of several international and national scientific conferences and summer schools in the Netherlands, the UK, France, Germany, and Iceland where I presented my work. I will continue my scientific career in the Sackler Laboratory for Astrophysics as a postdoctoral researcher with the intention to test, prove and tune the newly reconstructed SURFRESIDE setup, and to continue the investigation of more complex surface formation routes of interstellar molecules by using a double atomic beam line.

Acknowledgements

This PhD thesis is the collective result of hard work of many people. That is why I am sincerely grateful to all persons involved in my research during the past four years. These following couple of pages will allow me to mention and thank at least some of them. Among the people that I can name here, I would like to thank the computer department (Aart, David, Erik, and Tycho) as well as the support staff (Anita, Evelijn, Jeanne, Kirsten, and Liesbeth) for being always kind and helpful. A close collaboration with the machine workshop FMD/ELD of the Faculty W&N made this work possible. I express my gratitude to Ewie, Gijsbert and most of all to Martijn who always came to help when I needed technical support in the laboratory. With Martijn I do not only share the passion for science but also for climbing. Last but not least, my appreciation is extended to the electronic, glass-blower and cryogenic departments. It was my pleasure to work with every single one of you. Thank you.

Perhaps the most prominent place within this acknowledgement belongs to the co-authors of this thesis; in particular Claire Romanzin, Guido Fuchs, Herma Cuppen, Stefan Andersson, Suzanne Bisschop and Yorick van Boheemen. Their dedication and professionalism made our cooperation dynamic and successful. In addition, I am deeply grateful to the LASp group from Catania (Italy) who introduced me to the astrochemistry several years ago and with whom I kept collaborating also during my PhD. This inspiring collaboration resulted in a publication included in this thesis. I thank Gianni Strazzulla, Maria Elisabetta Palumbo, Giuseppe Baratta, Giuseppe Leto and Franco Spinella from Catania observatory, and Vito Mennella from Naples observatory. Stimulating discussion with Lou Allamandola, Xander Tielens, Marc van Hemert, Fedor Goumans, Carina Arasa and Erik Vigren improved the quality of this thesis.

The following paragraph is dedicated to my colleagues and friends from the Sterrewacht. I would like to thank the AstroChem group, but since there are too many of you I will not attempt to name all of you, since I would surely forget a few. Special gratitude goes to the Sackler Laboratory for Astrophysics. In the four years of my PhD, I have been lucky to meet exceptional people and colleagues and to develop close friendships. Herma, working with you is a pleasure. You taught me a lot, helping me throughout my PhD. Your friendship is precious to me. Jordy, you are a great friend, without you the Lab wouldn't have been the same. Claire, Edith, Guido, Harald, Joseph, Karin, Karoliina,

Nadine, and Suzanne, I enjoyed the time we spent together in and outside of the Lab. Michele, Emily, and little Francesca, I feel lucky I met such a great family and friends. To the new people in this group, Gleb, Jean-Baptiste, and Steven, I wish all the best. Dominic, Simon, Karoliina, Silvia, Ernst, and Francisco, you are the best office mates. Outside of work, I would like to mention a few friends that stayed by me throughout the years. Rafael, we shared so many great and unforgettable moments, you are a real friend. Kalle, our sailing trip along the West Swedish coast is one of the best adventures of my life. Nicola, you made our weekly climbing sessions a pleasure. Titti and Carina, you made me laugh like never before. Franco, Paola, and Daniele, thank you for making my time abroad less lonely, I consider you to be part of my family.

Last but not least, I would like to dedicate this thesis to my family and friends in Italy. Without them I wouldn't be where I am now. I always keep them close to my heart. Petra, I owe you everything, your boundless support and infinite love pulled me through the hardest times. Papà, Mamma and Ivana this thesis is for you.

Notes: